GASIFICATION STUDIES OF MODEL REFUSE DERIVED FUEL (RDF)

A Dissertation
Presented to
The Academic Faculty

by

Sireesha Aluri

In Partial Fulfillment
of the Requirements for the Degree
Doctor of Philosophy in the
School of Chemical and Biomolecular Engineering

Georgia Institute of Technology
August 2018

GASIFICATION STUDIES OF MODEL REFUSE DERIVED FUEL (RDF)

Approved by:

Dr. Pradeep K. Agrawal, Advisor
School of Chemical & Biomolecular Engineering
Georgia Institute of Technology

Dr. Ryan Lively, Committee Member
School of Chemical & Biomolecular Engineering
Georgia Institute of Technology

Dr. Carsten Sievers, Advisor
School of Chemical & Biomolecular Engineering
Georgia Institute of Technology

Dr. Yulin Deng, Committee Member
School of Chemical & Biomolecular Engineering
Georgia Institute of Technology

Dr. John Muzzy, Advisor
School of Chemical & Biomolecular Engineering
Georgia Institute of Technology

Dr. Derrick Flick, Committee Member
Lead R&D Manager
The DOW Chemical Company

Date Approved: [April 27, 2018]

ACKNOWLEDGEMENTS

The last five years at Georgia Tech have been very enlightening yet very challenging for me. There are many people without whom I would not have been able to achieve this milestone in my life. Firstly, I would like to thank my research advisors, Dr. Pradeep Agrawal, Dr. Carsten Sievers and Dr. John Muzzy. Their invaluable expertise and experience have helped me greatly in streamlining my research to achieve the set goals. It would not have been possible for me to reach this stage if not for their continuous mentorship, advice and guidance. I would also like to thank my committee members, Dr. Ryan Lively, Dr. Yulin Deng and Dr. Derrick Flick for their useful comments and suggestions, which helped me probe further into understanding the subject matter. The funding provided by The Dow Chemical Company for this research is greatly appreciated.

Several engineers and researchers have assisted me during the course of my Ph. D. in accomplishing various goals of my research. I extend my gratitude to Steve Lien for helping me build several experimental setups and for aiding me with troubleshooting various issues. I am extremely grateful to Dr. Ildar Musin, who has been the frontrunner in designing the BFBR and automating several components of the experimental setups that have been used in my research. I thank Dr. Scott Sinquefield for aiding with the design of the BFBR components. The assistance given by Brian Markowicz and Ashley Elayne with building and repairing the quartz reactor and other glass components is appreciated. I would also like to thank Tabassum Shah and Mike Buchanan for their valuable time and input in analyzing the inorganics present in the feed and char samples. I would like to extend my gratitude to Melinda Jue in Lively group whose ideas and assistance have helped

me conquer myriad obstacles. I would also like to thank Fengyi Zhang for his assistance with the mercury porosimetry runs.

I would like to thank the group members of Agrawal and Sievers group, especially, Akil Syed, Gautami Newalkar, Ildar Musin, Olga Simakowa, Chuck Okolie, Jungseob So, Guo Shiou Foo and Michael Stellato. The discussions with Akil Syed and Ildar Musin have in particular, been very helpful in orienting the research in the right direction. Time spent with Lisa Wiest, Elise Albuquerque, Mariana Rodrigues, Yimeng Lyu, Andrew Tricker, Qandeel Almas, Jason Lee and Alex Brittain will always be memorable. The novel methodology developed with quantifying EDX maps wouldn't have been possible without the assistance of Michael Stellato. I would like to thank Lehigh technologies and Polyquest Inc. for supplying rubber and PET particles for this research, free of cost. I would also like to thank the support staff in Ford ES&T and RBI buildings for helping me solve the day-to-day problems, especially, Kevin Guger, Jerry Nunn, Valarie Spradling, Kysten Riley, Kathy Huggins, Mary Williams and Hank (Major) White.

I have had the opportunity to have worked with an army of undergraduate students over the course of five years to have a continuous supply of the diverse RDF feed used for this study. I would like to thank Christopher Schmitt, Karina Psareva, Yiquiong Zhang, Wing Lam, Isil Deniz, Sneha Singh, Joe Cantatore, Courtney Smith, Alexandra Holderied, Cody Blackwell, Bailee Decker, Hannah McCullogh, Morgan Ooten, Alejandro da Silva, Nathan Tait, Ivana Chen, Hursh Sureka for their time and assistance to help me complete my research. In particular, the contribution of Alejandro da Silva in generating the required amounts of char in the heating rate study is greatly appreciated. Yiquiong Zhang, Isil Deniz and Wing Lam also deserve appreciation for their assistance with char generation.

The last five years have been a rollercoaster of experiences and many individuals are responsible for keeping me going during this time. Nothing would have begun without Bhanu Kishore, Jayaram Valluru, Swetha Rathan and Anusha Garapaty who helped me move to Atlanta on a day's notice. I have had the great fortune of making several friends in Atlanta whose positive impact on my life has helped me deal with the trials of grad school. I would especially like to thank my classmates, Lalit Darunte, Anshuman Sinha, Harrison Rose, Melinda Jue, Kathy Bates, Shan Tie, Xu Du and Andrew Star for their friendship and support through all these years. Special thanks to Gautami Newalkar, Udita Brahmachari and Chandrani Pramanik for their support and guidance during difficult times. Friendship with Rohan Awati, Gamze Eris, Pradnya Samant, Akshay Korde, Jaya Arya, Shilpa Mahamulkar, Trisha Sen and Simple Kumar will forever be cherished.

Lastly, I am grateful for the unconditional love and support of my family through all these years. I am forever indebted to my wonderful parents, Kalyani Pathaneni and Gadadhar Aluri for making me the person I am today. I am at a loss of words to express my love and admiration towards my amma, Ramalakshmi Pathaneni and my brother Hemanth Aluri for being the pillars of my life. I thank my husband, Prineet Ramakur, for always being there for me and believing in me when I didn't believe in myself. I could not have completed my Ph.D. without his love and support. I am also thankful to my in-laws, Chitra Ramakur, Vijay Kumar Ramakur and Kashyap Ramakur for their kindness and compassion.

TABLE OF CONTENTS

LIST OF TABLES

LIST OF FIGURES

LIST OF SYMBOLS AND ABBREVIATIONS

(σ/μ)	Coefficient of variation
μ	Mean
BET	Brunauer–Emmett–Teller
BFBR	Bubbling Fluidized Bed Reactor
CHNO	Carbon, Hydrogen, Nitrogen, Oxygen
DI	Deionized
DR	Dubinin-Radushkevich
DSC	Differential Scanning Calorimetry
DTG	Differential Thermo-gravimetric
EDX	Energy Dispersive X-ray spectroscopy
EPA	Environmental Protection Agency
FBR	Fluidized Bed Reactor
F_c	Carbon flow rate flowing in with the feed
FWHM	Full Width at Half Maximum
GC	Gas Chromatography
H/C	Hydrogen to carbon ratio
HDPE	High Density Polyethylene
HHR	High Heating Rate
HHV	Higher heating value
HPLC	High-Performance Liquid Chromatography
ICP - OES	Inductively Coupled Plasma – Optical Emission Spectroscopy
I_{D1}/I_G	Ratio of Raman band D1 over G band
I_{D3}/I_G	Ratio of Raman band D3 over G band

I_G/I_{all}	Ratio of Raman band G over all the bands (D1, D2, D3, D4, G)
IPCC	Intergovernmental Panel on Climate Change
K/C	Potassium to Carbon ratio
K/Si	Potassium to Silicon ratio
LDPE	Low Density Polyethylene
LHR	Low Heating Rate
LHV	Lower heating value
m_0	Initial mass at introduction of gasifying agent
m_{ash}	Final mass at the end of gasification
MFC	Mass Flow Controller
MSW	Municipal Solid Waste
m_t	Mass at time 't'
n_i	Number of carbon atoms in gas component 'i'
NTP	Normal Temperature and Pressure
O/C	Oxygen to carbon ratio
PACs	Polyaromatic Compounds
PAHs	Polynuclear Aromatic Hydrocarbons
PET	Polyethylene Terephthalate
PP	Polypropylene
PS	Polystyrene
R	Reactivity
RDF	Refuse Derived Fuel
SBR	Styrene Butadiene Rubber
SEM	Scanning Electron Microscopy
SLPM	Standard liters per minute

STP	Standard Temperature and Pressure
TCD	Thermal Conductivity Detector
TG	Thermo-gravimetric
TGA	Thermogravimetric Analyzer
V_i	Average volumetric flow rate of gas component ‘i’
X	Conversion
σ	Standard deviation

SUMMARY

Municipal Solid Waste (MSW) is the everyday garbage generated by households and commercial buildings. According to EPA, 251 million tons of MSW was generated in the USA in 2012. Even after recycling, 65.3 % of the waste was discarded in landfills or incinerators. An alternative solution for the disposal of the enormous amount of non-recycled MSW is its conversion to Refuse Derived Fuel (RDF) using certain pre-processing techniques. Since a large portion of the RDF is organic, it is possible to transform it to syngas (H_2 and CO) using pyrolysis and gasification techniques. This syngas can further be converted to fuels and chemicals or used for power generation using known techniques. In addition to energy recovery, the use of RDF as a feedstock leads to the overall reduction of discarded waste in landfills, while also meeting pollution control standards. Thus, the year-round availability, abundance and zero to negative costs make RDF a potential alternative feedstock for syngas production.

The biggest challenge in processing real RDF is its variability with location and season. Moreover, a mixture of several different components at small sample sizes induces variability in lab scale studies. To obtain reproducible results from a homogeneous feed source, a model RDF composition was established based on EPA data. This work aims at understanding the pyrolysis and gasification studies of the model RDF at both the fundamental level as well as industrially relevant conditions. The fundamental studies are discussed in the first three parts (Chapters 2 – 4) of the dissertation while the gasification of RDF pellets is investigated in a Bubbling Fluidized Bed Reactor (BFBR) in the fourth part (Chapter 5). Since gasification has a longer time-scale compared to pyrolysis, it is the

rate-limiting step in the conversion process. Thus, the experimental approach for the fundamental studies has been to independently study pyrolysis and gasification.

The first study analyzes the pyrolysis of individual components to define the model components that represent real RDF. Size reduction and effective mixing of nine components of model RDF composition allow for reproducible results in lab scale experiments. Selected individual components as well as the model RDF composite are subjected to pyrolysis by heating to 800 °C at a 20 K/min ramp rate. The pyrolysis results show that the decomposition profile, product yields, heat of decomposition, and gas composition of the model RDF can be predicted by adding the corresponding values of the individual components in the required proportions. The inorganic content of the individual component chars is found to have a profound effect on the gasification reactivities. Potassium and calcium have the largest catalytic effect during gasification, while silicon and phosphorous inhibit gasification. Potassium mobility and redistribution from orange peels in the model RDF to the other components is determined to be chiefly responsible for the synergistic gasification profile of the char.

The second study further explores the effect of potassium, calcium and silicon rich components in both CO_2 and steam gasification. Gasification of in-situ pyrolyzed char is performed at 800 °C in both CO_2 and steam separately. Potassium exhibits higher catalytic ability than calcium in both the gasifying mediums. The transient reactivity profiles in steam are further influenced by the production of hydrogen depending on the type and amount of inorganic content present. Catalytic activity of potassium is quantified by comparing reactivities of several potassium-doped Avicel (microcrystalline cellulose) chars with increasing amounts of potassium. A saturation is observed at 5% potassium

loading below 60% conversion. At higher conversions, a maximum is observed that is dependent on the [K / residual carbon] ratio. Reaction mechanisms for potassium are established during different stages of gasification in both CO_2 and steam. Although hydrogen inhibits the gasification reactivity of calcium-rich chars, the reactivity is enhanced when small amounts of hydrogen are introduced during the gasification of potassium-rich chars. The increased reactivity in steam is identified to be a result of the formation of a KOH phase instead of the K_2O phase present in CO_2 gasification. The same active sites participate in both CO_2 and steam gasification based on gas – switchover experiments. Co-gasification studies for model RDF char are carried out with the simultaneous introduction of CO_2 and steam of varying mixture ratios where steam is completely dominant over CO_2 even when the former is diluted by CO_2 down to 30%.

The third study focuses on the pyrolysis heating rate, one of the most significant pyrolysis conditions that affects the char reactivity. A quartz tube reactor is used to generate RDF char at both low heating rate (LHR) and high heating rate (HHR) conditions. Additionally, two different chars at HHR are produced at varying residence times. All the chars are characterized using SEM and EDX to understand the morphological changes and inorganic distribution as a function of pyrolysis conditions. HHR chars are found to be more macroporous than LHR chars and the pellet dimensions peak at intermediate conversions. Potassium distribution across the surface is incomplete at low exposure times (10 seconds) in HHR conditions. A new methodology is introduced where the potassium EDX maps are quantified using a MATLAB program. The novel methodology is capable of being extended to quantify other EDX mappings. Furthermore, several correlations are established between the CO_2 gasification reactivity of chars and the O/C ratio, H/C ratio,

surface areas and Raman band ratios. The initial reactivity of all the chars linearly correlated with the O/C ratio and the I_{D1} / I_G band ratio determined by Raman spectroscopy. Whereas, the overall reactivity presented a linear relationship with the combination of the macroporous and mesoporous surface areas of the chars.

The fourth and final study demonstrates the gasification of model RDF pellets in a custom designed multistage bubbling fluidized bed reactor (BFBR) with industrially relevant experimental conditions. The primary objective of this study is to decrease the tar formation and increase carbon recovery in the gas fraction. The novelty of the reactor design is in the three stages of the fluidized bed. The first stage (bottom zone) is where the feedstock is quickly heated to a high temperature to achieve rapid pyrolysis. The second stage (middle zone) has a larger cross-sectional area than the first zone to minimize entrainment of solids in the second zone and to increase the residence time to gasify char. The diameter of the third stage (top zone) is even larger to permit only the lightest particles (ash content) to leave the reactor with the gas flow. The flexibility of this reactor is demonstrated by the gasification of both pine particles and RDF pellets. CO_2 gasification of both feeds primarily produces CO followed by hydrogen. Since product CO_2 gas could not be distinguished from reactant CO_2 gas, further studies are conducted with steam. The use of steam as a gasifying agent increases both the hydrogen content (equal molar fraction as CO) and the carbon recovery in the gas fraction to about 72% from 56% in CO_2 gasification. $C_2 – C_4$ hydrocarbon content is considered as a tar proxy for comparison of different experimental conditions. An increase in the gasification temperature from 800 °C to 900 °C and the use of 500 ppm of oxygen increases the hydrogen content in the gas fraction and decreases the $C_2 – C_4$ hydrocarbons (tar content). The improved hydrogen in

the presence of oxygen is a result of an augmented temperature due to combustion heat. Additionally, introduction of oxygen increases the CO_2 fraction as expected from combustion. The experimental conditions for lowest tar content (tar proxies), highest carbon recovery in the gas fraction (86.4%) and the highest thermal efficiency (81.9%) are a combination of an increased temperature (930 °C) and the introduction of 500 ppm of oxygen in the gas feed.

.

CHAPTER 1. INTRODUCTION

The motivation behind the work done in this Thesis is explored in this Chapter. A discussion on the selected feedstock as a potential alternative energy source is followed by an overview of the recent literature on similar work. Finally, the objectives of this Thesis and the organization of the various studies conducted to achieve these objectives are summarized.

1.1 Need for alternative energy sources

One of the major challenges in the world is the increasing energy demand. As the world's population increases, the rate at which energy is consumed also increases. More than 80% of the current energy demand is supplied by fossil fuels [1]. Fossil fuels constitute oil, coal and natural gas. The visualization in Figure 1.1 shows the global consumption of fossil fuels over the last 200 years. As can be seen from the figure, the consumption rate has increased by more than 1300 times since the year 1800. Currently, crude oil is the largest energy source supplying 32% of the world's energy [2].

The task of predicting the right time at which fossil fuels will be entirely depleted is a complex problem. This is due to the discovery of new reserves and improvement in the technological potential to extract these reserves which evolves with time. However, a few studies have attempted to identify an exact time based on current data. Oil reserves are vanishing at the rate of 4 billion tonnes a year with over 11 billion tonnes of consumption

[3]. With the present consumption rate of fossil fuels deemed constant, studies have estimated that the oil deposits will last until 2052, natural gas until 2060 and coal until 2088 [3].

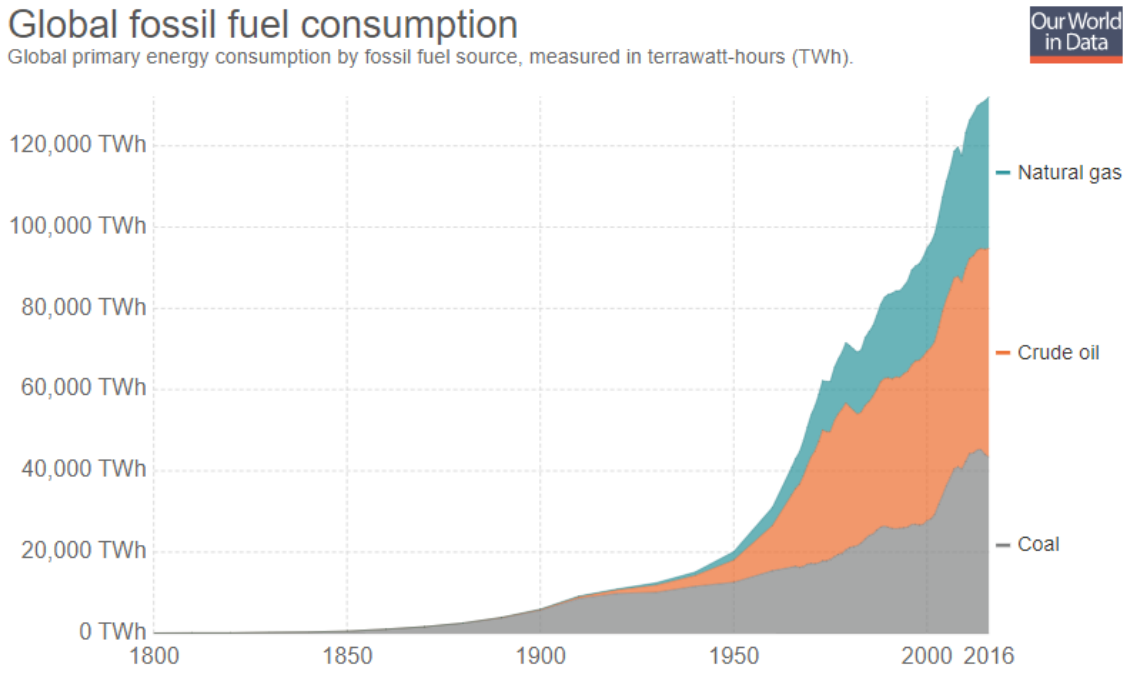

Figure 1.1. Global consumption of fossil fuels from 1800 to 2016. [2]

Although there is an incessant debate on whether the fossil fuels are going to last a couple hundred years or a few decades, the fact remains that they are a finite source of energy [3,4]. They are either going to be completely exhausted or become too expensive to realistically use. However, when the moment does arrive, an instantaneous switch cannot be made from the fossil fuel based energy to alternative energy. This is because the energy production is highly reliant on the infrastructure built around fossil fuels, which accounts for more than 80 percent of the total energy generated [1]. Thus, alternative energy sources must be studied and developed as early as possible to gradually replace fossil based energy.

While depleting fossil fuel sources may become a burning issue 50 – 100 years from now, there is another factor for limiting fossil fuel consumption: climate change. NASA has estimated that the temperature of Earth is going to increase by 2 – 6 °C in the next century [5]. Compared to the 5 °C increase in the last 5000 years, the predicted rate for the next century is alarmingly high. Fossil fuel consumption is a major contributor to this global warming as it produces large amounts of carbon dioxide. In addition to global warming that results in draughts and causes the sea-level to rise, fossil fuels also instigate significant air pollution.

To keep the average temperature rise below 2 degrees (as has been agreed in the UN Paris Agreement), the cumulative amount of carbon dioxide that can be emitted is called 'carbon budget'. In the recent Intergovernmental Panel on Climate Change (IPCC) report, a 50% probability of maintaining the temperature rise below 2 degrees was estimated to be around 275 billion tonnes of carbon [6]. If all of the known reserves (without the use of carbon capture and storage technology) were burned, a total of about 750 billion tonnes of carbon would be emitted [4]. Thus, around two-thirds of known reserves need to be left in the ground in order to meet our global climate targets. Although this is a simplification of the real situation, it highlights the importance of the need to switch from fossil fuel based energy to alternative energy sources.

The most common alternative energy sources are nuclear energy, solar energy, hydro energy, wind energy, geothermal energy and bioenergy. Although nuclear energy supplies about 9% of all the energy requirements of the USA, uncertainty regarding the safety and detrimental effects on the environment leave it less desirable [7]. The rest of the alternative energy sources combined meet 10% of the energy demand of the US [7]. The

major advantage of these energy sources is that since they are renewable, there is no fear of depletion. The use of these energy sources leaves little to no carbon footprint on the environment. Moreover, they are more readily accessible to individual use. However, the biggest hurdle for utilizing renewable energy sources like wind and solar energy is that they are intermittent. This intermittency makes it difficult to derive reliable continuous power from these sources. Although geothermal energy is renewable, it is very location specific and thus cannot significantly compensate for lower fossil fuel usage [8].

Bioenergy accounts for almost 50% of the total 10% energy demand met by alternative energy sources [7]. The wide availability, neutral carbon footprint and flexibility to be incorporated into existing infrastructure makes it the most utilized alternative energy source. However, the increasing concern about the sustainability of first generation biofuels due to competition with food production has raised attention to the potential of using lignocellulosic biomass waste for the production of second generation fuels and chemicals [9]. Due to the various advantages and disadvantages of each of the alternative energy sources, one particular substitute does not stand out. Instead of relying on a single alternative energy source to completely replace fossil-based energy, a combination of alternative energy sources would lead to a better solution.

1.2 Municipal Solid Waste (MSW) as a potential feedstock

The second generation biofuels are produced from biomass that is devoid of starches and simple sugars, called lignocellulosic biomass [10]. Biomass currently supplies 5% of all the U.S energy needs [7]. Since CO_2 produced from biomass is partially compensated by the CO_2 consumed while growing biomass, it is closer to neutral carbon footprint. Moreover, among all the available sources of renewable energy, only biomass

can be converted to liquid fuels and chemicals. The flexibility of using biomass as a co-feed with fossil fuels in the established infrastructure also makes it a valuable alternative feed source. Although biomass as an alternative fuel has many advantages, there are a few hurdles with processing biomass into fuels and chemicals.

The challenges with using biomass as a feedstock for fuels and chemicals include scalability and seasonal dependence. The unavailability of a particular feedstock all through the year requires large storage facilities. Moreover, the land available for cultivation of a particular crop and the variability of cultivated biomass with location limits the scale of the feedstock that can be processed. Extensive water and fertilizer use have also become a concern. Additionally, there are costs involved in the production and purchase of the biomass feedstocks which adds to the cost of the fuels produced.

Municipal solid waste (MSW), on the other hand, is the everyday waste produced in households and commercial buildings that has a year-round availability. What makes it appealing as a feedstock is its easy availability with a pre-existing collection and transportation infrastructure. Moreover, it has no other potential use like biomass feedstocks. The economics associated with MSW are very different from conventional biomass feedstocks. For instance, in a study, it was quoted that the conventional biomass costs about $44/dry ton to purchase as a feedstock, while there is a $30/ton tipping fee just to landfill the MSW material [11]. By charging this additional tipping fee, it is possible to achieve favorable economics for fuels synthesis even at a much smaller scale production.

It was estimated that a single individual generates 4.38 lbs of waste per day [12]. The abundance of this feedstock is reflected in EPA data, which shows that 251 million

tons of MSW were generated in the year 2012 across the country [12]. Even after recycling 87 million tons of material, a large part of the generated MSW (~65.3% i.e., 164 million tons) was discarded as landfill. In 2009, there were approximately 1,908 MSW landfill sites in the US [12]. In addition to requiring a vast area of land, landfills need to be properly closed to avoid methane and other gas leaks from the ground. Continuous monitoring and maintenance of these sites requires substantial financial support. The alternate process used to discard the non-recycled portion of MSW is incineration. Although it is cheaper than landfills, the uncontrolled burning of MSW leads to release of harmful pollutants into the atmosphere. Instead, MSW can be used as a potential feedstock for the production of fuels and chemicals. Besides recovery of substantial energy, the use of MSW as a feedstock can lead to a substantial reduction in the overall waste quantities requiring final disposal while meeting the pollution control standards. Thus, year-round availability, large quantities of waste generated and zero to negative cost make MSW a potential alternative feedstock for the production of fuels and chemicals.

One of the most utilized thermochemical pathways for converting organic feedstock into fuels, chemicals or electricity is gasification. MSW has potential as a gasifier feedstock because of its higher heating values (HHV) of about 10 - 16 MJ/kg, which is close to most conventional biomass feedstocks with HHVs of 15 - 20 MJ/kg [13,14]. The composition of the total MSW generated in 2012 (251 million tons) in the country is shown in Figure 1.2 [15]. Since more than 80% of MSW is organic, it is a suitable feedstock for producing syngas ($CO + H_2$).

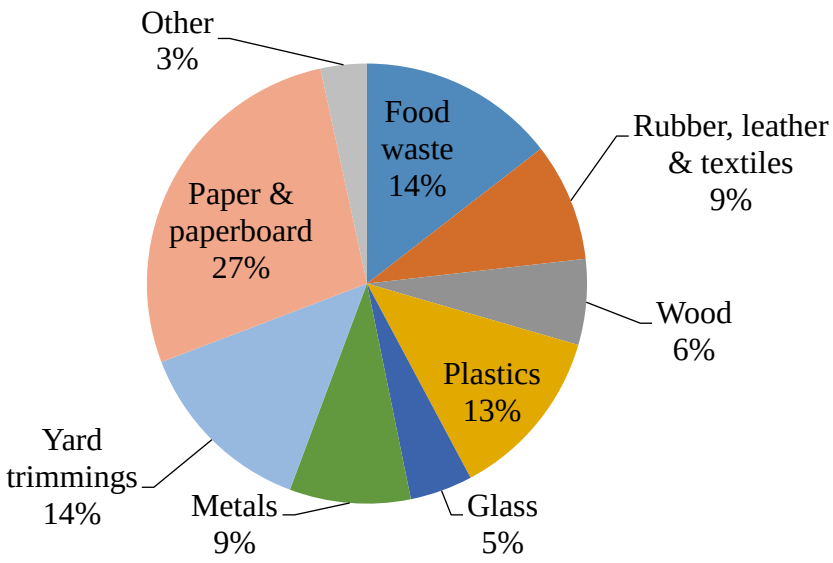

Figure 1.2. Composition of total MSW generated in 2012. [15]

Significant amounts of material from each category were recycled or composted in 2012. The highest recovery rates were achieved in paper and paperboard (more than 64%) and yard trimmings (19 million tons). Recycling these materials alone kept over 28% of the MSW generated out of landfills and incineration facilities. After recycling, the composition of the discarded portion (164 million tons) of MSW was altered as represented in Figure 1.3. The major components in the discarded portion were found to be food waste (21%), plastics (18%) and paper waste (15%).

MSW feedstock is heterogeneous and varies with location and season. The heterogeneous feedstock contains materials with widely varying sizes, shapes and composition. This can be difficult to feed into many gasifiers and can lead to variable gasification behavior if used in an as received condition. Significant differences in the results have been reported when MSW produced in different locations and in different

seasons was processed [11,16]. The studies show that the heterogeneous nature of MSW and the resulting variance of the properties, such as elemental composition, density, water content, and structure lead to inconsistent results. This variation is attributed to different trends of consumption of materials in different locations and seasons [17]. Thus, pre-processing techniques, like size reduction and sorting, are needed to make MSW suitable as a feedstock for MSW gasifiers.

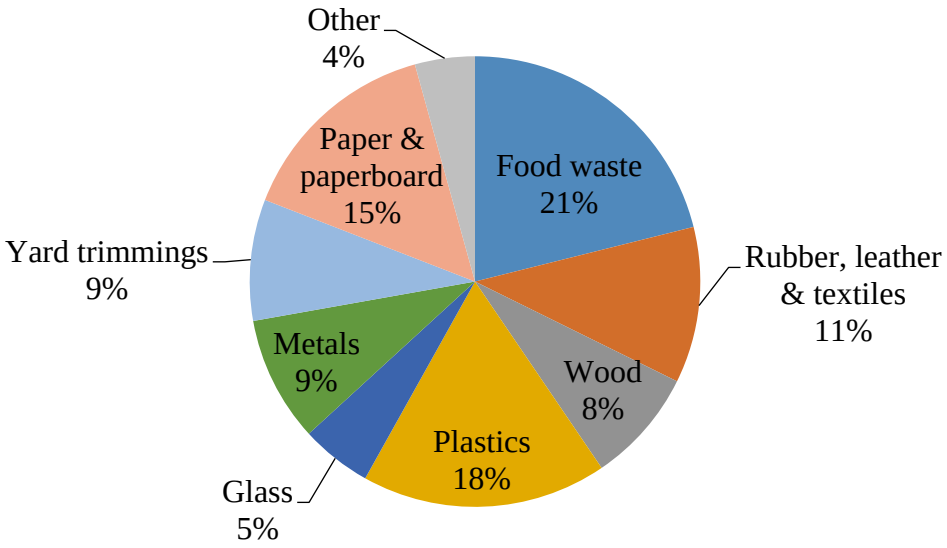

Figure 1.3. Composition of discarded portion of the MSW generated in 2012. [15]

Refuse derived fuel (RDF) is a processed form of MSW where significant size reduction, drying, screening, sorting, metal and glass separation and, in some cases, pelletization is performed to improve the handling characteristics and composition of the material to be fed to a gasifier [18]. A schematic of one combination of these pre-processing techniques is shown in Figure 1.4. This is followed by a drying step to form the final pellets to be gasified. This pre-processing step alters the composition of the waste by reducing the

metal, glass and moisture content of the discarded portion and increasing the volatile content of RDF.

Depending on the composition of the final RDF and the technology used, various types of RDFs can be made, such as coarse, fluffy, powdered or densified. It has a higher volumetric energy density since these products have significantly smaller volume than the original waste. This makes them a more compact source of energy. Compared to other forms of waste derived energy, they are also easier to transport and store. The briquettes and pellets can be used directly on a large scale as a gasification feed. RDF pellets are estimated to have a heating value of around 60% of coal [18].

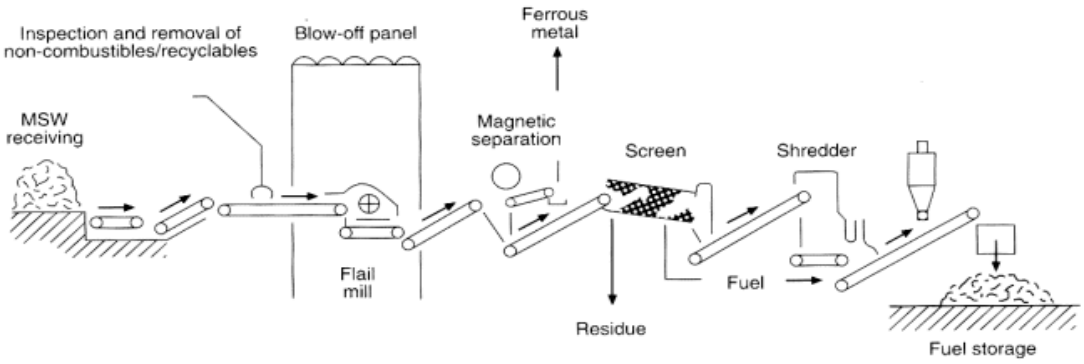

Figure 1.4. Pre-processing techniques used to convert Municipal Solid Waste (MSW) into Refuse Derived Fuel (RDF). [18]

1.3 Overview of gasification processes

Gasification involves conversion of carbonaceous feedstock primarily into syngas ($CO + H_2$) with a limited amount of oxygen present by the thermal decomposition of the organic matter. Combustion, on the other hand, results in the formation of carbon dioxide and water along with the heat of reaction. The released heat has lower value than the

multiple uses of syngas. Syngas acts as a useful intermediate and has applications in liquid fuels production, electricity generation and chemical synthesis and thus, is the preferred end-product [19,20]. The carbonaceous feedstock can be coal, coke, biomass, bitumen, and carbon-containing wastes. Biomass and waste constitute the renewable sources to produce syngas.

The gasification process involves moisture loss, pyrolysis of feed followed by the gasification step with a certain degree of overlap between the stages as shown in Figure 1.5. In the first stage of drying, the water from the feed evaporates. This is followed by a devolatilization or pyrolysis stage where the thermal scission of chemical bonds in the feed releases volatiles which are comprised of permanent gases (H_2, CO, CO_2, CH_4) and primary tars (condensable volatiles including water) [21]. As conversion proceeds, free radicals are formed, and the oxygen in the molecules is further liberated as CO or CO_2. Free radicals and small molecules combine to produce aromatic compounds by molecular weight growth and form secondary tars. Further reactions produce tertiary tars which grow in molecular weight with increase in temperature. The tertiary products are polycyclic aromatic hydrocarbons (PAHs) and are often the species found during gasification [22].

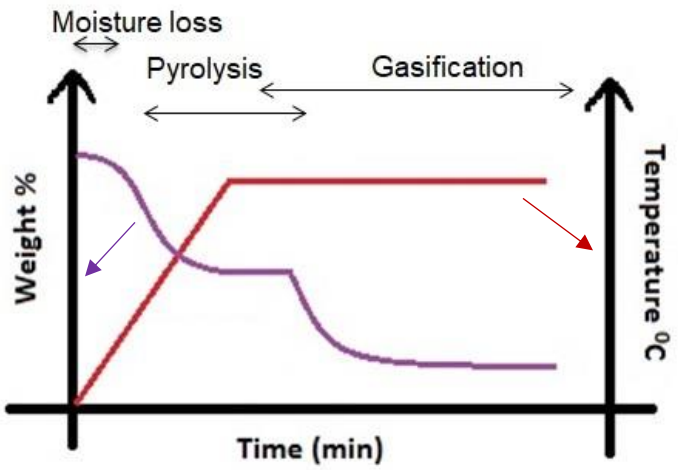

Figure 1.5. Overall weight loss profile with different stages of thermal treatment.

The primary tars are mixed oxygenates like phenols, alcohols, ketones, aldehydes, carbon acids and mono-aromatics [23]. At high temperatures, gasification takes over which thermally decomposes the primary products into smaller amounts of secondary and tertiary tars and a large quantity of light gases [24]. Secondary tars are predominantly composed of alkylated mono and diaromatics, pyridine, furans, thiophene, dioxin and xylene [23]. Tertiary tars like benzene, naphthalene, phenanthrene, pyrene, benzopyrene and polynuclear aromatic hydrocarbons (PAHs) are the most stable and difficult to crack catalytically. The formation of tertiary tar compounds is caused by both lignin and cellulose in the fuel. The hypothesis is that as size reduction of carbohydrate and lignin occurs during pyrolysis, less oxygenated and smaller molecular species and radicals are formed. These small molecules and radicals combine to produce aromatic compounds (PAHs) by molecular weight growth reactions [22].

Typically, a biomass feed loses around 75-85% of its initial weight during the first two stages. This leaves a solid non-volatile residue called char, which consists mainly of

carbon, with some oxygen, hydrogen and ash (inorganic content). During the third stage, the gasifying medium (CO_2, H_2O and O_2) reacts with char and converts the carbon into gases leaving behind an inert, mostly inorganic material called ash. The reactions of carbon with the gasifying agents, CO_2 and steam, are endothermic unlike the exothermic combustion reactions with oxygen. Additionally, the reactions between product gases are also common. Most common reactions that take place during the gasification stage are listed below [25–27]:

$$O_2 + C \rightarrow CO_2 + 393.8\ KJ/mol \qquad \text{Eq. (1.1)}$$

$$CO_2 + C \rightarrow 2CO - 172.6\ KJ/mol \qquad \text{Eq. (1.2)}$$

$$H_2O + C \rightarrow H_2 + CO - 131.4\ KJ/mol \qquad \text{Eq. (1.3)}$$

$$CO_2 + H_2 \rightarrow CO + H_2O - 41.2\ KJ/mol \qquad \text{Eq. (1.4)}$$

$$2H_2 + C \rightarrow CH_4 + 75\ KJ/mol \qquad \text{Eq. (1.5)}$$

$$CH_4 + H_2O \rightarrow CO + 3H_2 - 206\ KJ/mol \qquad \text{Eq. (1.6)}$$

A schematic depicting the whole process is shown in Figure 1.6. Since the time scale of pyrolysis is very short compared to the time scale of gasification of char, these two stages are considered to occur sequentially and can be studied separately [28]. Moreover, since the char gasification step is the rate limiting step during gasification of solid fuels, its kinetics primarily influence the design of the gasifier [29].

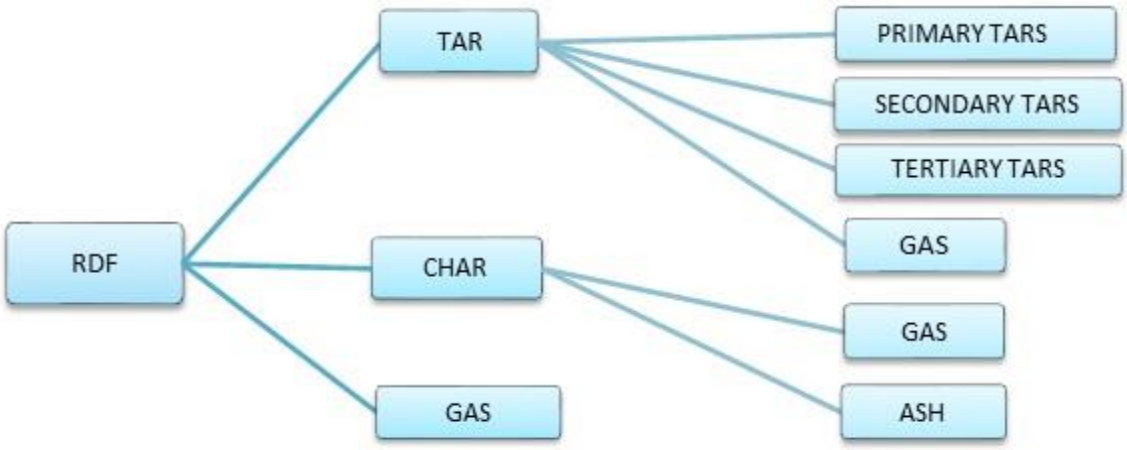

Figure 1.6. Schematic of reaction products formed during gasification.

1.4 Comparison of RDF gasification with biomass gasification

1.4.1 Biomass pyrolysis and gasification

The composition of biomass feedstocks varies based on the type and location. A summary of the variation in the C, H, O content and ash content of various biomasses is presented in Table 1.1 [30–33]. Different elemental composition of different feedstocks will lead to a difference in product distribution, lower heating value (LHV) and composition of the final products. A high cellulose and hemicellulose content in biomass leads to a higher content of volatiles in the products, while a high lignin content contributes to char formation [34]. Higher char yields are favored by high carbon content, low oxygen content, low H/C ratio and higher content of coke forming components like lignin. Lignin, being more aromatic (lower H/C ratio) than cellulose, tends to form more char as seen in Table 1.2 [35,36]. The particle size plays a vital role in determining gasification product distribution and composition. Heat flux and heat transfer rates through the complete particle are higher in small particles than the large ones. Thus, in very small particles, heat

transfer is high enough to avoid large temperature differences between the particle's exterior and interior [34]. For this reason, a reduction in particle size favors the formation of gases over tars and char. As the size increases, the temperature difference increases, and the overall process is controlled by heat transfer rate.

Table 1.1. Elemental composition of various biomass feedstocks

	Carbon%	Hydrogen%	Oxygen%	Ash%	Ref
Cedar wood	51.1	5.9	42.5	0.3	[30]
Rice husk	45.8	6	47.9	0.8	[31]
Jute stick	49.8	6.02	41.4	0.62	[32]
Corn cob	40.2	4.11	42.6	2.97	[33]

Table 1.2. Yields obtained from individual fast pyrolysis (> 100 °C/min) of the biomass constituents in different types of reactors with temperature between 500 and 800 °C [36]

	Char%	Tar%	Water%	Gas%
Cellulose	< 15	40 – 70	5 – 15	12 – 30
Hemicellulose	20 – 30	20 – 35	20 – 30	22 – 35
Lignin	30 – 45	15 – 35	8 – 15	12 – 35

Pyrolysis conditions (temperature, pressure, heating rate, and residence time) have been known to affect the thermochemical properties of char and in turn its gasification reactivity [21]. The effect of the pyrolysis temperature has been described in several references for different types of biomass [37–40]. Based on the general trend, an increase in pyrolysis temperature reduces the yield of char and tar and enhances the yield of light gases. This is attributed to cracking and steam reforming of tars and the water-gas-shift reaction that are known to occur at high temperatures. Nevertheless, high temperature has been found to deactivate the char in further gasification reactions by making it graphitic [41]. Residence time plays a critical role alongside the effect of temperature. As the char

is exposed to high temperatures for a long period of time, secondary reactions like tar cracking are accelerated resulting in a reduced tar yield [38].

An increase in the pyrolysis heating rate (typical of entrained flow and fluidized bed reactors) results in melting of the outer wall of the particle and a loss of the original cellular structure. SEM analysis on typical particles revealed the formation of bubbles due to simultaneous release of volatiles and softening of the solid matrix [22,42]. It has been found that the chars produced during rapid pyrolysis ($1.2 \times 10^4 - 3.3 \times 10^4$ °C/s) were more reactive in gasification than the chars produced at milder conditions (20 – 40 °C/min) [42]. A combination of high heating rates and high temperatures were noted to produce open structures due to the escape of volatiles and bursting of bubbles, so that gas diffusion during gasification is enhanced. An increase in the external pressure during pyrolysis reduces the cell wall thickness of biomass char particles, and forms char with larger voids [43,44]. The release of gases increases the pressure inside the particles. However, the bubbles do not rupture and burst because the external pressure does not allow the volatiles to release freely. This leads to secondary reactions inside the char particle and alters the gas and tar composition. In addition, it has been found that char generated at higher pressures is more graphitic than that produced at lower pressure, and there is a decrease in surface area of chars with an increase in pressure [45].

Inorganics present in the pyrolysis char are known to catalyze gasification reactions, specifically, alkali and alkaline earth metals (e.g. K and Ca) [46–48]. However, in addition to inorganics that have a catalyzing effect on the gasification process, the presence of deactivating inorganics has also been observed in various biomass feedstocks that act as scavengers (e.g. silica) [49]. Different types and quantities of these inorganics

present in different feedstocks result in varied gasification reactivity. Thus, the ash content and composition play a significant role in the determination of gasification reactivity at temperatures between 800 – 900 °C.

1.4.2 RDF or MSW pyrolysis and gasification

One of the first gasification studies of MSW was performed in a fluidized bed reactor (FBR) using solid waste collected from an incineration plant in Tokyo [50]. Since no pre-processing techniques were used to separate out the non-combustibles, the volatile matter of the feed was only about 60%. However, the study could achieve high LHV gas product by the use of high temperatures (~700 °C) and good contact between the heat transfer particles and the feed in the FBR. Several studies in the literature have considered different feed compositions to represent MSW / RDF, ranging from real waste to model MSW / RDF compounds. The effect of pyrolysis conditions was also investigated in these studies similar to the biomass literature. The effect of temperature in pyrolysis and gasification of real waste in a fixed bed reactor was explored [51,52]. Similar to biomass gasification, an increase in the gasification temperature increased the total gas yield and carbon conversion efficiency, which was attributed to higher production of primary gases, improved endothermic gasification reactions and increased cracking and reforming of tars. Since cellulose containing paper components were a major fraction of the collected waste, the cellulose decomposition peak observed in biomass (240 – 380 °C) also seemed to appear in the TGA decomposition curve of MSW / RDF in addition to the curves from other components of the feedstock. Also, an increase in surface area of chars was observed with an increase in temperature up to 700 °C.

The presence of common primary reacting species, such as cellulose and lignin, which may result in a similar composition of the reactive fraction of primary volatiles generated during pyrolysis, is a reason for good accordance between the values of the activation energies and the frequency factors of different starting materials used in one study (RDF, wood, and MSW) [53]. A pyrolysis study conducted on a mixture of municipal and industrial wastes (carpet disposal, plastic/metal/drinking cartons, paper and synthetic materials) found that the liquid obtained by slow pyrolysis (4 K/min and 550 °C) separates spontaneously into a water rich product and an oily product while all fast pyrolysis liquids contain only an oily product and a waxy material, but no separated water rich fraction [54]. The presence of this waxy material in the liquid products at high heating rates and short residence times was attributed to incomplete breakdown of long aliphatic hydrocarbons like poly-(ethylene-propylene)-copolymer present in the feed. It was observed that the distribution of metal ions towards oils is negligible which were retained on the fixed carbon. Many studies have been conducted with different pyrolysis conditions, feed material and particle sizes. A comparison of different studies in Table 1.3 shows the effect of feedstock type and pyrolysis conditions (temperature, heating rate and particle size) on product distribution and gas composition.

It can be seen from Table 1.3 that a change in feedstock (varying CHO content) and a slight variation of pyrolysis process conditions can lead to very different product distributions and compositions. This highlights the heterogeneous nature of MSW / RDF. The variation in temperature, similar to biomass, leads to higher gas yield and increased lighter gas fraction at higher temperature [53]. An increase in particle size increases secondary reactions and promotes the formation of complete combustion products like

CO_2, decreasing the gas quality [55]. Rapid heating was observed to increase the gas yield and decrease the liquid yield. The $C_1 – C_4$ hydrocarbons increased with increasing heating rate which led to a higher LHV of the gas to 24.8 MJ/m^3 [56]. Thus, rapid pyrolysis at 800 °C with a long residence time was found to be the optimum process condition for highest gas yield with a large heating value, which can be achieved in a fluidized bed reactor.

Table 1.3. Pyrolysis yields and gas compositions of MSW at different process conditions in a fixed bed reactor

	Cozzani [53]	Luo [55]	Efika [56]	Jiang [57]	Cozzani [53]	Luo [55]	Efika [56]
Feedstock	RDF pellets (Italy)	MSW (China)	RDF pellets (UK)	Mixture*	RDF pellets (Italy)	MSW (China)	RDF pellets (UK)
Particle size (mm)	-	< 5	1	50	-	10 to 20	1
Temperature (°C)	900	900	R.T - 800	800	500	900	R.T - 800
Heating rate (K/min)	60	10	20	20	60	10	350
Gas phase residence time (s)	6 - 22	-	9	-	6 - 22	-	9
C%	45.9	51.8	43.5	-	45.9	51.8	43.5
H%	6.8	5.76	5.9	-	6.8	5.76	5.9
O%	33.7	30.2	37	-	33.7	30.2	37
Ash%	12.3	4.93	12.8	-	12.3	4.93	12.8
Yield%							
Char	22	-	24.1	16.2	25	-	22.8
Gas	46	-	15.4	31.2	25	-	46.9
Liquid	32	-	53	52.6	50	-	23
Gas composition %							
H_2	34.3	22.4	2.6	-	17.5	18.3	1.5
CO	22.2	26.5	29.2	-	63.1	22	39.9
CO_2	13.3	34.2	57.1	-	11.6	43.2	24.5
CH_4	12.2	10.1	4.6	-	5.5	11.5	10.5
$C_2 – C_4$	17.9	5	5.8	-	2.3	5	23.5

* kitchen waste, paper, cloth, bamboo, plastics and glass

Gasification studies have been conducted on model MSW / RDF compositions, wherein the individual waste components were mixed together in the required proportion as laid out by environmental agencies [58–60]. The key findings show that the use of CO_2 and H_2O as gasifying media increases the carbon – to – gas conversion more than pure pyrolysis in a N_2 atmosphere. The main difference between steam gasification and partial gasification in air/CO_2 was identified to be the hydrogen to carbon monoxide molar ratio in the gaseous stream. Several studies have considered a single component of the waste in order to avoid problems of heterogeneity of feed and irreproducibility of results. The major constituents of RDF, plastic waste [61,62], paper waste [63,64] and food waste [65,66], were all found to yield varying amounts of gases and the composition was strongly dependent on the reactor configuration. Although plastics have a high carbon content and low oxygen content, the lack of char formation during pyrolysis showed that the observations made in biomass pyrolysis are not applicable to all feedstocks. Other studies have reported the gasification of waste components separately to compare the differences and similarities between the individual components [67,68].

The degradation temperature, ash content and product gas composition varied with different components, while the effect of temperature and the amount of oxygen present in the gasifying medium was found to be the same for all the components. Some studies conducted a pyrolysis study of individual components and also analyzed two-component mixtures of the same [69,70]. At high heating rates, there was no influence of one biomass over the other, but the influence of plastics when mixed with biomass material was marked with a change in overall conversion rate when compared with the sum of rates of individual components. A higher ratio of organic waste over petroleum based plastic waste resulted

in lower yields of volatile hydrocarbons, which is not surprising since plastic waste consists of ~100% volatile content.

1.4.3 Key results for biomass and RDF gasification

The major difference between biomass and RDF is found to be the feed composition and structure. RDF is highly heterogeneous with numerous components that have distinct decomposition characteristics. Although, a major portion of RDF consists of biomass-like compounds (cellulose, hemicellulose and lignin), there are fractions, like plastics and rubber that show very different decomposition profiles. Thus, the product composition varies with different feedstocks, and a certain difference in the product composition should be expected while comparing the results in the present study with the literature.

The major similarity between biomass and RDF feedstocks is the effect of pyrolysis conditions. High temperature, high heating rate, and longer residence time seem to increase the gas yield in all feedstocks. These conditions can be optimized in order to achieve high char reactivity during gasification. Moreover, the catalytic role of inorganics displayed in biomass gasification can be expected in RDF gasification since the various components in RDF consist of several inorganic species.

1.5 Objectives

Although there is substantial literature on RDF pyrolysis and gasification, a comprehensive study of the individual components present in RDF and their interaction with each other during the composite RDF gasification has not yet been undertaken. Moreover, studies have addressed the gasification of RDF either just at the fundamental

level or at a production stage (large capacity syngas production). A combination of both the studies for the same feed has not been researched in depth. This work aims at addressing both the issues by understanding the individual component behavior in a model RDF composition and the result of their interaction during the composite RDF gasification in CO_2 and steam. The work also involves applying the key results from the fundamental studies to the design of a bubbling fluidized bed reactor (BFBR) for the gasification of model RDF pellets and show its scale-up potential.

The fundamental studies involve discrete experimental studies of the pyrolysis and char gasification processes in order to independently optimize them. For this purpose, model RDF was pyrolyzed either in-situ in a thermogravimetric analyzer (TGA) or a tubular reactor at low heating rates (~20 K/min) to generate chars, which were then characterized. Char gasification was further studied separately by analyzing the weight change when exposed to a gasifying agent such as CO_2 or steam at high temperature (i.e. 700 – 1000 °C). Since char gasification is the slowest step, considerable effort was made to understand fundamental descriptors that affect char reactivity.

At present, both biomass-based and waste-based gasification processes are largely based on the coal gasification literature [71,72]. However, coal chars contain highly ordered carbon materials as opposed to biochar or waste-derived char that have a relatively disordered and heterogeneous char structure. Hence, a direct extension of the coal literature to understand the waste-derived char structure and reactivity might not be justified [73]. This makes the study of RDF gasification from the fundamental level more imperative and essential. With this in mind, the experimental study has been divided into four parts.

The first part is illustrated in Chapter 2, which focuses on the low-heating rate pyrolysis and gasification of model RDF in a thermogravimetric analyzer (TGA). The study begins with a detailed description of identifying a representative model RDF composition and the challenges in feed preparation. The individual components present in the model RDF composition are studied independently, and their relationship to the composite RDF pyrolysis and gasification was identified. Pyrolysis gases were analyzed using a micro-GC. Chars were further characterized for their physical attributes (nitrogen and CO_2 physisorption, SEM) as well as chemical characteristics (elemental analysis, ICP-OES, EDX). CO_2 gasification of the individual component chars and model RDF char was performed in a TGA. The weight loss as a function of temperature was determined to understand gasification reaction kinetics.

The catalytic activity of inorganics during the gasification stage is explored in the second part of the study in Chapter 3. Potassium and calcium were found to be the most catalytically active inorganic species present in the feed and were studied extensively in this chapter. Avicel (microcrystalline cellulose) was used as a model carbon compound to illustrate the catalytic effect of potassium. Avicel was chosen because it is a closer representative of the type of carbon present in the waste and because it does not contain any intrinsic inorganic elements. K_2CO_3 and $Ca(OH)_2$ were the oxides chosen to represent alkali and alkaline earth metals in the feed. Char gasification in both 100% CO_2 and 100% steam was also studied in this chapter to derive a relationship between the inorganics and the type of gasifying agent used. Reaction mechanisms were proposed for potassium-rich carbon gasification in both CO_2 and steam. Active site sharing was investigated by performing switchover experiments with the gasifying agents. Kinetic modeling in mixed

atmospheres of CO_2 and steam was performed to investigate the combined effect of the gasifying agents when they are exposed to carbon simultaneously.

Chapter 4 of the study investigates the variation in the char morphology and its gasification reactivity as a function of the pyrolysis heating rate. Pyrolysis heating rate is an important factor in determining both the char morphology and structure, which further affects its gasification reactivity. Studying the differences between the char generated from high heating rate (3000 – 10^4 °C/min) and low heating rate (20 °C/min) gives insight into the additional physicochemical parameters that affect gasification when the feed is the same. The tubular reactor used for low-heating rate pyrolysis in Chapter 2 was modified to generate char at the required high heating rates. Both of the chars were subjected to characterization techniques like mercury porosimetry, SEM and EDX, to identify the similarities and differences from the use of different heating rates. A new methodology was developed to quantify EDX maps using a novel MATLAB code for identifying the distribution of inorganics in various chars. The physicochemical properties of char were also investigated when the residence time was varied for the high heating rate chars. The resulting CO_2 gasification reactivity of all the chars was further considered to establish a structure-activity relationship.

Chapter 5 extends the gasification of model RDF to a bubbling fluidized bed reactor (BFBR). The experimental conditions for the BFBR such as, feed flow rate, gas flow rate and reaction temperature, were established based on the results from the first three studies. A three-stage fluidized bed reactor with increasing diameters was developed to produce a clean synthesis gas. The bottom stage and the middle stage were designed for pyrolysis and gasification reactions, respectively. The top stage acted as the disengagement zone to

separate the fine particles from the unconverted heavier particles. Both pine powder and RDF pellets were gasified using CO_2 and steam in the BFBR. Gasification conditions such as temperature, gasifying agent composition and gas flow rates were varied to achieve a high recovery of carbon in the gas fraction of the products and to minimize tar formation.

Finally, Chapter 6 summarizes the key learnings obtained from each of these studies. Also, recommendations for further studies are discussed.

1.6 References

[1] Global energy statistical yearbook, (2017). https://yearbook.enerdata.net/total-energy/world-consumption-statistics.html.

[2] V. Smil, Energy Transitions: Global and National Perspectives, Second Edi, ABC-CLIO, Santa Barbara, USA, 2016.

[3] The end of fossil fuels, Ecotricity. (2017). https://www.ecotricity.co.uk/our-green-energy/energy-independence/the-end-of-fossil-fuels (accessed February 12, 2018).

[4] H. Ritchie, How long before we run out of fossil fuels?, Our World Data. (2017). https://ourworldindata.org/how-long-before-we-run-out-of-fossil-fuels (accessed February 12, 2018).

[5] How is Today's Warming Different from the Past?, (2010). https://earthobservatory.nasa.gov/Features/GlobalWarming/page3.php (accessed February 12, 2018).

[6] L. V. Alexander, Climate Change 2013: The Physical Science Basis: Summary for Policymakers, 2014. https://www.ipcc.ch/pdf/assessment-report/ar5/wg1/WGIAR5_SPM_brochure_en.pdf.

[7] Monthly energy review April, (2017). https://www.eia.gov/energyexplained/?page=us_energy_home.

[8] M.A. Maehlum, Geothermal energy pros and cons, Energy Inf. (2013). http://energyinformative.org/geothermal-energy-pros-and-cons/.

[9] S.N. Naik, V. V. Goud, P.K. Rout, A.K. Dalai, Production of first and second generation biofuels: A comprehensive review, Renew. Sustain. Energy Rev. 14 (2010) 578–597. doi:10.1016/j.rser.2009.10.003.

[10] S.D. Stefanidis, K.G. Kalogiannis, E.F. Iliopoulou, C.M. Michailof, P.A. Pilavachi, A.A. Lappas, A study of lignocellulosic biomass pyrolysis via the pyrolysis of cellulose, hemicellulose and lignin, J. Anal. Appl. Pyrolysis. 105 (2014) 143–150. doi:10.1016/j.jaap.2013.10.013.

[11] C. Valkenburg, M. Gerber, C. Walton, S. Jones, B. Thompson, D. Stevens, Municipal Solid Waste (MSW) to Liquid Fuels Synthesis, Volume 1: Availability of Feedstock and Technology, 1 (2008) 1–43. http://www.pnl.gov/main/publications/external/technical_reports/PNNL-18144.pdf.

[12] Municipal Solid Waste (MSW) landfills, US EPA. (2017). https://www.epa.gov/landfills/municipal-solid-waste-landfills.

[13] Department of Energy, Methodology for Allocating Municipal Solid Waste to Biogenic and Non-Biogenic Energy, Energy Inf. Adm. Off. Coal. (2007) 1–18.

[14] A. Demirbas, Calculation of higher heating values of biomass fuels, Fuel. 76 (1997) 431–434. doi:10.1080/15567036.2015.1115924.

[15] US Environmental Protection Agency, Municipal Solid Waste Generation , Recycling , and Disposal in the United States : Facts and Figures for 2012, (2012) 1–14.

[16] J.D. Murphy, E. McKeogh, Technical, economic and environmental analysis of energy production from municipal solid waste, Renew. Energy. 29 (2004) 1043–1057. doi:10.1016/j.renene.2003.12.002.

[17] N. Couto, V. Silva, E. Monteiro, S. Teixeira, R. Chacartegui, K. Bouziane, et al., Numerical and experimental analysis of municipal solid wastes gasification process, Appl. Therm. Eng. 78 (2015) 185–195. doi:10.1016/j.applthermaleng.2014.12.036.

[18] M. McHenry, Waste to Energy Technologies, Murdoch Univ. (2006). http://www.see.murdoch.edu.au/resources/info/Tech/waste/ (accessed December 3, 2015).

[19] A. V. Bridgwater, Renewable fuels and chemicals by thermal processing of biomass, Chem. Eng. J. 91 (2003) 87–102. doi:10.1016/S1385-8947(02)00142-0.

[20] B. Prabowo, K. Umeki, M. Yan, M.R. Nakamura, M.J. Castaldi, K. Yoshikawa, CO_2–steam mixture for direct and indirect gasification of rice straw in a downdraft gasifier: Laboratory-scale experiments and performance prediction, Appl. Energy. 113 (2014) 670–679. doi:10.1016/j.apenergy.2013.08.022.

[21] C. Di Blasi, Combustion and gasification rates of lignocellulosic chars, Prog. Energy Combust. Sci. 35 (2009) 121–140. doi:10.1016/j.pecs.2008.08.001.

[22] M.W. Jarvis, T.J. Haas, B.S. Donohoe, J.W. Daily, K.R. Gaston, W.J. Frederick, et

al., Elucidation of Biomass Pyrolysis Products Using a Laminar Entrained Flow Reactor and Char Particle Imaging, Energy & Fuels. 25 (2011) 324–336. doi:10.1021/ef100832d.

[23] P. Morf, P. Hasler, T. Nussbaumer, Mechanisms and kinetics of homogeneous secondary reactions of tar from continuous pyrolysis of wood chips, Fuel. 81 (2002) 843–853. doi:10.1016/S0016-2361(01)00216-2.

[24] R.J. Evans, T.A. Milne, Chemistry of tar formation and maturation in the thermochemical conversion of biomass, in: Dev. Thermochem. Biomass Convers., Springer Netherlands, Dordrecht, 1997: pp. 803–816. doi:10.1007/978-94-009-1559-6_64.

[25] A. Demirbaş, Hydrogen Production from Biomass by the Gasification Process, Energy Sources. 24 (2002) 59–68. doi:10.1080/00908310252712307.

[26] G. Maschio, A. Lucchesi, G. Stoppato, Production of syngas from biomass, Bioresour. Technol. 48 (1994) 119–126. doi:10.1016/0960-8524(94)90198-8.

[27] R.N. André, F. Pinto, C. Franco, M. Dias, I. Gulyurtlu, M.A.A. Matos, et al., Fluidised bed co-gasification of coal and olive oil industry wastes, Fuel. 84 (2005) 1635–1644. doi:10.1016/j.fuel.2005.02.018.

[28] N.M. Laurendeau, Heterogeneous kinetics of coal char gasification and combustion, Prog. Energy Combust. Sci. 4 (1978) 221–270. doi:10.1016/0360-1285(78)90008-4.

[29] L. Wang, J. Sandquist, G. Varhegyi, B. Matas Güell, CO_2 gasification of chars prepared from wood and forest residue: A kinetic study, Energy & Fuels. 27 (2013) 6098–6107. doi:10.1021/ef401118f.

[30] M. Asadullah, T. Miyazawa, S.I. Ito, K. Kunimori, S. Koyama, K. Tomishige, A comparison of $Rh/CeO_2/SiO_2$ catalysts with steam reforming catalysts, dolomite and inert materials as bed materials in low throughput fluidized bed gasification systems, Biomass and Bioenergy. 26 (2004) 269–279. doi:10.1016/S0961-9534(03)00105-3.

[31] J.F. Vélez, F. Chejne, C.F. Valdés, E.J. Emery, C.A. Londoño, Co-gasification of Colombian coal and biomass in fluidized bed: An experimental study, Fuel. 88 (2009) 424–430. doi:10.1016/j.fuel.2008.10.018.

[32] M. Asadullah, T. Miyazawa, S.I. Ito, K. Kunimori, M. Yamada, K. Tomishige, Gasification of different biomasses in a dual-bed gasifier system combined with novel catalysts with high energy efficiency, Appl. Catal. A Gen. 267 (2004) 95–102. doi:10.1016/j.apcata.2004.02.028.

[33] Y.J. Lu, H. Jin, L.J. Guo, X.M. Zhang, C.Q. Cao, X. Guo, Hydrogen production by biomass gasification in supercritical water with a fluidized bed reactor, Int. J. Hydrogen Energy. 33 (2008) 6066–6075. doi:10.1016/j.ijhydene.2008.07.082.

[34] L. Wei, S. Xu, L. Zhang, H. Zhang, C. Liu, H. Zhu, et al., Characteristics of fast pyrolysis of biomass in a free fall reactor, Fuel Process. Technol. 87 (2006) 863–871. doi:10.1016/j.fuproc.2006.06.002.

[35] T.R. Nunn, J.B. Howard, J.P. Longwell, W.A. Peters, Product Compositions and Kinetics in the Rapid Pyrolysis of Milled Wood Lignin, Ind. Eng. Chem. Process Des. Dev. 24 (1985) 844–852. doi:10.1021/i200030a054.

[36] F.-X. Collard, J. Blin, A review on pyrolysis of biomass constituents: Mechanisms and composition of the products obtained from the conversion of cellulose, hemicelluloses and lignin, Renew. Sustain. Energy Rev. 38 (2014) 594–608. http://linkinghub.elsevier.com/retrieve/pii/S136403211400450X.

[37] C. Wu, V.L. Budarin, M.J. Gronnow, M. De Bruyn, J.A. Onwudili, J.H. Clark, et al., Conventional and microwave-assisted pyrolysis of biomass under different heating rates, J. Anal. Appl. Pyrolysis. 107 (2014) 276–283. doi:10.1016/j.jaap.2014.03.012.

[38] A. Sharma, V. Pareek, D. Zhang, Biomass pyrolysis - A review of modelling, process parameters and catalytic studies, Renew. Sustain. Energy Rev. 50 (2015) 1081–1096. doi:10.1016/j.rser.2015.04.193.

[39] R. Azargohar, K.L. Jacobson, E.E. Powell, A.K. Dalai, Evaluation of properties of fast pyrolysis products obtained, from Canadian waste biomass, J. Anal. Appl. Pyrolysis. 104 (2013) 330–340. http://dx.doi.org/10.1016/j.jaap.2013.06.016.

[40] R. Zanzi, K. Sjöström, E. Björnbom, Rapid pyrolysis of agricultural residues at high temperature, Biomass and Bioenergy. 23 (2002) 357–366. doi:10.1016/S0961-9534(02)00061-2.

[41] A.H. Tchapda, S. V. Pisupati, Characterization of an entrained flow reactor for pyrolysis of coal and biomass at higher temperatures, Fuel. 156 (2015) 254–266. doi:10.1016/j.fuel.2015.04.015.

[42] E. Biagini, M. Simone, L. Tognotti, Characterization of high heating rate chars of biomass fuels, Proc. Combust. Inst. 32 II (2009) 2043–2050. http://dx.doi.org/10.1016/j.proci.2008.06.076.

[43] E. Cetin, R. Gupta, B. Moghtaderi, Effect of pyrolysis pressure and heating rate on radiata pine char structure and apparent gasification reactivity, Fuel. 84 (2005) 1328–1334.

[44] J. Recari, C. Berrueco, S. Abelló, D. Montané, X. Farriol, Effect of temperature and pressure on characteristics and reactivity of biomass-derived chars, Bioresour. Technol. 170 (2014) 204–210. doi:10.1016/j.biortech.2014.07.080.

[45] G. Newalkar, K. Iisa, A.D. D'Amico, C. Sievers, P. Agrawal, Effect of temperature, pressure, and residence time on pyrolysis of pine in an entrained flow reactor,

Energy & Fuels. 28 (2014) 5144–5157. http://dx.doi.org/10.1021/ef5009715.

[46] K. Mitsuoka, S. Hayashi, H. Amano, K. Kayahara, E. Sasaoaka, M.A. Uddin, Gasification of woody biomass char with CO_2: The catalytic effects of K and Ca species on char gasification reactivity, Fuel Process. Technol. 92 (2011) 26–31. http://linkinghub.elsevier.com/retrieve/pii/S0378382010002791.

[47] P. Lahijani, Z.A. Zainal, A.R. Mohamed, M. Mohammadi, CO_2 gasification reactivity of biomass char: Catalytic influence of alkali, alkaline earth and transition metal salts, Bioresour. Technol. 144 (2013) 288–295. http://dx.doi.org/10.1016/j.biortech.2013.06.059.

[48] M. Jiang, J. Hu, J. Wang, Calcium-promoted catalytic activity of potassium carbonate for steam gasification of coal char: Effect of hydrothermal pretreatment, Fuel. 109 (2013) 14–20. http://dx.doi.org/10.1016/j.fuel.2012.06.100.

[49] K. Umeki, A. Moilanen, A. Gómez-Barea, J. Konttinen, A model of biomass char gasification describing the change in catalytic activity of ash, Chem. Eng. J. 207–208 (2012) 616–624. http://dx.doi.org/10.1016/j.cej.2012.07.025.

[50] M. Hasegawa, J. Fukuda, D. Kunii, Gasification of solid waste in a fluidized bed reactor with circulating sand, Conserv. Recycl. 3 (1979) 143–153.

[51] J. Wang, G. Cheng, Y. You, B. Xiao, S. Liu, P. He, et al., Hydrogen-rich gas production by steam gasification of municipal solid waste (MSW) using NiO supported on modified dolomite, Int. J. Hydrogen Energy. 37 (2012) 6503–6510. doi:10.1016/j.ijhydene.2012.01.070.

[52] W.K. Buah, A.M. Cunliffe, P.T. Williams, Characterization of Products from the Pyrolysis of Municipal Solid Waste, Process Saf. Environ. Prot. 85 (2007) 450–457. http://linkinghub.elsevier.com/retrieve/pii/S0957582007714489.

[53] V. Cozzani, C. Nicolella, L. Petarca, M. Rovatti, L. Tognotti, A Fundamental Study on Conventional Pyrolysis of a Refuse-Derived Fuel, Ind. Eng. Chem. Res. 34 (1995) 2006–2020. http://pubs.acs.org/doi/abs/10.1021/ie00045a010.

[54] I. Velghe, R. Carleer, J. Yperman, S. Schreurs, Study of the pyrolysis of municipal solid waste for the production of valuable products, J. Anal. Appl. Pyrolysis. 92 (2011) 366–375. doi:10.1016/j.jaap.2011.07.011.

[55] S. Luo, B. Xiao, Z. Hu, S. Liu, Effect of particle size on pyrolysis of single-component municipal solid waste in fixed bed reactor, Int. J. Hydrogen Energy. 35 (2010) 93–97. doi:10.1016/j.ijhydene.2009.10.048.

[56] E.C. Efika, J.A. Onwudili, P.T. Williams, Products from the high temperature pyrolysis of RDF at slow and rapid heating rates, J. Anal. Appl. Pyrolysis. 112 (2015) 14–22. http://linkinghub.elsevier.com/retrieve/pii/S0165237015000054.

[57] J.F. Jiang, Study on out heating pyrolysis technology of municipal solid waste, Wuhan: Huazhong University of Science and Technology, 2006.

[58] E. Kwon, K.J. Westby, M.J. Castaldi, Transforming Municipal Solid Waste (MSW) Into Fuel via the Gasification/Pyrolysis Process, 18th Annu. North Am. Waste-to-Energy Conf. 7 (2010) 53–60. doi:10.1115/NAWTEC18-3559.

[59] E.E. Kwon, M.J. Castaldi, Urban energy mining from municipal solid waste (MSW) via the enhanced thermo-chemical process by carbon dioxide (CO_2) as a reaction medium., Bioresour. Technol. 125 (2012) 23–9. http://www.sciencedirect.com/science/article/pii/S0960852412012631.

[60] U. Lee, J.N. Chung, H.A. Ingley, High-temperature steam gasification of municipal solid waste, rubber, plastic and wood, Energy & Fuels. 28 (2014) 4573–4587. http://dx.doi.org/10.1021/ef500713j.

[61] J.-W. Kim, T.-Y. Mun, J.-O. Kim, J.-S. Kim, Air gasification of mixed plastic wastes using a two-stage gasifier for the production of producer gas with low tar and a high caloric value, Fuel. 90 (2011) 2266–2272. http://www.sciencedirect.com/science/article/pii/S0016236111000913.

[62] R. Zevenhoven, M. Karlsson, M. Hupa, M. Frankenhaeuser, Combustion and Gasification Properties of Plastics Particles, J. Air Waste Manage. Assoc. 47 (1997) 861–870. http://www.tandfonline.com/doi/abs/10.1080/10473289.1997.10464461.

[63] I. Ahmed, A.K. Gupta, Characteristics of cardboard and paper gasification with CO_2, Appl. Energy. 86 (2009) 2626–2634. http://linkinghub.elsevier.com/retrieve/pii/S0306261909001160.

[64] G. Jin, H. Iwaki, N. Arai, K. Kitagawa, Study on the gasification of wastepaper/carbon dioxide catalyzed by molten carbonate salts, Energy. 30 (2005) 1192–1203.

[65] R. Muangrat, J. a. Onwudili, P.T. Williams, Influence of alkali catalysts on the production of hydrogen-rich gas from the hydrothermal gasification of food processing waste, Appl. Catal. B Environ. 100 (2010) 440–449. http://dx.doi.org/10.1016/j.apcatb.2010.08.019.

[66] I.I. Ahmed, A.K. Gupta, Pyrolysis and gasification of food waste: Syngas characteristics and char gasification kinetics, Appl. Energy. 87 (2010) 101–108. http://linkinghub.elsevier.com/retrieve/pii/S0306261909003523.

[67] L. Sørum, M.G. Grønli, J.E. Hustad, Pyrolysis characteristics and kinetics of municipal solid wastes, Fuel. 80 (2001) 1217–1227. http://www.sciencedirect.com/science/article/pii/S0016236100002180%5Cnhttp://www.sciencedirect.com/science/article/pii/S0016236100002180/pdfft?md5=2f7d8006d87c6cf26189be9b388f3ec1&pid=1-s2.0-S0016236100002180-main.pdf.

[68] M. Niu, Y. Huang, B. Jin, X. Wang, Oxygen Gasification of Municipal Solid Waste in a Fixed-bed Gasifier, Chinese J. Chem. Eng. 22 (2014) 1021–1026. http://www.sciencedirect.com/science/article/pii/S1004954114000500.

[69] J. Zheng, Y.-Q. Jin, Y. Chi, J.-M. Wen, X.-G. Jiang, M.-J. Ni, Pyrolysis characteristics of organic components of municipal solid waste at high heating rates., Waste Manag. 29 (2009) 1089–1094. http://dx.doi.org/10.1016/j.wasman.2008.06.034.

[70] N. Miskolczi, F. Ateş, N. Borsodi, Comparison of real waste (MSW and MPW) pyrolysis in batch reactor over different catalysts. Part II: Contaminants, char and pyrolysis oil properties, Bioresour. Technol. 144 (2013) 370–379. doi:10.1016/j.biortech.2013.06.109.

[71] L. a. Ruth, Energy from municipal solid waste: A comparison with coal combustion technology, Prog. Energy Combust. Sci. 24 (1998) 545–564. doi:10.1016/S0360-1285(98)00011-2.

[72] G. Lopez, M. Artetxe, M. Amutio, J. Alvarez, J. Bilbao, M. Olazar, Recent advances in the gasification of waste plastics. A critical overview, Renew. Sustain. Energy Rev. 82 (2018) 576–596. doi:10.1016/j.rser.2017.09.032.

[73] H. Wu, K. Yip, F. Tian, Z. Xie, C. Li, Evolution of char structure during the steam gasification of biochars produced from the pyrolysis of various mallee biomass components.pdf, (2009) 10431–10438.

CHAPTER 2. PYROLYSIS AND GASIFICATION STUDIES OF MODEL RDF USING THERMOGRAVIMETRIC ANALYSIS

2.1 Background

Municipal Solid Waste (MSW) is the everyday garbage generated in households and commercial buildings. According to the 2012 EPA study, 251 million tons of MSW were generated in the United States in 2012 [1]. Although there are several recycling facilities for the generated waste, 65.3 wt% of it ends up in landfills or incinerators. Landfills are known quandaries while incineration produces pollutants and requires higher temperatures and higher oxygen concentrations leading to low-value product gases [2]. Thus, it would be beneficial to find an alternative solution for utilizing the enormous amount of non-recycled MSW. Since a large portion of MSW is organic, it is possible to convert it to syngas (H_2 and CO) using pyrolysis and gasification techniques. MSW is available year round and can be an abundant source of energy. According to a study conducted in 2008, compared to the cost of conventional biomass as a feedstock of $44/dry ton, MSW has a negative cost with a tipping fee of $30/ton to dispose of it in a landfill [3]. Besides recovering a substantial amount of energy, the use of MSW as a feedstock can lead to the overall reduction of waste requiring disposal, while also meeting pollution control standards. Therefore, year-round availability, abundance of feed and zero to negative costs make MSW a potential alternative feedstock for the production of fuels and chemicals.

The major components in the discarded portion were found to be food waste (21%), plastics (18%) and paper waste (15%) [1]. However, the discarded portion contains considerable amounts of inorganic material like metal scraps and glass. Moreover, high variability in the feedstock of MSW negatively influences gasifier performance and results in poor reproducibility [4]. Thus, several pre-processing techniques, like size reduction and sorting, are needed to make MSW a suitable feedstock for gasifiers. Refuse derived fuel (RDF) is a processed form of MSW where significant size reduction, drying, screening, sorting, metal and glass separation and, in some cases, pelletization is performed to improve the handling characteristics and composition of the material to be fed to a gasifier [5]. This series of processes alters the composition of the waste by reducing the metal, glass and moisture content of the discarded portion and enhancing the volatile content of the RDF [5].

Pyrolysis is the thermal decomposition of organic matter in anaerobic conditions while gasification occurs in an oxygen deficient atmosphere. A partial oxidation condition in gasification is achieved with the use of either CO_2, steam or insufficient supply of air or oxygen [4,6,7]. Gasification has been studied extensively for coal and biomass [8–10]. As the temperature rises during gasification from ambient to the reaction temperature, drying occurs around 100 °C, followed by pyrolysis and gasification [11]. The pyrolysis step occurs over a short period of time at lower temperatures compared to gasification, although the two steps start to overlap around 700 °C [12]. This overlap makes it difficult to differentiate the products of pyrolysis and gasification. The present study was designed to only introduce the gasifying agent once the pyrolysis stage was completed.

Although volatile products are desired in pyrolysis processes, char can have a modest value as a soil enhancer or a source of energy via combustion [13]. Alternatively, the char can be gasified to produce additional syngas. Thus, it is important to study independent char reaction kinetics in order to develop an improved understanding of char gasification. The inorganic content is found to be the most important parameter to influence the gasification reactivity of char generated from pyrolysis [14]. It has been reported that alkali and alkaline earth metals (e.g., potassium and calcium) play a catalytic role during gasification [7,15]. This was found to be one of the driving forces for co-gasification studies of coal and biomass, wherein, the inorganics present in the biomass promote the gasification reactivity of coal and in turn, the blend [8,10]. However, certain deactivating inorganics, like silicon, have also been detected that act as scavengers, rendering the catalytic inorganics inactive [16]. Hence, both the amount and type of inorganics present in the feed were found to influence the gasification reactivity.

Four approaches have been described in the literature to analyze the gasification of MSW. The first set of studies considered a single representative MSW component in order to avoid complications due to the heterogeneity of the feed. Major constituents of MSW: plastic waste [6,17], paper waste [18,19] and food waste [20,21] produced varying product yields (char, tar and gas), that strongly depended on the reactor configuration and process parameters. While syngas (i.e., CO and H_2) is the most desirable output, CO_2 and $C_1 – C_4$ hydrocarbons are most commonly found in the pyrolysis gases depending on the feed constitution [6,18,20]. Plastics with low or no oxygen content yield more $C_1 – C_4$ hydrocarbons than paper and biomass components, which produce more CO and CO_2 due to the large amount of oxygen present in the feed [6,18,20]. Although plastics consist of

high carbon and low oxygen content, zero char yield for some plastics showed that the observations made in biomass pyrolysis are not uniformly applicable to all feedstocks [17].

The second set of studies used model MSW compositions, wherein the individual waste components were mixed together in the required proportion reported by the environmental agencies [4,22]. Other studies in the same category included real MSW/RDF as feed [23–25]. However, these studies were performed only with mixtures and not with individual components. Without an insight into which components contribute to which aspects of the results, it is difficult to extend the conclusions to other RDF compositions that may contain different feed components.

The third set of studies conducted gasification experiments on several individual components and compared the results between them to draw conclusions [26,27]. Nevertheless, these studies lacked a comparison with the composite comprising the selected individual components.

Finally, a fourth set of studies involved investigation of individual and two-component mixtures [28,29]. Despite their efforts to understand the similarities and differences between the individual components and blends, these studies did not include a blend of all the individual components studied. Since the behavior of a multicomponent mixture may differ from a two-component mixture, the conclusions cannot be easily extended to a model RDF composition.

In order to gain more insight into the cause and effect behavior in MSW/RDF gasification, a comparison of the composite with the primary components is essential. Our approach seeks to address this issue by defining the model RDF composition with

representative components. This is followed by a comparison and analysis of pyrolysis and gasification results of both the components and the composite. Pyrolysis studies were carried out in a thermogravimetric analyzer (TGA) by heating at 20 K/min from room temperature to 1000 °C in 200 ml/min of nitrogen flow. Large amounts of chars for elemental analysis were generated in a quartz tubular reactor at the same heating conditions. CO_2 gasification studies were performed on the chars generated in-situ in the TGA with the same conditions except at a constant temperature of 800 °C.

2.2 Materials and Methods

2.2.1 Raw materials and feed preparation

Major components in the discarded portion of MSW, as identified by EPA (2012), were the basis for the model RDF composition in this study [1]. Key components: plastics, paper and food waste, were further sub-categorized to form a representative basis for the model composition. However, minor fractions, like rubber, wood and textiles, were represented by a single or double constituent each. Low density polyethylene (LDPE), high density polyethylene (HDPE), polypropylene (PP), polystyrene (PS), and polyethylene terephthalate (PET) were considered within the plastics fraction. Whereas, the paper fraction was further divided into tissue paper, newspaper, office paper, paperboard, and magazine paper components. Food waste, in general, is segregated into two categories: pre-consumer waste (waste generated during food preparation) and post-consumer waste (leftover food) [30,31]. In order to have an appropriate representation of both types of food wastes, the former category was represented by orange peel, banana peel and potato peel while the latter, by mixed cereals (rice, wheat, corn and oats) and dry dog food (Milkbone

biscuits). LDPE was supplied as Microthene FN51000 (LyondellBasell), HDPE as Marlex 9018 (A-Top Polymers Inc.), PP as Profax 6301 (LyondellBasell), PS as Styron 615 (Americas Styrenics LLC) and PET as PQB7-76 Prime PET resin (Polyquest Inc.). Paper and food waste fractions were procured from local stores and resources. Rubber powder was supplied by Lehigh Technologies in the form of micronized rubber, Polydyne 40 and 200. The textile fraction was represented by $2/3^{rd}$ cotton fabric and $1/3^{rd}$ PET. Finally, the wood fraction was represented by pine wood chips.

Preliminary studies of the individual components were performed with a particle size of 2 mm or less as obtained from a Wiley mill. However, for studies involving a mixture of two or more components, an accurate representation of all the components in a micro scale run (5 – 15 mg) posed a challenge. To overcome this complexity, an additional size reduction step was performed. Individual component particle sizes of less than 106 μm were achieved in a Retsch MM 400 mixer mill. For all the experiments listed in this study for RDF composites, individual components of less than 106 μm were thoroughly mixed at 30 Hz and 3 minutes in the mixer mill. This was followed by heat pressing at an elevated temperature of 104 °C and 1000 psi pressure in a Wabash press. Subsequent pelletizing by hammer-driven hole punches was performed. The images of powder formed from < 106 μm particles, 2 mm pellet and 4 mm pellet are shown in Figure A.1. It is to be noted that, the additional size reduction step is only essential in a lab scale TGA study where low amounts of feed are commonly used. Moreover, the economics involved with high particle size reduction in an industrial scale process would be unfavorable. Additional feed processing steps were required for vegetable and fruit peels to improve handling characteristics. In this regard, all the peels were cut into small pieces and subjected to

drying in an oven at 110 °C overnight to remove excessive moisture and to avoid bacterial growth prior to size reduction.

2.2.2 Experimental methods and conditions

Two types of reactors were used to perform the low heating rate pyrolysis experiments. The first reactor is a semi-batch quartz reactor as shown in Figure 2.1. It consists of a tubular reactor with an inlet gas port on one end and a gas outlet on the other. The feed sample was loaded onto a quartz boat and placed inside the tubular reactor, and the tube itself was enclosed in a furnace to be heated up to 1000 °C. Two condensers were connected on the outlet end to cool down the hot pyrolysis gases released which were later collected in FlexFoil™ plus sample bags. The collected gases were analyzed in a Varian 490 micro-GC with four channels consisting of four 10 m long columns (two Molecular Sieve 5 Å, one Plot column, and one Al_2O_3 column) and four TCD detectors with the lowest detection limit of 10 ppm for all calibrated gases. The gas yield was established by assuming a basis of nitrogen tie element and by calculating the yield of each gas component from the gas composition. The yield was verified by passing the contents of the gas bag through a Sierra Top-Trak 822 mass flow meter and totalizer that calculated the total volume of gas in the bag. Char yield was determined based on the weight difference of the quartz boat before and after the pyrolysis run. Tar was quantified by liquid collected in the condenser flasks and by subsequent combustion gas analysis of the tars deposited on the tube walls. Depending on the experimental conditions used, product yields of gas, char and tar components vary during pyrolysis of RDF (typical values in Table 1.3).

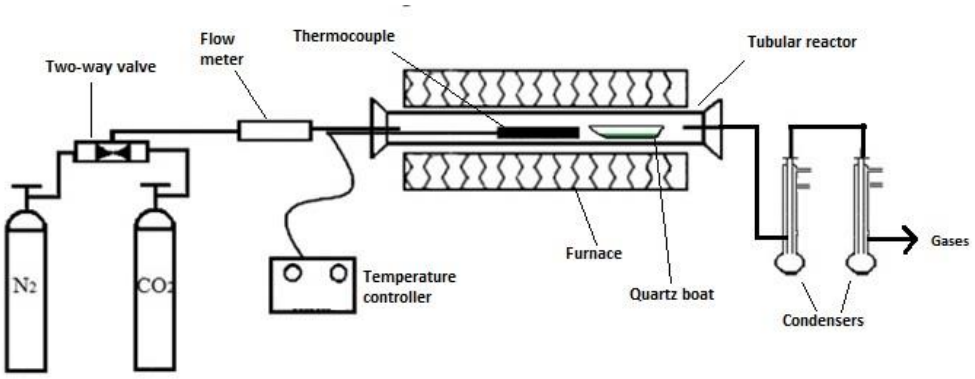

Figure 2.1. Quartz reactor setup.

The second reactor is an SDT-Q600 thermogravimetric analyzer (TGA) by TA Instruments. This system was used for both pyrolysis and gasification experiments. It records weight loss as a function of temperature and time and is also equipped with differential scanning calorimetry (DSC) measurement capability. The pyrolysis conditions used in both the reactors were 200 ml/min of N_2 flow, 20 K/min ramp rate and a final temperature of 800 to 1000 °C. Typical sample sizes used were about 10 mg in the TGA and 1 g in the quartz reactor unless otherwise specified. For gasification runs, the sample was heated at the same ramp rate of 20 K/min to 800 °C and was followed by an isothermal step of 15 minutes to stabilize the weight in the TGA. Subsequently, 100% CO_2 was introduced as the gasifying agent until complete carbon conversion was achieved as indicated by weight stabilization. The conversion (X) and reactivity (R) in these gasification experiments were determined according to the following formulae:

$$X = \frac{(m_0 - m_t)}{(m_0 - m_{ash})} \qquad \text{Eq. (2.1)}$$

$$R = \frac{-1}{(m_t - m_{ash})} \frac{dm_t}{dt} \qquad \text{Eq. (2.2)}$$

where,

m_0 = initial mass at the introduction of 100% CO_2

m_t = mass at time‘t’

m_{ash} = final mass at the end of the gasification run

A comparison of both these parameters for different feed samples gives insight into the gasification reactivity for the entire conversion range.

2.2.3 Characterization techniques

Ultimate analyses and Higher Heating Value (HHV) of model RDF feed and char samples were determined by Huffman Laboratories in Golden, CO. Inductively coupled plasma optical emission spectrometry (ICP-OES) with acid digestion and caustic fusion methods was conducted on all the individual char residues to determine the amount of inorganic content. Morphological features in different char samples were analyzed by scanning electron microscopy (SEM). A thermally assisted field emission SEM by Zeiss-LEO 1530 series was used for this purpose. The typical gun voltage used was about 4 – 5 kV. Samples were mounted on an aluminum stub using double-sided carbon tape and further coated with a 7 nm thick gold film using a Quorum Tech Q150T ES sputter coater for better conductivity of electrons during imaging. The SEM instrument, Zeiss-LEO 1530 series, used is also equipped with Energy Dispersive X-ray Spectroscopy (EDX). An accelerating voltage of 10 kV was used to envelop the entire range of X-ray emission peaks (Kα and Lα values) of the major inorganic species present. The penetration depth of the probe was estimated to be around 2 μm based on the accelerating voltage [32].

N_2 and CO_2 physisorption were utilized to establish the macropore and micropore surface areas of char samples. CO_2 adsorption has been found in the literature to have the

ability to assess the narrow microporosity (size <0.7 nm), whereas N_2 adsorption is kinetically restricted [33]. Thus, the combination of N_2 (77 K) and CO_2 (273 K) physisorption isotherms provides a complete assessment of the morphology of microporous chars. A Micromeritics Instruments ASAP 2020 was used for all adsorption measurements. A degassing step at 110 °C was used for 4 hours prior to analysis. Surface area was computed using the Brunauer−Emmett−Teller (BET) equation for N_2 and the Dubinin−Radushkevich (DR) equation for CO_2 [34,35].

2.3 Results and Discussion

2.3.1 Determination of model RDF composition

The range of decomposition temperatures, residual mass, and type of most abundant gaseous products during pyrolysis of individual components are listed in Table 2.1. All plastics were completely converted to volatile products with the exception of PET that formed a solid residue of 15 wt%. Since there was no oxygen present in most plastics (except for PET), the gas composition was dominated by C_2 – C_3 hydrocarbons, and the decomposition took place in a very narrow temperature range. PET showed a broader decomposition temperature range, substantial residue, and the presence of CO and CO_2 in the gas composition. This is possibly due to the presence of aromatic and carboxyl groups in its structure, as opposed to straight or branched alkyl chains in other polymeric plastics. The oxygen present in the PET structure was likely released in the form of CO_2 leaving behind free radicals that led to crosslinking reactions and ultimately, to the formation of char [36]. In contrast, although PS has a pendant benzene, it is easy to strip off and decompose to its monomer, styrene.

Table 2.1. Pyrolysis results of individual components

Component	Decomposition range (°C)	Residue weight%	Major gas components
LDPE	425 - 520	~0	C_2H_4, C_3H_6, CH_4 and H_2
HDPE	450 - 520	~0	
PP	400 - 500	~0	
PS	325 - 470	~0	
PET	390 – 510; 510 - 770	15	CO and CO_2 (200 – 550 °C) H_2 and CH_4 (550 – 900 °C)
Tissue paper	250 - 410	10	
Newspaper	220 – 410; 410 - 650	17	
Office paper	240 – 410; 410- 710	20	
Paperboard	245 – 400; 400 - 720	22	
Magazine paper	210- 410; 410 - 700	39	
Orange peel	150 – 380; 380 - 740	25	Mostly CO_2 with some CO (200 – 550 °C) H_2 and CH_4 (550 – 900 °C)
Banana peel	150- 420; 420 - 710	31	
Potato peel	180 – 375; 375 - 550	22	
Mixed cereals	210 – 500; 500 - 900	21	
Dry dog food	200 – 360; 360 - 640	23	
Pine wood	200 – 400; 400 - 700	15	CO and CO_2 (200 – 550 °C) H_2 and CH_4 (550 – 900 °C)
Cotton	270 – 410; 410 - 550	11	
Rubber	200 - 500	31	H_2, CH_4 and C_2H_4

Paper components primarily consist of cellulose along with some hemicellulose, lignin and inorganic elements [19]. Since hemicellulose starts decomposing at lower temperatures (~200 °C), the decomposition range of paper components was observed to be broader than that of plastic components. A second decomposition range (400 – 700 °C) with much lower rate of weight loss was observed for all paper components. This is

attributed to additional decomposition reactions taking place at higher temperatures, which is supported by the release of H_2 and CH_4, common cracking reaction products. The amount of residue at the end of pyrolysis was proportional to the amount of additives present in each paper component. For instance, tissue paper containing minimal additives had the least amount of char residue. While magazine paper containing several coating agents and pigments, had the highest residual char. In terms of decomposition ranges and gas composition, all paper components showed comparable pyrolysis results.

The decomposition range of food waste components was much broader compared to the rest of the RDF components. Food waste is similar to biomass and contains more oxygen than any other component [37]. This was apparent in the gas composition, where CO_2 was the dominant gas fraction produced. A similar secondary decomposition range, similar to paper components, was observed, associated with H_2 and CH_4 release. All the food components yielded char residues in 20 – 30% range. Based on the results, it is ascertained that in each category (plastics, paper, and food waste), components pyrolyzed in a similar manner. Moreover, wood and cotton showed similar results as paper, since the backbone of both species is hemicellulose, cellulose and additionally lignin in wood [38,39]. Rubber showed a single decomposition range where both the styrene-butadiene cleavage and further breakdown of butadiene and styrene are expected to take place [40]. Rubber had the highest char content among all the components present, which is attributed to low oxygen content and the high amount of carbon black added during its manufacture. Since components in three major categories (i.e., plastics, paper and food waste) did not show notable differences, the representatives for model RDF composition were selected based on EPA data (Figure A.2). Two components each from the major categories were

selected accompanied by the minor fractions (cotton, wood and rubber). These nine components constituted the model RDF composition for this study as shown in Figure 2.2 a with their TGA weight loss profiles in Figure 2.2 b.

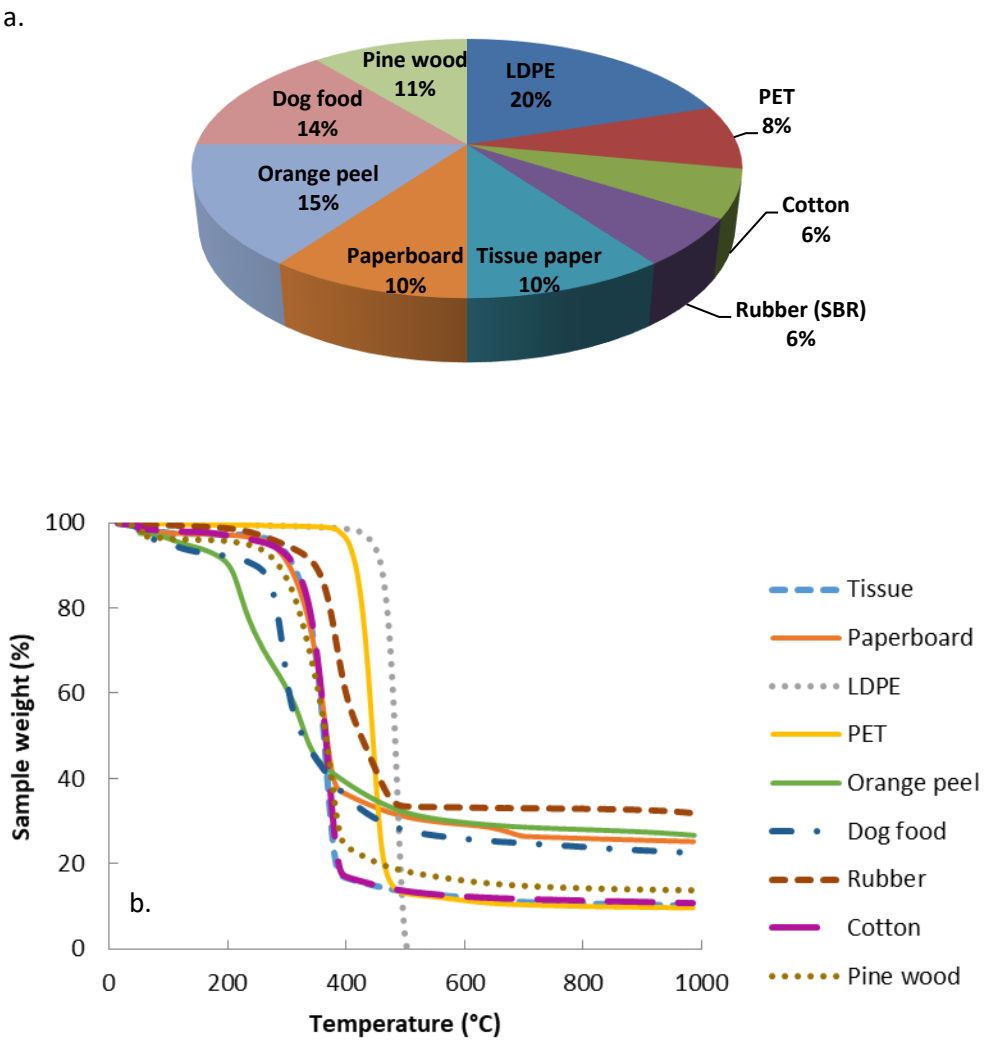

Figure 2.2 a. Model RDF composition b. Weight loss profiles of all the individual components present in model RDF.

Among the selected components of model RDF composition, LDPE and PET decomposed in a narrow temperature range, while orange peel and dog food converted over a broad range. The weight loss curve of paperboard coincided with tissue paper, cotton and

pine wood until 400 °C after which the high residue of paperboard was apparent with the weight stabilization at a higher level. Cotton and tissue paper almost entirely overlapped since cellulose is the primary constituent in both the species [19,39]. Rubber had a very unique weight loss profile that could be distinguished from the beginning. From the different curves observed, it is clear that the components present in RDF had diverse weight loss profiles during pyrolysis. Pyrolysis of the model RDF was performed, and the properties of RDF feed and RDF char are presented in Table 2.2. The CHNO contents of model RDF were found to be between that of the typical values of biomass and plastic, as expected [17,41]. The char yield was around 16 wt%, and based on the CHNO content of the char, more than 95% of H and O were released during pyrolysis. Moisture and ash content of RDF feed were found to be on the lower end of the literature values, probably due to manual mixing of pure individual components unlike the real MSW produced [4,23,24].

Table 2.2. Properties of model RDF and RDF char

RDF feed		
Moisture content (wt %)	~ 4	
HHV (kJ/kg)	24800	
N_2 surface area (m^2/g)	0.98	
CO_2 surface area (m^2/g)	22.6	
Density (g/cc)	0.4	
Weight %	RDF feed	RDF char*
Carbon	55.1	77.1
Hydrogen	7.65	0.84
Nitrogen	0.77	1.45
Oxygen	33	5
Ash	3.44	17

*RDF char generated at 20 K/min and heated to 1000 °C

Pyrolysis profiles of the model RDF composite were tested for reproducibility, as shown in Figure A.3. High overlap of the curves indicated a reproducibility greater than 95%. TG and DTG pyrolysis weight loss profiles of the model RDF composite are provided in Figure 2.3 a. Following the initial moisture loss, two distinct slopes were observed in the TG curve that are shown in the DTG curve as two distinguishable peaks. Based on the individual DTG curve data, the composite DTG curve was deconvoluted to identify the individual components. The first peak around 220 – 400 °C represented the decomposition of the paper components, cotton and pine, while the second peak around 400 – 520 °C is attributed to the decomposition of plastics. Food waste pyrolyzed across a broad range of 180 – 640 °C, while rubber coincided with both the peaks. The demarcation of peaks with components showed a certain independent behavior during pyrolysis. This was further explored with a comparison of the results from individual components and a RDF composite.

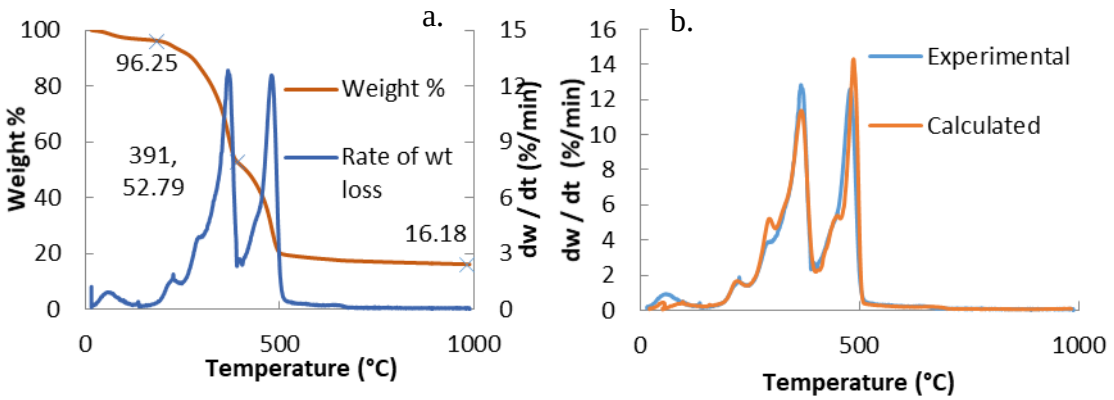

Figure 2.3 a. TG and DTG profiles of the model RDF composite b. Comparison of experimental RDF DTG curve with the linear addition of individual components in the calculated DTG curve.

2.3.2 Additive effect of individual components during pyrolysis

A comparison of the experimentally observed weight loss data and calculated weight loss data was performed. The calculated RDF decomposition curve was established by the addition of weighted curves of the individual components based on the composition shown in Figure 2.2 a. A comparison of experimentally observed and calculated DTG profiles of RDF composite is presented in Figure 2.3 b. The curves were reasonably similar with a high degree of overlap, which indicates that the components pyrolyzed independently without significant interaction. It should be noted that the diluting by N_2 may have prevented significant interaction between the pyrolysis gaseous products. Moreover, the observed char yield of the RDF composite of about 16.2% was also in excellent agreement with the predicted char yield of 15.8%. Thus, the pyrolysis weight loss profile and char yields of the RDF composite can be expressed as a sum of the pyrolysis weight loss profiles and char yields of the individual components, respectively.

The gas composition of the individual components and RDF composite was collected in three temperature ranges. The first was the low temperature regime of 100 – 600 °C, the second was the high temperature regime of 600 – 800 °C, and the third was the cooling regime of 800 – 400 °C. It was deemed appropriate to collect gases even in the cooling period since tars deposited on tube walls underwent secondary reactions to release gases at temperatures above 400 °C. A comparison of predicted and experimentally observed average gas composition data is reported in Table 2.3.

Table 2.3. Comparison of gas composition of experimental RDF pyrolysis with the cumulative addition of gas compositions of constituent components (calculated) at 20 K/min up to 800 °C

Component	RDF – calculated (mol %)	RDF – experimental (mol %)
H_2	29.7	27.24 ± 0.5
CH_4	16.1	17.16 ± 0.5
CO	26.2	25.72 ± 1
CO_2	16.1	15.59 ± 0.2
C_2H_4	8.32	10.03 ± 0.5
C_2H_6	0.71	0.76 ± 0.05
C_2H_2	0.88	1.22 ± 0.1
C_3H_8	0.17	0.18 ± 0.01
C_3H_6	1.30	1.38 ± 0.15
n-C_4H_{10}	0.05	0.08 ± 0.01
1-C_4H_8	0.21	0.26 ± 0.03
1,3 Butadiene	0.29	0.37 ± 0.05

The predicted gas composition was obtained by the addition of the weighted gas yields of the individual components. It is found that, in both cases, the lighter hydrocarbons, H_2, CH_4, CO, CO_2 and C_2H_4 were the major species present. C_2H_4, CO and CO_2 were dominant in the lower temperature regime, while H_2 and CH_4 were detected in the higher temperature regime and during the cooling period. The mole fractions of the first five major gas constituents formed during the experimental process were found to be very similar (less than 5% difference) to the predicted values. Acetylene and butane had larger differences, which could be due to the experimental error associated with the low amounts present. Since the differences associated with the two gas compositions were minimal, the gas composition of the RDF composite can be reasonably expressed as a sum of the gas compositions of the individual components.

The third product of pyrolysis, tar, was difficult to recover due to deposition on the reactor walls and conversion to coke at high temperatures. In addition to the tar recovered in the condensers, it was further quantified by combustion at the end of the pyrolysis to have a better mass closure. Table 2.4 shows the product yields measured during pyrolysis along with the addition of small amounts of oxygen. During pyrolysis without addition of oxygen, a large amount of tar was unrecovered due to deposition on walls in the unheated zone. This led to a poor mass balance of about 50%. However, with increasing oxygen content, gas fraction increased rapidly due to CO_2 formation, bringing the mass balance to 92%. The unquantified mass in all the three cases is expected to be a combination of water and tar. For pyrolysis with 5% oxygen, a negligible amount of tar was deposited in the condenser and on the walls of the reactor tube, indicating very limited tar formation. In the scope of this study, extensive tar composition analysis was not done.

Table 2.4. Product yields during pyrolysis (20 K/min to 800 °C) with and without residual oxygen

Products	**0% O_2**	**1% O_2**	**5% O_2**
Char	18.7%	18%	11.4%
Gas	24%	35.8%	80.6%
Tar (combustion gases + weight difference)	2.5% + 4.6%	0.4% + 4.6%	0.05%
Mass closure	49.8%	58.8%	92%

Further comparison of the heat effects involved during pyrolysis of both the individual components and the RDF composite is shown in Figure 2.4. All of the plastic, paper, cotton and pine components had endothermic heats associated with pyrolysis while food waste and rubber showed exothermic behavior, similar to the observations made in the literature [42–44]. The sum of these heats translated into almost a thermo-neutral step

for RDF pyrolysis. The calculated and experimental values were found to be close to zero due to the heat balance between the exothermic and endothermic components present. Although the heat values of experimental and calculated RDF pyrolysis do not seem very close immediately, when compared to the heat effects involved during gasification (e.g., CO_2 gasification by Boudouard reaction), the heat value of pyrolysis is three orders of magnitude lower [45]. Hence, the observed thermo-neutral behavior for RDF pyrolysis is deemed correct.

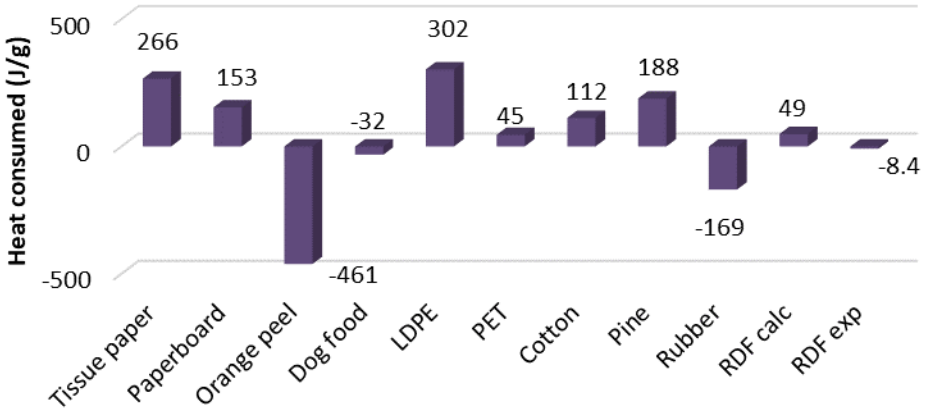

RDF calc – linear addition of heat effects of individual components; RDF exp – experimental observed pyrolysis heat effects of RDF

Figure 2.4. Heat effects involved in the pyrolysis of individual components and the RDF composite.

The ash content and the inorganic elements present in the chars from individual components and the RDF composite are compared in Table 2.5. The sum of the elements was well below the ash content as they were reported in elemental form and not the oxygenated form present in the ash. All the elements with concentrations less than 0.01 wt% were considered insignificant, but they were included in the table since they were above the detection limit.

Table 2.5. Ash content and inorganic elements present in model RDF char and the constituent components

Char Species*	Ash feed basis (%)	Ash char basis (%)	Ca (%)	K (%)	Mg (%)	Al (%)	P (%)	S (%)	Si (%)
Tissue Paper	~2	19.6	4	0.04	0.09	1.4	0.04	0.03	0.53
Paperboard	~16	71.1	5.5	0.04	0.3	2.6	0.06	0.09	6.8
PET**	~0.2	1.4	0.01	0.01	0.004	0.04	0.05	0.03	0
Orange peel	~3	12	0.68	3.8	0.11	0.005	0.23	0.14	0.07
Dog food	~4.5	19.9	4	0.52	0.23	0.02	2.3	0.03	0.34
Rubber	~3	9.4	0.11	0.11	0.11	0.1	0.03	1.7	2.8
Cotton	~2.8	24.3	0.56	0.02	0.16	0.03	0.06	0.04	0.06
Pine**	~0.3	2	0.07	0.05	0.03	0.002	0.004	0.007	~0
RDF (calculated)	3.35	21.5	2.11	1.05	0.15	0.52	0.54	0.27	1.48
RDF (measured)	3.5	21.2	2.17	1.13	0.18	1.13	0.52	0.14	1.41

*Generated at 20 K/min up to 800 °C **Accuracy not guaranteed due to very low ash content; All values in weight % and the inorganics are on char basis

Certain inorganic elements play a vital role in the gasification thus, it is essential to quantify their concentrations [7,15]. Paper components contained high amounts of calcium and aluminum, which can be attributed to the $CaCO_3$ and Al_2O_3 added during paper manufacture [46,47]. Although cotton had higher calcium and magnesium contents compared to the rest of the inorganics present in it, the absolute quantities of these elements were much lower when compared to the paper components. Additionally, paperboard contained a large amount of silicon, suspected to be an additive during its manufacture [48]. Orange peel contained large amounts of potassium, while dog food had a high content of calcium and phosphorous. This combination of calcium and phosphorous is suspected to be due to the presence of hydroxyapatite [$Ca_5(PO_4)_3(OH)$], a naturally occurring mineral in bones, which is the basis for dog food composition [49]. Since phosphorous binds

calcium in hydroxyapatite, it is expected to play an inhibitive role during gasification. Rubber contained high amounts of sulfur and silicon. The presence of sulfur is a result of vulcanization during rubber manufacture, while silicon was probably added as a filler during the preparation and could also be a result of the recycled tire material (containing dirt) [40,50].

The ash yield is an equally important parameter, since it defines the absolute quantity of inorganics present. The inorganics are supposedly present in their oxidized forms (CaO, Al_2O_3, K_2O etc.), and thus the ash holds reasonable amounts of oxygen, in addition to anions and carbonaceous matter [51,52]. All the components had ash contents below 5 wt% except for paperboard, which yielded 16 wt% of ash on the feed basis. The high content of ash in paperboard is attributed to the amount of additives added during its manufacture, which also includes a high amount of silicon [48]. PET and pine had the lowest ash yields. No inorganic elements were found in PET, while, potassium and calcium dominated the low amount of pine ash produced. Finally, inorganic elements indicated in both the calculated and experimental RDF composite showed that there were four major inorganics present in RDF: Ca, K, Al and Si. It is expected that the interaction between these elements would influence the gasification reactivity, which will be discussed in Section 3.4.

Pyrolysis studies were conducted with the RDF feed using three different particle sizes (less than 106 µm powder, 2 mm pellets, 4 mm pellets). The hypothesis was that the higher residence time of gases inside the pellet may lead to secondary reactions and produce more char and heavier gas components. At the same time, a decrease in the particle size may improve heat and mass transfer rates thus increasing gas yield and decreasing

char yield. However, the results showed that the differences between the gas composition, product yields and the TGA profiles (Figure A.4) of the different feed sizes were below 10% and thus do not show a significant difference. These differences are expected to be more pronounced with a larger particle or pellet size similar to the sizes used in the industrial scale gasification (~ 5 cm) [53,54]. Thus, for the pellet sizes studied, the feed size did not impact the pyrolysis behavior substantially.

2.3.3 Char morphology after pyrolysis

SEM images of RDF feed pellet with 4 mm diameter and RDF chars produced from 2 mm and 4 mm diameter feed pellets are presented in Figure 2.5. The feed was more flat and smooth as compared to the char pellets which were significantly more porous with rough surfaces as indicated in Figure 2.5 a, b and, c. The smooth structure of the feed is possibly due to the melted plastic during preparation of the feed pellets, which forms a smooth layer after re-solidification. The smooth layer did not affect the pyrolysis decomposition profile as verified by a comparison with the powdered feed (Figure A.4). A shrinkage in the pellet size was observed for both the pellets, where the 4 mm pellet reduced to 3.2 mm in diameter while the 2 mm pellet reduced to 1.3 mm in diameter.

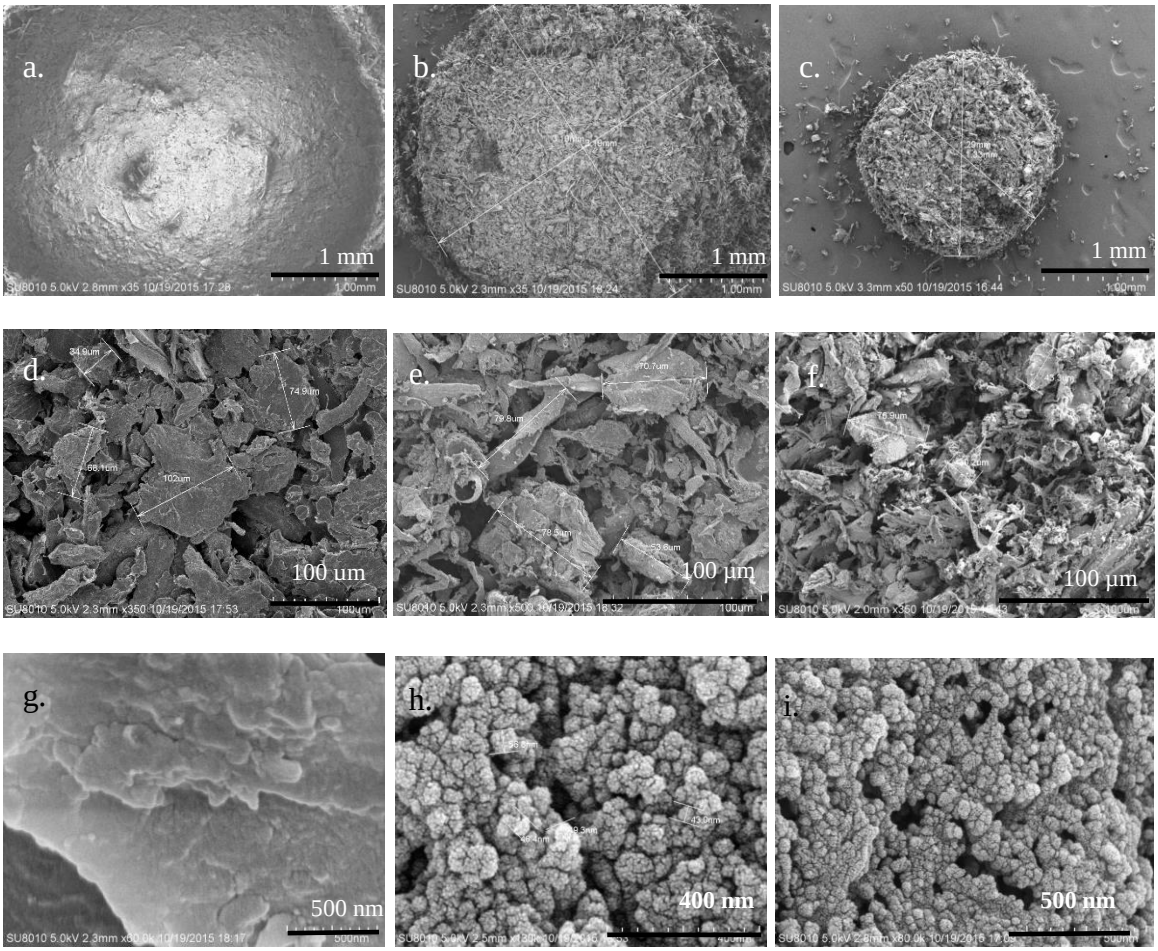

Figure 2.5 SEM pictures of a. RDF 4 mm feed at X35 b. RDF 4 mm char at X35 c. RDF 2 mm char at X35 d. RDF 4 mm feed at X350 e. RDF 4 mm char at X350 f. RDF 2 mm char at X350 g. RDF 4 mm feed at X80 K h. RDF 4 mm char at X80 K i. RDF 2 mm char at X80 K (chars generated at 20 K/min to a final temperature of 800 °C)

The second set of Figure 2.5 d, e and, f compares the individual particles comprising the pellet. Both the elongated fibrous paper, pine and textile particles and whole irregularly shaped food waste, rubber and PET particles were discernible in the images. Before pyrolysis, the particles were more distinguishable and less porous (Figure 2.5 d) than the particles after pyrolysis, which had a fluffy appearance with developed pore structures (Figure 2.5 e and f). Magnified images of the feed and the two pellets are shown in Figure 2.5 g, h and, i. Figure 2.5 g shows that the feed surface at even very high magnifications

(~80K X) is quite flat with a few bumps and irregularities. However, the two char pellets at the same magnification exhibited spherical nanostructures (Figure 2.5 h and i). These structures are expected to be the result of the pyrolysis process since they were absent in the feed. It is proposed that, at temperatures of 110 – 380 °C, plastics form a layer of melted polymer on the surface of the char, while some fractions of the feed like hemicellulose and cellulose start decomposing [55,56]. This leads to evolution of volatiles that are trapped under the melted plastic layer. At the same time, the char shrinks due to mass loss and forms clusters of leftover material leading to a porous overall structure. In order to verify the proposed evolution of char morphology, SEM images of 2 mm char generated at 250 °C and 400 °C were recorded (Figure 2.6). The SEM images in Figure 2.6 a and c depict the molten layer over individual particles, although the pore structure was not as well developed as the char generated at 800 °C (Figure 2.5). A further inspection of the chars at higher magnification (Figure 2.6 b and d) demonstrated the presence of trapped volatiles underneath a blanketed layer, which supports our hypothesis.

N_2 and CO_2 physisorption were utilized to measure surface area of RDF char. Nitrogen physisorption alone cannot determine the microporous surface area. Thus, carbon dioxide was utilized for complementary analysis [9,34]. The surface areas of RDF char determined by nitrogen and CO_2 physisorption were 15.5 m^2/g and 66 m^2/g, respectively. The difference in value is attributed to the microporous surface area, which is in line with the biomass char surface areas reported in literature [33].

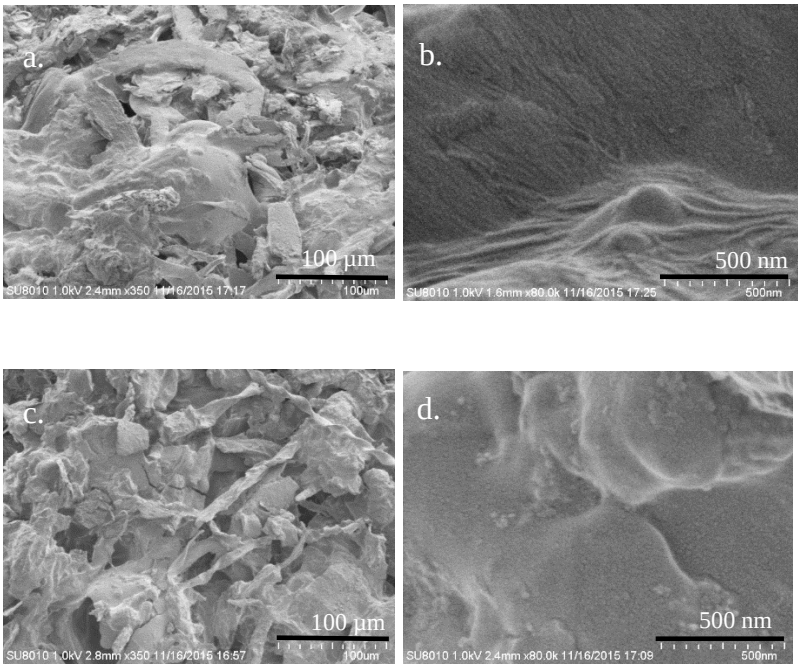

Figure 2.6 SEM pictures of a. RDF 2 mm char at 250 °C on X350 scale b. RDF 2 mm char at 250 °C on X80 K scale c. RDF 2 mm char at 400 °C on X350 scale d. RDF 2 mm char at 400 °C on X80 K scale.

2.3.4 Gasification studies of RDF composite and individual components

Char generated from pyrolysis was gasified with CO_2. The reactivity profile of the most reactive component of the RDF composite, orange peel, is compared with that of the least reactive component of RDF, rubber in Figure 2.7 a. The reactivity of orange peel (~0.15 min^{-1}) was nearly two orders of magnitude higher than the reactivity of rubber (~0.002 min^{-1}) at 50% conversion. All the samples had particle sizes less than 106 µm, and thus were devoid of internal transport effects. Different sample sizes in the crucible exhibited the same reactivity proving the absence of external mass transfer effects. Despite the lower BET surface area of orange peel char (28 m^2/g) as compared to rubber char (80 m^2/g), orange peel exhibited two orders of magnitude higher reactivity than rubber. Thus, this behavior is attributed to different types and amounts of inorganics present in the

assorted components (Table 2.5). The high reactivity of orange peel char is attributed to its high potassium content.

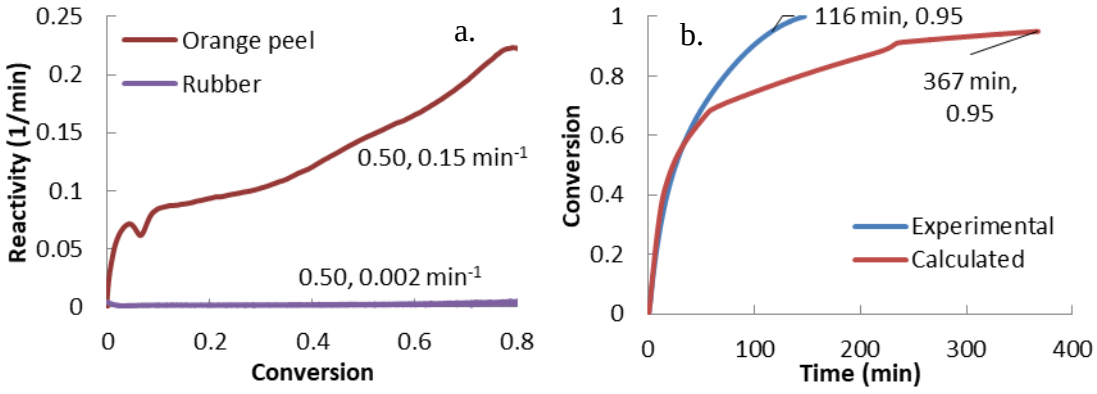

Figure 2.7 a. Reactivity profiles of orange peel and rubber chars in CO_2 gasification (chars generated at 20 K/min up to 800 °C) b. Conversion profiles of experimentally observed RDF composite char in CO_2 gasification and linear addition of individual conversion profiles (calculated curve) at the same conditions.

Based on previous results on biomass gasification, potassium plays a catalytic role during gasification [7]. Potassium induces electron density to the edge carbon active site and significantly changes the net charge by forming C-O-K [57]. Oxygen is transferred to the carbon active sites through the potassium, followed by the release of CO from the active carbon-oxygen complexes, by breaking the neighboring C-C bonds [58]. The catalytic effect of potassium was also apparent from the significant increase in the reactivity with conversion, as the potassium to carbon ratio increased. On the other hand, rubber contained negligible alkali or alkaline earth metals, which led to low gasification rates. Moreover, rubber contained a large amount of silicon that decreases the gasification reactivity when in contact with alkali or alkaline earth metals [16,59]. Silicon acts as a scavenger for alkali and alkaline earth metals by forming inactive silicates. Similar effects of K, Ca, Si, and P on gasification reactivity are seen in various components present in RDF, thus leading to a

broad range of gasification reactivities as presented in Figure A.5. Therefore, it was interesting to determine the extent to which different RDF components affect the gasification of each other.

A comparison of the observed gasification profile of RDF with the weighted addition of the profiles from the individual components is shown in Figure 2.7 b. The time taken by RDF to achieve 95% conversion experimentally was about 116 minutes, while it took 367 minutes to achieve the same conversion if all the components were gasifying independently. Thus, synergy was detected during the gasification of the RDF composite. This synergy is attributed to the role of potassium as a catalyst during RDF composite gasification. Potassium has mobility at high temperatures and thus can migrate over the surface [59]. This leads to potassium redistribution primarily from orange peel, to the rest of the components, thus, increasing the reactivity of the overall composite. The slightly lower rate below 40% conversion of the observed curve compared to the calculated curve is ascribed to the decreased amount of potassium available for orange peel gasification as a result of redistribution. However, the overall gasification rate of the experimentally observed RDF composite was much higher than the additive profile.

2.3.5 The origin of synergy during gasification

In order to understand the synergistic behavior better, a plot of reactivities of individual components and the RDF composite is shown in Figure 2.9 a. Two types of inorganics, alkali metals and alkaline earth metals can catalyze gasification reactions. The high potassium of orange peel resulted in the highest initial and average reactivities for this component. The calcium-rich components paper, paperboard and cotton had a high initial

reactivity but lower average reactivity. This indicates that calcium augmented the reactivity initially, but it sinters with time and thus loses its activity at higher conversions [15]. The decrease in reactivity of paperboard was much more pronounced, as in addition to calcium sintering, it had a high content of silicon that scavenged the calcium. Pine had small amounts of both calcium and potassium yet negligible silicon or phosphorous content and therefore showed intermediate reactivity. Dog food, as discussed, had a large amount of calcium but it is possibly bound with phosphorous in the inactive form of hydroxyapatite thus leading to a very low reactivity value. Both PET and rubber contained almost no alkali or alkali earth species and thus had very low reactivities.

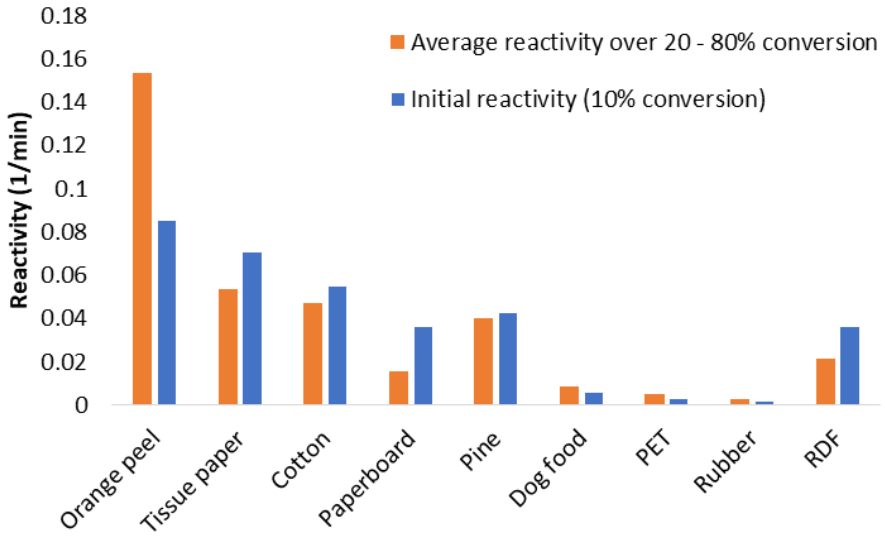

Figure 2.8. Average and initial gasification reactivities of individual component chars and RDF char.

As seen from Table 2.5, the most abundant inorganics in RDF were calcium, potassium, silicon and aluminum. Potassium and calcium were the major catalytic species present, and the decrease in reactivity of RDF is attributed both to sintering of calcium as

well as the scavenging effect of silicon present. To relate the observed reactivities to the inorganics present, a term called the inorganic index is introduced. It is defined as:

$$Inorganic\ index = \frac{(K + Ca)}{(Si + P)} X\ char\%$$

Aluminum is not included in the index (unlike the alkali index of coal literature that uses aluminum in the denominator), since it is not expected to play an inhibiting role below 900 °C [60]. A plot of inorganic index with the logarithm of time taken to gasify each component to 95% conversion is shown in Figure 2.9 a. The gasification times increased with decreasing inorganic index. However, the correlation was not linear, which implies that different inorganics had varied degrees of influence on the gasification reactivities. Orange peel had the lowest gasification time with the highest inorganic index. Moreover, potassium present in orange peel had higher catalytic activity than the other inorganics. Both PET and rubber had very low inorganic indices, hence possessed very high gasification times. Paper components contained calcium, which led to intermediate conversion time. Pine with very low ash content led to an unreliable inorganic index and thus was excluded from the plot.

The average reactivities over a conversion range of 20% to 80% are plotted as a function of the inorganic index in Figure 2.9 b. The plot follows a well-defined polynomial fit with an R^2 value of 0.971. The only data point lying outside the curve fit was dog food char that is suspected to contain calcium in the inactive form of hydroxyapatite [$Ca_5(PO_4)_3(OH)$]. Since the inactivity was not accurately represented by a simple ratio of Ca and P in the inorganic index, it differed from the expected value. Thus, the high R^2

value associated with the fit showed that the proposed inorganic index captured the reactivity trends of the different chars quite well.

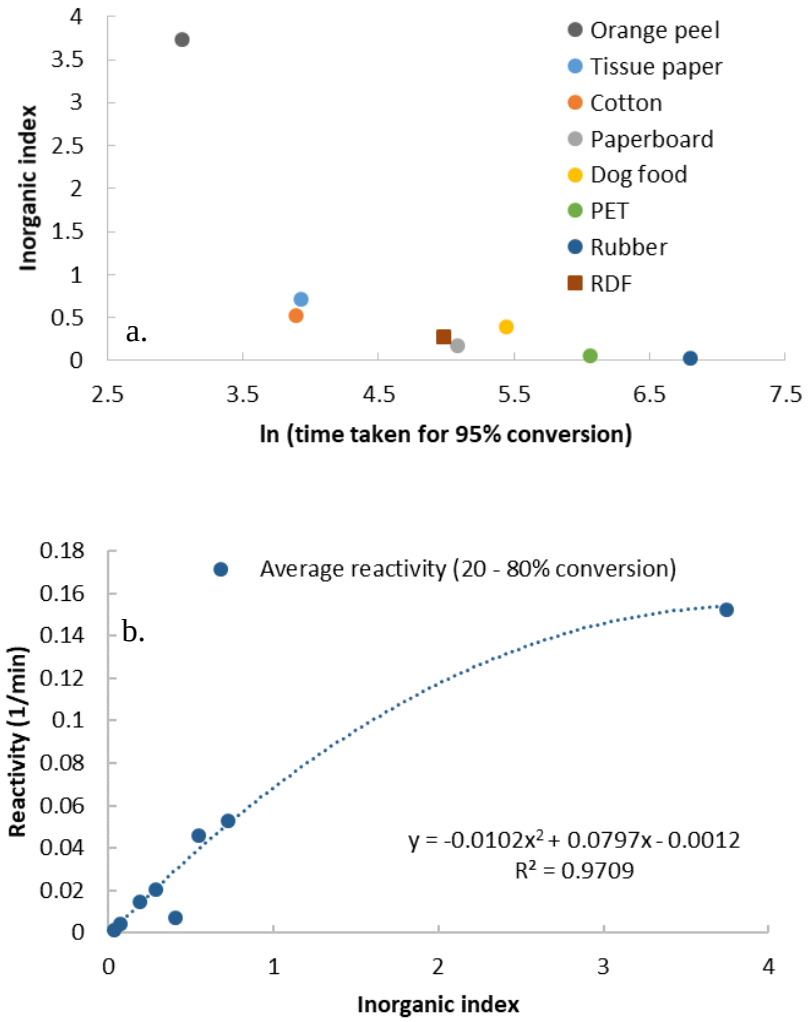

Figure 2.9 a. Variation of gasification times with inorganic index of individual component chars and RDF composite char b. Average reactivity over 20 – 80% conversion as a function of Inorganic index.

An SEM image and EDX maps of RDF char generated at 20 K/min and 800 °C are shown in Figure 2.10. Potassium (Figure 2.10 b) was found to be well dispersed across the entire region, while calcium (Figure 2.10 c) and silicon (Figure 2.10 d) were aggregated in

specific spots. This indicates that potassium had sufficient mobility to spread over the entire surface, while calcium sintered, and silicon remained localized.

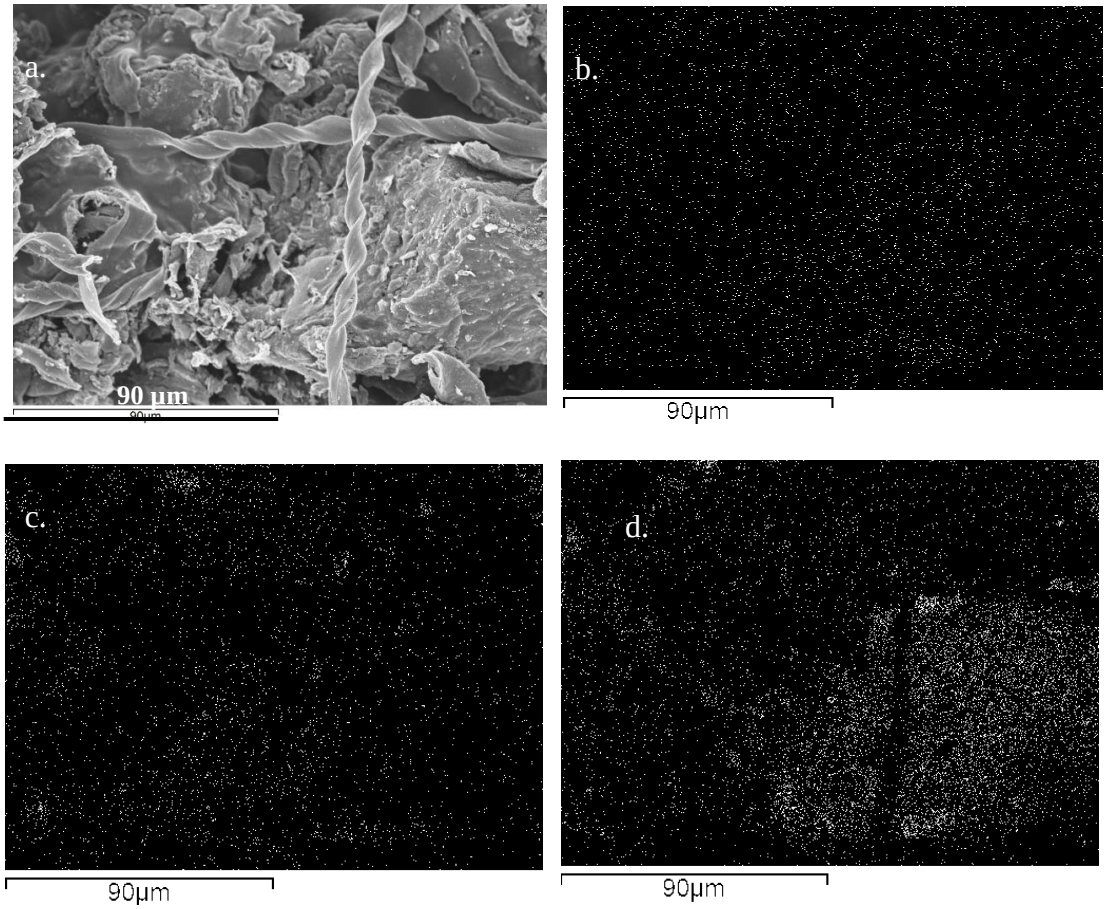

Figure 2.10 a. SEM micrograph of 2 mm RDF char generated at 20 K/min up to 800 °C b. Potassium content in the mapped area c. Calcium content in the mapped area d. Silicon content in the mapped area.

EDX maps were obtained for binary mixtures (50 – 50 weight %) of orange peel char and rubber char to identify potassium redistribution before and after pyrolysis. The EDX spectra of a physical mixture of the two chars generated by separate pyrolysis is given in Figure A.6, while a mixture of the two chars generated by combined pyrolysis of the mixed raw feeds is presented in Figure A.7. Figure A.6 shows that both potassium and silicon were segregated and could be used to identify orange peel and rubber chars

independently. However, Figure A.7 shows that, although silicon was segregated in rubber char particles, potassium was well distributed across the entire surface due to redistribution at high temperature pyrolysis (800 °C). This proves that potassium redistribution is possible from orange peel to other components during RDF composite pyrolysis.

2.3.6 Effect of particle size on the interaction of inorganics from orange peel and rubber char

The enhanced reactivity due to the re-distribution of potassium from orange peel char could be affected by the size of the orange peel particles used in contact with the other components. The hypothesis is that, with a larger particle size, the degree of contact between the orange peel particles and the other components would decrease which will reduce the rate of redistribution of potassium. To test this theory, 0.6 – 0.8 mm sized particles of orange peel were mixed with the least reactive component, rubber, of the same particle size range. This mixture was subjected to in-situ pyrolysis in the TGA at 20 K/min to 800 °C, followed by gasification in CO_2. The degree of synergy was compared to the same mixture of less than 106 µm size.

The conversion as a function of time is presented for the individual components and a 50 – 50 % mixture of orange peel and rubber of 0.6 to 0.8 mm size in Figure 2.11 a; of particle size less than 106 µm in Figure 2.11 b. The total time taken to achieve 95% conversion for orange peel and rubber particles below 106 µm was less than that for their counterparts of 0.6 to 0.8 mm particle size. The lower time required at smaller particle size can be attributed to a combination of lower mass transfer effects. The theoretical time required to achieve 89% conversion for the mixture of particle below 106 µm was 33%

lower (633 minutes) than that for the 0.6 – 0.8 mm mixture (971 minutes). This was based on the additive curves of orange peel and rubber mixtures assuming no interaction.

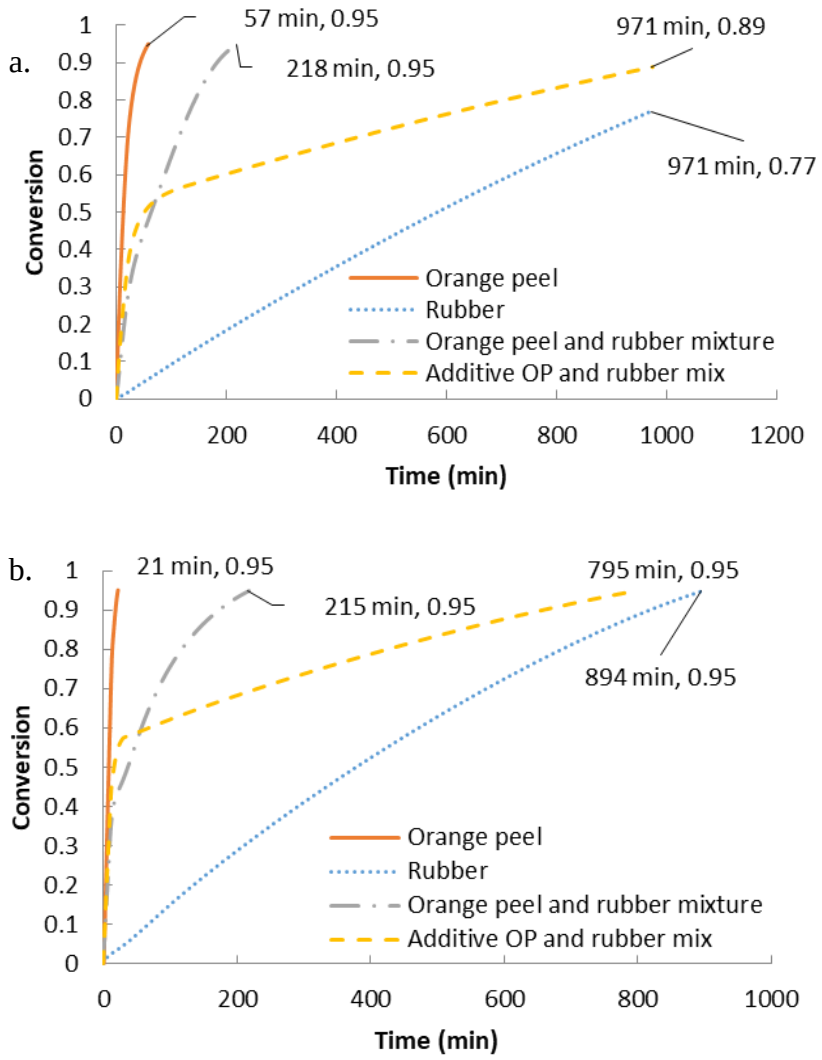

Figure 2.11. Time taken to convert orange peel char and rubber char individually and in a mixture form with a. 0.6 mm to 0.8 mm particles b. less than 106 µm particles in CO_2 gasification (chars generated at 20 K/min and heated to 800 °C).

However, experimentally observed overall conversion time (~ 95% conversion) for the mixture was approximately the same for both the particle sizes (218 minutes for 0.6 – 0.8 mm size range and 215 minutes for less than 106 µm size range). Although there was synergy present in both the particle size mixtures, the degree of synergy in both the cases

varied leading to a deviation between the predicted and the observed curves. This was analyzed in more detail with the comparison of the reactivity trends.

A comparison of the CO_2 gasification reactivity of the two particle size mixtures is shown in Figure 2.12. The initial reactivity of the smaller particle size mixture (< 106 µm) was about twice the reactivity of the 0.6 to 0.8 mm mixture at 10% conversion. However, reactivity of the smaller particle size mixture dropped drastically at 30% conversion and the following reactivity was about the same for the two mixtures. This sudden drop in reactivity is attributed to access to potassium by the more widely distributed silicon-rich rubber at smaller particle size. Although synergy seemed to be higher for lower particle size range mixture during initial conversion, the exacerbated silicon scavenging decreased the overall reactivity. Moreover, the lower initial reactivity in the larger particle size mixture could also be a result of greater transport effects. Therefore, the synergy observed during CO_2 gasification of RDF char is expected at all particle size ranges, nevertheless, the degree of the synergy is influenced by other factors.

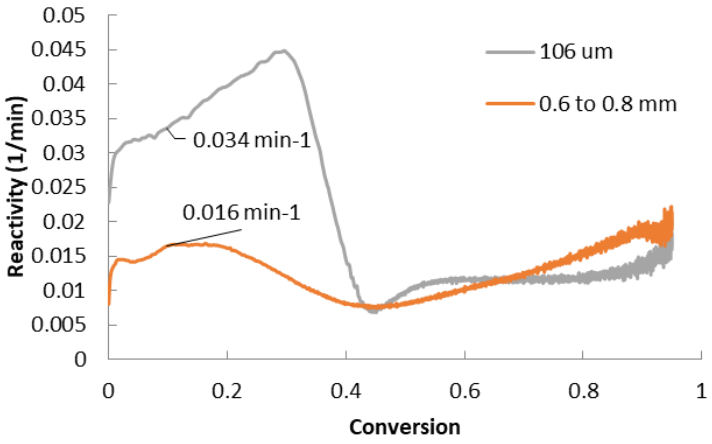

Figure 2.12. CO_2 gasification reactivity of 50 – 50% orange peel and rubber char mixtures of different particle sizes (chars generated at 20 K/min, heated to 800 °C).

2.4 Conclusions

The following conclusions have been drawn from this study:

a. Individual components within the major fractions of RDF (plastics, paper, food waste) have similar decomposition profiles during pyrolysis.
b. The decomposition rate, product yields and, gas composition of RDF composite pyrolysis can be expressed as a linear combination of those of the individual components comprising it.
c. Model RDF composite has a thermo-neutral pyrolysis profile where the heat effects can be represented by a linear combination of the heat effects of the individual component pyrolysis based on the weight fraction of the individual components present in the model RDF composite.
d. Char morphology of RDF char generated at 250 °C is attributed to trapped volatiles under a melted thermoplastic layer.
e. The time taken for the gasification of RDF composite is much lower than the time taken for the gasification of a combination of all the individual components.
f. The observed synergy in gasification reactivity is attributed to potassium redistribution from orange peel to the entire RDF composite. In addition, calcium from paper components has a catalytic effect for the initial gasification reactivity.
g. The inorganic index encompassing the catalytic inorganics (K, Ca) and inhibiting inorganics (Si, P) is a good indicator of the gasification reactivities of the components present.

h. Although synergy is present at all the tested particle size ranges, the degree of synergy is influenced by other factors like mass transfer effects and varying levels of silicon scavenging.

2.5 References

[1] US Environmental Protection Agency, Municipal Solid Waste Generation , Recycling , and Disposal in the United States : Facts and Figures for 2012, (2012) 1–14.

[2] U. Arena, Process and technological aspects of municipal solid waste gasification. A review, Waste Manag. 32 (2012) 625–639. http://dx.doi.org/10.1016/j.wasman.2011.09.025.

[3] C. Valkenburg, M. Gerber, C. Walton, S. Jones, B. Thompson, D. Stevens, Municipal Solid Waste (MSW) to Liquid Fuels Synthesis, Volume 1: Availability of Feedstock and Technology, 1 (2008) 1–43. http://www.pnl.gov/main/publications/external/technical_reports/PNNL-18144.pdf.

[4] U. Lee, J.N. Chung, H.A. Ingley, High-temperature steam gasification of municipal solid waste, rubber, plastic and wood, Energy & Fuels. 28 (2014) 4573–4587. http://dx.doi.org/10.1021/ef500713j.

[5] M. McHenry, Waste to Energy Technologies, Murdoch Univ. (2006). http://www.see.murdoch.edu.au/resources/info/Tech/waste/ (accessed December 3, 2015).

[6] J.-W. Kim, T.-Y. Mun, J.-O. Kim, J.-S. Kim, Air gasification of mixed plastic wastes using a two-stage gasifier for the production of producer gas with low tar and a high caloric value, Fuel. 90 (2011) 2266–2272. http://www.sciencedirect.com/science/article/pii/S0016236111000913.

[7] K. Mitsuoka, S. Hayashi, H. Amano, K. Kayahara, E. Sasaoaka, M.A. Uddin, Gasification of woody biomass char with CO_2: The catalytic effects of K and Ca species on char gasification reactivity, Fuel Process. Technol. 92 (2011) 26–31. http://linkinghub.elsevier.com/retrieve/pii/S0378382010002791.

[8] K. Li, R. Zhang, J. Bi, Experimental study on syngas production by co-gasification of coal and biomass in a fluidized bed, Int. J. Hydrogen Energy. 35 (2010) 2722–2726. http://dx.doi.org/10.1016/j.ijhydene.2009.04.046.

[9] A. Gomez, N. Mahinpey, Kinetic study of coal steam and CO_2 gasification: A new method to reduce interparticle diffusion, Fuel. 148 (2015) 160–167.

http://www.sciencedirect.com/science/article/pii/S001623611500085X.

[10] K. Sjöström, G. Chen, Q. Yu, C. Brage, C. Rosén, Promoted reactivity of char in co-gasification of biomass and coal: Synergies in the thermochemical process, Fuel. 78 (1999) 1189–1194.

[11] P. Kannan, a. Al Shoaibi, C. Srinivasakannan, Energy recovery from co-gasification of waste polyethylene and polyethylene terephthalate blends, Comput. Fluids. 88 (2013) 38–42. doi:10.1016/j.compfluid.2013.09.004.

[12] I. Ahmed, a. K. Gupta, Syngas yield during pyrolysis and steam gasification of paper, Appl. Energy. 86 (2009) 1813–1821. doi:10.1016/j.apenergy.2009.01.025.

[13] V. Belgiorno, G. De Feo, C. Della Rocca, R.M. a Napoli, Energy from gasification of solid wastes, Waste Manag. 23 (2003) 1–15.

[14] P. Lahijani, Z.A. Zainal, A.R. Mohamed, M. Mohammadi, CO_2 gasification reactivity of biomass char: Catalytic influence of alkali, alkaline earth and transition metal salts, Bioresour. Technol. 144 (2013) 288–295. http://dx.doi.org/10.1016/j.biortech.2013.06.059.

[15] M. Jiang, J. Hu, J. Wang, Calcium-promoted catalytic activity of potassium carbonate for steam gasification of coal char: Effect of hydrothermal pretreatment, Fuel. 109 (2013) 14–20. http://dx.doi.org/10.1016/j.fuel.2012.06.100.

[16] K. Umeki, A. Moilanen, A. Gómez-Barea, J. Konttinen, A model of biomass char gasification describing the change in catalytic activity of ash, Chem. Eng. J. 207–208 (2012) 616–624. http://dx.doi.org/10.1016/j.cej.2012.07.025.

[17] R. Zevenhoven, M. Karlsson, M. Hupa, M. Frankenhaeuser, Combustion and Gasification Properties of Plastics Particles, J. Air Waste Manage. Assoc. 47 (1997) 861–870. http://www.tandfonline.com/doi/abs/10.1080/10473289.1997.10464461.

[18] I. Ahmed, A.K. Gupta, Characteristics of cardboard and paper gasification with CO_2, Appl. Energy. 86 (2009) 2626–2634. http://linkinghub.elsevier.com/retrieve/pii/S0306261909001160.

[19] G. Jin, H. Iwaki, N. Arai, K. Kitagawa, Study on the gasification of wastepaper/carbon dioxide catalyzed by molten carbonate salts, Energy. 30 (2005) 1192–1203.

[20] R. Muangrat, J. a. Onwudili, P.T. Williams, Alkali-promoted hydrothermal gasification of biomass food processing waste: A parametric study, Int. J. Hydrogen Energy. 35 (2010) 7405–7415. http://dx.doi.org/10.1016/j.ijhydene.2010.04.179.

[21] I.I. Ahmed, A.K. Gupta, Pyrolysis and gasification of food waste: Syngas characteristics and char gasification kinetics, Appl. Energy. 87 (2010) 101–108. http://linkinghub.elsevier.com/retrieve/pii/S0306261909003523.

[22] E.E. Kwon, M.J. Castaldi, Urban energy mining from municipal solid waste (MSW) via the enhanced thermo-chemical process by carbon dioxide (CO_2) as a reaction medium., Bioresour. Technol. 125 (2012) 23–9. http://www.sciencedirect.com/science/article/pii/S0960852412012631.

[23] W.K. Buah, A.M. Cunliffe, P.T. Williams, Characterization of Products from the Pyrolysis of Municipal Solid Waste, Process Saf. Environ. Prot. 85 (2007) 450–457. http://linkinghub.elsevier.com/retrieve/pii/S0957582007714489.

[24] V. Cozzani, C. Nicolella, L. Petarca, M. Rovatti, L. Tognotti, A Fundamental Study on Conventional Pyrolysis of a Refuse-Derived Fuel, Ind. Eng. Chem. Res. 34 (1995) 2006–2020. http://pubs.acs.org/doi/abs/10.1021/ie00045a010.

[25] E.C. Efika, J.A. Onwudili, P.T. Williams, Products from the high temperature pyrolysis of RDF at slow and rapid heating rates, J. Anal. Appl. Pyrolysis. 112 (2015) 14–22. http://linkinghub.elsevier.com/retrieve/pii/S0165237015000054.

[26] M. Niu, Y. Huang, B. Jin, X. Wang, Oxygen Gasification of Municipal Solid Waste in a Fixed-bed Gasifier, Chinese J. Chem. Eng. 22 (2014) 1021–1026. http://www.sciencedirect.com/science/article/pii/S1004954114000500.

[27] L. Sørum, M.G. Grønli, J.E. Hustad, Pyrolysis characteristics and kinetics of municipal solid wastes, Fuel. 80 (2001) 1217–1227. http://www.sciencedirect.com/science/article/pii/S0016236100002180%5Cnhttp://www.sciencedirect.com/science/article/pii/S0016236100002180/pdfft?md5=2f7d8006d87c6cf26189be9b388f3ec1&pid=1-s2.0-S0016236100002180-main.pdf.

[28] J. Zheng, Y.-Q. Jin, Y. Chi, J.-M. Wen, X.-G. Jiang, M.-J. Ni, Pyrolysis characteristics of organic components of municipal solid waste at high heating rates., Waste Manag. 29 (2009) 1089–1094. http://dx.doi.org/10.1016/j.wasman.2008.06.034.

[29] N. Miskolczi, Co-pyrolysis of petroleum based waste HDPE, poly-lactic-acid biopolymer and organic waste, J. Ind. Eng. Chem. 19 (2013) 1549–1559. http://dx.doi.org/10.1016/j.jiec.2013.01.022.

[30] Food Waste Composting: Institutional and Industrial Application | Publications | UGA Extension, Univ. Georg. Ext. (2012). http://extension.uga.edu/publications/detail.cfm?number=B1189 (accessed December 10, 2015).

[31] R. Coordinator, A. County, C. Pilot, Task 1 – Market Conditions, (2003) 1–15.

[32] Energy Dispersive X-Ray Microanalysis (EDX / EDS) | Anderson Materials Evaluation, Inc., Andreson Mater. Eval. Inc. (2016). http://www.andersonmaterials.com/edx-eds.html (accessed January 26, 2016).

[33] G. Newalkar, K. Iisa, A.D. D'Amico, C. Sievers, P. Agrawal, Effect of temperature,

pressure, and residence time on pyrolysis of pine in an entrained flow reactor, Energy & Fuels. 28 (2014) 5144–5157. http://dx.doi.org/10.1021/ef5009715.

[34] M. V. Gil, J. Riaza, L. Álvarez, C. Pevida, F. Rubiera, Biomass devolatilization at high temperature under N_2 and CO_2: Char morphology and reactivity, Energy. 91 (2015) 655–662. http://linkinghub.elsevier.com/retrieve/pii/S0360544215011500.

[35] R. Azargohar, K.L. Jacobson, E.E. Powell, A.K. Dalai, Evaluation of properties of fast pyrolysis products obtained, from Canadian waste biomass, J. Anal. Appl. Pyrolysis. 104 (2013) 330–340. http://dx.doi.org/10.1016/j.jaap.2013.06.016.

[36] Adnan, J. Shah, M.R. Jan, Effect of polyethylene terephthalate on the catalytic pyrolysis of polystyrene: Investigation of the liquid products, J. Taiwan Inst. Chem. Eng. 51 (2014) 96–102. http://dx.doi.org/10.1016/j.jtice.2015.01.015.

[37] R. Muangrat, J. a. Onwudili, P.T. Williams, Influence of alkali catalysts on the production of hydrogen-rich gas from the hydrothermal gasification of food processing waste, Appl. Catal. B Environ. 100 (2010) 440–449. http://dx.doi.org/10.1016/j.apcatb.2010.08.019.

[38] A. Güngör, S. Önenç, S. Uçar, J. Yanik, Comparison between the “one-step” and “two-step” catalytic pyrolysis of pine bark, J. Anal. Appl. Pyrolysis. 97 (2012) 39–48.

[39] G. Dorez, L. Ferry, R. Sonnier, A. Taguet, J.-M. Lopez-Cuesta, Effect of cellulose, hemicellulose and lignin contents on pyrolysis and combustion of natural fibers, J. Anal. Appl. Pyrolysis. 107 (2014) 323–331. http://linkinghub.elsevier.com/retrieve/pii/S0165237014000771.

[40] G.G. Choi, S.H. Jung, S.J. Oh, J.S. Kim, Total utilization of waste tire rubber through pyrolysis to obtain oils and CO_2 activation of pyrolysis char, Fuel Process. Technol. 123 (2014) 57–64. http://dx.doi.org/10.1016/j.fuproc.2014.02.007.

[41] M. Jahirul, M. Rasul, A. Chowdhury, N. Ashwath, Biofuels Production through Biomass Pyrolysis —A Technological Review, Energies. 5 (2012) 4952–5001. http://www.mdpi.com/1996-1073/5/12/4952/.

[42] B. Saha, A.K. Ghoshal, Model-free kinetics analysis of ZSM-5 catalyzed pyrolysis of waste LDPE, Thermochim. Acta. 453 (2007) 120–127. doi:10.1016/j.tca.2006.11.012.

[43] M.A. Lopez-Velazquez, V. Santes, J. Balmaseda, E. Torres-Garcia, Pyrolysis of orange waste: A thermo-kinetic study, J. Anal. Appl. Pyrolysis. 99 (2013) 170–177. doi:10.1016/j.jaap.2012.09.016.

[44] P. Zhu, S. Sui, B. Wang, K. Sun, G. Sun, A study of pyrolysis and pyrolysis products of flame-retardant cotton fabrics by DSC, TGA, and PY–GC–MS, J. Anal. Appl. Pyrolysis. 71 (2004) 645–655. doi:10.1016/j.jaap.2003.09.005.

[45] H. Iwaki, S. Ye, H. Katagiri, K. Kitagawa, Wastepaper gasification with CO_2 or steam using catalysts of molten carbonates, Appl. Catal. A Gen. 270 (2004) 237–243.

[46] J. Pera, A. Amrouz, Development of Highly Reactive Metakaolin from Paper Sludge, Adv. Cem. Based Mater. 7 (1998) 49–56.

[47] A. Méndez, J.M. Fidalgo, F. Guerrero, G. Gascó, Characterization and pyrolysis behaviour of different paper mill waste materials, J. Anal. Appl. Pyrolysis. 86 (2009) 66–73. http://linkinghub.elsevier.com/retrieve/pii/S0165237009000710.

[48] M. Ash, Handbook of fillers, extenders, and diluents, Synapse Info Resources, 2007.

[49] The Importance of Raw Bones for Dogs and Cats, Heal. Pets by Mercola. (2012). http://healthypets.mercola.com/sites/healthypets/archive/2012/05/09/bone-supplements-for-pets.aspx (accessed August 25, 2017).

[50] H. Ismail, P.K. Freakley, Effect of multifunctional additive on filler dispersion in carbon-black- and silica-filled natural rubber compounds, Polym. Plast. Technol. Eng. 36 (1997) 873–889. doi:Doi 10.1080/03602559708000667.

[51] K.-Y. Chiang, C.-H. Lu, K.-L. Chien, The aluminum silicate catalyst effect on efficiency of energy yield in gasification of paper-reject sludge, Int. J. Hydrogen Energy. 38 (2013) 15787–15793. http://www.sciencedirect.com/science/article/pii/S0360319913017205.

[52] C. Zhou, Gasification and Pyrolysis Characterization and Heat Transfer Phenomena During Thermal Conversion of Municipal Solid Waste, 2014.

[53] S.S. Thipse, C. Sheng, M.R. Booty, R.S. Magee, J.W. Bozzelli, Chemical makeup and physical characterization of a synthetic fuel and methods of heat content evaluation for studies on MSW incineration, Fuel. 81 (2002) 211–217.

[54] G. Piao, S. Aono, S. Mori, S. Deguchi, Y. Fujima, M. Kondoh, et al., Combustion of refuse derived fuel in a fluidized bed, Waste Manag. 18 (1998) 509–512.

[55] F.-X. Collard, J. Blin, A review on pyrolysis of biomass constituents: Mechanisms and composition of the products obtained from the conversion of cellulose, hemicelluloses and lignin, Renew. Sustain. Energy Rev. 38 (2014) 594–608. http://linkinghub.elsevier.com/retrieve/pii/S136403211400450X.

[56] F. Gao, Pyrolysis of Waste Plastics into Fuels, PhD Thesis. (2010).

[57] S.G. Chen, R.T. Yang, Unified mechanism of alkali and alkaline earth catalyzed gasification reactions of carbon by CO_2, Energy & Fuels. 11 (1997) 421–427. http://dx.doi.org/10.1021/ef960099o.

[58] C.A. Mims, J.K. Pabst, Alkali-catalyzed carbon gasification kinetics: Unification of

H_2O, D_2O, and CO_2 reactivities, J. Catal. 107 (1987) 209–220. doi:10.1016/0021-9517(87)90286-7.

[59] M.P. Kannan, G.N. Richards, Gasification of biomass chars in carbon dioxide : dependence of gasification rate on the indigenous metal content, Fuel. 69 (1990) 747–753.

[60] D.W. Mckee, Gasification of graphite in CO_2 and water vapor- the catalytic effect of metal salts, Carbon N. Y. 20 (1982) 59–66.

CHAPTER 3. ROLE OF POTASSIUM AND CALCIUM IN THE CARBON DIOXIDE AND STEAM GASIFICATION OF MODEL RDF CHAR

3.1 Background

Gasification is considered as a potential alternative to combustion due to its merits of cleaner processing, lower volumes of flue gas treatment and higher overall energy efficiencies [1]. Gasification involves an initial de-volatilization or pyrolysis step followed by gasification reactions between the char and gasifying agents like CO_2, steam and O_2. The second step of char gasification is slower and is of higher significance during the thermochemical conversion of feed as it represents the rate-controlling factor in the gasification process.

Several researchers investigated the effect of physicochemical structure of the char on the gasification reactivity by studying pore structure parameters [2,3] and aromaticity of carbon [4,5]. While other researchers found that the effect of alkali and alkaline earth metals plays a vital role in determining the gasification rate, especially when the inorganic content is high [6,7]. Although the catalytic ability of each of the metals varies with varying gasifying agents and type of feed, potassium was found to be one of the most catalytically active metals for gasification [7–9]. Among alkaline earth metals, well-dispersed CaO was found to have a high catalytic ability during the gasification of coal and biomass char [10–12]. In contrast, other inorganic substances, such as silica, alumina and phosphates, lowered the reactivity of char [13]. Silica acted as a scavenger and reduced the gasification

reactivity of char by reacting with potassium to form a silicate, thus rendering it inactive [14].

Municipal Solid Waste (MSW) is the everyday garbage generated in households and commercial buildings. Based on US EPA data, more than 65% of the generated waste is discarded in landfills or incinerators despite several recycling facilities [15]. Since a large portion of MSW is organic, it is possible to convert it to syngas (H_2 and CO) by gasification. Refuse derived fuel (RDF) is a refined form of MSW obtained after several pre-processing techniques. This series of processes modifies the composition of the waste by reducing the heavy metal, glass and moisture content and improving the volatile content of RDF [16]. In Chapter 2, the model RDF composition was determined to be rich in potassium and calcium which act as intrinsic catalytic agents during the gasification stage.

This study explores both the independent and combined effect of the inherently present potassium and calcium in the feed using thermogravimetric analysis (TGA). The catalytic effect of potassium is quantified by studying varying amounts of potassium doped on Avicel (microcrystalline cellulose) char to mimic the biomass-like carbon structure. Multiple mechanisms have been postulated where the reactive potassium species is expected to exist either in a metallic potassium phase, an intercalate type potassium-carbon compound, or a surface oxygen-potassium complex [17–19]. The CO_2 and steam gasification reactivities in this study are used to identify the most suitable mechanism for potassium-catalyzed gasification. Furthermore, gasification reactivity of potassium and calcium rich feeds in the presence of hydrogen is investigated. Finally, co-gasification of model RDF char involving a mixture of CO_2 and steam is studied to identify the dynamics of multiple gasifying agents with inorganic-bound active sites.

3.2 Materials and methods

3.2.1 Experimental materials and feed preparation

The components in the discarded portion of MSW, as identified by EPA (2012), were the basis for the model RDF composition in this study [15]. The model RDF composition consists of 9 different components as shown in Figure 3.1. Identification of the representative components for model RDF composition is described in detail in Chapter 2. The food components were orange peel and dry dog food (Milkbone biscuits). The plastic fraction was represented by LDPE supplied as Microthene FN51000 (LyondellBasell) and the PET as PQB7-76 Prime PET resin (Polyquest Inc.). Tissue paper and paperboard obtained from local stores constituted the paper fraction. Rubber powder (Polydyne 200) supplied by Lehigh Technologies, cotton fabric and pine wood made up the minor components present in the model RDF composition.

Particle size reduction was carried out in two steps to achieve less than 106 µm particle sizes. The first step was cutting-based grinding in a Thomas Scientific Wiley mill that reduced the particle sizes to less than 2 mm. A Retsch MM 400 mixer mill was further employed to achieve the additional particle size reduction to less than 106 µm size. The fine particles were thoroughly mixed at 30 Hz and 3 minutes in the MM 400 mixer mill to achieve a homogeneous mixture. The elemental analysis and physical properties of the model feed mixture and its char are given in Table 3.1. It is to be noted that, the size reduction to less than 106 µm is only essential in a lab scale TGA study where low amounts of feed are commonly used. Moreover, the economics involved in grinding down to a fine particle size in an industrial scale process would be unfavorable.

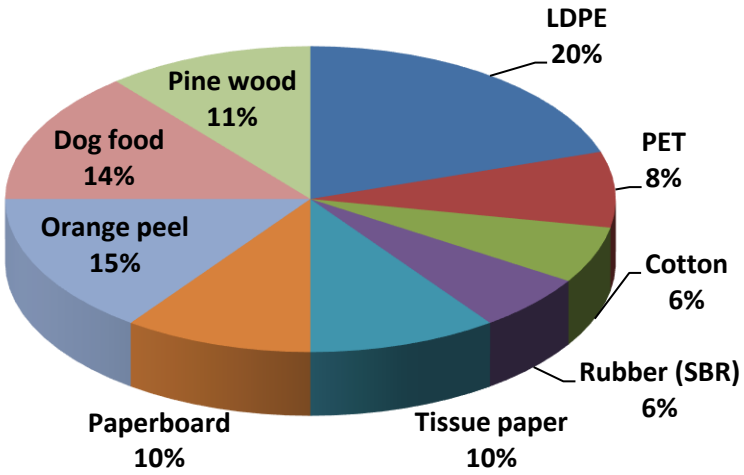

Figure 3.1. Model RDF feed composition.

Table 3.1. Properties of model RDF feed and char

RDF feed		
Moisture content (wt %)	~ 4	
Density (g/cc)	0.4	
Weight %	**RDF feed**	**RDF char**
Carbon	55.1	77.1
Hydrogen	7.65	0.84
Nitrogen	0.77	1.45
Oxygen	33	5
Ash	3.44	17

3.2.2 Experimental reactors for char generation and gasification

Two types of reactors were used in this study. The first reactor is a thermogravimetric-analyzer (TGA). An STA 449 F3 TGA by Netzsch Instruments was used to carry out the majority of steam and CO_2 gasification experiments. For the reactions with hydrogen studies, SDT-Q600 TGA by TA Instruments was utilized. They recorded weight loss as a function of temperature and time. Unless otherwise stated, pyrolysis was carried out in-situ inside the TGA at 20 K/min ramp rate to a final temperature of 800 °C

with 200 ml/min of nitrogen flow. Flat crucibles were employed in the Netzsch TGA that allowed the use of sample sizes as high as 25 mg without mass transfer effects. However, it should be noted that the sample sizes were about 3 – 4 mg at the beginning of the gasification stage since about 80% of mass loss occurs during pyrolysis. An isothermal step of 30 minutes was introduced between the pyrolysis and gasification steps to stabilize the weight in the TGA. Subsequently, 100% CO_2 or steam were introduced at 200 ml/min for gasification until complete carbon conversion was achieved as indicated by weight stabilization. The conversion (X) and reactivity (R) in these gasification experiments were determined according to the following formulae:

$$X = \frac{(m_0 - m_t)}{(m_0 - m_{ash})} \qquad \text{Eq. (3.1)}$$

$$R = \frac{-1}{(m_t - m_{ash})} \frac{dm_t}{dt} \qquad \text{Eq. (3.2)}$$

where,

m_0 = initial mass at the introduction of 100% CO_2

m_t = mass at time‘t’

m_{ash} = final mass at the end of the gasification run

The second reactor is a semi-batch quartz reactor as shown in Figure 3.2. It was primarily used for Avicel char generation in large amounts. Avicel is a microcrystalline cellulose that was used for a part of this study as a representative carbon source (similar to biomass) without inorganics. It was purchased from Sigma Aldrich as Avicel PH-101. The quartz reactor is primarily a tubular quartz tube situated inside a furnace with an inlet gas port on one end and a gas outlet on the other. The feed sample was loaded in a quartz boat

that was placed in the heated part of the quartz tube. Two condensers were connected on the outlet end to cool down the hot pyrolysis gases released. When required, the released gases were collected in FlexFoil™ plus samples bags supplied by SKC Inc. They were analyzed in a Varian 490 micro-GC with four channels consisting of four 10 m long columns (two Molecular Sieve 5 Å, one Plot column, and one Al_2O_3 column) and four TCD detectors with the lowest detection limit of 10 ppm for all gases. The gas yield was established by assuming a basis of nitrogen tie element and by calculating the yield of each gas component from the gas composition.

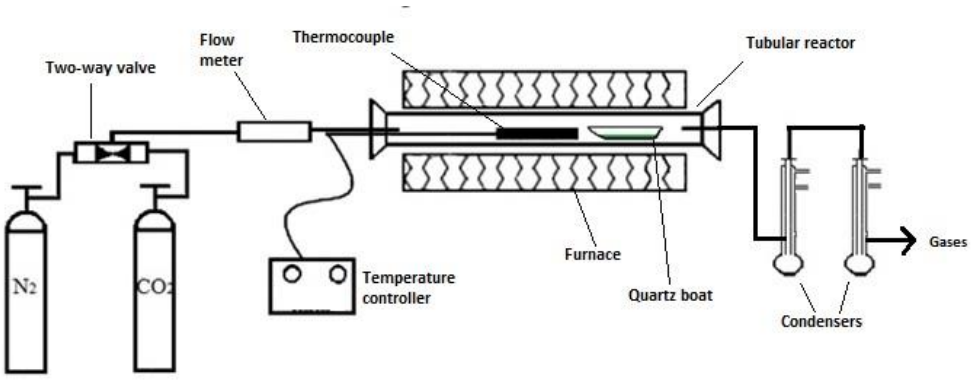

Figure 3.2. Quartz reactor setup.

3.2.3 Avicel char preparation and characterization

Avicel char prepared from the quartz reactor at 20 K/min and heated to 800 °C was doped with potassium for inorganic studies. Varying amounts of potassium from 0.2% – 13% was dispersed on Avicel char using incipient wetness impregnation [20]. Potassium carbonate was used as the source of potassium unless otherwise stated. The chars were dried overnight in an oven at 110 °C. Inorganic content of the prepared seven chars was identified by ICP-OES (Inductively coupled plasma- optical emission spectrometry)

performed by the analytical testing lab at the Renewable Bioproducts Institute (Georgia Tech). Similar analysis was utilized to determine the inorganic content of rubber chars loaded with potassium, with the only difference in the sample preparation method. A caustic fusion method was used for rubber chars instead of acid digestion method due to the large amount of silicon present.

3.3 Results and Discussion

3.3.1 Steam and CO_2 gasification of RDF and inorganic-rich RDF components

Gasification rate of chars in steam is higher than in CO_2, thus making steam gasification much more attractive than CO_2 gasification [21,22]. Of all the thermochemical processes, steam gasification offers the highest stoichiometric yield of hydrogen [23]. However, blocking of active sites by dissociative chemisorption of H_2 as C(H) with increasing gasification of pure carbon has been shown in the literature [24,25]. Hence, in steam gasification, absorbed hydrogen could occupy available active sites for the reaction leading to reduced reactivity. Also, temperature, feed properties, and especially the type and amount of inorganics present in the char influence the reactivity in different ways, in different gasification media [26,27]. The catalytically active inorganics in model RDF char are potassium and calcium. Thus, calcium-rich tissue paper and potassium-rich orange peel components were chosen as representatives to analyze the independent effect of each inorganic in CO_2 and steam gasification.

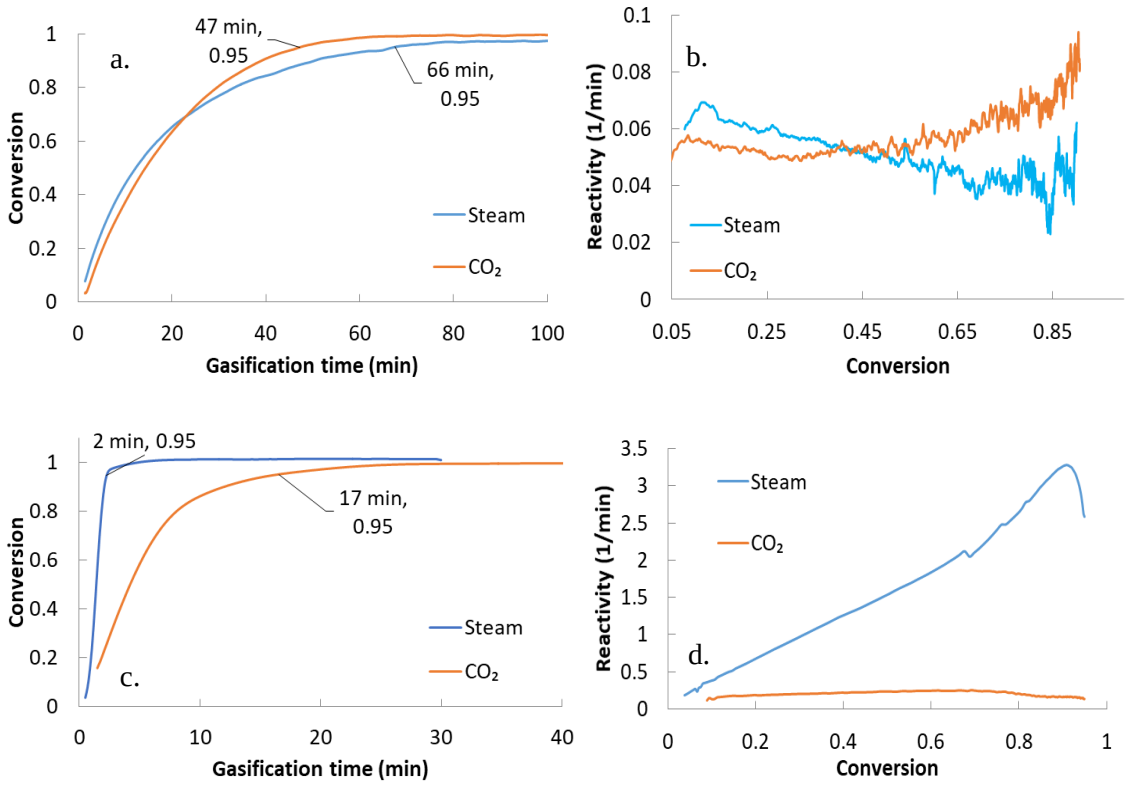

Figure 3.3. Gasification at 800 °C in CO_2 and steam a. time taken by tissue paper char b. reactivity of tissue paper char c. time taken by orange peel char d. reactivity of orange peel char.

All the chars were generated by heating at 20 K/min and holding at 800 °C for 30 minutes in nitrogen flow. Thereafter, the chars were subjected to either 100% CO_2 or 100% steam gasification at 800 °C. Time taken for 95% conversion and variation of gasification reactivity with conversion of the two chars are shown in Figure 3.3. Overall conversion rate of tissue paper char was higher in CO_2 than in steam. However, a slightly increasing trend in CO_2 and a decreasing trend in steam was observed from Figure 3.3 b. The increasing reactivity trend in CO_2 gasification is attributed to an increasing ratio of inorganics to carbon which is not as drastic as expected, due to calcium sintering [28]. The ratio of inorganics to remaining carbon increases with both the gasifying media, however,

hydrogen inhibition in steam gasification dominates the inorganic effect, leading to a drop in reactivity with increasing conversion [29].

Table 3.2. Ash content and inorganics present in model RDF char and the constituent components

Char Component*	Ash char basis (%)	Ca (%)	Fe (%)	K (%)	Mg (%)	Al (%)	P (%)	S (%)	Si (%)
Tissue Paper	19.6	4	0.08	0.04	0.09	1.4	0.04	0.03	0.53
Paperboard	71.1	5.5	0.25	0.04	0.3	2.6	0.06	0.09	6.8
PET**	1.4	0.01	0.12	0.01	0.004	0.04	0.05	0.03	0
Orange peel	12	0.68	0.007	3.8	0.11	0.005	0.23	0.14	0.07
Dog food	19.9	4	0.02	0.52	0.23	0.02	2.3	0.03	0.34
Rubber	9.4	0.11	0.001	0.11	0.11	0.1	0.03	1.7	2.8
Cotton	24.3	0.56	0.01	0.02	0.16	0.03	0.06	0.04	0.06
Pine**	2	0.07	0.002	0.05	0.03	0.002	0.004	0.007	~0
RDF	21.2	2.17	0.013	1.13	0.18	1.13	0.52	0.14	1.41

*Generated at 20 K/min up to 800 °C **Accuracy not guaranteed due to very low ash content
All values in weight % and the inorganics are on char basis

Potassium-rich orange peel char was gasified in a steam environment at the same temperature of 800 °C. Potassium is inherently more catalytic than calcium, hence, higher reactivity values were expected [7]. Orange peel char gasification was extremely rapid in a steam environment and it only took about 2.3 minutes to achieve 95% conversion as opposed to 17 minutes in CO_2 based on Figure 3.3 c. From Figure 3.3 d, steam reactivity of orange peel char was found to be 6 times higher than the reactivity in CO_2 at 50% conversion. This difference between the two gasification agents is attributed to the amount of potassium present in orange peel char (Table 3.2) and its mobility. However, another contributor to the increased reactivity in steam was found to be the formation of KOH as discussed in section 3.3.5. Due to the mobility of a large amount of potassium, active sites are not affected by hydrogen inhibition until very high conversion levels. Consequently,

potassium is found to be highly catalytically active in a steam environment thus leading to a continuous increase in reactivity that dominates over the effect of hydrogen inhibition.

RDF char is a combination of eight different components and thus a variety of inorganics act simultaneously during gasification. The major inorganics present in RDF char that influence gasification reactivity are potassium, calcium and silicon (Table 3.2). Steam gasification of RDF char was carried out at the same conditions (800 °C) and the results were compared to CO_2 gasification profiles. The time taken to achieve 95% conversion in both the gasifying atmospheres did not vary significantly as seen in Figure 3.4 a. However, differences between the two gasifying agents can be observed in the reactivity trends of RDF char as shown in Figure 3.4 b. Steam gasification had higher overall gasification reactivity than CO_2 gasification. As observed during orange peel char gasification, potassium is highly active in a steam atmosphere. A reasonable amount of potassium present in RDF char led to a higher reactivity in steam especially during the initial conversion. Steam reactivity dropped as conversion increased which may be a result of the combined effect of hydrogen inhibition, calcium sintering and silicon scavenging [14]. Relatively, CO_2 gasification reactivity was almost constant for the entire conversion period. Based on the comparison of reactivities in Figure 3.4 b, despite the effect of hydrogen inhibition, steam gasification is preferable over CO_2 gasification.

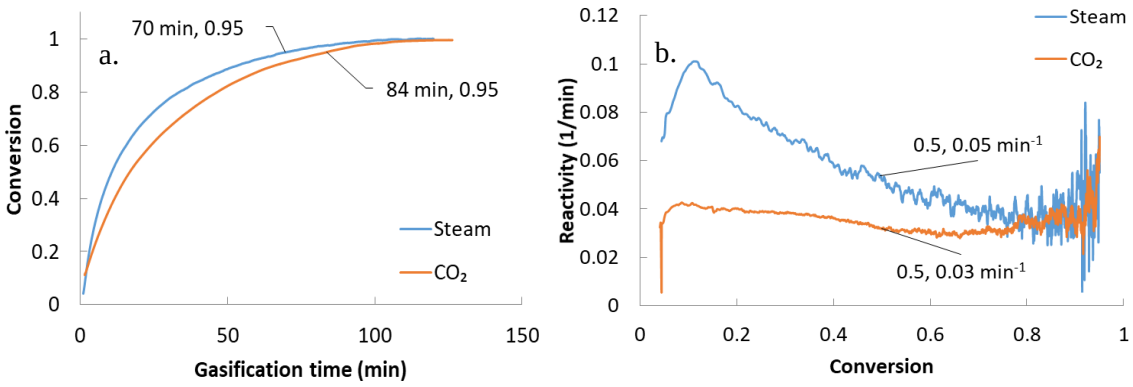

Figure 3.4. Gasification of RDF char at 800 °C in CO_2 and steam a. time taken for complete conversion b. reactivity over the conversion range.

3.3.2 Gasification reactivity of Avicel chars as a function of amount of potassium

Potassium has the highest catalytic activity compared to all the inorganics present in RDF char as concluded in the previous section 3.3.1. To quantify the effect of potassium on gasification reactivity in both steam and CO_2, several samples of Avicel (microcrystalline cellulose) char were prepared with varying amounts of potassium. Avicel char was first generated in the quartz reactor by heating at 20 K/min up to 800 °C. Various amounts of potassium from 0.2% to 13% were loaded onto Avicel chars using the incipient wetness impregnation method [20]. Potassium carbonate was used as the source of potassium. Prepared chars were dried overnight in an oven at 110 °C. Seven different chars were prepared and were analyzed with an acid digestion method followed by ICP-OES (Inductively coupled plasma- optical emission spectrometry) by the analytical testing lab at the Renewable Bioproducts Institute (Georgia Tech).

The seven potassium-loaded Avicel chars were subjected to both steam and CO_2 gasification independently. Steam gasification reactivity of the chars with increasing conversion is shown in Figure 3.5. With increasing potassium content, steam gasification

reactivity increased up to 5% potassium loading where saturation was detected. With further increase in potassium content, steam reactivity curves overlapped with the 5% potassium loading curve up to 60% conversion, beyond which a drop in reactivity was observed. A similar observation was noted in the literature [30]. The drop in reactivity or maximum occurred at different conversion levels depending on the amount of potassium present in the char. The higher the potassium content in the char, the earlier the maximum with respect to conversion. This dependency of the maximum on the potassium content was verified by analyzing the reactivity curves in CO_2 gasification. The variation of CO_2 gasification reactivity of the seven chars with conversion is presented in Figure 3.6.

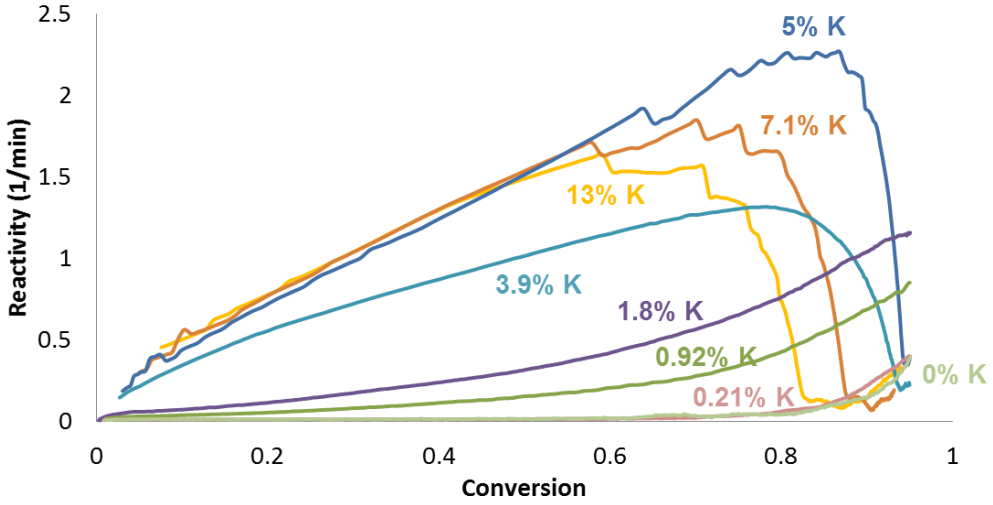

Figure 3.5. Variation of steam gasification reactivity of potassium-loaded Avicel chars with conversion at 800 °C.

Similar to steam reactivity profiles, CO_2 gasification reactivity curves showed an increasing trend with increasing potassium content, up until 5% loading where saturation was reached. With further increase in potassium content, there was no significant increase in the reactivity. Furthermore, a similar maximum in the reactivity curves was noticeable in CO_2 gasification at higher conversion levels, which was a function of the amount of

potassium content present. Since the maximum occurred irrespective of the gasification medium, it is assumed to be an effect of the gasification process. A likely explanation is that the maximum occurs when the amount of potassium present in the residual char is so high that it encapsulates the char, creating an outer layer that impedes the flow of the gasification agent, thus leading to a drop in reactivity.

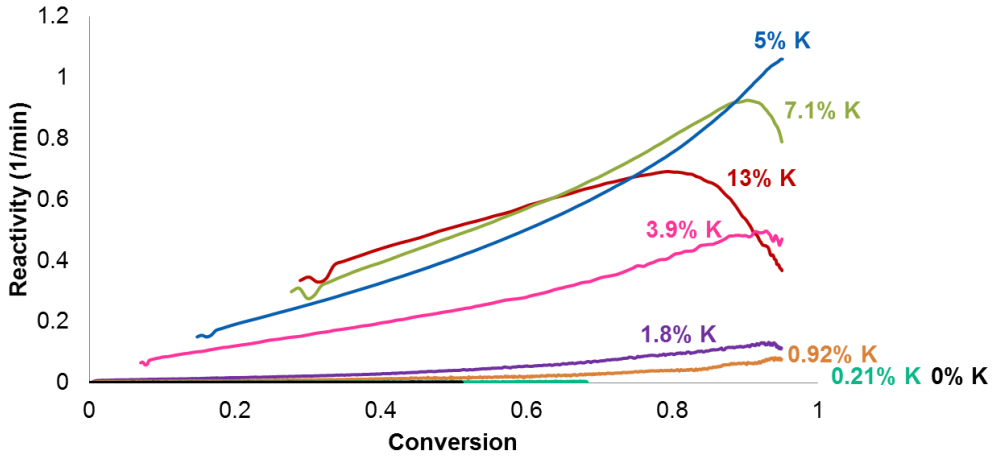

Figure 3.6. Variation of CO_2 gasification reactivity of potassium-loaded Avicel chars with conversion at 800 °C.

The hypothesis was verified by comparing the amount of potassium and the amount of residual carbon present at each of the maxima observed. Potassium over carbon ratio was determined at the maximum point in each of the curves that showed a drop in reactivity. The K/C ratios in steam and CO_2 gasification were compared discretely as shown in Table 3.3. In CO_2 gasification, the ratio was similar for the two curves that showed maxima in reactivity. Similarly, in steam gasification, all the three chars had the maxima at similar K/C ratios. This similarity in K/C ratios proves that when a fixed value of K/C ratio is reached, irrespective of the initial potassium content and the gasifying agent, potassium impedes the gasification process and leads to a drop in reactivity. The

observation supports the hypothesis of encapsulation of residual char by potassium during the gasification process.

Table 3.3. Relationship between K/C ratios and the maxima in steam and CO_2 reactivity of potassium-loaded Avicel chars (chars generated by heating at 20 K/min up to 800 °C)

Sample char	K/C at the drop
CO_2 gasification	
Avicel char with 7.1% K	0.88
Avicel char with 13% K	0.86
Steam gasification	
Avicel char with 5% K	0.46
Avicel char with 7.1% K	0.37
Avicel char with 13% K	0.47

The relationship of gasification reactivity of potassium-loaded Avicel chars with the amount of potassium loading was further studied. Figure 3.7 compares the CO_2 and steam reactivity variation at 50% and 80% conversion level.

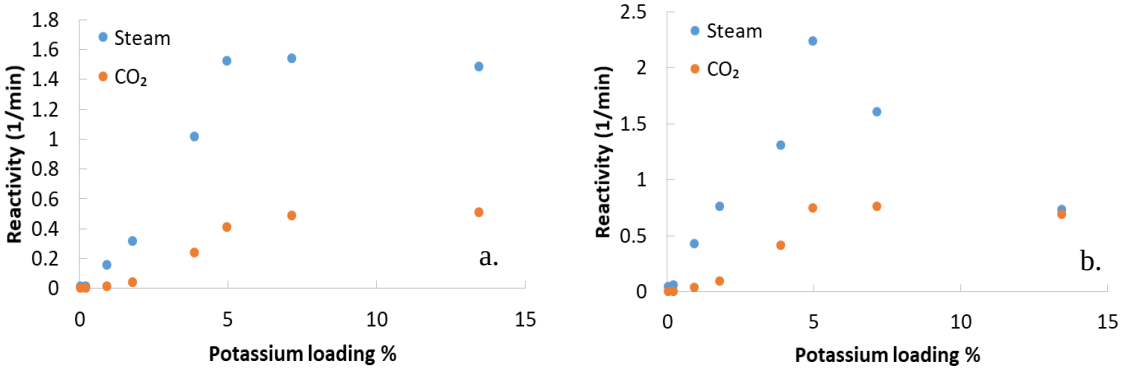

Figure 3.7. Relationship of gasification reactivities of potassium-loaded Avicel chars with the amount of potassium loading at a. 50% conversion b. 80% conversion.

In Figure 3.7 a, at 50% conversion, after a gradual increase in reactivity with increasing potassium loading, a saturation was reached at 5% potassium content. The

profiles of both CO_2 and steam gasification were similar at 50% conversion with the only difference being the magnitude of the reactivity values. At 80% conversion, Figure 3.7 b showed an increasing trend in reactivity with increasing potassium loading up until 5% potassium content. Instead of reaching a saturation level as observed at 50% conversion, the reactivities dropped drastically with an increase in potassium loading. This decrease in reactivity is attributed to the potassium over residual carbon ratio (K/C ratio) which is very high when 80% of the carbon has been converted. It is consistent with the observations from Table 3.3, Figure 3.5 and Figure 3.6.

The scavenging effect of silicon results in very low reactivity in both CO_2 and steam gasification [13]. Addition of potassium to rubber chars was considered to quantify the amount of potassium required to overcome the detrimental effect of silicon. As expected, with increasing potassium content, reactivity of potassium-doped rubber chars was enhanced as shown in Figure B.1 a. A ratio of potassium over silicon was a good indicator to understand the combined effect of potassium and silicon in the CO_2 gasification of potassium-loaded rubber chars. Rubber char contained a predetermined amount of silicon which was capable of scavenging a fixed amount of potassium. When the amount of potassium added exceeded this limit, the excess potassium was free to migrate on the surface. At different conversion levels, the amount of silicon-free potassium over residual carbon varied and thus led to different reactivity values. The effect of the K/Si ratio on the gasification reactivity of potassium-loaded rubber chars is shown in Figure B.1 b. As expected, both 50% conversion and 80% conversion reactivity curves showed an increasing trend with increasing K/Si ratio. However, higher reactivity at 80% conversion at high K/Si ratio was due to the increased amount of silicon-free potassium over residual

carbon. The two observations imply that, when there is an additional amount of potassium present beyond the amount of potassium that can be scavenged by silicon, there is a positive shift in the slope of the reactivity curve due to the availability of free potassium.

3.3.3 Chemical environment of potassium in CO_2 and steam gasification

Before gasification in either CO_2 or steam, Avicel char was first heated up in a nitrogen flow to the reaction temperature of 800 °C, held constant at that temperature for 15 minutes and then exposed to the gasification agent. During this ramp-up from room temperature to the reaction temperature, potassium-loaded Avicel char loses weight as shown in Figure B.2. This weight loss (moisture-free) in each of the chars was found to be linearly dependent on the amount of potassium present in those chars as shown in Figure 3.8.

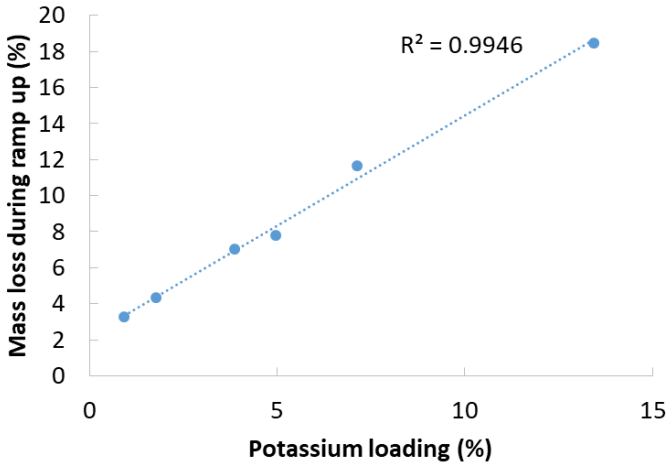

Figure 3.8. Relationship of weight loss during ramp-up of all the potassium-loaded Avicel chars with the amount of potassium present in the chars.

The weight loss is attributed to change(s) in the chemical form of potassium during the heat-up. To explore this further, gases evolved during the heat-up stage of Avicel char

with 7.1% K loading were collected from the quartz reactor. Gases released from the chemical change of K_2CO_3 were isolated by taking a difference of the gas composition of pure Avicel char and 7.1% K loaded-Avicel char. The majority of the gases evolved were CO and CO_2. Two reactions were considered to explain the evolution of the two gases from K_2CO_3 [31,32]. Based on both the product to reactant weight ratios and gas composition analysis, the following combination of reactions were considered to be the most plausible explanation for K_2CO_3 decomposition during the ramp-up stage:

$$K_2CO_3 + C \rightarrow 2K + CO + CO_2 \qquad \text{Eq. (3.3)}$$

$$K_2CO_3 + C \rightarrow K_2O + 2\,CO \qquad \text{Eq. (3.4)}$$

The general consensus is that potassium exists in an unknown oxide state before CO_2 gasification begins. It then reacts with the gasifying agent and the carbon present in the char to complete the gasification process. The generalized mechanism where potassium exists in different oxidation states is as follows [33,34]:

$$CO_2 + K_xO_y \leftrightarrow CO + K_xO_{y+1} \qquad \text{Eq. (3.5)}$$

$$K_xO_{y+1} + C \rightarrow K_xO_y + (CO) \qquad \text{Eq. (3.6)}$$

$$(CO) \leftrightarrow CO \qquad \text{Eq. (3.7)}$$

This study aims at presenting a reaction mechanism with more specific details on the oxidation state of potassium during gasification. Potassium carbonate was decomposed into metallic potassium and K_2O based on Eqs. 3.1 and 3.2. In CO_2 gasification, metallic potassium is expected to react with CO_2 and release CO while forming a potassium oxide

[18]. This oxidized form of potassium, typically in the form of K_2O, reacts with carbon in the char and releases CO while reducing back to metallic potassium. The following two reactions summarize the cycle:

$$2\,K + CO_2 \leftrightarrow K_2O + CO \qquad \text{Eq. (3.8)}$$

$$K_2O + C \leftrightarrow 2K + CO \qquad \text{Eq. (3.9)}$$

This cycle repeats until the carbon in the char is completely converted. Similarly, in steam gasification, metallic potassium reacts with steam to produce potassium hydroxide along with hydrogen [35]. Potassium hydroxide further reacts with carbon in the char to release more hydrogen and reduce the hydroxide to either metallic potassium or K_2O and K_2CO_3. These reactions are not expected to be elementary reactions but a sum of a sequence of reactions and are presented below [35]:

$$2K + 2H_2O \leftrightarrow 2KOH + H_2 \qquad \text{Eq. (3.10)}$$

$$6KOH + 2C \leftrightarrow 2K + 3H_2 + 2K_2CO_3 \qquad \text{Eq. (3.11)}$$

$$4KOH + C \leftrightarrow K_2O + K_2CO_3 + 2H_2 \qquad \text{Eq. (3.12)}$$

Potassium oxide and potassium carbonate are expected to convert into metallic potassium following Eq. 3.9 and Eqs. 3.3 or 3.9, respectively. The cycle repeats itself with the formation of metallic potassium, potassium hydroxide / potassium oxides until the entire char is converted. The two proposed reaction mechanisms for CO_2 and steam gasification are thus summarized in Figure 3.9.

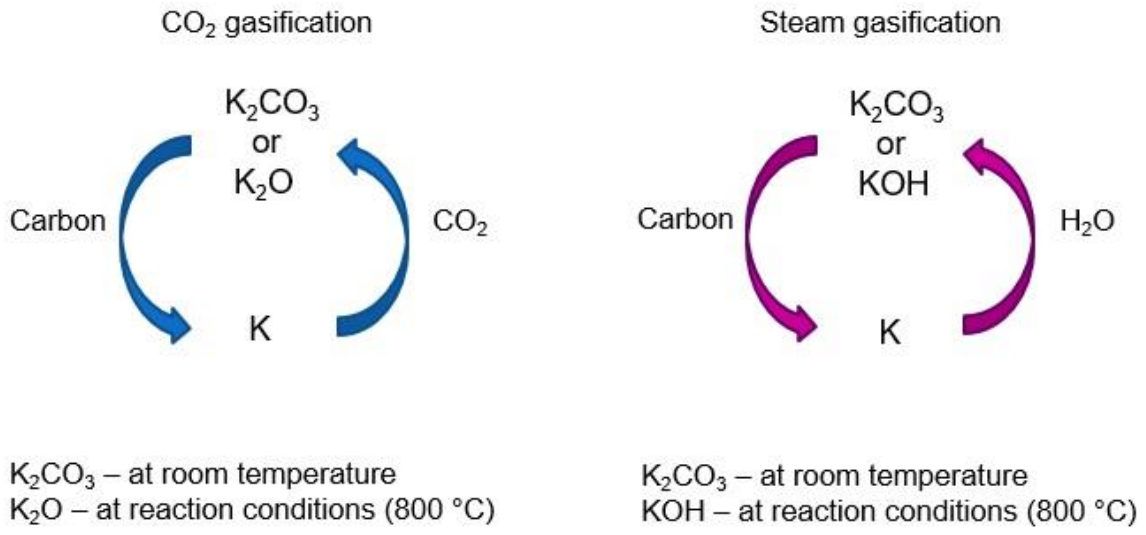

Figure 3.9. Proposed reaction mechanism of potassium-catalyzed CO_2 and steam gasification.

3.3.4 Chemical environment of calcium in CO_2 and steam gasification

Although not as catalytically active as potassium in gasification, calcium has a significant catalytic effect on char gasification reactivity [11,12]. The initial phase of calcium present in the feed changes phases during the gasification process due to both changes in temperature and the reacting medium.

Weight change analysis was performed on calcium hydroxide in the TGA in both CO_2 and steam atmospheres. In CO_2 gasification, calcium hydroxide was heated in nitrogen to 150 °C at 20 K/min. After a hold time of 30 minutes to remove moisture completely, the sample was heated to 800 °C at 20 K/min. It was held at 800 °C for 15 minutes to stabilize weight and the gas was switched over to CO_2. With a final hold time of 125 minutes, the weight loss profile for the entire process was plotted as a function of time as shown in Figure 3.10. The weight loss during the ramp-up at 400 °C was almost the same as

expected from the decomposition of $Ca(OH)_2$ to CaO [36]. The weight ratio of CaO / $Ca(OH)_2$ is 0.76 while the experimentally observed weight change ratio was 0.72. With CO_2 introduction, a weight increase was observed with a weight change ratio of 1.63, which when compared to the weight ratio of $CaCO_3$ / CaO of 1.78, gives an error below 10% [37]. The weight increase is gradual during CO_2 flow due to mass transfer limitations. Thus, calcium exists most likely as CaO before the CO_2 switchover and as $CaCO_3$ during CO_2 gasification.

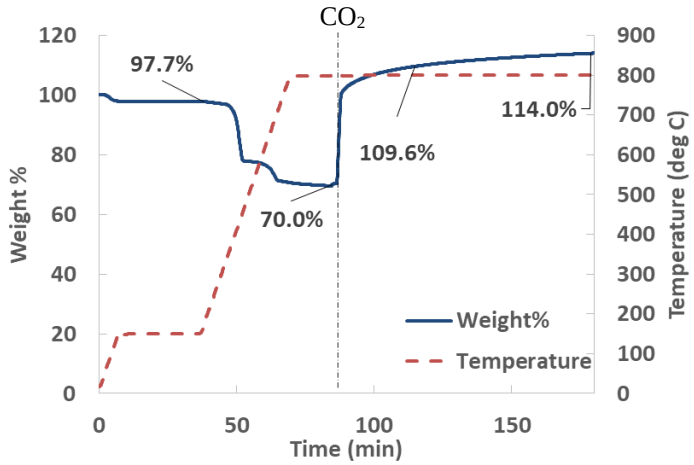

Figure 3.10. Weight change analysis of calcium hydroxide in CO_2.

A similar weight change analysis was conducted for calcium hydroxide in steam gasification as shown in Figure B.3. Although the weight loss during the ramp-up in steam gasification was consistent with the weight loss in CO_2 gasification ramp-up, no change in weight was observed in the steam environment. This indicated that CaO is stable in the steam environment. However, with additional carbon present (feed), new reactions could occur that would change the chemical phase of calcium [10]. Also, it should be noted that calcium could be present in other chemical forms in the feed that could lead to different chemical phases of calcium during the different stages of gasification [38].

3.3.5 Effect of hydrogen on CO_2 gasification of feeds with varying inorganic content

In-situ hydrogen produced during steam gasification was found to be detrimental to the gasification reactivity as noted in section 3.3.1. Active sites were deemed to be blocked by hydrogen product inhibition as steam gasification progressed [29,39]. To test the case of the effect of hydrogen in CO_2 gasification, different inorganic-rich chars were gasified at 800 °C in an atmosphere containing a small amount of hydrogen (96.5% CO_2 + 3.5% H_2). Both tissue paper char and RDF char had a decreasing reactivity trend in steam gasification which was attributed to hydrogen inhibition (Figure 3.3 b and Figure 3.4 b). Hydrogen inhibition in both these chars was verified by gasifying them independently in 3.5% H_2 and balance CO_2 and comparing the reactivity with their corresponding CO_2 gasification reactivity as shown in Figure 3.11.

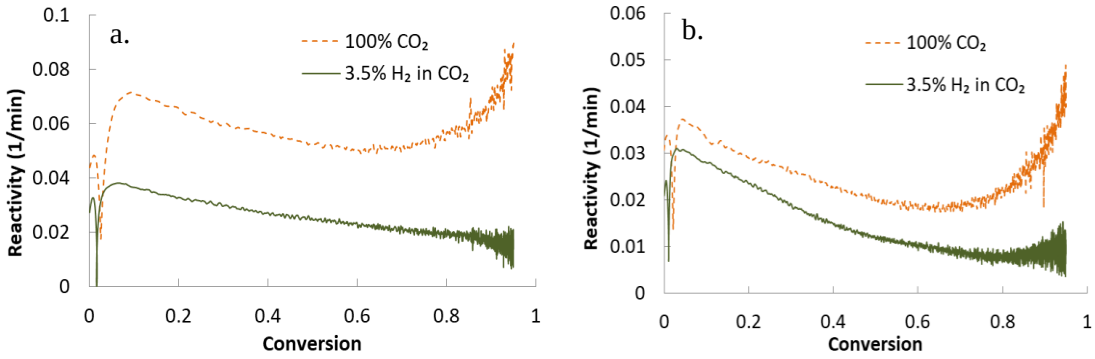

Figure 3.11. Comparison of CO_2 gasification reactivity with gasification reactivity in 3.5% hydrogen and the balance CO_2 for a. Tissue paper char b. RDF char.

As expected, overall gasification reactivity of both the chars was lower in the presence of hydrogen as compared to a pure CO_2 atmosphere. This decrease in reactivity is possibly due to hydrogen inhibition of active sites. The difference in the magnitude of the reactivities in the two gasification atmospheres was higher for tissue paper char than RDF char. The greater difference in tissue paper char implies that calcium-catalyzed

gasification is largely influenced by hydrogen presence. Since RDF char is a mixture of several components and also contains potassium in reasonable amounts, the difference in the reactivities in the two gasification atmospheres was lower.

To understand the interaction between hydrogen and potassium-catalyzed gasification reactivity, orange peel char and 5% potassium – loaded Avicel char were subjected to gasification in 3.5% hydrogen with balance CO_2. A comparison of the gasification reactivities of the two components in pure CO_2 atmosphere and 3.5% H_2 in CO_2 atmosphere is presented in Figure 3.12. Counterintuitively, both the potassium rich samples exhibited higher reactivity in hydrogen atmosphere than pure CO_2 atmosphere. This high reactivity in the presence of hydrogen is attributed to the formation of KOH which seems to have higher catalytic activity than K_2O or K_2CO_3.

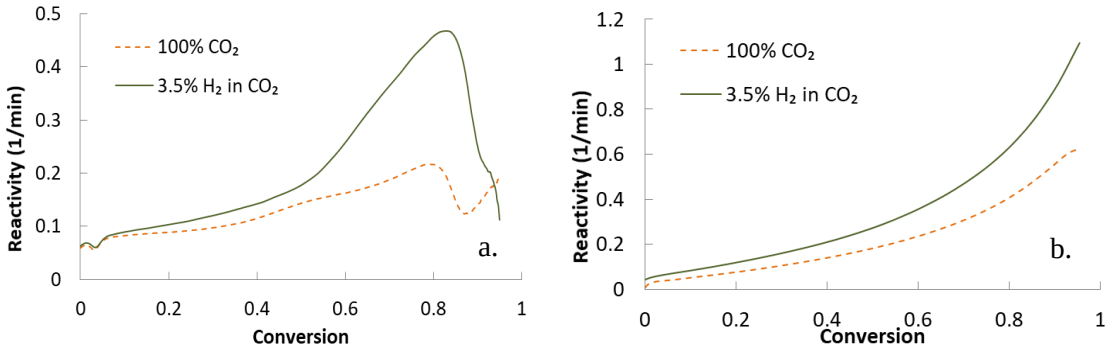

Figure 3.12. Comparison of CO_2 gasification reactivity with gasification reactivity in 3.5% hydrogen and the balance CO_2 for a. Orange peel char b. Avicel char with 5%K.

This hypothesis was tested by performing gasification of 7% potassium-loaded Avicel char, where the source of potassium was KOH instead of K_2CO_3, in both pure CO_2 as well as hydrogen mixed with CO_2 conditions (3.5% H_2 in 96.5% CO_2) at 800 °C. The reactivity of this sample was further compared with the reactivity of 7% potassium-loaded

Avicel char where K_2CO_3 was the source of potassium. A comparison of the reactivities of the two samples with the same amount of potassium but in different chemical forms (K_2CO_3 and KOH) in the two gasifying atmospheres is shown in Figure 3.13. Similar to the results observed in Figure 3.12 b, 7% potassium-loaded Avicel char with K_2CO_3 as the source, had higher reactivity in the presence of hydrogen rather than a pure CO_2 atmosphere. However, 7% potassium-loaded Avicel char with KOH as the source exhibited an overlap of curves in both the atmospheres, indicating that the hydrogen present had no effect on the reactivity. Moreover, an overlap of reactivity of potassium added as K_2CO_3 in hydrogen conditions with the reactivity curves of potassium added as KOH in both the gasifying atmospheres is observed. This confirmed that the increased reactivity of 7% K added as K_2CO_3 sample in hydrogen presence was due to the formation of KOH. The results also imply that potassium forms KOH in the presence of hydrogen or steam and thus has higher reactivity in steam conditions than CO_2 conditions where it is probably present in the form of K_2O [18,35].

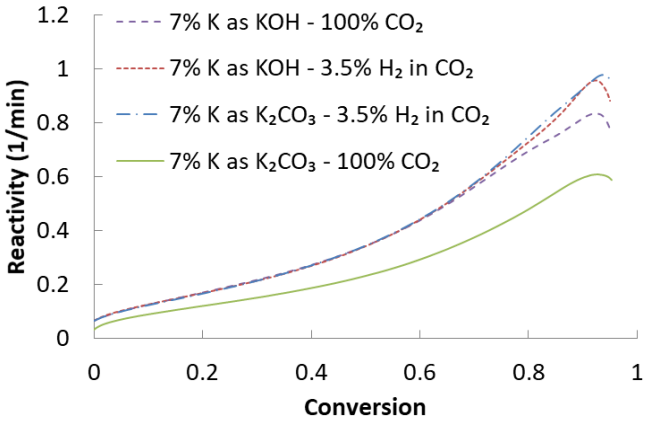

Figure 3.13. Comparison of gasification reactivities of 7% potassium added as KOH and K_2CO_3 on Avicel char in pure CO_2 atmosphere and 3.5% H_2 in CO_2 atmosphere.

3.3.6 Role of active sites in the co-gasification of RDF with CO_2 and steam

While steam and CO_2 gasification reactivities differ in magnitude and dependency on conversion, active sites distribution has been an ambiguous subject. Literature has been found that argues for the same active sites for both gasifying agents [40,41] as well as separate active sites for the gasifying agents [42,43]. In this study, active site distribution was investigated by considering a gas-switchover experiment where RDF char was treated with CO_2 and steam alternatively. RDF char reactivity is plotted as a function of conversion for gas – switchover test and compared to pure CO_2 and pure steam gasification reactivities in Figure 3.14.

Gasification was started in steam atmosphere and the gas was switched over to CO_2 after 3 minutes. After a 9 minute exposure to CO_2, the gas was again switched back to steam and, the cycle was repeated until complete char conversion was achieved. As can be seen from the Figure 3.14, steam exposure to char reduced the subsequent initial char reactivity in CO_2. This decrease in reactivity is attributed to hydrogen inhibition of active sites in steam gasification leading to lower reactivity in CO_2 that is gradually recovered. On the other hand, CO_2 exposure to char enhanced the subsequent initial char reactivity in steam. CO_2 is projected to regenerate the active sites by desorbing hydrogen thus leading to increased initial reactivity in steam. This trend was repeatable as seen from the Figure 3.14, which implies that the same active sites are participating in both the gasification environements. Thus, the results support active site sharing between the two gasifying agents as suggested by Roberts et al. [40] and Umemoto et al. [41].

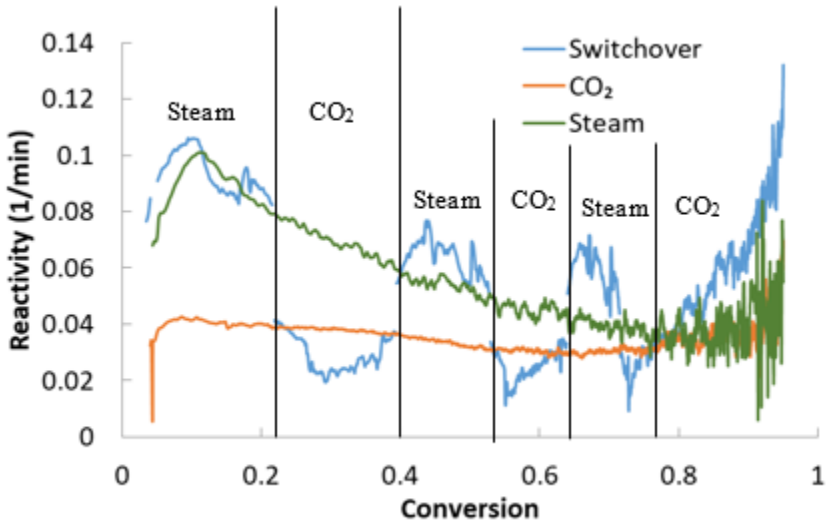

Figure 3.14. Comparison of RDF char reactivity in a gas switchover experiment with the gasification reactivities in pure steam and CO_2 atmospheres.

Co-gasification studies were considered to understand how the active sites are distributed when they are exposed to both CO_2 and steam at the same time. Pure CO_2 and steam gasification runs with the balance nitrogen are compared with CO_2 and steam mixtures to understand the effect of partial pressure on gasification reactivity in Figure 3.15. Both the mixtures of 50% CO_2 and 50% steam run and 70% CO_2 and 30% steam run showed a complete overlap with their corresponding steam reactivity (balance N_2) trend. This implies that the active sites had more affinity towards steam than CO_2 even when the former is present at a lower ratio than the other. Umemoto et al., found similar results which were improved upon by a model that they suggested [41]. Based on the results of the current study, it is concluded that steam completely dominates over CO_2 during co-gasification, even down to 30% steam and 70% CO_2 mixtures.

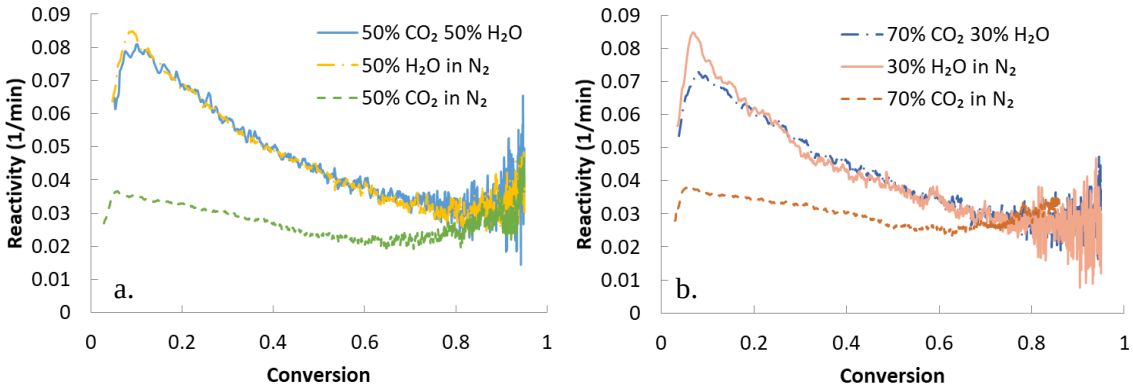

Figure 3.15. Co-gasification reactivity trends of model RDF char in a. 50% CO_2 and 50% steam b. 70% CO_2 and 30% steam environments.

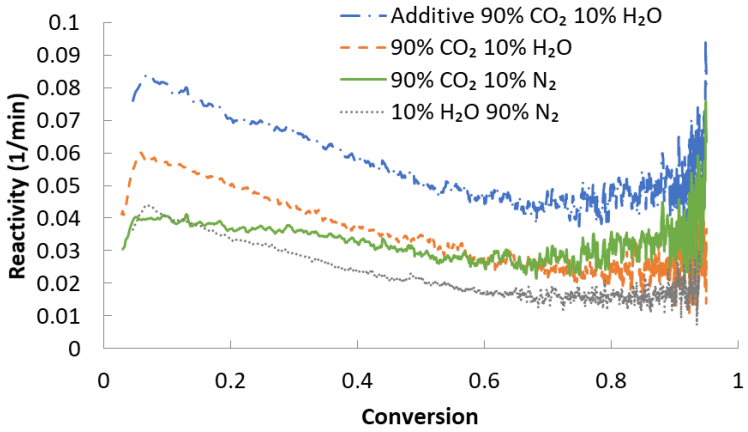

Figure 3.16. Co-gasification reactivity trend of 90% CO_2 and 10% steam mixture and comparison with the corresponding pure CO_2 and steam environments and its additive profile (calculated from the pure CO_2 and steam runs).

When the partial pressure of steam was further decreased to 10% steam with the balance 90% CO_2, no more overlap of the pure steam curve with the co-gasification curve was observed as seen from Figure 3.16. Instead, co-gasification was synergistic with the reactivity at 50% conversion being 44% higher than the corresponding steam partial pressure run. However, the reactivity was also 40% lower than the additive reactivity curve that assumed independent active sites and was calculated from the pure CO_2 and steam

curves. This implies that although the reactivity appears synergistic, co-gasification does not adapt independent active sites for 10% steam and 90% CO_2 mixture. Instead, the reason for the difference was found to be the lowered reactivity of 10% steam with the balance nitrogen run as shown in Figure B.4. There is a significant drop in reactivity from 30% steam to 10% steam which probably occurs due to lower saturation level (surface coverage) on the surface as the steam becomes too diluted [40,42,43]. When the same fraction of steam (10%) is introduced with CO_2 (90%), the surface is completely saturated with the oxygen supplied by CO_2 which shows the expected reactivity trend as the other co-gasification runs (Figure B.5).

3.4 Conclusions

The effect of catalytic inorganics like potassium and calcium were studied during the gasification in both CO_2 and steam. Model RDF char consists of eight different components but only select inorganic-rich components were independently studied. Calcium-rich tissue paper char, potassium-rich orange peel char and model RDF char were gasified separately in CO_2 and steam. Steam gasification reactivity of calcium-rich tissue paper char was comparable to its CO_2 gasification reactivity although they followed opposite trends with conversion due to hydrogen inhibition in steam gasification. Steam gasification reactivity of potassium-rich orange peel char was very high compared to its CO_2 gasification reactivity. The major reason for this increased reactivity was found to be the amount of potassium present in the orange peel and the formation of KOH in the presence of steam. Although steam gasification had higher overall reactivity than CO_2 gasification for model RDF char, the reactivity in steam dropped with conversion which was attributed to inhibition by hydrogen product.

The catalytic effect of potassium was also detected during the gasification of microcrystalline cellulose – Avicel char showing that the results can be extended to other carbon sources. A number of samples were prepared with varying amounts of potassium on Avicel char which were gasified in both CO_2 and steam. A saturation in the gasification reactivity was observed at 5% potassium loading on Avicel chars below 60% conversion. At higher conversions, a maximum was observed that was dependent on the [K / residual carbon] ratio for both steam and CO_2 gasification. This dependency was ascribed to a potassium layer encapsulating the remaining char that acts as a barrier for the gasifying agents to diffuse through. Reaction mechanisms for potassium were established during different stages of gasification in both CO_2 and steam. K_2CO_3 decomposed during the ramp-up stage before gasification and propagated gasification through a proposed set of phase-change reactions. The predominant chemical phases of potassium are proposed to be K_2O and metallic potassium in CO_2 gasification and KOH and metallic potassium in steam gasification.

Even with large amounts of silicon, addition of potassium to rubber char increased its gasification reactivity. However, for similar potassium loading, rubber chars had lower overall reactivity than Avicel chars due to silicon scavenging. Calcium salt decomposed to CaO during the ramp-up stage before gasification and converted to $CaCO_3$ in CO_2. Hydrogen inhibition was observed in RDF char and calcium-rich tissue paper char. However, potassium-rich chars demonstrated a higher reactivity in hydrogen presence due to the formation of KOH, which was a better gasification catalyst than K_2CO_3 or K_2O. The same active sites participated in both CO_2 and steam gasification based on the gas – switchover experiment. During co-gasification using steam and CO_2 at the same time,

steam was found to be dominant even down to 30% steam and 70% CO_2 mixtures. For 10% steam and the balance nitrogen, decreased gasification reactivity was attributed to lower surface saturation. Replacing nitrogen with CO_2 led to complete surface saturation and thus a higher reactivity.

3.5 References

[1] M.S. Masnadi, J.R. Grace, X.T. Bi, C.J. Lim, N. Ellis, From fossil fuels towards renewables : Inhibitory and catalytic effects on carbon thermochemical conversion during co-gasification of biomass with fossil fuels, Appl. Energy. 140 (2015) 196–209. http://dx.doi.org/10.1016/j.apenergy.2014.12.006.

[2] I. Aarna, E.M. Suuberg, Changes in reactive surface area and porosity during char oxidation, Symp. Combust. 27 (1998) 2933–2939.

[3] S. Manocha, V.B. Chauhan, L.M. Manocha, Porosity Development on Activation of Char from Dry and Wet Babbool Wood, Carbon Lett. 3 (2002) 133–141. http://carbonlett.org/PublishedPaper/year_abstract.asp?idx=296.

[4] Z. Bouraoui, M. Jeguirim, C. Guizani, L. Limousy, C. Dupont, R. Gadiou, Thermogravimetric study on the influence of structural, textural and chemical properties of biomass chars on CO_2 gasification reactivity, Energy. 88 (2015) 703–710. http://dx.doi.org/10.1016/j.energy.2015.05.100.

[5] C. Sheng, Char structure characterised by Raman spectroscopy and its correlations with combustion reactivity, Fuel. 86 (2007) 2316–2324.

[6] Y. Huang, X. Yin, C. Wu, C. Wang, J. Xie, Z. Zhou, L. Ma, H. Li, Effects of metal catalysts on CO_2 gasification reactivity of biomass char, Biotechnol. Adv. 27 (2009) 568–572. http://dx.doi.org/10.1016/j.biotechadv.2009.04.013.

[7] K. Mitsuoka, S. Hayashi, H. Amano, K. Kayahara, E. Sasaoaka, M.A. Uddin, Gasification of woody biomass char with CO_2: The catalytic effects of K and Ca species on char gasification reactivity, Fuel Process. Technol. 92 (2011) 26–31. http://linkinghub.elsevier.com/retrieve/pii/S0378382010002791.

[8] M.J. Veraa, A.T. Bell, Effect of alkali metal catalysts on gasification of coal char, Fuel. 57 (1978) 194–200.

[9] P.L. Walker Jr, O.P. Mahajan, M. Komatsu, Catalysis of lignite char gasification by various exchanged cations-dependence of activity on reactive atmosphere, Prepr. Div. Fuel Chem., Am. Chem Soc. 24 (1979) 10–16.

[10] A. Linares-solano, D. Lecea, Calcium-catalysed carbon gasification in CO_2 and steam, Fuel. 69 (1990) 21–27.

[11] L.R. Radović, P.L. Walker, R.G. Jenkins, Effect of lignite pyrolysis conditions on calcium oxide dispersion and subsequent char reactivity, Fuel. 62 (1983) 209–212.

[12] B. Acharya, A. Dutta, P. Basu, An investigation into steam gasification of biomass for hydrogen enriched gas production in presence of CaO, Int. J. Hydrogen Energy. 35 (2010) 1582–1589. http://dx.doi.org/10.1016/j.ijhydene.2009.11.109.

[13] M.P. Kannan, G.N. Richards, Gasification of biomass chars in carbon dioxide : dependence of gasification rate on the indigenous metal content, Fuel. 69 (1990) 747–753.

[14] K. Umeki, A. Moilanen, A. Gómez-Barea, J. Konttinen, A model of biomass char gasification describing the change in catalytic activity of ash, Chem. Eng. J. 207–208 (2012) 616–624. http://dx.doi.org/10.1016/j.cej.2012.07.025.

[15] US Environmental Protection Agency, Municipal Solid Waste Generation , Recycling , and Disposal in the United States : Facts and Figures for 2012, (2012) 1–14.

[16] M. McHenry, Waste to Energy Technologies, Murdoch Univ. (2006). http://www.see.murdoch.edu.au/resources/info/Tech/waste/ (accessed December 3, 2015).

[17] S.G. Chen, R.T. Yang, Unified mechanism of alkali and alkaline earth catalyzed gasification reactions of carbon by CO_2, Energy & Fuels. 11 (1997) 421–427. http://dx.doi.org/10.1021/ef960099o.

[18] T. Yokoyama, Tanaka, Toyoshima, Miyahara, Yoshida, X-Ray photoelectron spectroscopic study of the surface of carbon doped with potassium carbonate, Chem. Lett. (1980) 599–602.

[19] W.Y. Wen, Mechanisms of alkali metal catalysis in the gasification of coal, char, or graphite, Catal. Rev. Eng. 22 (1980) 1–28.

[20] M. Perez, H. Armendariz, J.A. Toledo, A. Vazquez, J. Navarrete, A. Montoya, A. Garcia, Preparation of Ni / ZrO_2 – SO_4^{2-} catalysts by incipient wetness method : effect of nickel on the isomerization of n -butane, J. Mol. Catal. A Chem. 149 (1999) 169–178.

[21] A. Sattar, G.A. Leeke, A. Hornung, J. Wood, Steam gasification of rapeseed , wood , sewage sludge and miscanthus biochars for the production of a hydrogen-rich syngas, Biomass and Bioenergy. 69 (2014) 276–286. http://dx.doi.org/10.1016/j.biombioe.2014.07.025.

[22] C.D. Le, S.T. Kolaczkowski, Steam gasification of a refuse derived char : Reactivity

and kinetics, Chem. Eng. Res. Des. 102 (2015) 389–398.

[23] P. Parthasarathy, K.S. Narayanan, Hydrogen production from steam gasification of biomass : Influence of process parameters on hydrogen yield - A review, Renew. Energy. 66 (2014) 570–579. http://dx.doi.org/10.1016/j.renene.2013.12.025.

[24] D.I. Pineda, J. Chen, Modeling hydrogen inhibition in gasification surface reactions, Int. J. Hydrogen Energy. 40 (2015) 6059–6071. http://dx.doi.org/10.1016/j.ijhydene.2015.03.063.

[25] K.J. Huttinger, W.F. Merdes, The carbon-steam reaction at elevated pressure: formations of product gases and hydrogen inhibitions, Carbon N. Y. 30 (1992) 883–894.

[26] C. Dupont, S. Jacob, K. Ould, M. Grateau, F. Labalette, D.D.S. Perez, How inorganic elements of biomass influence char steam gasification kinetics, Energy. 109 (2016) 430–435.

[27] N.B. Klinghoffer, M.J. Castaldi, A. Nzihou, Influence of char composition and inorganics on catalytic activity of char from biomass gasification, Fuel. 157 (2015) 37–47. http://dx.doi.org/10.1016/j.fuel.2015.04.036.

[28] M. Jiang, J. Hu, J. Wang, Calcium-promoted catalytic activity of potassium carbonate for steam gasification of coal char: Effect of hydrothermal pretreatment, Fuel. 109 (2013) 14–20. http://dx.doi.org/10.1016/j.fuel.2012.06.100.

[29] D.L. Biederman, A.J. Miles, F.J. Vastola, P.L. Walker, Carbon-carbon dioxide reaction: Kinetics at low pressures and hydrogen inhibition, Carbon N. Y. 14 (1976) 351–356.

[30] K. Kirtania, J. Axelsson, L. Matsakas, P. Christakopoulos, K. Umeki, E. Furusjö, Kinetic study of catalytic gasification of wood char impregnated with different alkali salts, Energy. 118 (2017) 1055–1065.

[31] D.W. Mckee, C.L. Spiro, K.E. J, P.G. Lamby, Catalytic Effects of Alkali Metal Salts in the Gasification of Coal Char, Prepr. ACS Meet. 27 (1982) 74–86.

[32] B.J. Wood, K.M. Sancier, The Mechanism of the Catalytic Gasification of Coal Char: A Critical Review, Catal. Rev. 26 (1984) 233–279. http://dx.doi.org/10.1080/01614948408078065.

[33] F. Kapteijn, J.A. Moulijn, Kinetics of the potassium carbonate- catalysed CO_2 gasification of activated carbon*, Fuel. 62 (1983) 221–225.

[34] J.A. Moulijn, M.B. Cerfontain, F. Kapteijn, Mechanism of the potassium catalysed gasification of carbon in CO_2*, Fuel. 63 (1984) 1043–1047.

[35] C. Di Blasi, A. Galgano, C. Branca, Effects of Potassium Hydroxide Impregnation

on Wood Pyrolysis, Energy & Fuels. 23 (2009) 1045–1054.

[36] C. Zhou, T. Stuermer, R. Gunarathne, W. Yang, W. Blasiak, Effect of calcium oxide on high-temperature steam gasification of municipal solid waste, Fuel. 122 (2014) 36–46. http://dx.doi.org/10.1016/j.fuel.2014.01.029.

[37] H.C. zur Loye, K. Dwight, R. Kershaw, J.K. Pabst, A. Wold, R.J. Lang, Gasification of carbon using calcium oxide, Mater. Res. Bull. 19 (1984) 459–463.

[38] R.J. Lang, R.C. Neavel, Behavior of calcium as a steam gasification catalyst, Fuel. 61 (1982) 620–626.

[39] J. Gadsby, C.N. Hinshelwood, K.W. Sykes, The Kinetics of the Reactions of the Steam-Carbon System, Proc. R. Soc. A Math. Phys. Eng. Sci. 187 (1946) 129–151. http://rspa.royalsocietypublishing.org/cgi/doi/10.1098/rspa.1946.0071.

[40] D. Roberts, D. Harris, Char Gasification Kinetics in Mixtures of CO_2 and H_2O: The Role of Partial Pressure in Determining the Extent of Competitive Inhibition, Energy & Fuels. 28 (2014) 7643–7648. http://pubs.acs.org/doi/abs/10.1021/ef502101b.

[41] S. Umemoto, S. Kajitani, S. Hara, Modeling of coal char gasification in coexistence of CO_2 and H_2O considering sharing of active sites, Fuel. 103 (2013) 14–21. http://dx.doi.org/10.1016/j.fuel.2011.11.030.

[42] K. Jayaraman, I. Gökalp, S. Jeyakumar, Estimation of synergetic effects of CO_2 in high ash coal-char steam gasification, Appl. Therm. Eng. 110 (2017) 991–998. http://dx.doi.org/10.1016/j.applthermaleng.2016.09.011.

[43] F. Li, Q. Yan, J. Huang, J. Zhao, Y. Fang, J. Wang, Lignite-char gasification mechanism in mixed atmospheres of steam and CO_2 at different pressures, Fuel Process. Technol. 138 (2015) 555–563. http://dx.doi.org/10.1016/j.fuproc.2015.06.035.

CHAPTER 4. EVOLUTION OF REFUSE DERIVED FUEL (RDF) CHAR MORPHOLOGY, PHYSICOCHEMICAL CHARACTERISTICS, AND GASIFICATION REACTIVITY AS A FUNCTION OF PYROLYSIS HEATING RATE AND RESIDENCE TIME

4.1 Background

Alternative energy sources must be studied and developed as early as possible to gradually replace fossil-based energy. This increased need is a response to the inevitable depletion of fossil fuels and to the increasingly alarming environmental problems like global warming [1,2]. Municipal Solid Waste (MSW) gasification represents an alternative source of energy that remains largely unexplored, but one that could become an important source as the world economies become less fossil-fuel dependent. MSW consists of a mixture of garbage components generated by households on a day-to-day basis. After recycling, the major components present in the discarded portion of MSW were paper and paperboard (27.4%), food waste (14.5%), yard trimmings (13.5%), and plastics (12.7%), which are all organic and thus promising sources of gasification [3]. The large availability of MSW across the globe makes it incredibly cheap to acquire as a feedstock. Hence, increased use of this alternative fuel would decrease the cost of waste disposal, reduce environmental concerns (size of landfill areas, release of pollutants), and provide significant amounts of energy.

Refuse derived fuel (RDF) is a refined form of MSW derived using certain pre-processing techniques. These techniques modify the composition by reducing the heavy metal, glass and moisture content thus making it more organic-rich [4]. A gasification process involves an initial drying step, followed by feed pyrolysis and finally the char gasification stage with the last stage being the slowest [5]. Since gasification of char is the rate determining step, increasing the reactivity of char gasification is of importance. Several pyrolysis processing conditions have been identified in biomass literature that affect the char gasification reactivity.

Chapters 2 and 3 have shown that alkali and alkaline earth metals like potassium and calcium enhance reactivity while silicon and phosphorous inhibit it, which is also confirmed by other studies [6–8]. Other parameters that play a role in the process are particle size, which is inversely proportional to syngas yield [9], and final temperature in the reactor, which increases reaction kinetics and gas yield at high temperatures [10]. One of the most important parameters that determines char structure and yield, and consequently, the rate of syngas production is heating rate. It has been reported that under high heating rates, biomass particles swell and the resulting char exhibits macropores that facilitate gasification reactions because the surface area of the particle is increased [11–14]. However, under high heating rates, tar yield is increased because vapor residence time is minimized, and secondary reactions are limited [15,16]. Moreover, a study also revealed that when mixtures of biomass and plastics were co-pyrolyzed under high heating rates, the resulting char contained larger pore sizes since melted plastic caused internal volatile pressure to build up until the gases could finally escape [16]. The study also found that

both the organic and aqueous phase products of pyrolysis were enhanced as a result of a synergistic effect between biomass and the polymers [16].

Although the effect of heating rate on the gasification process has been extensively studied for biomass, similar comprehensive studies for mixtures, such as MSW or RDF, are limited. This study explores the effect of pyrolysis heating rate on the char morphology, its physical and chemical properties and the resultant char gasification reactivity. A tubular quartz reactor was used to generate RDF char at both a high heating rate (HHR) and a low heating rate (LHR). The char morphology and the resulting inorganic distribution was analyzed using Scanning Electron Microscopy (SEM) and Energy Dispersive X-ray Spectroscopy (EDX). The elemental and inorganic composition, surface areas and the type of carbon resulting from the two different heating rates were also explored. Moreover, all the described char properties were investigated for the HHR char at two different residence times. Furthermore, CO_2 gasification reactivity of all the chars was determined from experiments performed in a Thermogravimetric Analyzer (TGA) and was analyzed based on the different pyrolysis conditions used.

4.2 Materials and Methods

4.2.1 Experimental materials and feed preparation

A representative RDF feed composition for the purpose of lab-scale studies was identified by individual component pyrolysis experiments which is explained in detail in Chapter 2. The basis for the selection of these preliminary components was the composition of the discarded portion of MSW, as identified by EPA for 2012 [3]. The model RDF composition consists of 9 different components as shown in Figure 4.1. Plastics, paper

waste and food waste were the major components in the discarded portion of MSW and thus constitute 77% of the model composition. The plastic fraction contains LDPE supplied as Microthene FN51000 (LyondellBasell) and PET as PQB7-76 Prime PET resin (Polyquest Inc.). Tissue paper and paperboard obtained from local stores constituted the paper fraction. Food waste was represented by dried orange peel powder and dog food prepared from Milkbone biscuits. Lehigh Technologies provided the rubber powder (Polydyne 200) that was part of the minor components present in the model composition along with cotton fabric and pine wood powders.

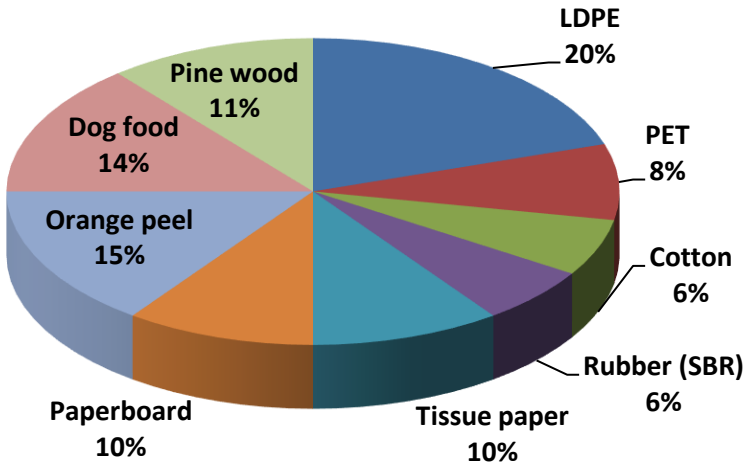

Figure 4.1. Model RDF feed composition.

A particle size reduction of individual components to less than 106 µm was required to achieve reproducible thermogravimetric analysis (TGA) profiles where less than 10 mg sample sizes of nine different components were used. This was carried out using two different types of grinders. A Thomas Scientific Wiley mill was utilized to achieve particle sizes of less than 2 mm via cutting-based grinding. Orange peel, dog food and pine wood could be ground down to less than 106 µm size by re-grinding the material two more times

in the Wiley mill. While further size reduction of paper components and cotton to less than 106 μm was accomplished by employing a Retsch MM 400 mixer mill. The impact-based grinding in the mixer mill could reduce the fibrous components to the required size. Finely ground LDPE, PET and rubber particles were purchased directly from the vendors.

A homogeneous mixture of all the fine particles was obtained by thoroughly mixing the individual components at 30 Hz and 3 minutes in the MM 400 mixer mill. The elemental analysis and physical properties of the model feed mixture are given in Table 4.1. The mixture was further pressed at a pressure of 5000 psi in a Wabash hot press which was evacuated and heated to 127 °C. The hold time at the high pressure was about 10 minutes. RDF pellets of 1.59 mm X 1 mm were formed from the pressed sheet with the use of a solid stud hole-punch. As can be seen from Figure 4.2, the RDF pellets created in this fashion are homogeneous, intact and of very similar size and shape. It is to be noted that, although extensive size reduction for lab scale studies is essential, the high cost of extensive particle size reduction in an industrial scale process would be unfavorable.

Table 4.1. Properties of model RDF feed

RDF feed	
Moisture content (wt %)	~ 4
Density (g/cc)	0.4
Weight %	**Elemental analysis**
Carbon	55.8
Hydrogen	8.06
Nitrogen	0.64
Oxygen	34.2

Figure 4.2. RDF pellets formed from the pressed sheet of the RDF mixture.

4.2.2 High heating rate and low heating rate char generation

The reactor used for the generation of low heating rate char and high heating rate char is a semi-batch quartz reactor as shown in Figure 4.3. The quartz reactor is essentially a tubular quartz tube placed inside a furnace with two gas ports on either side of the tube which act as the inlet and outlet for the purge nitrogen gas. For low heating rate char generation, the feed sample was loaded in a quartz boat that was placed in the quartz tube enclosed inside the furnace. Nitrogen gas flowing at 500 ml/min through the tube for 60 minutes in order to purge the system of oxygen. The sample was then heated from the room temperature to 800 °C at 20 K/min with no hold time. Subsequently, the furnace was cooled back down to the room temperature. The char thus produced is named RDF low heating rate (LHR) char for the purpose of discussion in this study. Additionally, a condenser was connected on the outlet end to cool down the volatiles before the gases were released into the fume hood.

In order to generate the high heating rate RDF char, the quartz reactor setup was marginally modified. Instead of a closed end at the outlet side of the quartz tube, a cap with

an opening was used. A push rod was inserted through the opening in the cap with the help of a septum to avoid gas leaks. The push rod was flexible enough to push and retract the quartz boat with the sample into the heated zone. A purge nitrogen flow of 500 ml/min was used for 60 minutes to purge the system of any residual oxygen. The sample boat was left in the unheated part of the quartz tube while the furnace was heated to 800 °C. Once the reaction temperature was reached, the sample boat was pushed into the heated part of the reactor using the push rod and left there for the required amount of residence time. This study has two samples generated at 15 minutes and 10 seconds in the heated zone. Subsequently, the quartz tube was retracted from the heated zone back into the unheated part of the tube using the push rod. Meanwhile, the furnace was cooled back down to room temperature. The char generated using this method is named RDF high heating rate (HHR) char. Using average conductivity and convective heat transfer coefficients from literature, the heating rate using this method is estimated to be 58 K/s [17,18].

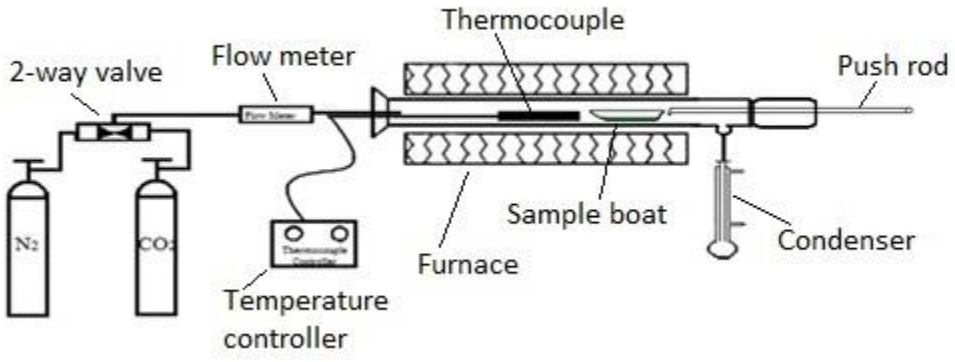

Figure 4.3. Quartz reactor setup for pyrolysis char generation in both LHR and HHR conditions

4.2.3 Char characterization

RDF char generated at different experimental conditions was subjected to several characterization techniques to understand the char morphology and its physical and chemical structure. Scanning electron microscopy (SEM) was employed to analyze the morphological features in all the char samples. A Hitachi SU8010 SEM with high resolution image grabber was used for this purpose. A typical gun voltage of 3 – 5 kV was selected. The char samples were mounted on an aluminum stub using double-sided carbon tape. Since the samples were non-conductive, they were coated with a 7 nm thick gold film using a Quorum Tech Q150T ES sputter coater to have better conductivity of electrons during imaging. Several images were captured with increasing magnification. Energy Dispersive X-ray Spectroscopy (EDX) was conducted on the samples using a Zeiss-LEO 1530 series SEM. EDX analysis was performed to acquire the inorganic distribution over the char surface. An accelerating voltage of 10 kV was used to envelop the entire range of X-ray emission peaks (Kα and Lα values) of the major inorganic species present. The penetration depth of the probe was estimated to be around 2 μm based on the accelerating voltage [19].

The feed and char samples were sent to Huffman Laboratories, Golden, CO to determine the elemental composition through ultimate analyses with direct oxygen measurement. Inductively coupled plasma optical emission spectrometry (ICP-OES) was used to determine the amount of inorganic content in all the char residues by the analytical testing lab at the Renewable Bioproducts Institute (RBI) at Georgia Tech. The sample preparation was done by the caustic fusion method in order to accurately measure the silicon content in the samples [20]. The macroporous and mesoporous surface area was

determined using a Micromeritics AutoPore IV mercury porosimeter. Both low pressure and high pressure analyses were performed to measure all the pore sizes accurately. Raman spectra in this study were recorded at room temperature in open atmosphere using a confocal Raman microscope, Alpha-Witek 300R, with a back-scattered light configuration. The detector is equipped with an Oxxius laser at 532 nm as its light source for Raman spectroscopy. A 20X objective was used that resulted in a resolution of 665 nm. A 70% variable laser power, 30 seconds integration time and three accumulations were selected. Single spectrum scans were obtained using the WITeC control software on a computer.

4.2.4 Methodology for quantifying EDX maps

The EDX mapping of the SEM images of different char samples qualitatively shows the inorganic distribution across the sample surface. However, the comparison between two EDX maps is vague and inconclusive when the images are directly compared. To have definitive analysis of the generated EDX maps, a new methodology using MATLAB software was developed (Appendix C.3). Since the distribution of potassium and silicon are of interest in this study, the EDX maps of the two inorganics were processed through the program. Since any external data other than the mapped image could interfere with the calculation, the program crops the image so as to remove the scale bar.

The dots present in the EDX mapping of potassium and silicon are representative of that particular inorganic element detected by the instrument across the focused surface. The MATLAB code calculated the number of dots present in the EDX maps of potassium and silicon by measuring the pixel intensity in each of the images. The image was divided into a 10X10 grid of 100 equal sized rectangles. The number of dots, and the percentage area occupied by the dots in each rectangle was determined. A 10X10 grid was chosen so

as to analyze each part of the SEM image more closely. The MATLAB code also generated heat maps of the 10X10 grid with the brightness of each rectangle proportional to the number of particles present in them. Thus, the higher the brightness of the rectangle in the grid, the more concentrated that particular element is in that region.

This new methodology helped in quantifying the otherwise qualitative EDX mapping data. Moreover, this method could be used to quantify EDX maps of any element and thus is expected to be worthwhile for broad use.

4.2.5 Char gasification

A thermogravimetric-analyzer (TGA) was used to carry out all the char gasification experiments. Runs were conducted in an SDT-Q600 TGA by TA Instruments which recorded weight loss as a function of temperature and time. Both the HHR and LHR char samples were subjected to a heat-up condition of 20 K/min ramp rate to the reaction temperature of 800 °C with 200 ml/min of nitrogen flow. The sample sizes were about 3 – 5 mg and some volatile loss was recorded during the heat-up stage. These were the volatiles that were unconverted during the short exposure time at high temperature. An isothermal step of 15 minutes was added before introducing CO_2 into the system in order to stabilize the sample weight in the TGA. Subsequently, 100% CO_2 was introduced at 200 ml/min for gasification until complete carbon conversion was achieved as indicated by weight stabilization. The conversion (X) and reactivity (R) in these gasification experiments were determined according to the following formulae:

$$X = \frac{(m_0 - m_t)}{(m_0 - m_{ash})} \qquad \text{Eq. (4.1)}$$

$$R = \frac{-1}{(m_t - m_{ash})} \frac{dm_t}{dt} \qquad \text{Eq. (4.2)}$$

where,

m_0 = initial mass at the introduction of 100% CO_2

m_t = mass at time‘t’

m_{ash} = final mass at the end of the gasification run

4.3 Results and Discussion

4.3.1 Changes in the char structure at different pyrolysis heating rates

4.3.1.1 Char morphology of low heating rate (LHR) and high heating rate (HHR) chars

Char morphology was modified during the pyrolysis of RDF pellets at different heating rates. RDF char pellets shrunk radially during LHR pyrolysis from 1.59 mm to ~1.33 mm with slightly higher axial length after pyrolysis. On the other hand, with HHR pyrolysis, radial shrinking of RDF pellets was a little higher from 1.59 mm to ~1.22 mm. However, an expansion of the char pellet was observed axially where the length of the pellet increased from 1 mm to 1.2 mm. This increase in axial length in contrast to the radial length is suspected to be a result of RDF feed pellet preparation where high pressures were applied axially on the feed material. This high pressure is expected to have compressed the material to a great extent which is relieved when the feed pellet is heated during pyrolysis thus leading to an expansion in the axial direction.

Figure 4.4 shows that the char generated at LHR was more intact with more of the original char structure preserved, while, char generated at HHR showed large cavities on

the char surface. RDF HHR char surface suggests sudden release of volatiles in a short span of time resulting in crater-like openings on the char surface. HHR pyrolysis resulted in a smoother char surface compared to LHR char indicating that melting and swelling occurred simultaneously. During devolatilization at HHR conditions in N_2 at atmospheric pressure, the particle is expected to swell first and then melt, evolving into a droplet before it ruptures and loses its volatile matter [11]. LHR pyrolysis char preserved the fibrous structure of the feed even after pyrolysis at 800 °C. On the other hand, HHR pyrolysis resulted in softening of the char surface with the creation of macropores that could be the result of a rapid release of volatiles. Cross sectional surfaces of the LHR char and HHR char were also compared (Figure C.1). Similar to the lateral surface of the pellets, the base area of the HHR char pellet was more porous and smoother than the intact LHR char pellet. Furthermore, the fibrous structure was preserved in the base area of the LHR char similar to the lateral surface. Deep crater-like formations were also noticeable in the base area of HHR char indicating that the volatiles escaped from all directions inside the pellet.

At high magnification (20,000 X), both the LHR pyrolysis char and HHR pyrolysis char exhibited a porous structure as shown in Figure 4.4 e and f. Several carbon nanospheres were detected in both the chars indicating that the fundamental micropore structure of the two chars is similar. Our results are in agreement with the results observed by Trubetskaya et al., who saw that under slower heating conditions, plasticization on the char surface is hindered by cross-linking prior to bridge-breaking [21]. While at high heating rates, the char behaves similar to bituminous coals and is assumed to undergo significant bridge-breaking before it starts to cross-link.

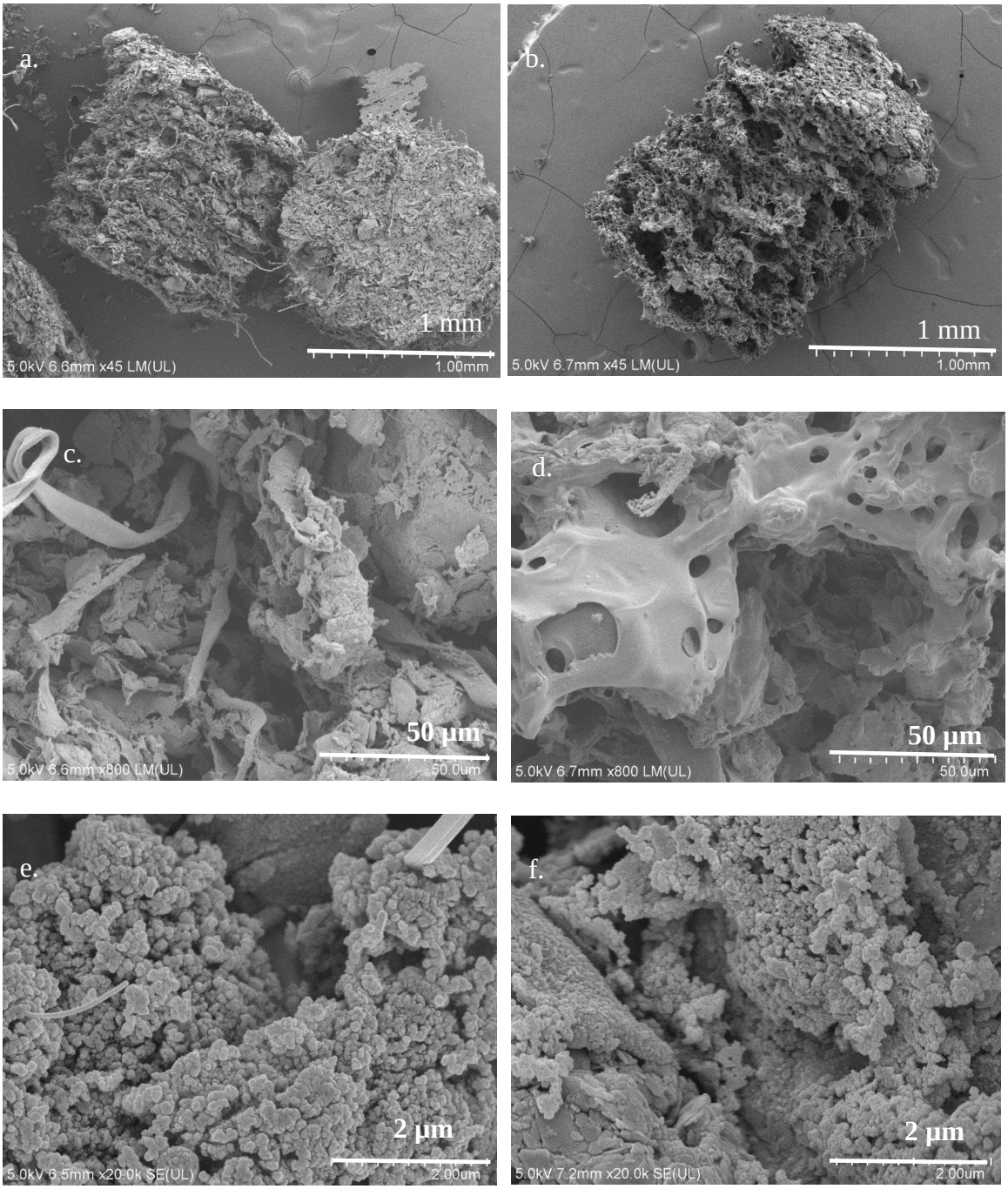

Figure 4.4. SEM images of RDF char generated at 800 °C with a. LHR at X45 magnification b. HHR at X45 magnification c. LHR at X800 magnification d. HHR at X800 magnification e. LHR at X20 K f. HHR at X20 K.

4.3.1.2 Char structure evolution with increasing temperature for LHR and HHR pyrolysis conditions

RDF char was generated at HHR but was only heated up to 250 °C to understand the evolution of char morphology as temperature increases. Figure 4.5 indicates that at 250 °C, RDF HHR char retains its feed like structure. The diameter was still the same at around 1.59 mm, implying that the shrinking process had not yet begun. However, the feed pellet had an average height of 1 mm which had increased to 1.62 mm indicating that the expansion in the longitudinal direction had peaked. Since the temperature is still low for volatiles to be released, this expansion is probably due to the pressure relief which was induced during the hot pressing of the feed material. At a higher magnification of 150X, melted pockets were observed on the surface of the char at multiple locations. These melted pockets are possibly melted LDPE (M.P. – 120 to 140 °C) which constitutes about 20% of the feed composition. A number of pellets were analyzed to make sure this was not an isolated phenomenon that only occurred on one pellet. Although the other component particles could still be distinguished and were similar to the SEM images of the feed pellets, they had a softer and smoother appearance which implies melting at 250 °C.

At 400 °C the RDF char showed a more porous structure (Figure 4.6) than the char generated at 250 °C. This was expected as more volatiles are released as the temperature increases to 400 °C creating more pores on the surface. The length of the pellet had however decreased to ~1.4 mm from 1.6 mm at 250 °C, which indicates loss of volatiles and mass that has decreased the length despite the higher initial increase at 250 °C. Although, it needs to be noted that, compared to the feed pellet height of 1 mm, there is an increase in the pellet height at 400 °C. Macropores are noticeable on the longitudinal

surface of the char although they are not as high as the final char produced at 800 °C (Figure 4.4) since the plastic fraction has not yet devolatilized. Swollen bubbles with cracks clearly indicate that volatiles were trapped inside the melted structures which have expanded and finally cracked due to the sudden release of volatiles. Large pores were also observed on the smoother surface which suggest that melting and devolatilization happen simultaneously. Higher magnification SEM images of the chars support these observations (Figure C.2).

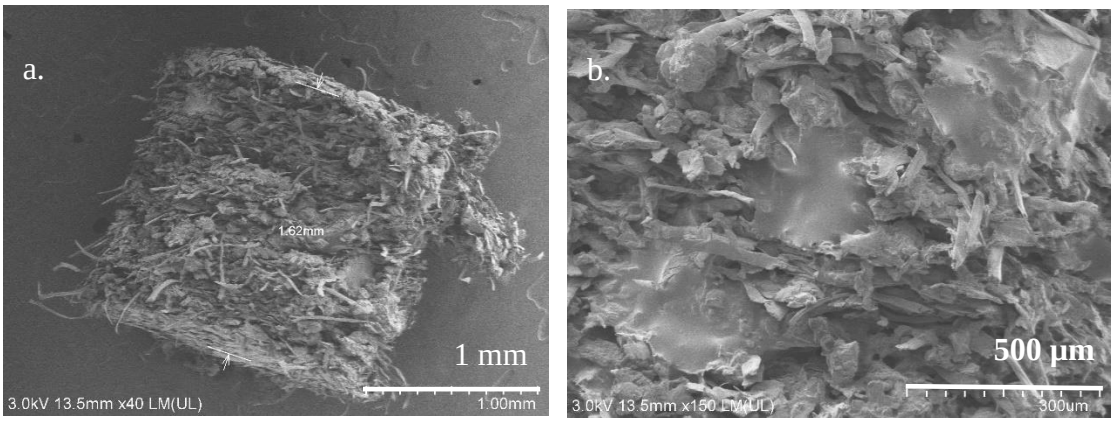

Figure 4.5. SEM images of RDF char generated at HHR and 250 °C with a. X40 magnification b. X150 magnification.

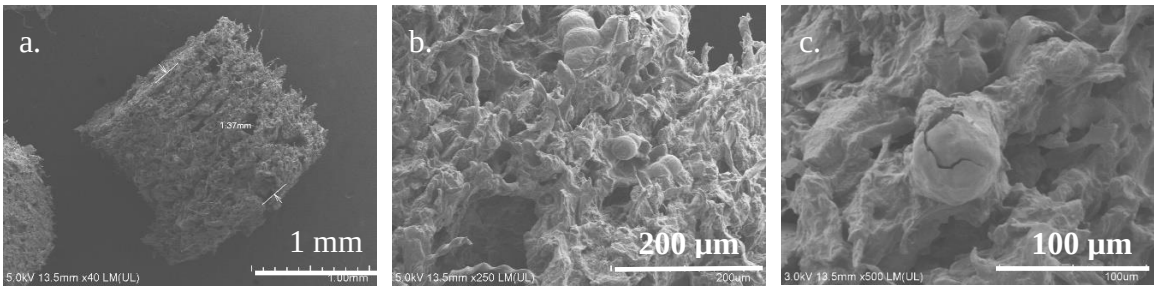

Figure 4.6. SEM images of RDF char generated at HHR and 400 °C with a. X40 magnification b. X250 magnification c. X500 magnification.

Similar to the char generated at HHR, RDF char pellets were generated at LHR by heating to 250 °C and 400 °C to observe the char structure evolution with increasing temperature. Figure 4.7 presents the SEM images of the LHR chars generated at the two temperatures. The melted viscous layer was clearly visible in the char generated at 250 °C that covered the swollen particles underneath, similar to the observation made with the HHR char (Figure 4.5). While char generated at 400 °C was more porous than the char generated at 250 °C, the lower porosity of the char indicated that further release of volatiles is yet to occur. Char morphology evolution at 400 °C was incomplete as evident from the comparison with the char generated at 800 °C (Figure 4.4 c). The major difference between the char morphology of the LHR and HHR chars was the absence of large macropores and lower overall porosity with the char generated at LHR as compared to the HHR char. This is due to the sudden release of volatiles in the HHR char where the feed is rapidly heated to high temperatures.

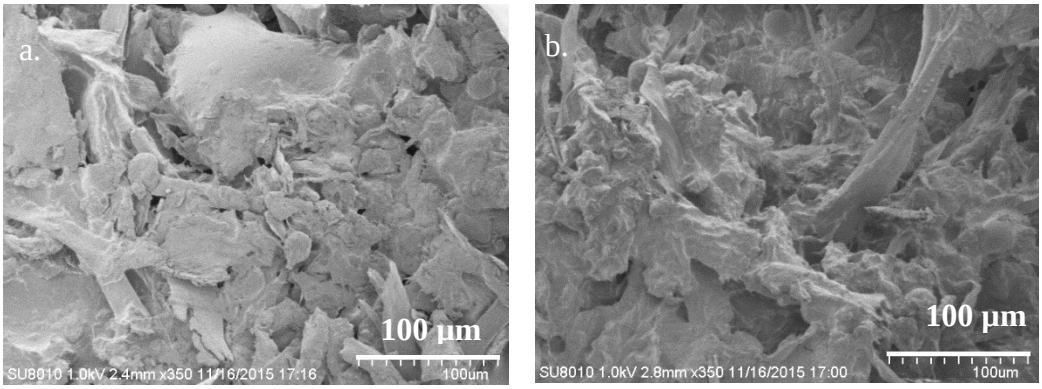

Figure 4.7. SEM images of RDF char generated at LHR with X350 magnification heated to a. 250 °C b. 400 °C.

4.3.2 Changes in the physicochemical properties of the HHR char pellets as a function of residence time

4.3.2.1 Char morphology of different residence time pellets

High heating rate pyrolysis of RDF feed pellets was carried out at 800 °C for varying residence times of 15 minutes and 10 seconds. The lower residence time of 10 seconds was chosen to determine char morphological evolution as the feed is suddenly exposed to high temperature. Figure 4.8 shows the char morphology when the RDF feed pellets were exposed to 800 °C for 10 seconds. The char dimensions indicate a radial shrinking of RDF pellets from 1.59 mm to ~1.27 mm similar to the HHR char with a residence time of 15 minutes (~1.22 mm). However, the vertical expansion was higher at 10 seconds exposure with an increase from 1 mm to about 1.6 mm as opposed to 1.2 mm at 15 minutes residence time. This indicates that although the pressure induced during the feed preparation has been relieved, the volatiles have not been completely released at this point. This observation is similar to the effect of temperature during HHR char generation. As seen in section 4.3.1.2, the pellet length increases to 1.6 mm at 250 °C and then decreases eventually as the temperature is increased further to 400 °C and 800 °C.

Although macropores and crater-like formations were observed in the 10 seconds residence time char, the abundance of these pores and craters is lower compared to those formed on the 15 minutes residence time char (Figure 4.4 b). Char morphological evolution of the 10 seconds residence time char was similar to the 15 minutes residence time char, confirming that a rapid release of volatiles occurs immediately as the char is exposed to high temperatures. Ultra-macropores that could be measured using SEM ranged from 30

μm to 220 μm (Figure C.3 a). At high magnification, char surface was saturated with nanospherical structures (Figure C.3 b) similar to the observation made with the 15 minutes residence time char (Figure 4.4 f). This implies that the formation of these structures begins as soon as the feed is exposed to high temperatures.

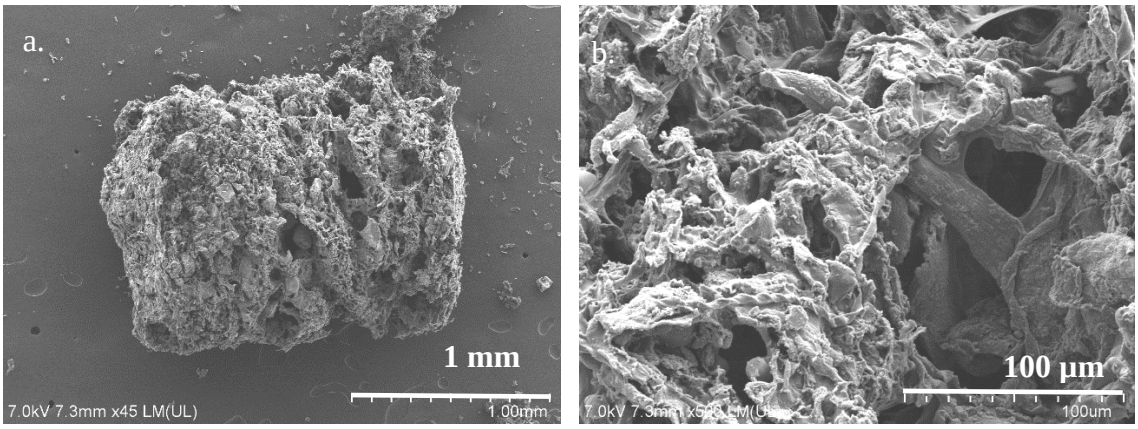

Figure 4.8. SEM images of RDF char produced at HHR and 800 °C for 10 seconds with a. X45 magnification b. X500 magnification.

4.3.2.2 Elemental composition of different heating rate and residence time chars

RDF chars produced at low heating rate and high heating rate (with different residence times) were analyzed to determine the elemental composition with respect to the carbon, hydrogen, nitrogen and oxygen content. The inorganic content of the samples is discussed in section 4.3.2.3. The composition distribution for the aforementioned samples is shown in Table 4.2. Chars generated at both LHR and HHR for 15 minutes contain similar elemental composition indicating that 15 minutes residence time at 800 °C is sufficient for complete pyrolysis and results in similar char composition as the low heating rate pyrolysis. In both cases, RDF pellets loses around 85% of its weight during pyrolysis. Most of the volatiles released during pyrolysis contain carbon, hydrogen and oxygen based

on the comparison of CHNO content of chars and feed. Although the relative concentration of oxygen compared to the other components in all the chars is relatively high, it is to be noted that around 95% of the original oxygen present was released during pyrolysis. On the other hand, more than 98% of the original hydrogen was released during pyrolysis for the LHR char and the HHR char with 15 minutes residence time.

Table 4.2. Elemental composition of different heating rate and residence time RDF chars

Sample	C (%)	H (%)	N (%)	O (%)
RDF LHR char	73.6	0.91	1.35	12.3
RDF HHR char 15 min	72.1	0.95	1.14	12.4
RDF HHR char 10 s	69.5	2.15	1.48	12.9

The largest difference between the two residence time pellet chars at high heating rate is the hydrogen content. The higher amount of hydrogen present in low residence time HHR char is expected to be a result of incomplete de-volatilization during the short exposure time [22,23]. The char yield for the low residence time HHR char was also comparatively higher at around 17% as compared to 15% of LHR char and 15% of 15 minutes residence time HHR char. Thus, the absolute quantities of all the elements in the low residence time HHR char were more than their corresponding values in the 15 minutes residence time char. Further exposure to higher temperatures during subsequent gasification is expected to complete the volatilization of the unconverted elements. A relationship between the elemental composition and the gasification reactivity is discussed in section 4.3.3.2.

4.3.2.3 Role of pyrolysis residence time on the distribution of inorganics in RDF pellets

The inorganic composition of the different chars is expected to be similar since the feed material is the same for all the different chars produced. However, vaporization of certain inorganics like potassium during pyrolysis has been reported [24,25]. The extent of vaporization could change for the char generated at different conditions. Thus, ICP-OES was carried out to determine the composition of inorganics in the feed pellet and the chars produced at different heating rates and residence times (Table C.1). The analysis revealed similar inorganic composition in all the long exposure chars. On the other hand, RDF HHR char with 10 seconds residence time contained more potassium than the other chars which is probably due to lowered loss of potassium vaporization during a short exposure to high temperature.

Potassium present in the feed is expected to be redistributed during pyrolysis based on the previous observations in Chapter 2 and in literature [26]. However, the extent of redistribution may vary as the feed is exposed to high temperatures for different residence times. EDX was performed to determine the inorganic mapping in the chars generated at different conditions. The inorganic distribution of the four major inorganics present in RDF LHR char is presented in the Figure C.4. EDX mapping shows that potassium is well distributed on the char surface due to its mobility, while, silicon is restricted to rubber and paperboard samples [26]. Calcium on the other hand is more distributed than silicon but is still found segregated in certain spots, possibly due to sintering [27]. Similar to the observations made for RDF LHR char, potassium is well distributed on the char surface with higher aggregation of calcium and complete isolation of silicon to rubber and

paperboard particles in the RDF HHR char with 15 minutes residence time (Figure 4.9). This shows that heating rate does not affect inorganic distribution significantly.

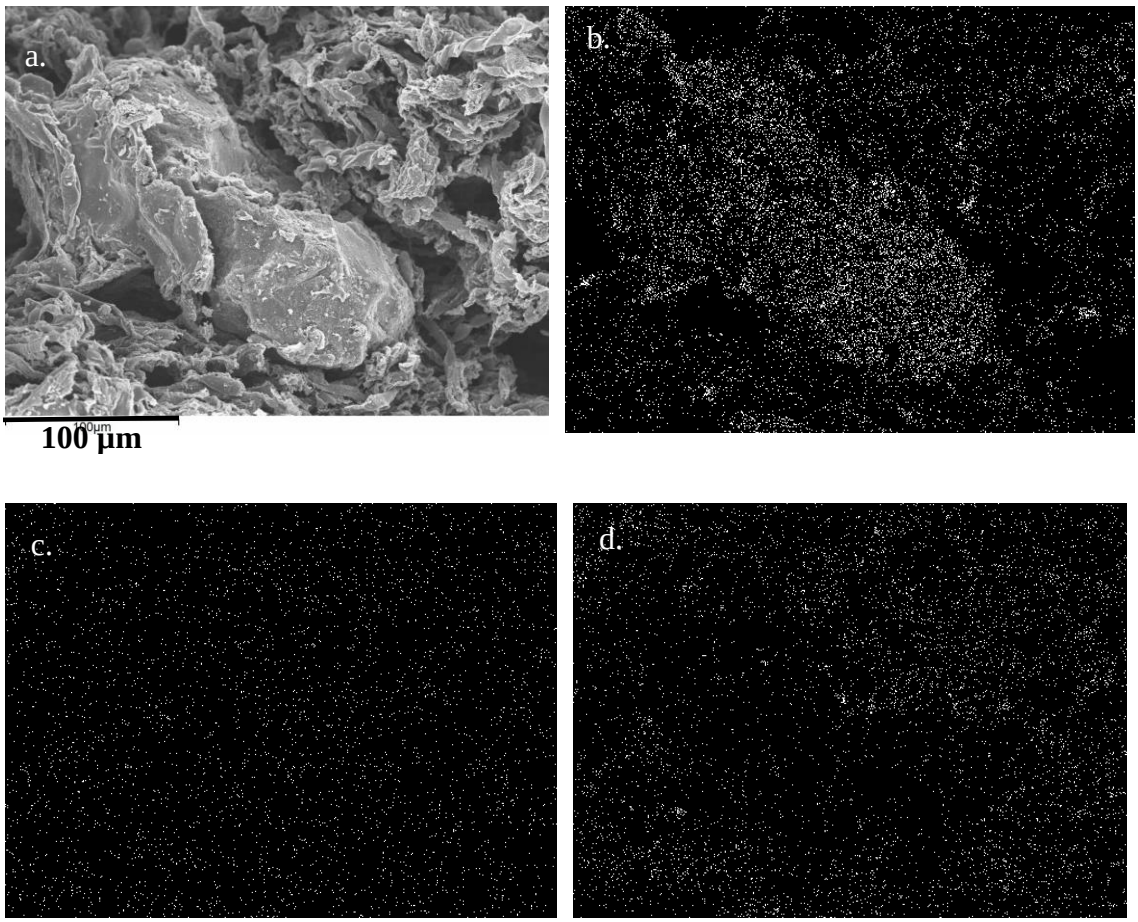

Figure 4.9. EDX analysis of RDF HHR char with 15 minutes residence time at 800 °C with a. SEM image b. Silicon mapping c. Potassium mapping d. Calcium mapping.

Potassium appeared less dispersed across the surface for lower residence time RDF HHR char (Figure 4.10) when compared with the higher residence time char (Figure 4.9). This implies that the lower residence time at higher temperature resulted in an incomplete redistribution of potassium across the surface. However, this conclusion is based on qualitative visual comparison of the EDX mapping images and thus is not completely

reliable. In order to establish a quantitative comparison of the elemental mappings, a new methodology was developed on MATLAB. This method divides the image into equally spaced sections, counts the particles in each section and, reports the distribution level quantitatively. A more detailed description of the method is given in section 4.2.4.

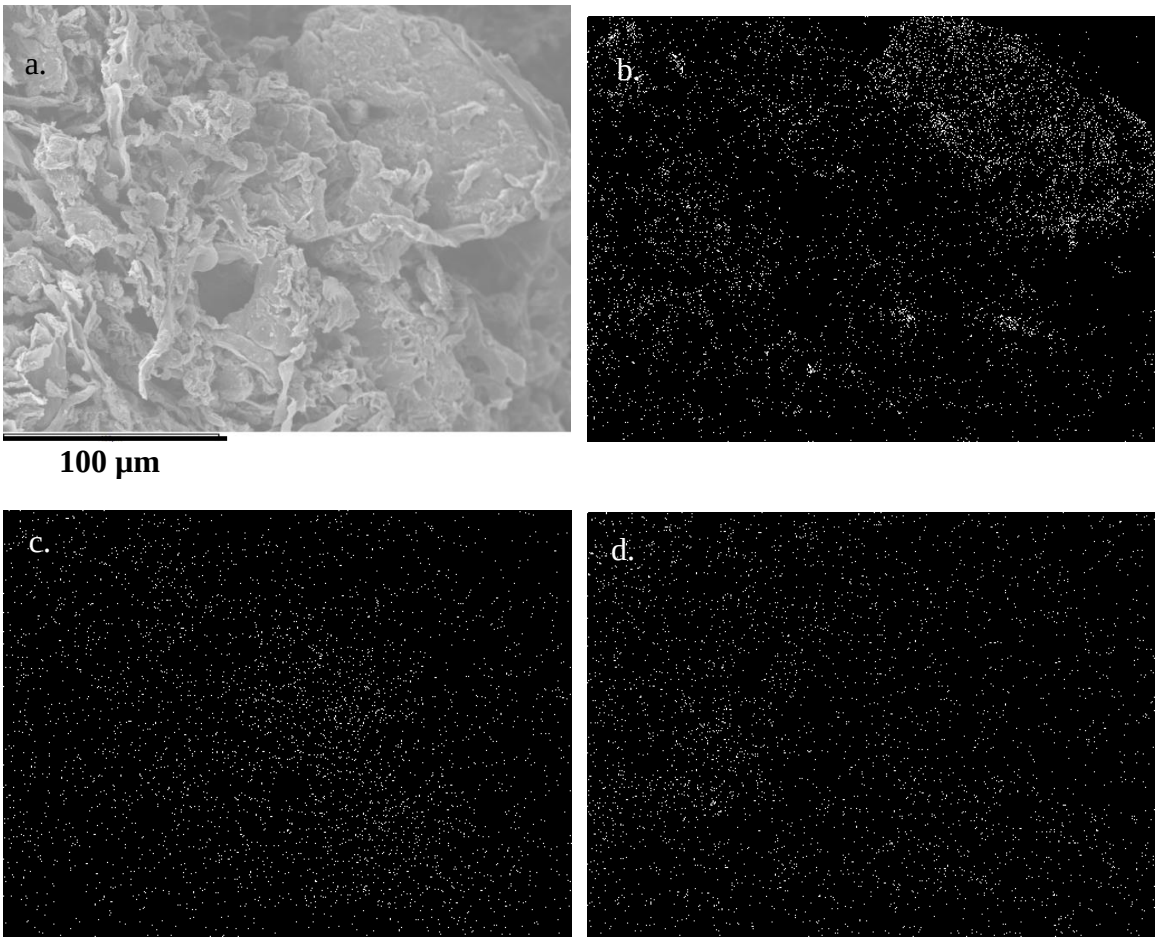

Figure 4.10. EDX analysis of RDF HHR char with 10 seconds residence time at 800 °C with a. SEM image b. Silicon mapping c. Potassium mapping d. Calcium mapping.

Figure 4.11 presents the SEM image of RDF HHR char with 15 minutes residence time and the corresponding heat maps generated by the MATLAB program. The image was divided into a 10X10 grid of 100 equal sized rectangles. The heat map of the grid shows that the potassium is well distributed across the entire surface with the lighter

rectangles indicating the density of particles in each section. The few dark areas in the heat map correspond to the regions with shadows in the SEM. These regions are not in focus and thus do not contribute any data. In contrast, the presence of bright rectangles at the center of the silicon heat map signifies that silicon is concentrated in those spots compared to the rest of the image surface. Thus, silicon is restricted to one particle on the SEM image, which is possibly rubber char. By comparing the potassium and silicon heat maps we can conclude that potassium is distributed to even the silicon rich particle indicating redistribution with 15 minutes residence time. This is confirmed with the quantitative analysis of the number of particles in each rectangle which is reported as the percentage of area occupied by the dots in each region in Table 4.3.

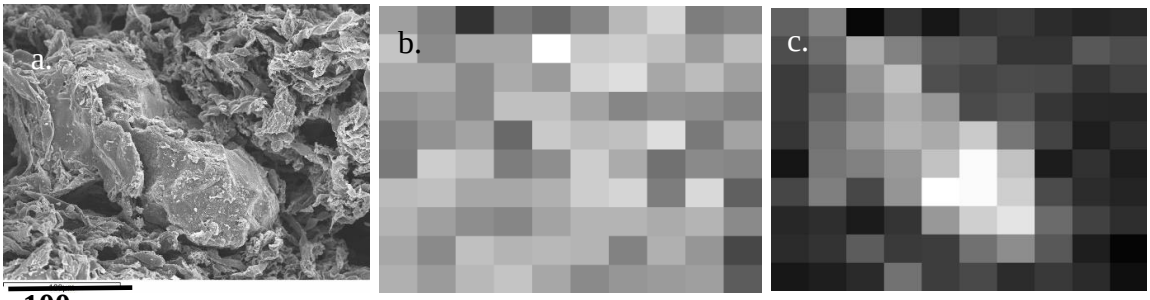

Figure 4.11. RDF HHR char with 15 minutes and annealing at 800 °C a. SEM image b. Potassium heat map c. Silicon heat map (Heat maps generated by MATLAB program).

The area covered by the dots in each of the rectangles in potassium heat map (Table 4.3 a) was evenly distributed across the whole surface. The average of the occupied area was about 1.91 with a standard deviation of 0.404. This led to a coefficient of variation (σ/μ) of 0.211. On the other hand, the average of the area occupied in each of the rectangles of silicon heat map (Table 4.3 b) was about 6.31 with a standard deviation of 4.18 resulting in a coefficient of variation of 0.662. This variation clearly shows that silicon is restricted

to the particle in the center while potassium is well distributed across the surface. The highlighted values in both the tables indicate the position of the silicon rich particle. Comparison of the corresponding areas of potassium and silicon of these highlighted rectangles shows that potassium is equally abundant in the silicon-rich spots.

Table 4.3. Percentage area covered by dots in each rectangle of the MATLAB generated 10X10 grid of a. potassium heat map b. silicon heat map of RDF HHR char with 15 minutes residence time and 800 °C

a.	C1	C2	C3	C4	C5	C6	C7	C8	C9	C10
R1	1.9	1.5	0.59	1.43	1.2	1.6	2.2	2.5	1.5	1.6
R2	2.3	1.6	**2.0**	**2.0**	3.0	2.4	2.4	2.3	1.8	2.2
R3	2.0	2.0	**1.6**	**2.0**	1.8	2.5	2.6	2.0	2.2	1.9
R4	1.7	1.8	**1.6**	**2.3**	**2.3**	1.9	1.6	1.7	1.7	1.5
R5	1.5	1.7	**1.9**	**1.2**	**2.4**	**2.2**	2.3	2.6	1.4	1.9
R6	1.4	2.4	**2.3**	**1.5**	**1.7**	**2.4**	**2.0**	1.3	1.6	1.6
R7	2.2	2.3	2.0	**2.0**	**2.1**	**2.4**	**2.5**	1.5	2.6	1.1
R8	2.1	1.9	1.7	1.6	**1.9**	**2.1**	**2.1**	2.0	2.1	1.6
R9	2.0	1.6	2.3	2.1	2.2	2.1	**1.5**	2.1	1.8	0.8
R10	2.1	1.8	2.2	2.3	2.0	1.6	1.8	1.8	1.9	1.1

b.	C1	C2	C3	C4	C5	C6	C7	C8	C9	C10
R1	6.8	9.2	0.6	3.6	1.6	3.8	4.1	3.1	2.5	2.8
R2	5.4	7.5	**12.1**	**9.1**	6.2	5.8	3.7	3.7	6.2	5.4
R3	4.1	6.1	**10.4**	**13.4**	5.5	4.8	5.2	5.1	3.6	4.5
R4	4.1	7.1	**9.3**	**12.1**	**10.6**	5.2	5.8	3.8	2.8	2.7
R5	3.7	7.9	**10.6**	**12.6**	**11.9**	**14.2**	8.2	4.7	2.1	3.3
R6	1.5	8.3	**9.0**	**10.7**	**13.6**	**17.6**	**13.6**	2.0	3.4	2.1
R7	4.9	8.9	5.0	**10.4**	**17.9**	**17.6**	**14.5**	5.3	3.1	2.5
R8	2.7	3.3	1.9	3.6	**10.7**	**14.5**	**16.0**	7.5	4.5	3.2
R9	3.0	3.6	6.4	4.1	4.2	7.9	**9.9**	6.2	2.1	0.3
R10	1.6	2.1	3.0	8.0	4.3	5.1	3.1	4.0	3.0	1.0

The SEM image of RDF HHR char with 10 seconds residence time was processed similarly with the MATLAB program to generate heat maps for potassium and silicon as

shown in Figure 4.12. The heat map of the grid shows that the potassium is concentrated at the center while it is lower at the corners. It is proposed that the amount of time (10 seconds) that the char was exposed to high temperatures was insufficient for complete potassium redistribution on the surface. The silicon heat map indicates that silicon is restricted to the single particle at the edge of the SEM image. By comparing the potassium and silicon heat maps, it can be deduced that the silicon rich particle shows a very low amount of potassium. To confirm these observations quantitatively, the percentage area covered by the dots in each rectangle is reported in Table 4.4 similar to the RDF HHR char with 15 minutes residence time.

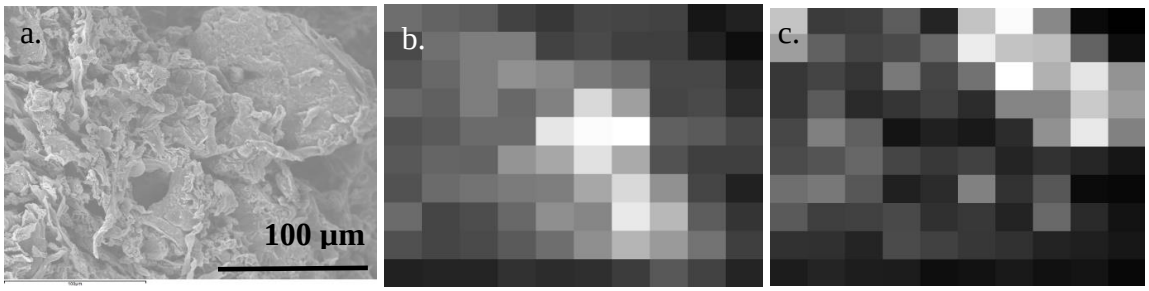

Figure 4.12. RDF HHR char with 10 seconds and annealing at 800 °C a. SEM image b. Potassium heat map c. Silicon heat map (Heat maps generated by MATLAB program).

The highest area covered by the rectangles in the potassium heat map (Table 4.4 a) was concentrated in the central region (highlighted in blue). The average of the occupied area in all the rectangles was about 1.82 with a standard deviation of 0.935. This resulted in a coefficient of variation (σ/μ) of 0.514 which is higher than the value observed for the longer residence time RDF HHR char. For the silicon heat map, the average area occupied by the dots in all the rectangles (Table 4.4 b) was calculated to be 3.31 with a standard deviation of 2.508 with a resultant coefficient of variation of 0.759. Thus, silicon has a high

coefficient of variation and is confined to a single particle, similar to the observation made with longer residence time char. However, potassium is also restricted to the particle in the center (highlighted in blue) and does not show redistribution to the silicon-rich area (highlighted in red). This confirms that 10 seconds at 800 °C is not enough time for complete redistribution of potassium across the entire surface.

Table 4.4. Percentage area covered by dots in each rectangle of the MATLAB generated 10X10 grid of a. potassium heat map b. silicon heat map of RDF HHR char with 10 seconds residence time and 800 °C

a.	C1	C2	C3	C4	C5	C6	C7	C8	C9	C10
R1	2.0	1.8	1.7	1.2	1.0	**1.3**	**1.2**	**1.2**	0.4	0.6
R2	1.3	2.0	2.3	2.3	1.2	**1.3**	**1.1**	**1.1**	0.6	0.2
R3	1.6	1.9	2.3	2.6	2.5	2.2	**2.0**	**1.3**	**1.3**	**0.7**
R4	1.9	1.7	2.3	1.9	2.3	3.9	**2.9**	**1.2**	**1.3**	**0.8**
R5	1.5	1.6	1.9	1.9	**4.1**	**4.5**	**4.6**	**1.7**	**1.6**	**1.3**
R6	1.6	1.8	1.8	**2.7**	**3.0**	**4.0**	**3.1**	1.5	1.13	1.1
R7	1.5	1.9	2.1	2.2	2.3	**3.0**	**3.9**	2.6	1.23	0.6
R8	1.9	1.2	1.4	1.9	2.6	2.4	**4.2**	**3.3**	1.68	0.9
R9	1.4	1.2	1.3	1.6	2.0	2.6	**3.3**	**2.8**	2.07	1.1
R10	0.6	0.6	0.6	0.9	0.8	0.8	1.1	1.6	1.18	0.6

b.	C1	C2	C3	C4	C5	C6	C7	C8	C9	C10
R1	8.1	2.4	2.6	3.9	1.5	**8.0**	**10.4**	**5.6**	0.4	0.0
R2	6.5	4.0	2.8	3.1	4.2	**9.7**	**8.0**	**7.8**	4.1	0.6
R3	2.3	2.8	2.2	5.0	2.9	4.7	**10.5**	**7.3**	**9.4**	**6.1**
R4	2.3	3.8	1.7	2.2	2.7	1.8	**5.5**	**5.5**	**8.3**	**6.5**
R5	2.9	5.3	3.9	0.8	1.3	1.0	1.8	**6.0**	**9.6**	**5.3**
R6	3.1	3.5	4.2	2.9	2.3	2.7	1.5	2.1	1.6	0.9
R7	4.6	4.9	3.6	1.3	1.8	5.3	2.1	3.6	0.4	0.3
R8	3.7	2.6	2.7	3.0	2.0	2.3	1.4	4.3	1.7	0.8
R9	2.0	2.0	1.5	3.1	2.7	2.3	2.0	1.4	1.3	0.9
R10	1.1	1.5	1.2	1.1	0.6	0.7	1.0	0.7	0.8	0.3

4.3.2.4 Type of carbon present in different heating rate and residence time chars

The carbon structure present in the chars has been found to be affected by the type of thermal treatment used to generate the chars [7,28]. Only one band is produced in the Raman spectra of perfect graphite, at about 1580 cm^{-1} (called the G band), that corresponds to the stretching vibration mode with E_{2g} symmetry in the aromatic layers of the graphite crystal [29]. As the perfect graphitic carbon changes into unstructured carbon, additional bands induced by the defects in the microcrystalline lattices emerge around 1150 - 1200, 1350, 1500 - 1530, and 1620 cm^{-1} [30]. The 1350 cm^{-1} band is called the D1 band, which corresponds to a graphitic lattice vibration mode with A_{1g} symmetry and is indicative of the in-plane imperfections such as defects and heteroatoms [31]. The 1620 cm^{-1} band, called the D2 band, is the result of a lattice vibration similar to the G band but involving graphene layers which are not directly sandwiched between two other graphene layers [29]. The defect band, D3, corresponding to the amorphous sp^2 bonded carbon, such as organic molecules in poorly organized materials with 3 – 5 rings. It appears between 1500 – 1530 cm^{-1}. This is expected to be the primary type of carbon that contributes to char reactivity [29,31]. The defect band between 1150 – 1200 cm^{-1} is indicative of very poorly ordered materials (sp^2 and sp^3 hybridized carbon bonds, C–C and C=C stretching vibrations of polyenes) and is called D4 [32]. A combination of all the bands results in a composite Raman spectrum that needs to be deconvoluted.

Several band combinations for spectral analysis were considered in the literature, and a combination of four Lorentzian-shaped bands (G, D1, D2, D4) and a Gaussian-shaped band (D3) was found to be the best combination for the 5-peak analysis [29,31]. Thus, the same band shapes were utilized in this study. Since band area is a function of the

peak intensity and the full width at half maximum (FWHM), using only the intensity ratio may not fully represent the evolution of a band. Thus, to characterize the carbon structure completely and to enable comparison between different samples, band area ratios have been utilized. Since RDF char is a combination of 8 different components, multiple spectra for each char sample were obtained and deconvoluted separately. An average of the band ratios for the different spectra of each char sample were used for comparison.

The band ratios of I_{D1}/I_G, I_{D3}/I_G and I_G/I_{all} have been used to represent the extent of graphitization of the carbon present in each of the char samples. The values for the band ratios of the chars produced at different heating rates and residence times are presented in Table 4.5. The decrease of I_{D1}/I_G and I_{D3}/I_G ratios with increasing residence time for HHR chars indicates the transformation of the amorphous carbon into crystalline form as it is exposed to high temperatures for a longer time. The lower I_{D1}/I_G and I_{D3}/I_G ratios for the LHR char compared to HHR char are probably due to the longer exposure of the char to high temperatures as it cools down slowly as compared to the HHR chars which are removed from the high temperature immediately after their respective exposure times. This implies a more organized char structure is formed with increasing exposure time. The small increase in the I_G/I_{all} ratio with increasing residence time at high temperatures also supports this argument. More organized carbon present in the RDF HHR char with 15 minutes residence time and LHR char is thus expected to result in lower reactivity compared to the HHR char with 10 seconds residence time.

Table 4.5. Raman spectral data of RDF chars produced at different heating rates and residence times

	RDF HHR char 10 seconds	RDF HHR char 15 minutes	RDF LHR char
I_{D1} / I_G	5.64	4.38	3.88
I_{D3} / I_G	1.61	1.27	1.05
I_G / I_{all}	0.100	0.106	0.109

4.3.3 Gasification reactivity of different heating rate and residence time pellets

4.3.3.1 CO_2 gasification reactivity of different heating rate and residence time pellets

RDF HHR chars generated at a high heating rate (~ 58 K/s) with varying residence times along with the low heating rate (20 K/min) RDF char were considered to understand the changes in the CO_2 gasification reactivity as a result of varying pyrolysis conditions. All the char samples were heated again in the TGA at 20 K/min to 800 °C in N_2 with a 15 minutes hold to stabilize the weight, before exposing the sample to CO_2. The reproducibility of these runs was verified by running multiple samples at the same conditions. The degree of overlap suggested more than 95% reproducibility.

The time taken to achieve complete conversion of the char in CO_2 is presented in Figure C.5. High heating rate (HHR) char samples generated at different residence times of 15 minutes and 10 seconds take around the same time (~ 90 minutes) to achieve 95% conversion. However, the low heating rate (LHR) char takes longer (124 minutes) to reach the same conversion level. The high heating rate RDF char generated at 10 seconds did not exhibit complete potassium redistribution unlike the HHR char generated at 15 minutes as discussed in section 4.3.2.3. Nevertheless, during gasification in the TGA, all the char

samples are subjected to a low heating rate (20 K/min) ramp to the reaction temperature of 800 °C before introducing CO_2. This temperature program is expected to have achieved the required potassium redistribution across the surface for all the samples. Thus, the difference in the overall conversion time of the HHR and LHR char samples is suspected to be a result of other char properties like surface areas and elemental composition.

Gasification reactivities of the three chars varying with increasing conversion is shown in Figure 4.13. Reactivity trends of the two heating rate chars showed that the overall reactivity of the char samples generated at HHR at both residence times show a reactivity increase compared to the LHR char. Comparison of the high heating rate chars generated at different residence times of 10 seconds and 15 minutes indicates that the reactivity of the 10 seconds char is higher than the 15 minutes char at lower conversion levels. This reactivity of the lower residence time char drops below the higher residence time char around 50% conversion, beyond which the higher residence time char has higher reactivity. This trend exhibited more than 90% reproducibility and thus is not considered an artifact. As the differences in the inorganic content and distribution levels are minimal between the char samples, surface areas, H/C ratios, O/C ratios, the type of carbon present, or a combination of these properties are expected to play a role in determining the reactivities of different char samples [11,22,33].

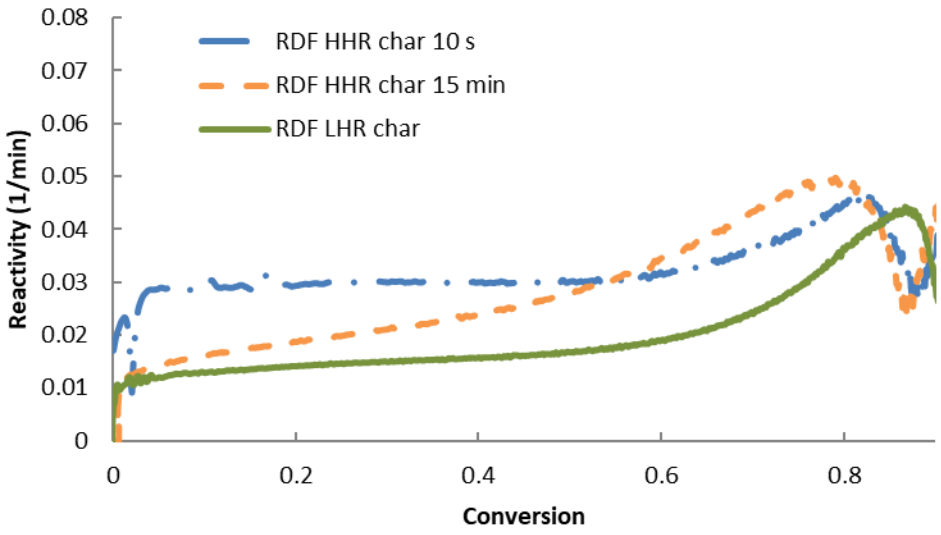

Figure 4.13. CO_2 gasification reactivities of different heating rate and residence time RDF chars annealed at 800 °C.

One reason for the higher reactivity of the HHR chars could be a higher number of active sites created due to rapid pyrolysis that prevents the re-polymerization of heavier aromatics (which have a low H/C ratio) [33]. Since the feed material for all of the chars is the same, the differences with the inorganic content of the chars is minimal. Thus, surface areas of the chars are also expected to have a major influence on the gasification reactivity. Finally, the type of carbon present in each of the chars may still be different at the beginning of the gasification. Therefore, initial char gasification reactivity could be affected by the extent of graphitization of the carbon present. These relationships are further explored in the next section to explain the variation in the char reactivities with changing conversion level.

4.3.3.2 Relationship of surface areas, elemental composition and type of carbon with gasification reactivities

The CO_2 gasification reactivities of the RDF char generated at low heating rate, high heating rate with 15 minutes residence time, and high heating rate with 10 seconds residence time were considered in three ways. The first was an averaged reactivity over 20 – 80% conversion level, also termed overall reactivity. The second is the reactivity at 50% conversion, considered to be a good indicator of the average reactivity value [34,35]. The third is the initial reactivity as defined in this study as the reactivity at 10% conversion level. The three versions of the CO_2 gasification reactivities of the three char samples were plotted as a function of several different char parameters in Figure 4.14.

The first char property that was considered was the H/C ratio. This was derived from the elemental composition of each of the chars discussed in section 4.3.2.2. The H/C ratio has been used as an indicator of the amorphous, more reactive carbon [22,33,36]. Thus, for a higher H/C ratio the gasification reactivity will be greater. However, in this study the H/C ratio failed to capture the reactivity trend at 50% conversion as well as the average of 20 – 80% conversion (Figure 4.14 a). Although it shows a certain linear relationship with the char reactivities at initial conversion (10% conversion), O/C ratio is more successful in capturing the initial reactivities (10% conversion) of the three chars in a linear trend with a high R^2 fit (Figure 4.14 b).

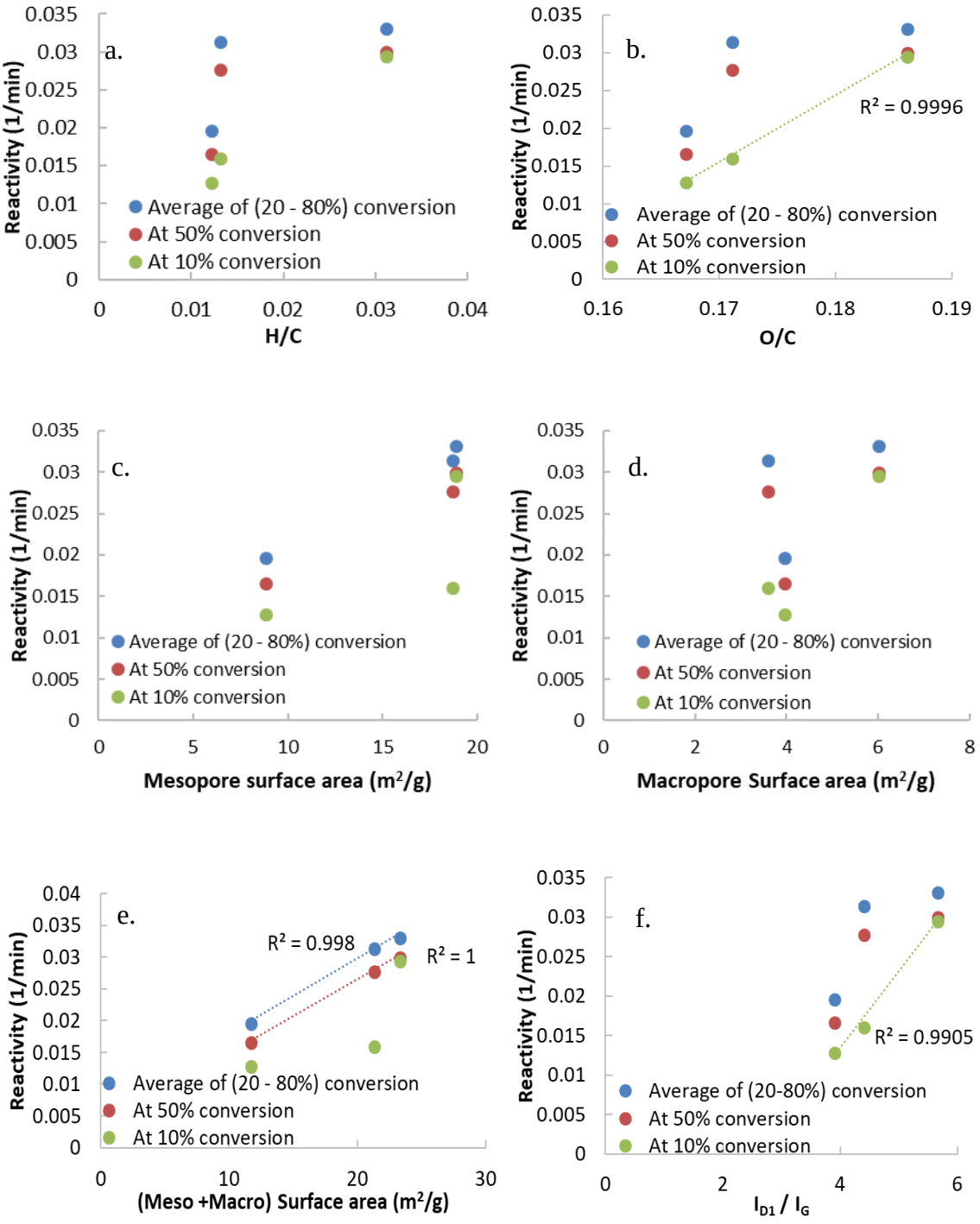

Figure 4.14. Variation of CO_2 gasification reactivity of different heating rate and residence time RDF chars annealed at 800 °C as a function of a. H/C ratio b. O/C ratio c. Mesopore surface area d. Macropore surface area e. Mesopore and Macropore surface area f. I_{D1} / I_G band ratio.

O/C is considered to be an indicative parameter of more amorphous carbon [37,38]. At higher residence time, the char is expected to become very carbonaceous and the disordered aromatic sheets start aligning. Oxygen present in high residence time and high temperature chars is reported to be present in the form of stable ether linkages that act as cross-links between the aromatic sheets [38]. Lack of oxygen atoms can thus be considered as an indicator of a higher degree of graphitization. The role of oxygen atoms could also be to provide reactive sites in the char structure. In prior research [36] as well as in Chapter 3, it was concluded that the oxygen present in the char is directly involved in the gasification reaction. This is supported by the linear correlation of the initial CO_2 reactivities of all the chars with the O/C ratio.

As noted in section 4.3.1.1, the chars generated from high heating rate pyrolysis were extremely macroporous and thus mercury porosimetry was utilized to measure the macroporous (> 50 nm) and mesoporous surface area (2 – 50 nm) of the chars. Studies have shown that the increase in the pore volume is primarily a result of an increase in the mesopores and macropores, as opposed to the micropores during the gasification process [39–41]. In these studies, neither the size nor the number of micropores changed significantly throughout the reaction. They found that there is only a slight widening of the micropores in the beginning followed by a significant increase in mesoporosity and macroporosity as the conversion increased [39]. Since micropore volume contributes heavily to the calculation of the total surface areas, the basis for normalization of intrinsic reaction rates is suggested to be focused on the mesoporous and macroporous volumes [41].

Figure 4.14 c shows the relationship of CO_2 gasification reactivity with the mesoporous surface area as measured by mercury porosimetry. Mesoporous surface area alone fails to explain the reactivity changes, similar to the macroporous surface area alone in Figure 4.14 d. However, when the reactivity of the three chars was plotted against a combination of mesoporous and macroporous surface areas, the overall reactivity (both at 50% conversion and average of 20 – 80% conversion) showed a highly linear trend as seen in Figure 4.14 e [39,41]. Finally, the type of carbon present in each of the chars was considered to explain the gasification reactivity trends. The ratio of I_{D1} / I_G was found to be a good indicator of the char microstructure order and was chosen to represent the amorphous or the reactive carbon present in the char samples [29]. Figure 4.14 f presents a linear trend for the reactivity at 10% conversion of all the chars. This suggests that although the type of carbon influences the initial reactivity, with increasing exposure time at high temperature, the carbon structure in all the chars becomes similar and no longer plays a role in the overall gasification reactivity.

Therefore, based on the relationship of the gasification reactivity with different char properties, it is concluded that the initial reactivity trend was very well related to the O/C ratio and the band ratio I_{D1} / I_G, while the overall reactivity showed a highly linear relationship with the combination of mesopore and macropore surface areas. Nonetheless, it should be noted that a correlation is not necessarily causation. It is possible that some or all of these parameters are playing a role and interrelationships could exist between the parameters themselves.

4.4 Conclusions

High heating rate (HHR) char was more macroporous than the low heating rate (LHR) char. Large crater like openings on HHR char are indicative of sudden release of volatiles as the feed was exposed to high temperatures. The morphological evolution of the chars as the temperature increased to 800 °C was studied by examining the chars generated at intermediate temperatures in both LHR and HHR conditions. Although melting and pore evolution were observed with both the chars at 250 °C and 400 °C, the major difference was the absence of large macropores and lower overall porosity of the LHR char compared to the HHR char. Char morphological evolution was similar at 10 seconds residence time as compared to 15 minutes residence time char at high heating rates. This confirmed that rapid release of volatiles occurs immediately when the char is exposed to high temperatures. However, the vertical expansion of the pellet was higher at 10 seconds residence time indicating that complete volatile release has not yet occurred due to shorter exposure time. Based on the elemental analysis, the higher amount of hydrogen present in low residence time HHR char is expected to be a result of incomplete de-volatilization during the short exposure time.

Both LHR char and HHR char with 15 minutes residence time exhibited similar inorganic distribution across the surface. However, at a low residence time of 10 seconds, HHR char displayed incomplete potassium distribution on the surface compared to 15 minutes residence time char. A new MATLAB code was introduced to quantify the EDX maps. The insufficient potassium distribution in the lower residence time HHR char was confirmed by the quantitative comparison of the heat maps. Raman analysis revealed that

the amorphous carbon increased as the residence time of the char at high temperatures decreased.

RDF HHR char at both residence times had higher CO_2 gasification reactivity than the LHR char. Longer residence time HHR char had lower initial reactivity than shorter residence time char. However, the reactivity trend is reversed at higher conversions. This variation in the reactivity was explained with the use of several different char parameters. Although potassium distribution varied for the two residence time chars, the heat-up phase before the gasification at 800 °C would have ensured similar potassium distribution in the lower residence time char. Instead, the O/C content and the band ratio I_{D1}/ I_G were found to be good indicators for the initial reactivity of these chars, while, a combination of macroporous and mesoporous surface area related very well with the overall reactivity of all the chars.

4.5 References

[1] The end of fossil fuels, Ecotricity. (2017). https://www.ecotricity.co.uk/our-green-energy/energy-independence/the-end-of-fossil-fuels (accessed February 12, 2018).

[2] G.A. Florides, P. Christodoulides, Global warming and carbon dioxide through sciences, Environ. Int. 35 (2009) 390–401. http://dx.doi.org/10.1016/j.envint.2008.07.007.

[3] US Environmental Protection Agency, Municipal Solid Waste Generation , Recycling , and Disposal in the United States : Facts and Figures for 2012, (2012) 1–14.

[4] M. McHenry, Waste to Energy Technologies, Murdoch Univ. (2006). http://www.see.murdoch.edu.au/resources/info/Tech/waste/ (accessed December 3, 2015).

[5] I.I. Ahmed, A.K. Gupta, Pyrolysis and gasification of food waste: Syngas characteristics and char gasification kinetics, Appl. Energy. 87 (2010) 101–108. http://linkinghub.elsevier.com/retrieve/pii/S0306261909003523.

[6] K. Mitsuoka, S. Hayashi, H. Amano, K. Kayahara, E. Sasaoaka, M.A. Uddin, Gasification of woody biomass char with CO_2: The catalytic effects of K and Ca species on char gasification reactivity, Fuel Process. Technol. 92 (2011) 26–31. http://linkinghub.elsevier.com/retrieve/pii/S0378382010002791.

[7] P. Lahijani, Z.A. Zainal, A.R. Mohamed, M. Mohammadi, CO_2 gasification reactivity of biomass char: Catalytic influence of alkali, alkaline earth and transition metal salts, Bioresour. Technol. 144 (2013) 288–295. http://dx.doi.org/10.1016/j.biortech.2013.06.059.

[8] K. Umeki, A. Moilanen, A. Gómez-Barea, J. Konttinen, A model of biomass char gasification describing the change in catalytic activity of ash, Chem. Eng. J. 207–208 (2012) 616–624. http://dx.doi.org/10.1016/j.cej.2012.07.025.

[9] S. Luo, B. Xiao, Z. Hu, S. Liu, Effect of particle size on pyrolysis of single-component municipal solid waste in fixed bed reactor, Int. J. Hydrogen Energy. 35 (2010) 93–97. http://linkinghub.elsevier.com/retrieve/pii/S0360319909016462.

[10] J. Zheng, Y.-Q. Jin, Y. Chi, J.-M. Wen, X.-G. Jiang, M.-J. Ni, Pyrolysis characteristics of organic components of municipal solid waste at high heating rates., Waste Manag. 29 (2009) 1089–1094. http://dx.doi.org/10.1016/j.wasman.2008.06.034.

[11] E. Cetin, B. Moghtaderi, R. Gupta, T.. Wall, Influence of pyrolysis conditions on the structure and gasification reactivity of biomass chars, Fuel. 83 (2004) 2139–2150. http://linkinghub.elsevier.com/retrieve/pii/S0016236104001437.

[12] E. Cetin, R. Gupta, B. Moghtaderi, Effect of pyrolysis pressure and heating rate on radiata pine char structure and apparent gasification reactivity, Fuel. 84 (2005) 1328–1334.

[13] E. Biagini, M. Simone, L. Tognotti, Characterization of high heating rate chars of biomass fuels, Proc. Combust. Inst. 32 II (2009) 2043–2050. http://dx.doi.org/10.1016/j.proci.2008.06.076.

[14] M. Guerrero, M.P. Ruiz, M.U. Alzueta, R. Bilbao, A. Millera, Pyrolysis of eucalyptus at different heating rates: Studies of char characterization and oxidative reactivity, J. Anal. Appl. Pyrolysis. 74 (2005) 307–314.

[15] W.T. Tsai, M.K. Lee, Y.M. Chang, Fast pyrolysis of rice husk: Product yields and compositions, Bioresour. Technol. 98 (2007) 22–28. doi:10.1016/j.biortech.2005.12.005.

[16] Y. Xue, S. Zhou, R.C. Brown, A. Kelkar, X. Bai, Fast pyrolysis of biomass and waste plastic in a fluidized bed reactor, Fuel. 156 (2015) 40–46. doi:10.1016/j.fuel.2015.04.033.

[17] G.M. Savage, Thermal conductivity and specific heat of densified refuse derived

fuel, Waste Manag. Res. 7 (1989) 83–92. doi:10.1177/0734242X8900700109.

[18] A.O. Oyedun, T. Gebreegziabher, C.W. Hui, Co-pyrolysis of biomass and plastics waste: A modelling approach, Chem. Eng. Trans. 35 (2013) 883–888. doi:10.3303/CET1335147.

[19] Energy Dispersive X-Ray Microanalysis (EDX / EDS) | Anderson Materials Evaluation, Inc., Andreson Mater. Eval. Inc. (2016). http://www.andersonmaterials.com/edx-eds.html (accessed January 26, 2016).

[20] M.B. Haysom, Z.A. Ostatek-Boczynski, Rapid, Wet Oxidation Procedure for the Estimation of Silicon in Plant Tissue, Commun. Soil Sci. Plant Anal. 37 (2006) 2299–2306. doi:10.1080/00103620600819420.

[21] A. Trubetskaya, P.A. Jensen, A.D. Jensen, M. Steibel, H. Spliethoff, P. Glarborg, Influence of fast pyrolysis conditions on yield and structural transformation of biomass chars, Fuel Process. Technol. 140 (2015) 205–214. doi:10.1016/j.fuproc.2015.08.034.

[22] K.M. McDonald, W.D. Hyde, W.C. Hecker, Low temperature char oxidation kinetics: effect of preparation method, Fuel. 71 (1992) 319–323. doi:10.1016/0016-2361(92)90081-X.

[23] L.R. Radović, P.L. Walker, R.G. Jenkins, Effect of lignite pyrolysis conditions on calcium oxide dispersion and subsequent char reactivity, Fuel. 62 (1983) 209–212.

[24] T. Wigmans, H. Haringa, J.A. Moulijn, Role of the influence of potassium during pyrolysis of medium volatile coal, Fuel. 63 (1984) 870–872. doi:10.1016/0016-2361(84)90085-1.

[25] D.A. Sams, T. Talverdian, F. Shadman, Kinetics of catalyst loss during potassium-catalysed CO_2 gasification of carbon, Fuel. 64 (1985) 1208–1214. doi:10.1016/0016-2361(85)90176-0.

[26] M.P. Kannan, G.N. Richards, Gasification of biomass chars in carbon dioxide : dependence of gasification rate on the indigenous metal content, Fuel. 69 (1990) 747–753.

[27] M. Jiang, J. Hu, J. Wang, Calcium-promoted catalytic activity of potassium carbonate for steam gasification of coal char: Effect of hydrothermal pretreatment, Fuel. 109 (2013) 14–20. http://dx.doi.org/10.1016/j.fuel.2012.06.100.

[28] H. Wu, K. Yip, F. Tian, Z. Xie, C. Li, Evolution of char structure during the steam gasification of biochars produced from the pyrolysis of various mallee biomass components.pdf, (2009) 10431–10438.

[29] C. Sheng, Char structure characterised by Raman spectroscopy and its correlations with combustion reactivity, Fuel. 86 (2007) 2316–2324.

[30] O. Beyssac, B. Goffé, J.P. Petitet, E. Froigneux, M. Moreau, J.N. Rouzaud, On the characterization of disordered and heterogeneous carbonaceous materials by Raman spectroscopy, Spectrochim. Acta - Part A Mol. Biomol. Spectrosc. 59 (2003) 2267–2276. doi:10.1016/S1386-1425(03)00070-2.

[31] A. Sadezky, H. Muckenhuber, H. Grothe, R. Niessner, U. Poschl, Raman microspectroscopy of soot and related carbonaceous materials : Spectral analysis and structural information, Carbon N. Y. 43 (2005) 1731–1742. doi:10.1016/j.carbon.2005.02.018.

[32] X. Li, J. Hayashi, C. Li, FT-Raman spectroscopic study of the evolution of char structure during the pyrolysis of a Victorian brown coal, Fuel. 85 (2006) 1700–1707. doi:10.1016/j.fuel.2006.03.008.

[33] C. Fushimi, K. Araki, Y. Yamaguchi, A. Tsutsumi, Effect of heating rate on steam gasification of biomass. 1. Reactivity of char, Ind. Eng. Chem. Res. 42 (2003) 3922–3928. doi:10.1021/ie030056c.

[34] C. Guizani, F.J. Escudero Sanz, S. Salvador, The gasification reactivity of high-heating-rate chars in single and mixed atmospheres of H_2O and CO_2, Fuel. 108 (2013) 812–823. doi:10.1016/j.fuel.2013.02.027.

[35] M. Perander, N. DeMartini, A. Brink, J. Kramb, O. Karlström, J. Hemming, A. Moilanen, J. Konttinen, M. Hupa, Catalytic effect of Ca and K on CO_2 gasification of spruce wood char, Fuel. 150 (2015) 464–472. doi:10.1016/j.fuel.2015.02.062.

[36] S. Li, A. Sanna, J.M. Andresen, Influence of temperature on pyrolysis of recycled organic matter from municipal solid waste using an activated olivine fluidized bed, Fuel Process. Technol. 92 (2011) 1776–1782. doi:10.1016/j.fuproc.2011.04.026.

[37] G. Newalkar, K. Iisa, A.D. D'Amico, C. Sievers, P. Agrawal, Effect of temperature, pressure, and residence time on pyrolysis of pine in an entrained flow reactor, Energy & Fuels. 28 (2014) 5144–5157. http://dx.doi.org/10.1021/ef5009715.

[38] J. Pastor-Villegas, C.J. Durán-Valle, C. Valenzuela-Calahorro, V. Gómez-Serrano, Organic chemical structure and structural shrinkage of chars prepared from rockrose, Carbon N. Y. 36 (1998) 1251–1256. doi:10.1016/S0008-6223(97)00200-5.

[39] I. Aarna, E.M. Suuberg, Changes in reactive surface area and porosity during char oxidation, Symp. Combust. 27 (1998) 2933–2939.

[40] L.R. Radovic, L.P.J. Walker, R.G. Jenkins, Importance of carbon active sites in the gasification of coal chars, Fuel. 62 (1983) 849–856.

[41] F. Mermoud, S. Salvador, L. Van de Steene, F. Golfier, Influence of the pyrolysis heating rate on the steam gasification rate of large wood char particles, Fuel. 85 (2006) 1473–1482. doi:10.1016/j.fuel.2005.12.004.

CHAPTER 5. ENHANCING THE CARBON RECOVERY IN THE GAS FRACTION AND REDUCING THE TAR CONTENT IN THE BUBBLING FLUIDIZED BED REACTOR (BFBR) GASIFICATION OF MODEL RDF PELLETS

5.1 Background

In Chapter 4, the various differences in the char physicochemical properties and its gasification reactivity as a function of heating rate were examined. While chapters 2 and 3 focused on the fundamental analysis of the RDF gasification through TGA studies at low heating rate, this chapter will discuss the industrially relevant high heating rate gasification of RDF pellets in a Bubbling Fluidized Bed Reactor (BFBR).

The possibility of carrying out both pyrolysis and gasification in a continuous flow process makes BFBR an attractive choice. In a BFBR, the superficial gas velocity is usually several times larger than the minimum fluidization velocity that causes the drag forces on the particles to equal the weight of the particles in the bed and gives it a fluid-like behavior [1]. This fluid-like state produces intense mixing and promotes high gas–solid contact that results in high heat and mass transfer rates [2,3]. Moreover, a BFBR provides good process flexibility by accommodating variations in the fuel type and quality and by use of different fluidizing agents. The ability to modify the reactor temperatures and gas residence times, to add reagents along the reactor height and to operate with or without a specific catalyst make BFBR particularly suitable for gasification [4–6].

BFBR is usually operated below 900 °C to avoid ash melting and sintering that can cause bed de-fluidization [1,7]. Moreover, BFBR gasification is beneficial to increase the feed- to- syngas conversion efficiency [8]. Air and steam are the most common gasifying agents used in fluidized bed processing of organic solids [9–12]. However, oxygen is sometimes used instead of air in order to decrease the amount of nitrogen present in the product gas which would otherwise require an additional separation step downstream [13,14]. The disadvantage of using oxygen or steam is that they are more expensive than air even though they produce a more valuable product gas. The selection of a particular gasifying agent thus depends on the economics of the feed material and the reactor under consideration.

During gasification, tars and polyaromatic hydrocarbons (PAHs) are released along with the gas which can cause environmental and operational issues [15,16]. The continuous build-up of condensable organic compounds has been one of the main concerns for industrially operated fluidized bed reactors since in addition to plugging the downstream lines, valuable carbon is lost in the depositions which could otherwise be recovered in the gas fraction [17,18]. Two approaches for the reduction of tar formation are categorized as primary clean-up and secondary clean-up. Primary clean-up involves modification of the experimental conditions inside the reactor to obtain less tar (including use of an in-bed catalyst) [15,19,20]. Alternatively, in secondary clean-up, the gas fraction along with the condensable volatiles is introduced into a secondary reactor to separate the tars using various techniques (thermal or catalytic tar cracking, tar reforming and wet scrubbing) [17,21,22]. Although secondary clean-up methods have proven to be very effective, they might not always be economically viable and will require high energy input

when very low tar content is desired in the downstream processing [17]. Hence, it is beneficial to utilize primary clean-up methods to reduce the load on secondary clean-up techniques. This can be done by optimizing the gasifier performance in the BFBR by reducing the tar content and maximizing the carbon recovery in the gas fraction.

The present study intends to achieve higher carbon recovery in the gas fraction by modifying the BFBR experimental conditions (primary clean-up technique). Two types of feed, pine powder and RDF pellets, were gasified in a custom designed BFBR with three stages. Steam and CO_2 were used as the gasifying agents around 800 °C with further modification of experimental conditions for steam gasification of RDF pellets. Although dolomite and olivine have been effective tar reduction catalysts for biomass gasification, studies have found that they are rather inactive for RDF and other waste derived feed gasification studies [15,17]. Thus, only the gasification temperature and the gasifying medium were altered to identify conditions for highest carbon recovery in the gas fraction with reduced tar formation.

5.2 Materials and methods

5.2.1 BFBR construction

A new reactor design is introduced to separate the particles at different stages of gasification in the fluidized bed. The designed fluidized bed reactor has three stages with increasing diameter to separate particles based on their density. The three stages are intended for pyrolysis in the bottom zone, gasification of char in the middle zone and disengagement for ash removal in the top zone. Figure 5.1 shows a schematic of the designed three stage fluidized bed reactor with dimensions. The feed that enters the reactor

from the bottom undergoes pyrolysis in the bottom zone and releases volatiles. Lower density char rises up into the larger diameter middle zone and is gasified by the gasifying agent (CO_2 /steam) that is also the fluidizing medium. The middle zone has the highest axial length to achieve complete gasification by providing sufficient residence time for the char particles. Following complete gasification, lowest density ash particles rise up into the disengagement zone and leave the reactor along with the fluidization medium.

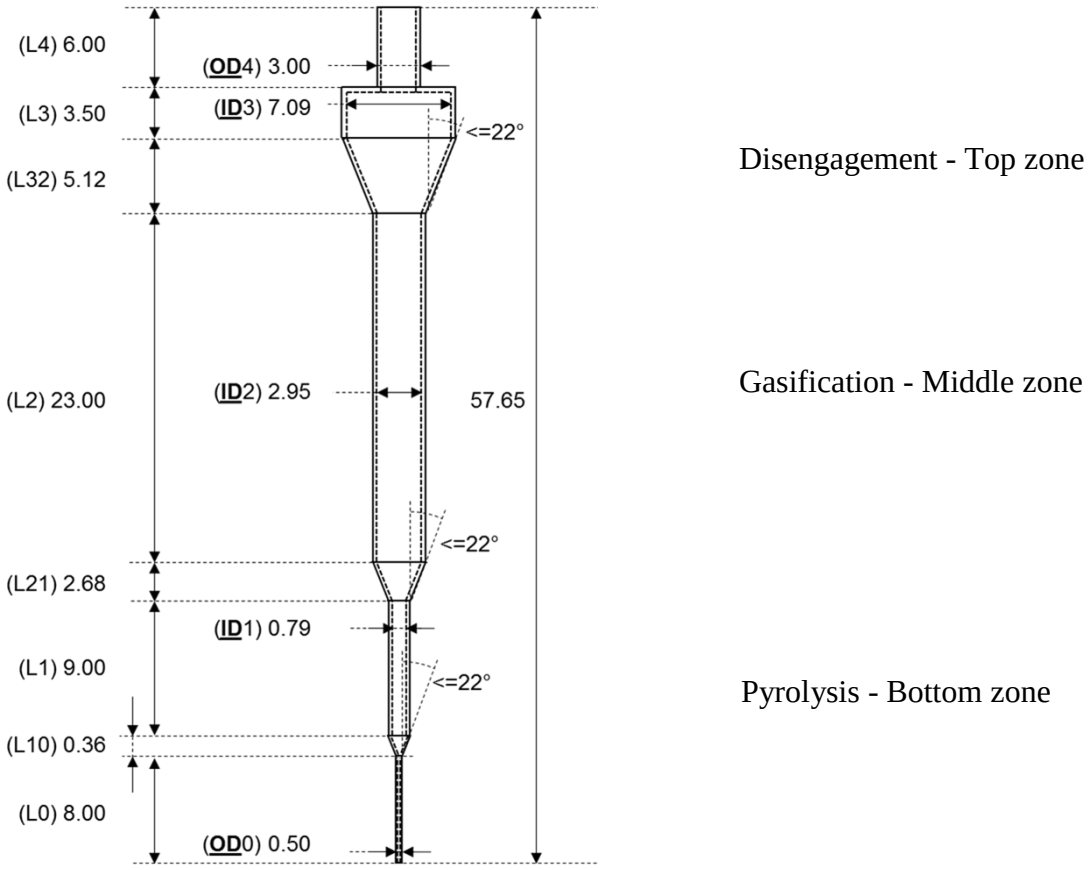

Figure 5.1. Schematic of the three-stage reactor designed for fluidized bed gasification (dimensions in inches).

Although each zone is designed to separate the pyrolysis and gasification stages, as fluidized particles occupy both the bottom and the middle zones, an overlap of pyrolysis

and gasification steps is expected in both the zones. Reactions between gas species also continue to occur in the top zone.

The exact dimensions of the fluidized bed reactor were established based on the minimum fluidization velocity and the terminal velocity of all the different particles in the reactor [2,23]. In addition to the feed particles introduced from the bottom, bed material was used in the reactor for better heat transfer and fluidization [2]. As the feed pellets pyrolyze, they convert into char particles which have a lower density. These char particles lose further weight until only the ash content remains. Thus, four different types of particles are present in the reactor during the gasification process. The two velocities that define the limits of the operating velocity of a particle to be suspended in the fluidization regime are minimum fluidization velocity and terminal velocity [2,23]. Since the volumetric flow rate of the fluidizing medium remains the same in all the three zones, different diameters were chosen to separate the particles using superficial velocity. Superficial velocity is defined as the volumetric flow rate divided by the cross-sectional area [24]. By identifying the superficial velocity required in each zone, the cross-sectional area was estimated which in turn provided the required diameters of the three zones.

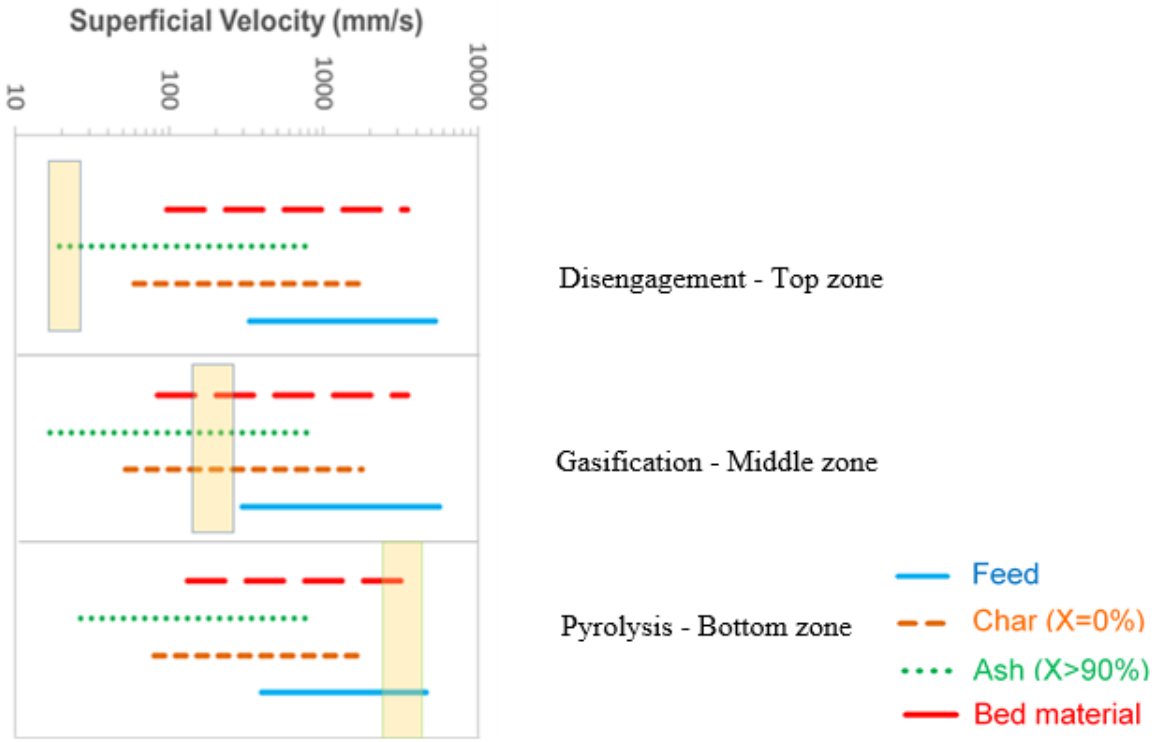

Figure 5.2. Selection of superficial gas velocity required in each zone of the multistage fluidized bed reactor.

The fluidization velocity range for the four types of particles are plotted in Figure 5.2. Since superficial velocity is inversely proportional to the cross-sectional area; the higher the velocity, the lower the diameter of the stage. Since all the particles except the bed material and feed are to be removed from the bottom zone, a high superficial velocity is selected that would carry over char and ash into the next zone. This results in a lower diameter for the bottom zone. The middle zone can accommodate all the particles except the feed and thus has intermediate superficial velocity and diameter. Finally, the disengagement zone is designed to separate the ash particles from all the other particles and has the lowest superficial velocity that results in a larger diameter for the top zone.

Thus, the operating superficial velocities in each zone dictated the required diameter of the three stages in the fluidized bed reactor (Figure 5.1).

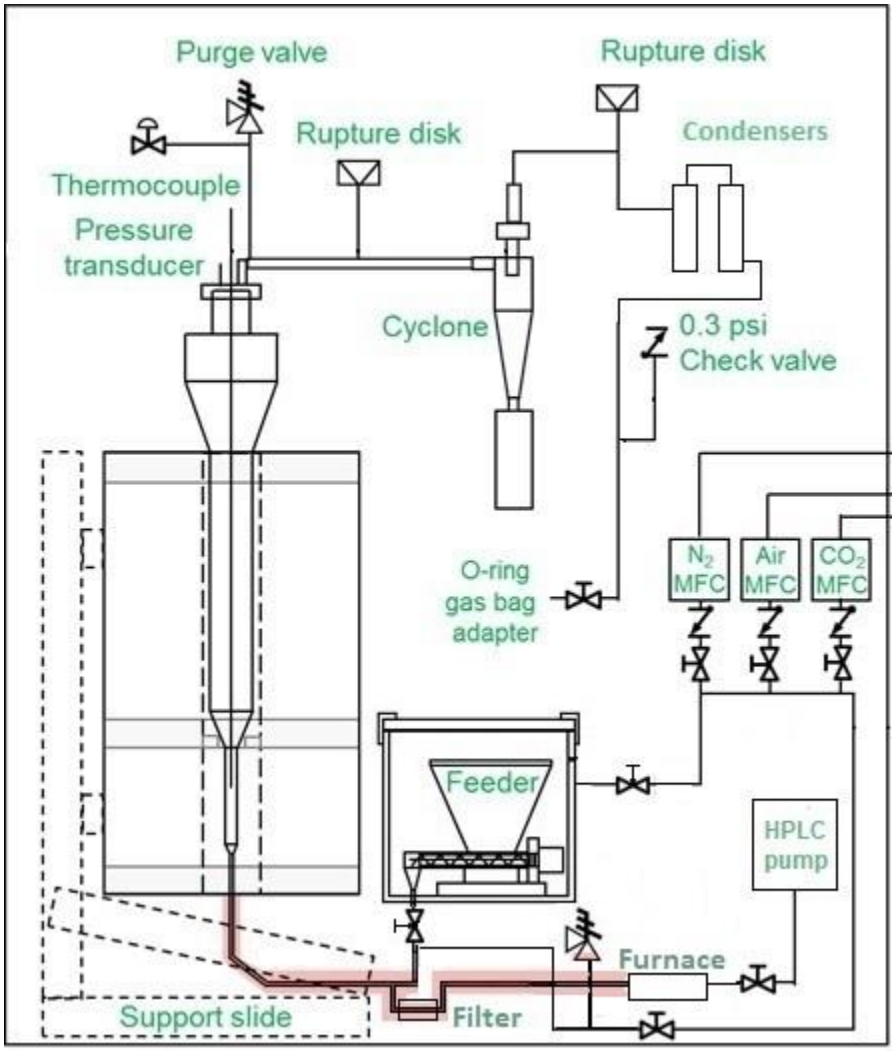

Figure 5.3. Schematic of the entire reactor setup.

A picture of the reactor setup is shown in Figure D.1 and the overall design of the reactor system is shown in Figure 5.3. Gases and steam are introduced upstream using mass flow controllers. Solid feed is introduced through a screw feeder connected to a motor that is set to rotate at a certain RPM (rotations per minute) based on the required feed flow rate. Feed falls into the feeding line by gravity and is pneumatically carried into the reactor by

the upstream gases. The introduction of the feed into the high temperature furnace leads to pyrolysis, gasification, and eventual formation of low density particles and ash. The final combination of light particles and gases are carried out of the furnace into a cyclone separator where most solids over 10 μm are separated from the gas. The gas stream is further passed through a two-tube condenser to collect water and lighter volatiles. The cyclone and all the gas lines are heat-traced upstream of the condenser. Finally, the gases are led out through the exhaust check valve, while small gas samples are collected in parallel into a gas bag for analysis in a Micro GC.

High weight capacity support structure was built from steel unistrut inside a walk-in fume hood. The base unistrut beams were attached with anchors into the concrete under the floor. Part of the frame was built on top of the slide and used to support the furnace, quartz tube, pressure gauges, and rupture disks. The rest of the stationary frame was built into shelves to hold the cyclone, condensers, feeder, steam generator, furnace power supply, and NI LabVIEW hardware. The majority of gas lines were built using Swagelok fittings and stainless steel tubing. Both straight and corrugated stainless steel tubing in 0.25 to 0.5-inch diameters were used to allow for flowrates of 30+ standard liters per minute (SLPM).

Steam was generated in a customized setup for steam gasification reactions. Deionized water (DI) water was pumped using an Agilent quaternary HPLC pump (Model number G1311A) that was capable of flowing water down to 0.2 ml/min. The set water flow was introduced into a pre-heated line to heat the water from room temperature to 60 °C. The pre-heated water was further sent into a furnace inside a 0.5-inch diameter tubing packed with glass wool (necessary for complete vaporization of water without pulsations).

The superheated steam out of the furnace then mixed with the bulk nitrogen gas before entering the three-stage fluidized bed reactor. All the lines downstream of the steam generation furnace were heated above 200 °C to avoid condensation of steam. A 425 µm filter was installed in the furnace downstream tubing to avoid feed entrainment into the steam line.

The auger screw feeder set-up is shown in Figure D.2. A 0.5-inch diameter augur screw was used to provide a constant feeding rate. The 3d model was made in Solidworks to the needed scale. The feeder was printed using Taulman3D n-vent filament on a Lulzbot Mini printer. The driving force for the rotation was provided by the 28BYJ-48 5-12V Stepper Motor with ULN2003 Driver Board. The logic for the stepper motor was controlled via Arduino Mega 2560 board with a custom C script allowing LabView to send desired rotation per minute rates via serial commands at 9600 baud. The entire feeder was placed in a pressurized tank to seal the gases from leaking out and air from leaking in. A 0.5-inch outer diameter tube was welded through one side of the pressurized tank to provide a feed exhaust path. A ball valve was used to separate the feeding line from the gas inlet line below. When required, the ball valve was opened, and the feed was introduced by gravity into the gas line below along with a small flow rate of nitrogen (200 ml/min) to avoid backflow of bulk gases.

The Mellen Split-Hinged Vertical Tubular Furnace (SV12-4.25x24V-3Z-AACT) has three 8” heated zones with independent temperature controls (PS205) and feedback through thermocouples. The heating elements are rated for 1200 °C temperature. The RS485 communication protocol is connected to the Labview. The furnace has 4.25” inner diameter and a 2-inch adiabatic section with removable vestibules between the two bottom

zones to provide a high temperature gradient. This feature was added in order to maintain a temperature difference between the pyrolysis and gasification zones. Mellen's active cooling technology installed in the form of controllable air streams through the inside of the heated sections gains control over heat loss from each section and is able to achieve even higher vertical gradients. A long sight-port was placed along the length of the tube. This provides clear visual feedback on the fluidization behavior of the particles in each zone. The furnace was placed on a stainless steel slide that allows opening it outside the fume hood.

A NI LabVIEW interface was created for interfacing with data collection and controls. The cDAQ-9178 CompactDAQ was assembled with 0-20 mA analog output, +/- 10 V analog output, thermocouple reader, analog current input detector, analog voltage input detector, and RS-485 converter. The LabView script records all the data collected to an MS Excel file for logging. The interface is used to establish set-points and observe real-time readings for the devices connected. Additionally, it provides easy shutdown buttons to either stop the experiment or purge the reactor. A screenshot of the Labview graphical user interface is shown in Figure D.3.

The three zones of the furnace are controlled using three Omega CN7000 series temperature controllers embedded in the power supply connected to three solid state relays and three thermocouples for each zone of the reactor. The temperatures and set points are displayed on the controllers themselves which are interfaced to the computer via the RS485 serial communication protocol. The temperatures, set points, and alarm thresholds are displayed on the front page of the graphical user interface. Additionally, the heat traced lines have embedded thermocouples underneath the insulation. The temperatures are

manually set via a variable voltage controller, but actively monitored via the thermocouples.

The pressure in the gas lines is monitored via Omega MMG015C1P4C0T4A5 pressure transducers (15 PSIG, 4 - 20 mA, 1/4-18 MNPT). The transducers are connected on the gas line before the reactor and at the top of the quartz tube flange. The signal is read by a NI Compact DAQ 9207 module and displayed on the NI Labview user interface. The gas lines before and after the reactor, have two Swagelok low pressure proportional relief valves (SS-RL4S8, 0.7 bar set pressure) installed.

5.2.2 Experimental materials and feed preparation

Both pine and RDF pellets were used in this study as feed materials. Debarked and chipped Loblolly pine (*Pinus taeda*) wood was obtained from Oglethorpe, GA. It was ground in a Wiley mill and particles in the range of 250-425 µm were used for the BFBR gasification runs. Nine individual components were selected for the model RDF composition as shown in Figure 5.4. The process for model component selection is discussed in detail in Chapter 2. All the individual components were ground down to less than 106 µm particle size (details in section 2.2.1) and mixed together in a Retsch mixer mill MM 400 at 30 Hz for 3 minutes. A 4X4 inch flat mold was filled with 16 g of the mixed RDF powder and placed in a Wabash press to create a pressed RDF sheet. The press was evacuated and heated to 127 °C at a pressure of 5000 psi with a hold time of 10 minutes. RDF pellets were formed from the pressed sheet with the use of a solid stud hole-punch. The RDF pellets created in this fashion are homogeneous, intact and of similar size and shape. The dimensions of around 30 pellets were measured using an optical

microscope. The average diameter was about 1.84 mm with a standard deviation of 0.093 mm while the average height was 1.42 mm with a standard deviation of 0.087 mm.

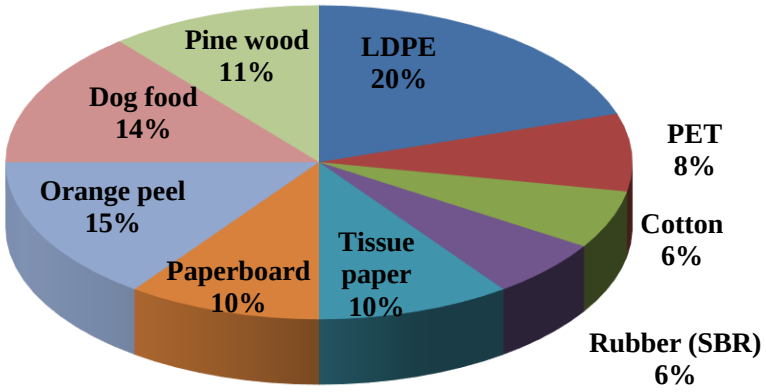

Figure 5.4. Model RDF composition.

Fluidization of Geldart Type-D large particles, such as the RDF feed pellets, is difficult due to their bulky nature [25]. This can be countered by utilizing a bed material of a different particle size. Silica was not utilized as a bed material in this study in order to avoid silicon scavenging during the gasification process, as evident from the results from Chapters 2 and 3. Although alumina (0.25 – 0.425 mm) was used in the preliminary runs, high entrainment of alumina particles in the disengagement zone along with particle agglomeration at high temperatures deemed it unfit as a bed material. As mentioned previously, dolomite and olivine have been found to be ineffective for the gasification of waste derived fuels [17]. Hence, spherical zirconia particles of 0.3 mm diameter (supplied by Advanced Materials Inc.) were considered as the bed material for the RDF gasification runs in the BFBR. Use of zirconia as bed material resulted in appropriate fluidization inside the bed along with the reduction of bed material entrainment. As an added advantage,

zirconia has been reported to have catalytic ability in selective oxidation of tar [26]. This is expected to be beneficial in reduction of tar formation during gasification.

5.2.3 Experimental conditions for gasification in the BFBR

The fluidized bed reactor design is flexible to accommodate different feed sizes of varying densities by modifying the fluidizing gas flow rates. Two different feeds were considered in this study: pine and RDF pellets. The total flow rate of the fluidizing gas was 12 - 15 SLPM for pine gasification while it was 18 SLPM for RDF pellet gasification. RDF pellets needed a higher flow rate than pine for successful fluidization since they have a larger particle size (~1.84 mm) than pine (250 – 425 μm). In addition to the bulk gas flow, additional nitrogen was introduced through the feeder to avoid backflow of gases into the feeder. The nitrogen flow rate through the feeder was 0.4 SLPM for CO_2 gasification while it was 0.2 SLPM for steam gasification. A mixture of 20% steam and 80% nitrogen (99.999%, Airgas) was used in steam gasification while CO_2 gasification was carried out with 99.99% CO_2 gas (Instrument grade, Airgas) for both pine and RDF pellet gasification. In the steam gasification runs with oxygen addition, 100 ppm and 500 ppm of oxygen was supplied from a 1.041% oxygen in nitrogen gas cylinder (Airgas).

Although the furnace is capable of maintaining the two stages of the fluidized bed at relatively different temperatures, use of a lower temperature (~600 °C) in the pyrolysis zone led to higher tar deposition and eventually de-fluidization. In order to rectify this issue, both the bottom zone and the middle zone were maintained at least at 800 °C for pyrolysis and gasification of RDF pellets. The specific temperatures used in each experiment are given along with the results in section 5.3. The furnace encloses only the

bottom zone and the middle zone, hence, heat tape was wrapped outside the disengagement zone to achieve the required 450 °C temperature (limited by silicone rubber O-ring on the flange), although it was partially heated from the heat inside the gasification zone. The downstream tubing connecting to the cyclone and the cyclone itself were wrapped in heat tape and were maintained at 250 °C. Finally, the lines connecting the cyclone to the condenser were heated to 180 °C. The hot vapors were condensed in the condenser using a coolant (Kryo 30, Lauda) that was circulated inside at -20 °C.

A feed flow rate of about 7 - 8 g/h of both pine and RDF pellets was used in the CO_2 gasification. On the other hand, about 1.5 – 2.5 g/h of the two feeds was used in steam gasification. Lower feed flow rate was employed in steam gasification since the gasification rate in diluted conditions (20% steam, 80% nitrogen) is low as observed from the TGA studies in section 3.3.7. A higher feed flow rate in the diluted conditions would lead to feed build-up in the reactor and eventually result in de-fluidization. Additionally, the feed flow rate controlled by the screw feeder depended on the packing which marginally varied from one run to another. Hence, the exact feed flow rate of each run was determined by subtracting the feed in the feeder and the feeding line before and after the experimental run.

5.2.4 Gas and char analytical techniques

A schematic of the gas collection setup for the fluidized bed reactor is shown in Figure 5.3 b. The outlet connection from the condenser passes through a 0.3 psi check valve to avoid backflow of gases and air into the reactor. The check valve also serves the purpose of purging an additional amount of gas during gas collection. The line downstream from

the check valve connects to an O-ring gas bag adapter. Flexfoil™ plus sample gas bags of 10 L capacity were used for collection of gas samples. The collected gases were analyzed in a Varian 490 micro-GC with four channels consisting of four 10 m long columns (two Molecular Sieve 5 Å, one Plot column, and one Al_2O_3 column) and four TCD detectors with the lowest detection limit of 10 ppm for all gases. The gas flow rates were established by assuming a basis of nitrogen as a tie element and by calculating the flow rate of each product gas component from the gas composition. Carbon yield in the gas fraction was determined by converting the gas flow rates (cm^3/min) to carbon flow in gas components (g C/min) using ideal gas volume at NTP conditions and carbon molecular weight as shown below:

$$\text{Carbon yield in the gas fraction} = \frac{\sum\left(\frac{V_i}{24.04\ x\ 1000}\right) x\ 12.01\ x\ n_i}{F_c} \qquad \text{Eq. (5.1)}$$

Where,

V_i = Average volumetric flow rate of gas component 'i' (sccm)

n_i = number of carbon atoms in gas component 'i'

F_c = Carbon flow rate in with the feed (g C/min)

The particles (char and ash) retained in the cyclone separator and the char coated bed material were collected and weighed. The carbon content in both the cyclone material and the bed material was determined using a Thermogravimetric analyzer (TGA). An SDT-Q600 thermogravimetric analyzer (TGA) by TA Instruments was used for this purpose which records weight loss as a function of temperature and time. Typical sample sizes used

were about 5 mg for the cyclone material and 70 mg for the bed material in the TGA. The experimental conditions used in the TGA to determine the volatile content of the char were similar to the gasification conditions used in Chapter 2. The sample was heated to 800 °C at 20 K/min with 200 ml/min of N_2 flow with a 15 minute hold and exposed to 200 ml/min of CO_2 until complete devolatilization was achieved. Since the volatile content contains elements in addition to carbon, the carbon content in the bed material and cyclone material was determined by multiplying the respective material weight with the fraction of volatile content and the carbon present in the char (77.07%) as determined by elemental analysis.

5.3 Results and discussion

5.3.1 Comparison of CO_2 gasification of pine and RDF pellets in the BFBR

Initial gasification runs in the BFBR were conducted with pine powder of 250 – 425 µm particle size. Both the bottom and the middle zone were maintained at 815 °C while the disengagement zone was around 450 °C. Gasification was carried out with 12 SLPM of 100% CO_2 as the fluidizing medium along with 0.4 SLPM of nitrogen as a tracer gas. The gas composition of this experiment is presented in Figure 5.5.

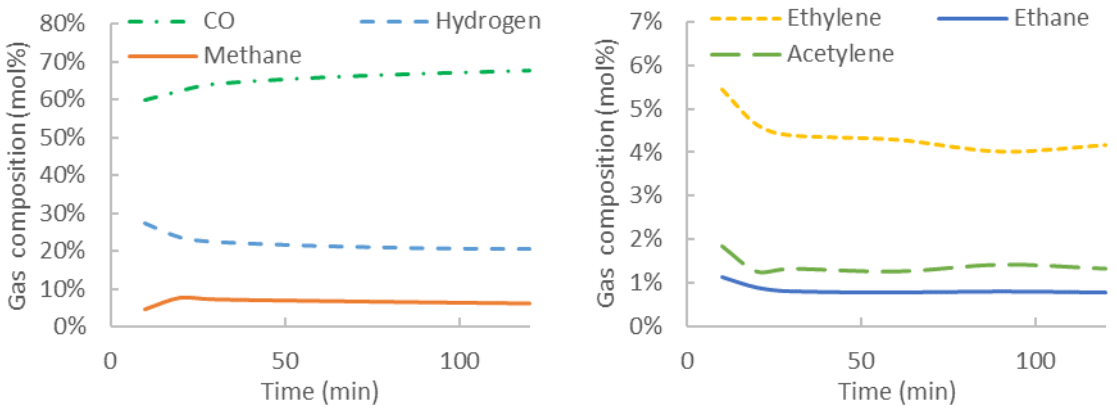

Figure 5.5. Gas composition from the CO_2 gasification of pine powder in the BFBR at 815°C with the a. major components b. minor components (nitrogen and CO_2 free basis).

Since CO_2 was the gasifying medium in excess of the stoichiometric requirement, it was difficult to differentiate the product CO_2 gas from the reactant CO_2. Thus, the composition is plotted on a CO_2 and N_2 free basis. Steady state composition was achieved in 30 minutes with CO as the major gas component. The other components were hydrogen and methane with the C_2 hydrocarbons forming the minor components. Syngas (CO + H_2) constituted about 88% of the total product gases implying a good quality product gas. Concentration of carbon monoxide was considerably higher than that of hydrogen, similar to the observations made in literature [27]. The primary reactions considered during gasification by CO_2 and steam are as follows [6,15]:

$C + CO_2 \rightarrow 2\,CO$ ΔH = +172 KJ/mol Eq. (5.2)

$C + H_2O \rightarrow CO + H_2$ ΔH = +131 KJ/mol Eq. (5.3)

$C + 2H_2 \rightarrow CH_4$ ΔH = -75 KJ/mol Eq. (5.4)

$CO + H_2O \rightarrow CO_2 + H_2$ ΔH = -41 KJ/mol Eq. (5.5)

$CH_4 + H_2O \rightarrow CO + 3H_2$ ΔH = +206 KJ/mol Eq. (5.6)

$CH_4 + 2H_2O \rightarrow CO_2 + 4H_2$ ΔH = +165 KJ/mol Eq. (5.7)

Since this experiment was conducted using 100% CO_2 as the gasifying medium, the reaction shown in Eq. 5.2 dominates the other reactions (methane reforming, water gas reaction and reactions between the product gases) to primarily form CO. Another minor pathway for the release of more CO is the reverse water gas shift reaction (reverse of Eq. 5.5) where CO_2 reacts with product hydrogen to form CO and water. One major difference of this study with the literature is the formation of larger amounts of C_2 hydrocarbons [27,28]. This difference is expected to be a result of the reactor configuration used in this study, where the bottom zone promotes pyrolysis reactions before the feed pellets can rise up into the gasification zone (middle zone). This results in a higher amount of pyrolysis products than that observed in a conventional BFBR with only two stages.

Although the composition data gives an insight into product distribution, the absolute flow rates of the gases released are more relevant when carbon yield in the gas fraction is being analyzed. The molar gas flow rates of the product gases on a nitrogen and CO_2 free basis is presented in Figure D.4. A feed flow rate of 7.26 g/h was recorded in this experiment which resulted in a carbon recovery of 53.3% in the gas fraction. The reproducibility of the run was verified by repeating the experiment with the same conditions.

Flexibility of the constructed BFBR was demonstrated by the gasification of higher particle size (1.84 mm diameter, 1.42 mm height) RDF pellets using the same reactor configuration. This was achieved by increasing the fluidizing gas flow rate to 18 SLPM

with 0.4 SLPM nitrogen tracer gas. 100% CO_2 gasification of RDF pellets was carried out using the same temperatures (~815 °C) as the pine gasification run. The resulting gas composition is shown in Figure 5.6.

Similar to pine gasification, steady state with the gas composition was achieved after 30 minutes with the largest gas fraction occupied by CO. Use of 100% CO_2 as the gasifying agent resulted in the large fraction of CO (Eq. 5.2). However, a large quantity of ethylene is also observed in the major gas components, unlike pine gasification. This is most likely derived from LDPE which constitutes 20% of the model RDF composition (Figure 5.4). The reactor configuration might also have helped in the production of ethylene since the bottom zone promotes pyrolysis reactions. A similar result is the production of 1, 3 butadiene which is likely released from the styrene-butadiene rubber present in the RDF feed (Figure 5.4) that is absent in the pine gasification. The differences with the literature reported values for BFBR gasification of RDF are again in the amount of the $C_2 - C_4$ hydrocarbons produced [5]. As discussed before, larger amounts of pyrolysis products compared to traditional fluidized bed reactors are to be expected with this reactor configuration.

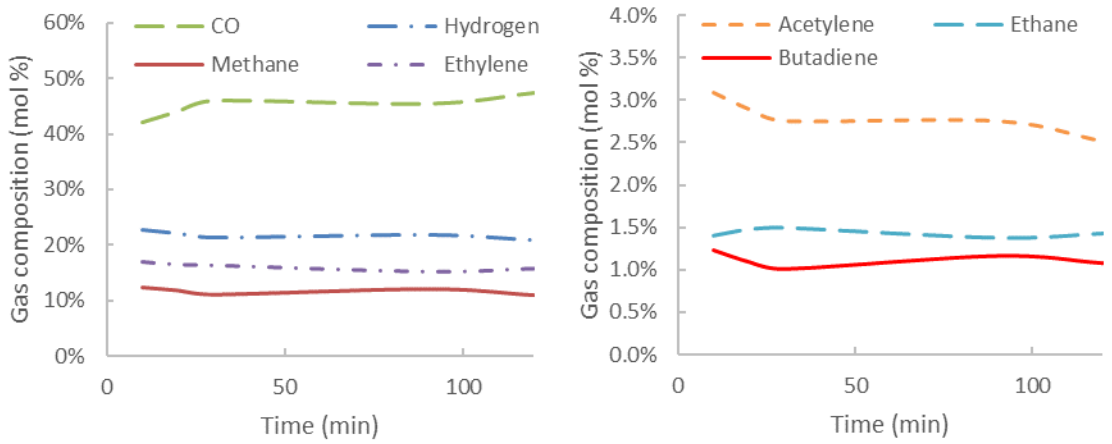

Figure 5.6. Gas composition from the CO_2 gasification of RDF pellets in the BFBR at 815°C with the a. major components b. minor components (nitrogen and CO_2 free basis).

The absolute gas flow rates of the CO_2 gasification of RDF pellets are reported in Figure D.5. The feed flow rate of the pellets was about 7 g/h with a carbon recovery of 57.2% in the gas fraction. The carbon recovery is marginally higher than the recovery in pine, however, the inability to quantify product CO_2 gas is a major drawback in identifying the exact carbon recovery. Additional carbon present in the cyclone material and the bed material was quantified by determining the volatile content present in the solids using a TGA. Bed material collected from the CO_2 gasification of RDF in the BFBR consisted of zirconia and partially converted char. With a 2.8% mass loss in the TGA when heated to 800 °C (Figure D.6 a), bed material accounted for 14.3% of carbon fed. On the other hand, cyclone material was dominated by unconverted char and some ash. It contained 76% volatiles (Figure D.6 b) that added up to 5.6% of carbon fed. Adding the carbon recovered in gases and the solids, a total carbon mass closure of 77.1% was achieved. The rest of the carbon is expected to be present in the tars and in the coke depositions on the walls of the reactor. In addition to the carbon loss as tar depositions, tar formation also causes plugging

of downstream lines and leads to several operational issues [16]. Hence, the experimental conditions in later studies were modified to achieve higher carbon recovery in the gas fraction which indirectly implies a reduction in the tar formation.

5.3.2 Comparison of steam gasification of pine and RDF pellets in the BFBR

Steam gasification of pine in the BFBR was carried out with a mixture of 20% steam and 80% nitrogen with a total flow of 15 SLPM. Although the amount of steam required for complete gasification of the feed was in excess of the stoichiometric requirement, the gas flow rates needed for fluidization were much higher resulting in the additional amount of nitrogen as the fluidizing medium. An additional 0.2 SLPM of nitrogen was introduced through the feeder to avoid backflow of gases. The middle zone was around 815 °C while the bottom zone was at 830 °C. Figure 5.7 shows the gas composition of the steam gasification of pine powder in the BFBR. One major advantage of steam gasification over CO_2 gasification was that, CO_2 could be quantified as a product gas since it is no longer introduced as a reactant.

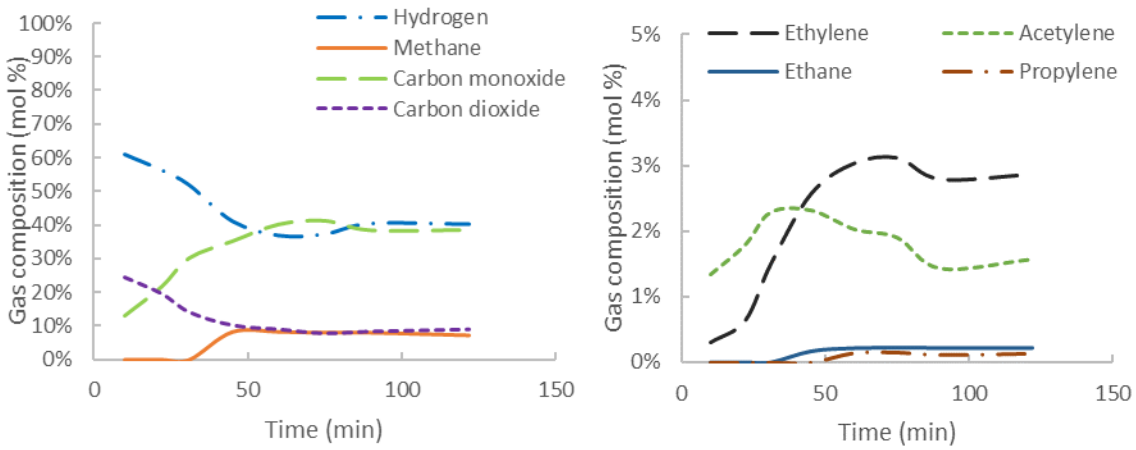

Figure 5.7. Gas composition from the steam gasification of pine powder in the BFBR at 830°C with the a. major components b. minor components (nitrogen free basis).

In contrast to the gas composition from CO_2 gasification of pine (Figure 5.5 a), equal molar yields of hydrogen and CO were observed in the steam gasification. The equal molar release of CO and hydrogen can be explained with the water gas reaction shown in Eq. 5.3. Since steam is the reacting agent in this case, the water gas shift reaction (Eq. 5.5) and methane reforming reactions (Eqs. 5.6 and 5.7) are also more likely to occur. However, a higher hydrogen fraction than CO in the pure steam gasification of biomass has been reported [11,29]. The difference is probably due to the higher temperature used in the other studies (860 °C and 950 °C) as compared to 830 °C used in this experiment. It is also to be noted that the papers reported the composition data for 100% steam gasification runs whereas in this case, the steam is diluted down to 20%. As discussed before, reactor configuration also allows more pyrolysis products than the conventional fluidized bed reactors leading to larger fractions of CO and C_2 – C_4 hydrocarbons.

CO_2 was found to be in equal molar ratio with methane which are the next major gas components. In addition to the C_2 hydrocarbons seen in CO_2 gasification (Figure 5.5

b), propylene is also present in the steam gasification products of pine. Introduction of steam is expected to have resulted in the steam reforming of heavier hydrocarbons (tars) leading to a wider range of relatively light hydrocarbons [4]. Generalized tar reforming reactions used for gasification of carbonaceous feedstocks are summarized below [6,30]:

$$C_nH_m(tar) + nH_2O \rightarrow \left(n + \frac{m}{2}\right) H_2 + nCO \qquad \text{Eq. (5.8)}$$

$$C_nH_m(tar) + nCO_2 \rightarrow \left(\frac{m}{2}\right) H_2 + 2nCO \qquad \text{Eq. (5.9)}$$

$$C_nH_m(tar) \rightarrow \left(\frac{m}{2}\right) H_2 + nC \qquad \text{Eq. (5.10)}$$

$$C_nH_{2n+2}(alkanes) \rightarrow C_nH_{2n}(alkenes) + H_2 \qquad \text{Eq. (5.11)}$$

$$C_nH_{2n}(alkenes) \rightarrow C_nH_{2n-2}(alkynes) + H_2 \qquad \text{Eq. (5.12)}$$

Steam reforming of tars is expected to follow Eq. 5.8 where steam reacts with tars and converts them into hydrogen and CO, while reforming of tars in the presence of CO_2 follows Eq. 5.9. Thermal cracking of tars (Eq. 5.10), alkanes (Eq. 5.11) and alkenes (Eq. 5.12) could also produce hydrogen in both CO_2 and steam gasification. The absolute gas flow rates of the product gases are reported in Figure D.7. The time taken to achieve steady state product gas flow is higher at 90 minutes as opposed to 30 minutes in CO_2 gasification. This is expected to be a result of the dilution factor in steam gasification that resulted in lower surface saturation of the feed leading to lower reactivities as observed in Section 3.3.7 and by others [31,32]. Although all the steam gasification runs in this chapter have been performed with 20% steam, future studies could be aimed at increasing the steam input to decrease the time taken to achieve steady-state gas composition. A feed flow rate

of 2.5 g/h was recorded in this experiment which resulted in a carbon recovery of 50.9% in the gas fraction similar to the carbon recovery in CO_2 gasification. However, it is to be noted that the carbon recovery measured in CO_2 gasification also accounts for the carbon supplied by the reacting medium CO_2, and hence a direct comparison might not be justified.

A higher total flow rate of 18 SLPM (as opposed to 15 SLPM for pine) of 20% steam and 80% nitrogen mixture was used for the steam gasification of RDF pellets in the BFBR. The higher flow rate was used to fluidize the heavier RDF pellets. An additional 0.2 SLPM nitrogen gas was injected through the feeder to avoid backflow of bulk gases. The bottom zone and the middle zone were maintained at 800 °C and the resulting gas composition is shown in Figure 5.8. A slightly larger fraction of CO (~28%) was released compared to hydrogen (~24%) as opposed to equal molar ratios of the two products in steam gasification of pine. This is expected to be a result of the higher temperature used in steam gasification of pine (~ 830 °C) as opposed to 800 °C in RDF steam gasification. The effect of temperature on hydrogen yield is discussed in more detail in Section 5.3.3.

A wider range of hydrocarbons were released in the RDF steam gasification as compared to the CO_2 gasification of RDF (Figure 5.6) which are expected to be a result of steam reforming reactions [4,6]. In addition to CO_2 and methane in equal molar yields, ethylene is also produced in the same molar ratio. This increase in ethylene concentration is typical of RDF gasification (Figure 5.6) since 20% of the RDF composition is LDPE. Similarly, 1, 3 butadiene is also a product of the SBR present in the RDF feed. Moreover, acetylene concentrations are higher (~3.6%) in RDF steam gasification as compared to pine

(~1.4%). Cracking of ethylene or higher hydrocarbons (Eq. 5.12) could be a partial source of the additional acetylene observed in RDF gasification [11].

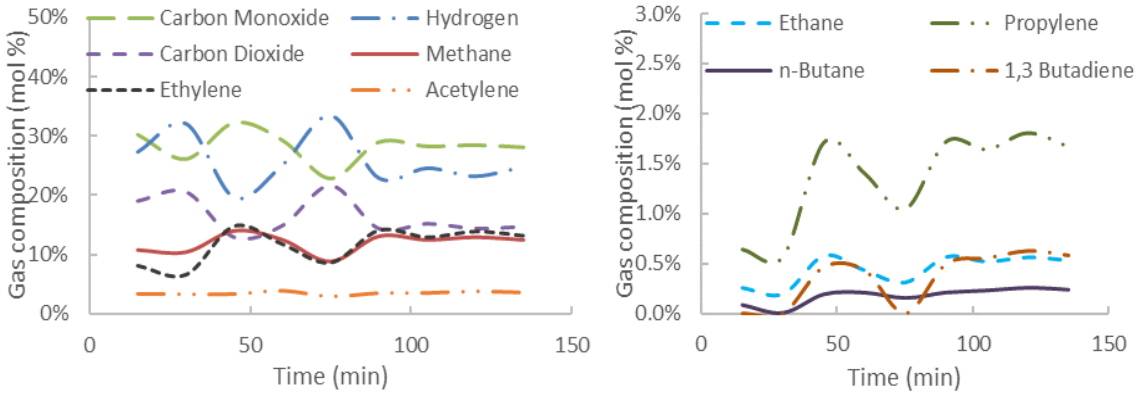

Figure 5.8. Gas composition from the steam gasification of RDF pellets in the BFBR at 800 °C with the a. major components b. minor components (nitrogen free basis).

The absolute gas flow rates of the steam gasification of RDF pellets is presented in Figure 5.9. The general trend of the gases is similar to the trend observed in the gas composition where steady state gas flow rates are achieved at 90 minutes. Feed flow is a function of feed packing inside the screw feeder that rotates at a set RPM. This explains the peak observed around 45 minutes for all the gases, which is a result of sudden release of feed pellets from the feeder. The flow rates are not used for comparison since the feed flow rates slightly vary from run to run. The feed flow rate of the pellets was about 2.4 g/h with a carbon recovery of 72.4% in the gas fraction. The higher carbon recovery in the steam gasification of RDF compared to the CO_2 gasification of RDF (57.2%) is attributed both to the larger fraction of hydrocarbons produced and the ability to quantify the CO_2 fraction in the product gases.

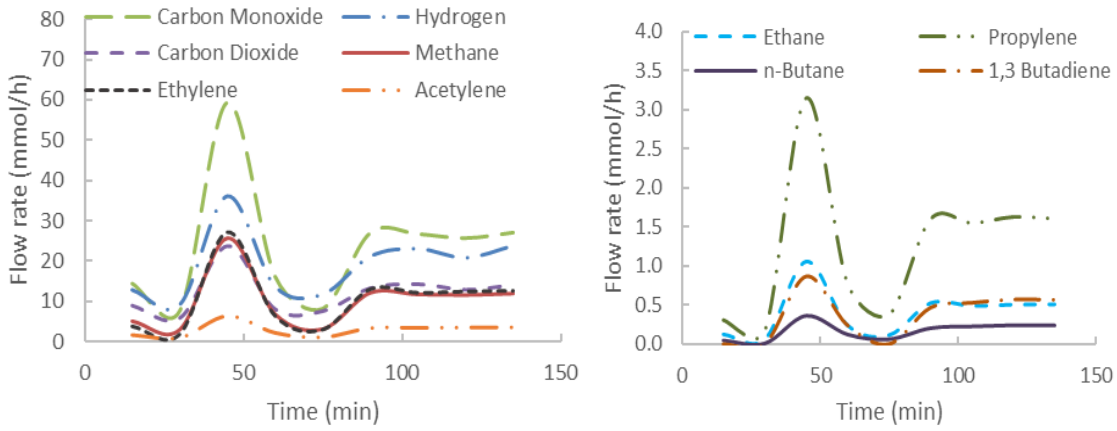

Figure 5.9. Product gas flow rates from the steam gasification of RDF pellets in the BFBR at 800 °C with a. major components b. minor components (nitrogen free basis).

5.3.3 Variation of gasification temperature in steam gasification of RDF pellets

Gasification temperature plays a vital role in the product yields as well as the product distribution. Several researchers have found that increased gasification temperature results in an increased gas yield and lowered tar formation [15,33,34]. However, increased temperature exacerbates ash agglomeration especially when the ash contains alkali compounds [6,35] in addition to demanding higher energy consumption. Moreover, temperature is limited by reactor material and generation of contaminants such as NOx [19]. For these reasons, although the gasification temperature was increased to improve the gas yield, the temperature was limited to 900 °C. The steam gasification of RDF pellets was conducted with 20% steam and 80% nitrogen mixture at two additional gasification temperatures.

Gasification temperature was increased to 830 °C for the gasification zone (middle zone) with the bottom zone set at 815 °C in the first experiment with all the other experimental parameters maintained at the same conditions as the steam gasification run at

800 °C (section 5.3.2). A total flow rate of 18 SLPM was used with an additional 0.2 SLPM of nitrogen gas through the feeder. A feed flow rate of 1.405 g/h was recorded and the resulting flow rates of the released gases from the experiment are presented in Figure 5.10.

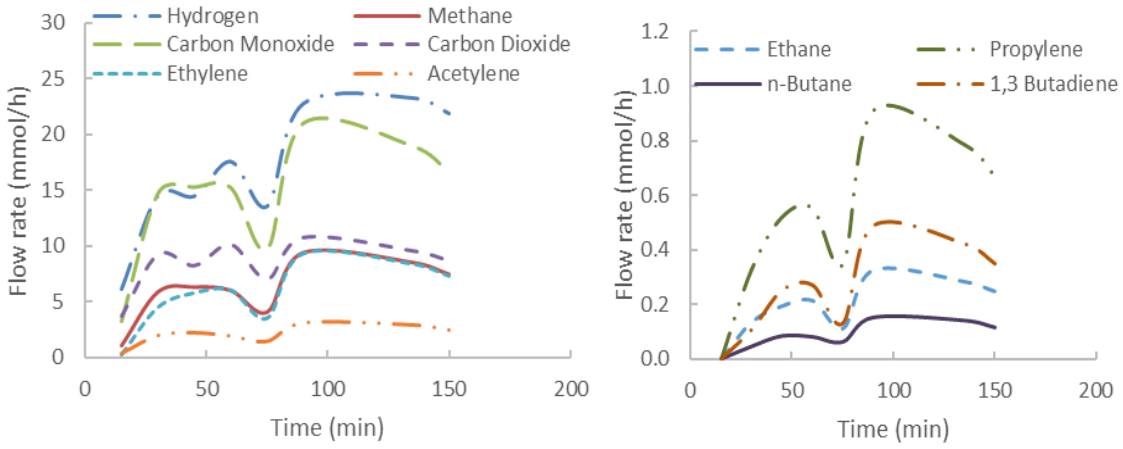

Figure 5.10. Product gas flow rates from the steam gasification (20% steam, 80% N_2) of RDF pellets in the BFBR at 830°C with a. major components b. minor components (nitrogen free basis).

At the higher gasification temperature of 830 °C, the product gas flow rates show a trend reversal with respect to hydrogen and carbon monoxide fractions. In Figure 5.9, since the gasification temperature is at 800 °C, CO dominates over hydrogen as the major gas component. This increase in hydrogen yield at increased gasification temperature suggests cracking reactions of higher hydrocarbons (Eqs. 5.10, 5.11, 5.12) and steam reforming of tars (Eq. 5.8) are promoted. With increasing temperature, permanent gases like CO, H_2, CO_2, methane, ethylene and cyclopentadiene radicals (responsible for the increase of PAHs) are likely generated by cleaving of functional groups of secondary tars (benzene, phenol and other aromatic compounds) [15]. A similar effect was also observed when the steam gasification results of pine (Figure 5.7) and RDF were compared (Figure 5.8), where an increase in temperature resulted in an increased yield of hydrogen for pine gasification.

While butadiene and ethane were produced in equal molar ratio at 800 °C (Figure 5.9 b), the relative concentration of butadiene with respect to ethane increased at 830 °C, which is attributed to promoted cracking reactions (Eq. 5.12). It is to be noted that since the feed flow rates vary between the two runs (800 °C and 830 °C), only a qualititave comparison of the product gas flow rates can be made.

Another run was carried out with a further increase of gasification temperature to 900 °C. The bottom zone was maintained at 800 °C with the same gas flow rate of 18 SLPM (20% steam and 80% nitrogen). A feed flow rate of 1.564 g/h was noted, and the flow rates of the product gases are plotted in Figure 5.11. Since the screw feeder in use operates by turning the screw at a set RPM, the feed pellets discharged from the feeder are a function of pellet packing in the feeder. Although the amount of RDF pellets loaded into the feeder is fixed at 25 g, if the packing varies slightly from run to run, it leads to a certain variability in the feed flow. A sudden release of a large number of feed pellets into the reactor results in large product gas pulses as seen at 75 minutes. However, it takes 90 minutes to achieve a steady state gas composition, similar to other steam gasification runs.

A comparison of the compositions of the gases at the three different gasification temperatures is shown in Figure 5.12. As discussed before, an increase in gasification temperature (middle zone) results in an increase in the hydrogen fraction of the gas. This could be a result of improved tar reforming reactions (steam reforming, tar cracking) which would also explain an increase in the acetylene fraction with an increase in temperature [11,15]. A decrease in CO and an increase in CO_2 concentrations is also observed with increasing temperature. Although this trend combined with the hydrogen increase indicates

a positive shift in the water gas shift reaction, it has to be noted that the reaction is mildly exothermic (Eq. 5.5) and thus is unlikely to increase at higher temperature. The increase in both hydrogen and CO_2 at higher temperatures is consistent with the decrease in methane via Eq. 5.7.

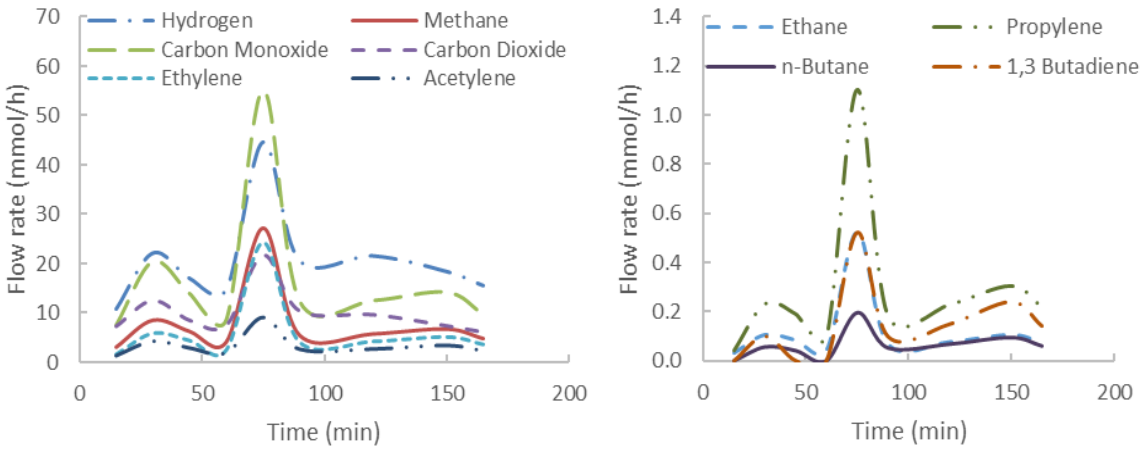

Figure 5.11. Product gas flow rates from the steam gasification (20% steam, 80% N_2) of RDF pellets in the BFBR at 900°C with a. major components b. minor components (nitrogen free basis).

The $C_2 – C_4$ hydrocarbon fractions also decrease (except acetylene) with increasing temperature. These fractions have been considered proxy tars in some studies where the yields of these products followed the yields of tar compounds [17,36]. These studies observed that very low tar concentrations are always coupled with decreased fractions of $C_2 – C_4$ hydrocarbons, indicating that their yield could be used as an indicator of the amount of tar generated. Thus, these components are considered 'tar equivalents' in this study, which indicate that the higher temperature reduces formation of tars and increases gas yield. Although the carbon recovered in the gas fraction of the three runs was very similar at 72.4%, 72.4% and 73.6% for gasification at 800 °C, 830 °C and 900 °C respectively, the higher hydrogen yield could be contributing towards the increased gas yield at higher

temperatures. This greater gas yield at higher temperatures is likely a combination of increased gas production during the initial pyrolysis phase, steam reforming of tars (including cracking) and the endothermic reactions of char gasification [15].

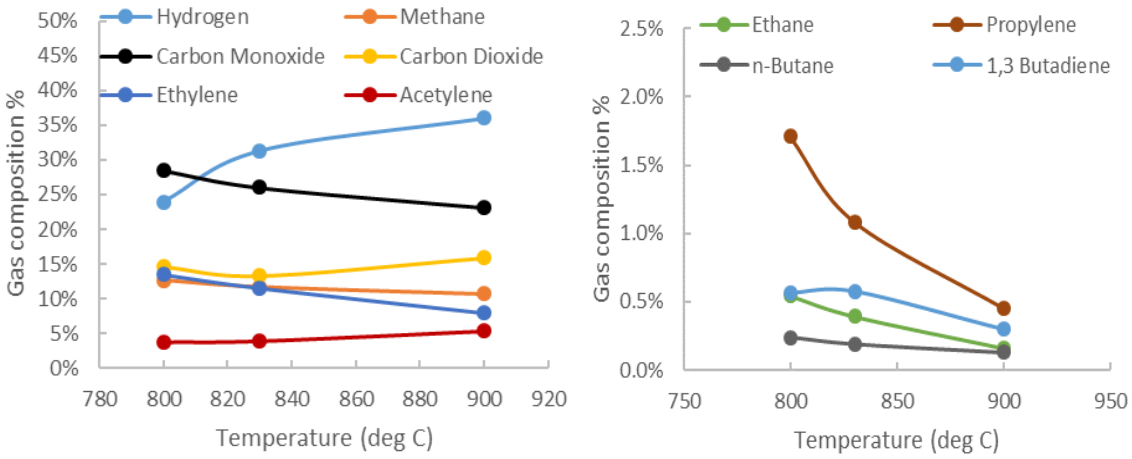

Figure 5.12. Variation of steady state gas composition as a function of gasification temperature in the steam gasification of RDF pellets (20% steam, 80% nitrogen mixture).

5.3.4 Introduction of small amounts of oxygen in the steam gasification of RDF pellets

Gasification products primarily depend on feed composition, temperature, heating rate and the gasifying agent used [6,37]. The feed constitution and heating rate for this study are inherently fixed as the study analyzes RDF feed pellet gasification in the BFBR where the heating rate depends on the temperature inside the reactor. Gas yield and composition as a function of gasification temperature has been discussed in the previous section. The type of gasifying agent used has also been addressed by considering both CO_2 and steam as gasifying agents in sections 5.3.1 and 5.3.2. However, introduction of small amounts of oxygen has been found to be beneficial for increasing the gas yield [12,14]. Use of minor amounts of oxygen in the reacting medium serves two purposes: it increases

the carbon recovery in the gas fraction by promoting combustion reactions (formation of CO_2) and, it provides combustion heat that reduces the energy required to reach the gasification temperature [14,38]. In this study, varying amounts of oxygen were introduced into the steam gasification of RDF pellets to improve the gas yield. Additionally, introduction of oxygen at two different locations inside the reactor was performed to understand if combustion reactions could be targeted at the tar species.

5.3.4.1 Oxygen introduced with the feed from the bottom of the BFBR

Oxygen required for the experiments was supplied by a 1.041% oxygen in a balance nitrogen cylinder. 5% oxygen required for the stoichiometric combustion of the feed amounted to 100 ppm of oxygen in the fluidizing mixture of steam, nitrogen and oxygen. 100 ppm of oxygen was introduced from the bottom of the reactor along with the fluidizing gas mixture (18 SLPM of 20% steam and 80% nitrogen mixture). An additional 0.2 SLPM of nitrogen was introduced through the feeder. Both the bottom zone and the middle zone were maintained at 800 °C. A feed flow rate of 1.583 g/h was recorded and the resulting product gas composition on a nitrogen free basis is presented in Figure 5.13.

The product gas distribution is very similar to 20% steam and 80% nitrogen gasification of RDF pellets without oxygen (Figure 5.9). Carbon monoxide is the major gas component closely followed by hydrogen. Methane and ethylene are produced in equal molar ratios with a slightly higher CO_2 fraction. The small increase in CO_2 concentration could be due to the very low amount of oxygen introduced into the system. Ethane and butadiene are also present in equal molar ratios similar to the steam gasification without oxygen. This shows that although 100 ppm oxygen has stoichiometric ability of achieving

5% conversion with the set feed flow rate, the oxygen is too dilute to cause significant changes in the product gas distribution.

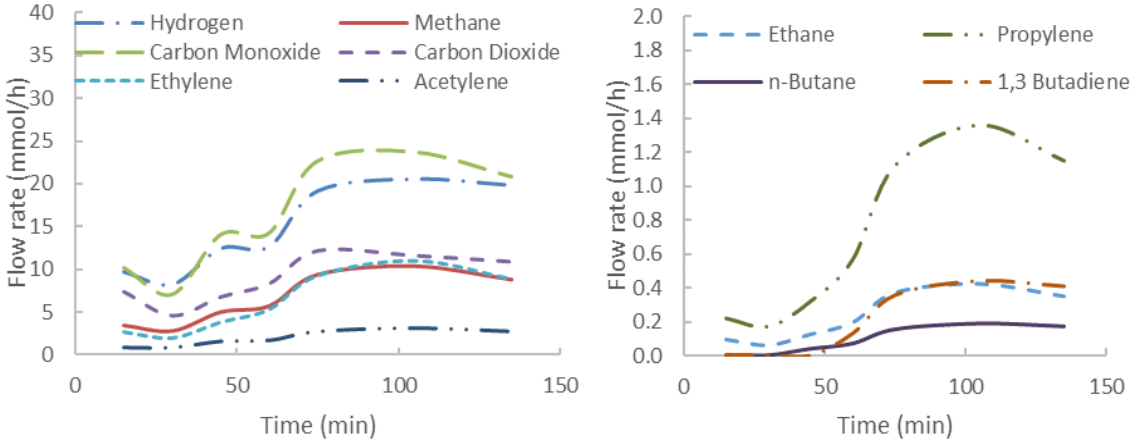

Figure 5.13. Product gas flow rates from the steam gasification (20% steam, 80% N_2) of RDF pellets in the BFBR with 100 ppm of oxygen at 800°C with a. major components b. minor components (nitrogen free basis).

The oxygen content was further increased to 500 ppm (20% oxygen required for complete stoichiometric combustion) and introduced into the steam gasification of RDF pellets with 20% steam and 80% nitrogen mixture. Both the bottom zone and the middle zone temperature were set to 800 °C, however, the temperature in the gasification zone (middle zone) increased to 830 °C while the temperature in the bottom zone increased to 820 °C due to combustion heat. The gas flow rates of the 500 ppm oxygen with 20% steam and 80% nitrogen gasification of RDF pellets are shown in Figure 5.14.

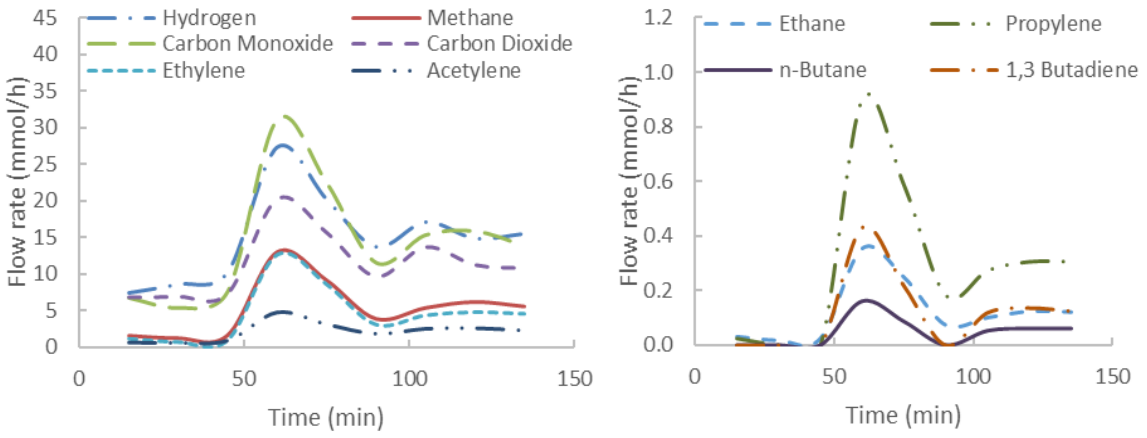

Figure 5.14. Product gas flow rates from the steam gasification (20% steam, 80% N_2) of RDF pellets in the BFBR with 500 ppm of oxygen at 830°C with a. major components b. minor components (nitrogen free basis).

Counterintuitively, when the oxygen content is increased to 500 ppm, both hydrogen and CO are produced in equal molar ratios as opposed to a higher CO fraction as seen with 100 ppm oxygen run (Figure 5.13). This increase in hydrogen flow rate is attributed to an increase in the reactor temperature due to combustion heat rather than the oxygen present. The CO_2 content however increased as expected with higher amount of oxygen. The rest of the gas components followed similar trends as seen before with 100 ppm oxygen. The comparison of product gas compositions of the steam gasification runs with and without oxygen is presented in Figure 5.15.

As can be seen from the Figure 5.15, the gas composition does not vary significantly between the steam gasification without oxygen and with 100 ppm oxygen. There is a minute increase in CO_2 concentration and a small decrease in C_2 and C_4 hydrocarbon fractions which hints at very little combustion reaction if any. However, when the oxygen concentration is increased to 500 ppm, there is a clear increase in CO_2 concentration with a marked decrease in C_2 – C_4 hydrocarbons implying significant

combustion reaction in the reactor. The occurance of combustion is also apparent from the temperature increase to 830 °C, as mentioned previously. An increase in hydrogen concentration is supposedly a result of this temperature increase. This hypothesis was verified by comparing the gas composition data of the present run with that of the steam gasification of RDF pellets without oxygen, however, at the same temperature of 830 °C. The gas compositions of these two experiments along with the baseline of steam gasification at 800 °C is presented in Table 5.1.

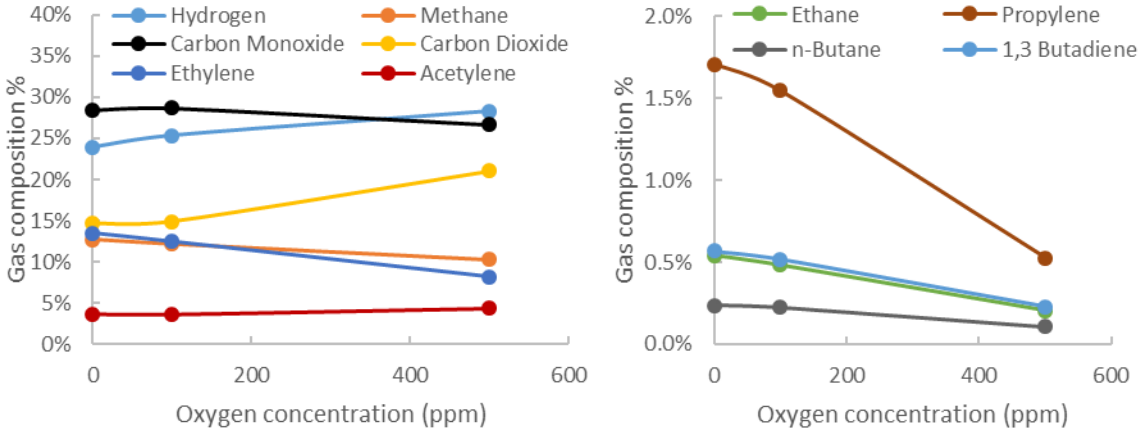

Figure 5.15. Variation of steady state gas composition as a function of amount of oxygen introduced into the steam gasification of RDF pellets (20% steam, 80% nitrogen mixture).

Table 5.1. Product gas composition data of RDF pellet steam gasification in the BFBR at 800 °C and 830 °C without oxygen and at 830 °C with 500 ppm oxygen (nitrogen free basis)

Gas components	800 °C, 20% steam	830 °C, 20% steam, 500 ppm O_2	830 °C, 20% steam
Hydrogen	24.0%	28.3%	31.3%
Methane	12.7%	10.3%	11.7%
CO	28.5%	26.7%	26.0%
CO_2	14.7%	21.1%	13.3%
Ethylene	13.5%	8.2%	11.5%
Ethane	0.5%	0.2%	0.4%
Acetylene	3.7%	4.4%	3.8%
Propylene	1.7%	0.5%	1.1%
n-Butane	0.2%	0.1%	0.2%
1,3 Butadiene	0.6%	0.2%	0.6%

The gas composition of steam gasification of RDF pellets with 500 ppm oxygen indicates that in addition to an increase in the CO_2 content, there is a reasonable increase in the hydrogen concentration when compared to the base run at 800 °C. When the gas composition is compared to that of the steam gasification at 830 °C, there is a similar increase in the hydrogen content and not the CO_2 concentration thus verifying that enhanced hydrogen production is a result of an increase in temperature. This result is similar to the effect of temperature in section 5.3.3 where enhanced hydrogen generation was attributed to improved thermal cracking and tar reforming reactions (steam reforming, tar cracking) [11,15]. Moreover, there is a significant decrease in the $C_2 – C_4$ hydrocarbons (tar proxies) in the presence of oxygen indicating that the tar content is also decreased due to promoted combustion reactions. The carbon recovered in the gas fraction of steam

gasification without oxygen, with 100 ppm oxygen and with 500 ppm oxygen is very similar at 72.4%, 71.2% and 74.6% respectively. Hence, with small addition of oxygen into the steam gasification run, tar content can be reduced and a larger fraction of hydrogen can be derived from the combustion heat.

5.3.4.2 Oxygen introduced from the top into the disenagagement zone

The introduction point of oxygen into the BFBR during the steam gasification of RDF pellets is investigated in this section. Several studies have observed that the 'splash zone' between the dense bed and the freeboard is the location where the tar pre-cursors are formed [36,39,40]. These tar pre-cursors further polymerize and form the heavy tars and polyaromatic compounds (PACs) that result in depositions over the reactor walls and downstream tubing. In addition to plugging the lines downstream, formation of heavy tars and PACs results in a loss of carbon that could otherwise be recovered in the gas fraction. 500 ppm of oxygen was introduced from the top into the area where the gasification zone ends and the disengagement zone begins to determine if the combustion reaction could be targeted at the tar pre-cursor species.

The bulk fluidizing gas was 20% steam and 80% nitrogen with a 18 SLPM total flow rate. Temperature in the bottom zone and the middle zone was set to 800 °C; however, similar to the run with oxygen introduction from the bottom, the temperature of the middle zone increased to 827 °C and the bottom zone to 825 °C due to combustion heat. The increase in the bottom zone temperature is probably due to the heat carried over by the fluidizing particles. A feed flow rate of 1.32 g/h was recorded. The product gas flow rate produced at these conditions is presented in Figure 5.16. Steady state gas composition was

achieved around 100 minutes with a slightly higher error in the steady state gas flow rates of some components (~18%).

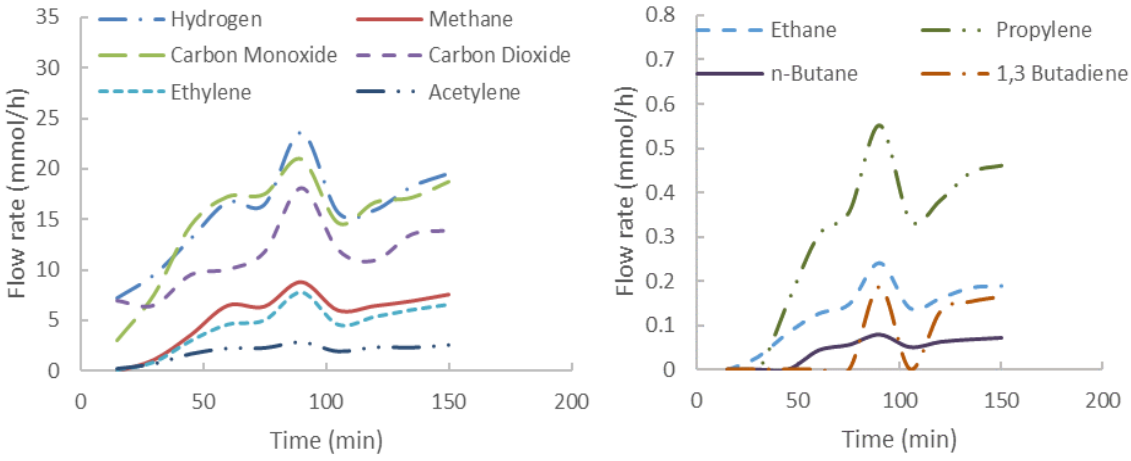

Figure 5.16. Product gas flow rates from the steam gasification (20% steam, 80% N_2) of RDF pellets in the BFBR with 500 ppm of oxygen introduced from the top at 827°C with a. major components b. minor components (nitrogen free basis).

Table 5.2. Product gas composition data of RDF pellet steam gasification in the BFBR at 830 °C with 500 ppm oxygen injection from bottom and top (nitrogen free basis)

Gas components	20% steam 500 ppm O_2 830 °C, Bottom injection	20% steam, 500 ppm O_2 827 °C, Top injection
Hydrogen	28.3%	28.0%
Methane	10.3%	10.7%
CO	26.7%	26.8%
CO_2	21.1%	20.3%
Ethylene	8.2%	9.2%
Ethane	0.2%	0.3%
Acetylene	4.4%	3.7%
Propylene	0.5%	0.7%
n-Butane	0.1%	0.1%
1,3 Butadiene	0.2%	0.2%

Both CO and hydrogen are produced in almost equal molar ratios followed by CO_2, similar to the trend observed in the steam gasification run with bottom oxygen injection (Figure 5.14). The next major gas component is CO_2 whose concentration is higher than

methane and ethylene, as expected from oxygen injection. Since the feed flow rates varied between the two runs, the product gas flow rates cannot directly be compared. Instead, a comparison of the gas compositions of the steam gasification of RDF pellets with different oxygen injection points is presented in Table 5.2.

The gas composition of the two gasification experiments are very similar, indicating that the point of introduction of oxygen inside the reactor does not affect the gasification process. Instead, the product gas composition is rather largely dependent on the temperature and the gasification reactant mixture composition. Although air staging has had an effect on the gas composition in traditional fluidized bed reactors [39], the results differ in this study likely due to the reactor configuration. Since the conventional fluidized bed reactors only have one or two stages (reaction zone, disengagement zone), the tar pre-cursors were identified within the transition zone where the partially reacted particles underwent secondary reactions [39,40]. Conversely, this study employs a reactor configuration with three different stages where most of the pyrolysis reactions occur in the bottom zone with the gasification reactions taking place in the middle zone. By the time the particles reach the splash zone (area between the gasification zone and disengagement zone), most of the particles have been considerably gasified and thus this zone does not hold a similar significance in this study.

5.3.5 Combination of temperature variation and oxygen introduction during the steam gasification of RDF pellets

The results from sections 5.3.3 and 5.3.4 suggest that a higher temperature of 900 °C and 500 ppm of oxygen introduction during the steam gasification of RDF pellets in the

BFBR decrease the tar content and increase the hydrogen fraction in the product gases. These two conditions were used simultaneously to minimize tar yield and to recover more carbon into the gas fraction. 18 SLPM of a 20% steam and 80% nitrogen mixture was used as the fluidizing gas with 500 ppm of oxygen introduced from the bottom. The temperature of the gasification zone (middle zone) was set to 900 °C which was increased to 930 °C due to combustion heat during the run. The bottom zone increased to 860 °C from 840 °C. A feed flow rate of 1.709 g/h was recorded with the resulting gas flow rates plotted in Figure 5.17.

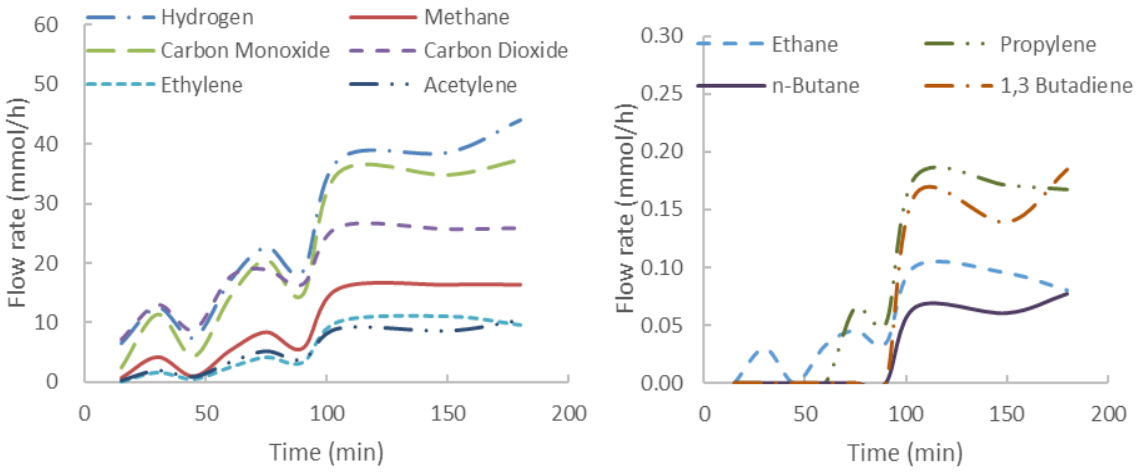

Figure 5.17. Product gas flow rates from the steam gasification (20% steam, 80% N_2) of RDF pellets in the BFBR with 500 ppm of oxygen introduced from the bottom at 930°C with a. major components b. minor components (nitrogen free basis).

Hydrogen has the highest gas flow rate closely followed by CO. A large flow rate of CO_2 is also observed that is likely derived from the combustion reactions with the injected oxygen. The acetylene flow rate also increased to the same level as ethylene and among the rest of the C_2 – C_4 hydrocarbons, alkynes and alkenes are favored compared to alkanes indicating improved cracking reactions at 930 °C. A comparison of the composition

variation with changes in the two experimental parameters (temperature, oxygen introduction) is presented in Table 5.3.

Steam gasification without oxygen, however, at an elevated temperature of 900 °C results in a large fraction of hydrogen and a carbon recovery of 73.6% in the gas fraction. When this composition data is compared to the experiment with lowered temperature of 830 °C and 500 ppm of oxygen introduction, the hydrogen fraction is lower, while, the CO and CO_2 fractions are higher. This is expected since with introduction of oxygen, combustion reactions that result in CO_2 and H_2O are promoted which indirectly decrease the hydrogen fraction. The carbon recovery in this experiment was similar at 74.6%. Since both higher temperature and oxygen introduction decrease tar content, a combination of both of these experimental conditions was utilized for the final experimental run.

Table 5.3. Product gas composition data of RDF pellet steam gasification (20% steam) in the BFBR with changes in gasification temperature and oxygen introduction (nitrogen free basis)

Gas components	900 °C	S.P. 800 °C A.V. 830 °C 500 ppm O_2	S.P. 900 °C A.V. 930 °C 500 ppm O_2
Hydrogen	36.1%	28.3%	29.0%
Methane	10.7%	10.3%	11.6%
CO	23.1%	26.7%	26.0%
CO_2	15.9%	21.1%	18.7%
Ethylene	7.9%	8.2%	7.5%
Ethane	0.16%	0.21%	0.07%
Acetylene	5.3%	4.4%	6.8%
Propylene	0.45%	0.53%	0.13%
n-Butane	0.13%	0.11%	0.05%
1,3 Butadiene	0.30%	0.23%	0.12%

The set temperature of 900 °C rises up to 930 °C due to combustion heat when oxygen is introduced into the reactor. The gas composition is rich in both hydrogen as well

as CO_2 since higher temperature promotes hydrogen production while oxygen forms more CO_2. Moreover, there is a marked decrease in the $C_2 – C_4$ hydrocarbon content (tar proxies) indicating that the tar content has also diminished. Finally, the carbon recovery in the gas fraction increased significantly to 86.4% indicating that the combination of higher temperature (930 °C) and 500 ppm of oxygen into steam gasification of RDF pellets results in the lowest tar production and highest carbon recovery in the gas fraction.

Although a decrease in the $C_2 – C_4$ hydrocarbons is desirable in a tar reduction perspective, they are more valuable with respect to heat content and as chemical precursors than CO_2.. In order to understand if the introduction of oxygen decreased the product gas value, a comparison of the Lower Heating Values (LHV) of the product gases of the different steam gasification runs with and without oxygen and at different temperatures is listed in Table 5.4. All the product gases except CO_2 contributed towards the LHV calculation. Two types of LHV values are reported in the table. The first LHV is the heating value of the product gases based on 1 Nm^3 of the steady-state gas volume generated. While the second LHV is the heating value of the product gases based on 1 kg of feed consumed.

Table 5.4. Lower heating values and thermal efficiency of product gases from the steam gasification of RDF pellets in the BFBR with and without oxygen and at different gasification temperatures (nitrogen free basis)

	20% steam 800 °C	20% steam 900 °C	20% steam 500 ppm O_2 830 °C	20% steam 500 ppm O_2 930 °C
LHV (MJ/Nm^3) Gas volume basis	21.9	18.0	17.1	17.9
LHV (MJ/kg) Feed mass basis	17.4	18.0	16.3	18.7
Thermal efficiency	76.3%	78.8%	71.5%	81.9%

The heating value of the product gases based on the sheer volume of the product gases is the highest for the steam gasification run at 800 °C since considerable amounts of $C_2 – C_4$ hydrocarbons were produced. The lowest heating value is for the steam gasification run with 500 ppm oxygen at 830 °C. This is because of increased CO_2 concentration in the product gases that does not contribute towards the LHV of the gas. When the LHV based on the amount of feed used is compared, the steam gasification run at 930 °C with 500 ppm oxygen has the highest value. This is due to significant carbon recovery in the gas fraction (86.4%) and an absolute increase in the volume of the gas produced. Steam gasification runs at 800 °C and 900 °C without oxygen have lower LHV on the feed mass basis because of lower carbon recoveries in the gas fraction (72.4% and 73.6% respectively) even though they have higher fractions of $C_2 – C_4$ hydrocarbons.

LHV values of all the experimental runs are at par or higher compared to the values obtainedfor steam gasification of biomass [6,12,14,41] validating the process conditions used. An efficient parameter used to identify optimum gasification conditions is thermal efficiency, defined as the ratio of LHV of product gas per kg of feed consumed over the LHV of the feed per kg of feed [14]. Table 5.4 shows the thermal efficiencies for the different experimental runs based on the RDF feed LHV (22.82 MJ/kg). It is seen that the final experiment with higher temperature and oxygen has the highest thermal efficiency.

5.4 Conclusions

Gasification of RDF pellets and pine was carried out in a custom designed multistage bubbling fluidized bed reactor (BFBR). The three-stage BFBR was designed in order to separate particles based on their particle size and densities. The first stage (bottom

zone) is designed to quickly heat the feedstock to a high temperature to achieve rapid pyrolysis. The second stage has a larger cross-sectional area in order to minimize entrainment of unconverted feed and to increase the residence time to gasify char and decompose volatiles into low molecular weight gases. The diameter of the third stage is even greater to permit only the ash particles (lowest density) to leave the reactor with the gases.

The primary objective of this research was to reduce tar generation and improve carbon recovery in the gas fraction. CO_2 gasification of pine and RDF pellets was carried out around 800 °C where the major product gas was CO followed by hydrogen and methane. The CO_2 product gas could not be distinguished from the reactant CO_2 gas. Therefore, CO_2 was excluded in calculating the carbon recovery, leading to a low estimate of carbon (~55%). A larger variety of product gases were generated in the steam (20% steam 80% nitrogen) gasification of pine and RDF pellets which are likely a result of steam reforming reactions. Almost equal molar fractions of hydrogen and CO were generated since steam was used as the gasification agent. The carbon recovery in the gas fraction during RDF pellet steam gasification was increased to 72.4%, which is expected to be a result of generation of $C_2 – C_4$ hydrocarbons (steam reforming of higher hydrocarbons) as well as the ability to quantify CO_2 as a product gas.

A further increase of carbon recovery in the gas fraction and decrease in tar production for steam gasification of RDF pellets was investigated by modifying the experimental conditions. Increasing the gasification temperature in the middle zone resulted in higher hydrogen production and less $C_2 – C_4$ hydrocarbons. $C_2 – C_4$ hydrocarbons are considered as proxy tars since they have been identified to follow the

same trend as tar production [36]. Thus, increased temperature resulted in reduced tar generation. Lower tar production and higher gas fraction at increasng temperatures is most likely a combination of enhanced gas production during the initial pyrolysis phase, steam reforming of tars (including cracking) and the endothermic reactions of char gasification. Carbon recovery remained relatively similar for the three temperatures since the hydrogen fraction does not contribute to the carbon in the gas fraction.

The second parameter studied in this work is the introduction of small amounts of oxygen in the steam gasification of RDF pellets. An increase of oxygen from 0 ppm to 500 ppm resulted in an increase in the CO_2 concentration in the gas fraction as expected. Counterintuitively, the hydrogen fraction increased with increasing oxygen concentration. This was a result of an increase in the temperature of the gasification zone due to the release of combustion heat. This was verified by conducting the same experiment in oxygen free conditions but at the increased temperature. Addition of oxygen also resulted in decreased $C_2 – C_4$ hydrocarbons indicating reduced tar production. The carbon recovery in the gas fraction; however, did not increase significantly with the introduction of oxygen, even with enhanced CO_2 production. This is probably due to the reduced generation of $C_2 – C_4$ hydrocarbons.

Similar gas compositions obtained from oxygen injection from top and bottom indicated that for the current BFBR design, oxygen injection point is immaterial. The highest carbon recovery in the gas fraction (86.4%), lowest tar generation (lowest tar proxies) and the highest thermal efficiency (81.9%) was obtained by a combination of increased temperature (930 °C) and 500 ppm of oxygen in the steam gasification of RDF pellets.

5.5 References

[1] U. Arena, Process and technological aspects of municipal solid waste gasification. A review, Waste Manag. 32 (2012) 625–639. http://dx.doi.org/10.1016/j.wasman.2011.09.025.

[2] F. Parrillo, E. Maggio, A. Pettinau, O. Annoscia, A. Saponaro, Fluidized Bed Gasification of Biomass : Design and Operating Criteria From a Pilot Scale Study, in: Sixth Int. Symp. Energy from Biomass Waste, 2016: pp. 14–17.

[3] U. Arena, F. Di Gregorio, Energy generation by air gasification of two industrial plastic wastes ina pilot scale fluidized bed reactor, Energy. 68 (2014) 735–743. doi:10.1016/j.energy.2014.01.084.

[4] G. Ruoppolo, P. Ammendola, R. Chirone, F. Miccio, H_2-rich syngas production by fluidized bed gasification of biomass and plastic fuel, Waste Manag. 32 (2012) 724–732. doi:10.1016/j.wasman.2011.12.004.

[5] U. Arena, F. Di Gregorio, Gasification of a solid recovered fuel in a pilot scale fluidized bed reactor, Fuel. 117 (2014) 528–536. doi:10.1016/j.fuel.2013.09.044.

[6] Z.A.B.Z. Alauddin, P. Lahijani, M. Mohammadi, A.R. Mohamed, Gasification of lignocellulosic biomass in fluidized beds for renewable energy development: A review, Renew. Sustain. Energy Rev. 14 (2010) 2852–2862. doi:10.1016/j.rser.2010.07.026.

[7] G. Xiao, B. Jin, Z. Zhong, Y. Chi, M. Ni, K. Cen, R. Xiao, Y. Huang, H. Huang, Experimental study on MSW gasification and melting technology, J. Environ. Sci. 19 (2007) 1398–1403. doi:10.1016/S1001-0742(07)60228-9.

[8] P. Quaak, H. Knoef, S. Hubert E., Energy from biomass: a review of combustion and gasification technologies. Vol 23, World Bank Publications, 1999.

[9] S. Begum, M.G. Rasul, D. Akbar, D. Cork, An Experimental and Numerical Investigation of Fluidized Bed Gasification of Solid Waste, Energies. 7 (2014) 43–61. doi:10.3390/en7010043.

[10] Y.D. Kim, C.W. Yang, B.J. Kim, K.S. Kim, J.W. Lee, J.H. Moon, W. Yang, T.U. Yu, U. Do Lee, Air-blown gasification of woody biomass in a bubbling fluidized bed gasifier, Appl. Energy. 112 (2013) 414–420. doi:10.1016/j.apenergy.2013.03.072.

[11] M.S. Masnadi, J.R. Grace, X.T. Bi, C.J. Lim, N. Ellis, Y.H. Li, A.P. Watkinson, Single-fuel steam gasification of switchgrass and coal in a bubbling fluidized bed: A comprehensive parametric reference for co-gasification study, Energy. 80 (2015) 133–147. doi:10.1016/j.energy.2014.11.054.

[12] D. Barisano, G. Canneto, F. Nanna, E. Alvino, G. Pinto, A. Villone, M. Carnevale, V. Valerio, A. Battafarano, G. Braccio, Steam/oxygen biomass gasification at pilot scale in an internally circulating bubbling fluidized bed reactor, Fuel Process. Technol. (2015). doi:10.1016/j.fuproc.2015.06.008.

[13] M.L. Mastellone, L. Zaccariello, D. Santoro, U. Arena, The O_2-enriched air gasification of coal, plastics and wood in a fluidized bed reactor, Waste Manag. 32 (2012) 733–742. doi:10.1016/j.wasman.2011.09.005.

[14] J. Gil, M.P. Aznar, M.A. Caballero, E. Francés, J. Corella, Biomass Gasification in Fluidized Bed at Pilot Scale with Steam−Oxygen Mixtures. Product Distribution for Very Different Operating Conditions, Energy & Fuels. 11 (1997) 1109–1118. doi:10.1021/ef9602335.

[15] D. Serrano, M. Kwapinska, A. Horvat, S. Sanchez-Delgado, J.J. Leahy, Cynara cardunculus L. gasification in a bubbling fluidized bed: The effect of magnesite and olivine on product gas, tar and gasification performance, Fuel. 173 (2016) 247–259. doi:10.1016/j.fuel.2016.01.051.

[16] M. Siedlecki, R. Nieuwstraten, E. Simeone, W. De Jong, A.H.M. Verkooijen, Effect of magnesite as bed material in a 100 kW_{th} steam-oxygen blown circulating fluidized-bed biomass gasifier on gas composition and tar formation, Energy and Fuels. 23 (2009) 5643–5654. doi:10.1021/ef900420c.

[17] U. Arena, L. Zaccariello, M.L. Mastellone, Fluidized bed gasification of waste-derived fuels, Waste Manag. 30 (2010) 1212–1219. doi:10.1016/j.wasman.2010.01.038.

[18] C. Li, K. Suzuki, Tar property, analysis, reforming mechanism and model for biomass gasification-An overview, Renew. Sustain. Energy Rev. 13 (2009) 594–604. doi:10.1016/j.rser.2008.01.009.

[19] J.W. Kook, H.M. Choi, B.H. Kim, H.W. Ra, S.J. Yoon, T.Y. Mun, J.H. Kim, Y.K. Kim, J.G. Lee, M.W. Seo, Gasification and tar removal characteristics of rice husk in a bubbling fluidized bed reactor, Fuel. 181 (2016) 942–950. doi:10.1016/j.fuel.2016.05.027.

[20] M.L. Mastellone, L. Zaccariello, Gasification of polyethylene in a bubbling fluidized bed operated with the air staging, Fuel. 106 (2013) 226–233. doi:10.1016/j.fuel.2012.12.049.

[21] C. Pfeifer, H. Hofbauer, Development of catalytic tar decomposition downstream from a dual fluidized bed biomass steam gasifier, Powder Technol. 180 (2008) 9–16. doi:10.1016/j.powtec.2007.03.008.

[22] M.A. Caballero, J. Corella, M.P. Aznar, J. Gil, Biomass gasification with air in fluidized bed. Hot gas cleanup with selected commercial and full-size nickel-based catalysts, Ind. Eng. Chem. Res. 39 (2000) 1143–1154. doi:10.1021/ie990738t.

[23] S. Kraft, F. Kirnbauer, H. Hofbauer, Investigations using a cold flow model of char mixing in the gasification reactor of a dual fluidized bed gasification plant, Powder Technol. 316 (2017) 687–696. doi:10.1016/j.powtec.2016.10.032.

[24] D. Gidaspow, Multiphase flow and fluidization: continuum and kinetic theory descriptions, Academic press, 1994.

[25] D. Geldart, Types of gas fluidization, Powder Technol. 7 (1973) 285–292. doi:10.1016/0032-5910(73)80037-3.

[26] S. J. Juutilainen, P. A. Simell, A. O. I. Krause, Zirconia: selective oxidation catalyst for removal of tar and ammonia from biomass gasification gas. Applied Catalysis B: Environmental. 62 (2006) 86-92.

[27] T. Renganathan, M. V. Yadav, S. Pushpavanam, R.K. Voolapalli, Y.S. Cho, CO_2 utilization for gasification of carbonaceous feedstocks: A thermodynamic analysis, Chem. Eng. Sci. 83 (2012) 159–170. doi:10.1016/j.ces.2012.04.024.

[28] M.A. Lopez-Velazquez, V. Santes, J. Balmaseda, E. Torres-Garcia, Pyrolysis of orange waste: A thermo-kinetic study, J. Anal. Appl. Pyrolysis. 99 (2013) 170–177. doi:10.1016/j.jaap.2012.09.016.

[29] K. Li, R. Zhang, J. Bi, Experimental study on syngas production by co-gasification of coal and biomass in a fluidized bed, Int. J. Hydrogen Energy. 35 (2010) 2722–2726. doi:10.1016/j.ijhydene.2009.04.046.

[30] L. Wang, C.L. Weller, D.D. Jones, M.A. Hanna, Contemporary issues in thermal gasification of biomass and its application to electricity and fuel production, Biomass and Bioenergy. 32 (2008) 573–581. doi:10.1016/j.biombioe.2007.12.007.

[31] D. Roberts, D. Harris, Char Gasification Kinetics in Mixtures of CO_2 and H_2O: The Role of Partial Pressure in Determining the Extent of Competitive Inhibition, Energy & Fuels. 28 (2014) 7643–7648. http://pubs.acs.org/doi/abs/10.1021/ef502101b.

[32] F. Li, Q. Yan, J. Huang, J. Zhao, Y. Fang, J. Wang, Lignite-char gasification mechanism in mixed atmospheres of steam and CO_2 at different pressures, Fuel Process. Technol. 138 (2015) 555–563. http://dx.doi.org/10.1016/j.fuproc.2015.06.035.

[33] P. Chaiprasert, T. Vitidsant, Promotion of coconut shell gasification by steam reforming on nickel-dolomite, Am. J. Appl. Sci. 6 (2009) 332–336. doi:10.3844/ajassp.2009.332.336.

[34] F. Pinto, C. Franco, R.N. André, C. Tavares, M. Dias, I. Gulyurtlu, I. Cabrita, Effect of experimental conditions on co-gasification of coal, biomass and plastics wastes with air/steam mixtures in a fluidized bed system, Fuel. 82 (2003) 1967–1976. doi:10.1016/S0016-2361(03)00160-1.

[35] M.M. Yu, M.S. Masnadi, J.R. Grace, X.T. Bi, C.J. Lim, Y. Li, Co-gasification of biosolids with biomass: Thermogravimetric analysis and pilot scale study in a bubbling fluidized bed reactor, Bioresour. Technol. 175 (2015) 51–58. doi:10.1016/j.biortech.2014.10.045.

[36] D. Ross, R. Noda, M. Horio, A. Kosminski, P. Ashman, P. Mullinger, Axial gas profiles in a bubbling fluidised bed biomass gasifier, Fuel. 86 (2007) 1417–1429. doi:10.1016/j.fuel.2006.11.028.

[37] K. Sjöström, G. Chen, Q. Yu, C. Brage, C. Rosén, Promoted reactivity of char in co-gasification of biomass and coal: Synergies in the thermochemical process, Fuel. 78 (1999) 1189–1194.

[38] Y. Wang, C.M. Kinoshita, Experimental analysis of biomass gasification with steam and oxygen, Sol. Energy. 49 (1992) 153–158. doi:10.1016/0038-092X(92)90066-J.

[39] M.L. Mastellone, L. Zaccariello, Gasification of polyethylene in a bubbling fluidized bed operated with the air staging, Fuel. 106 (2013) 226–233. doi:10.1016/j.fuel.2012.12.049.

[40] M. Mayerhofer, S. Fendt, H. Spliethoff, M. Gaderer, Fluidized bed gasification of biomass - In bed investigation of gas and tar formation, Fuel. 117 (2014) 1248–1255. doi:10.1016/j.fuel.2013.06.025.

[41] H. Karatas, H. Olgun, F. Akgun, Experimental results of gasification of cotton stalk and hazelnut shell in a bubbling fluidized bed gasifier under air and steam atmospheres, Fuel. 112 (2013) 494–501. doi:10.1016/j.fuel.2013.04.025.

CHAPTER 6. CONCLUSIONS AND RECOMMENDATIONS FOR FUTURE WORK

6.1 Conclusions

The overarching goal of this dissertation was to understand the gasification behavior of model Refuse Derived Fuel (RDF) pellets at both a fundamental level as well as at conditions of practical significance. The feedstock considered in this study is a combination of nine different components representative of the real waste. The chars used for fundamental analysis were produced at a low heating rate (20 K/min) either in a TGA or a tubular quartz reactor. Further, char gasification was studied separately in the TGA by analyzing the weight change when exposed to a gasifying agent, such as CO_2 or steam, at high temperature (i.e. 700 – 1000 ℃). The industrially relevant experimental conditions (high heating rate, high temperature, continuous flow reaction) were further implemented in the gasification studies of model RDF pellets in a Bubbling Fluidized Bed Reactor (BFBR).

Chapter 2 dealt with the low-heating rate pyrolysis and gasification of model RDF in a thermogravimetric analyzer (TGA). After identifying the components for the model RDF composition, a comparison of the individual component pyrolysis and gasification behavior, with that of the RDF composite was performed. Pyrolysis of model RDF composite was similar to the additive profiles of the individual components, with respect to the decomposition rate, product yields, heat of reaction and gas composition. In contrast,

the CO_2 gasification reactivity of RDF composite was much higher than the gasification reactivity of a combination of all the individual components. The observed synergy is attributed to potassium redistribution from orange peel to the other constituents of the RDF composite. Additionally, calcium from paper components had a catalytic effect for the initial gasification reactivity. The proposed inorganic index encompassing the catalytic inorganics (K, Ca) and inhibiting inorganics (Si, P) is a good indicator of the gasification reactivities of all the components.

Since potassium and calcium proved to be efficient catalytic agents during gasification, the catalytic activity of these inorganics in both CO_2 and steam was explored further in Chapter 3. Avicel (microcrystalline cellulose devoid of intrinsic inorganics) was used as a model carbon compound to illustrate the catalytic effect of potassium. A saturation in the gasification reactivity was observed at 5% potassium loading on Avicel chars below 60% conversion. At higher conversions, a maximum was observed that was dependent on the [K / residual carbon] ratio for both steam and CO_2 gasification. The predominant chemical phases of potassium are proposed to be K_2O and metallic potassium in CO_2 gasification, while they are KOH and metallic potassium in steam gasification. Counterintuitively, potassium-rich chars demonstrated a higher reactivity when hydrogen was present due to the formation of KOH, which is a better gasification catalyst than K_2CO_3 or K_2O [1,2]. The same active sites participated in both CO_2 and steam gasification based on gas – switchover experiments. During co-gasification using steam and CO_2 at the same time, steam was found to be dominant even down to 30% steam and 70% CO_2 mixtures.

In Chapter 4, the effect of the pyrolysis heating rate on the physicochemical properties of the char and its gasification reactivity were investigated. RDF feed pellets

were pyrolyzed at both high heating rate (HHR, 3500°C/min) and low heating rate (LHR, 20 °C/min) conditions and were characterized using several techniques. HHR chars were more macroporous than LHR chars possibly due to the sudden release of volatiles when the char was exposed to high temperatures in HHR pyrolysis. Although the distribution of inorganics in HHR and LHR chars was similar, the low residence time HHR char resulted in incomplete potassium distribution compared to high residence time HHR char. This was confirmed by quantitative EDX maps generated by a novel image recognition methodology using a MATLAB code. The O/C content and the Raman band ratio, $I_{D1}/ I_{G,}$ were found to be good indicators for the initial reactivity of the chars in CO_2 gasification. A combination of macroporous and mesoporous surface area related very well with the overall reactivity of all the chars.

In Chapter 5, the continuous gasification of model RDF pellets was performed in a BFBR. A three-stage fluidized bed reactor was developed for CO_2 and steam gasification of the feed to recover the maximum amount of carbon in the gas fraction and to reduce tar formation. The flexibility of the constructed BFBR was demonstrated by the successful gasification of both pine and model RDF pellets separately. CO_2 gasification resulted in a large fraction of CO while steam gasification produced almost equal molar concentrations of hydrogen and CO. C_2 - C_4 hydrocarbons were considered as tar proxies for the purpose of comparison of results from different experimental conditions [3]. An increase in gasification temperature in the middle zone of the BFBR led to the formation of more hydrogen and lowered the $C_2 – C_4$ hydrocarbons (tar). This is most likely a combination of enhanced gas production during the initial pyrolysis phase, steam reforming of tars (including cracking) and the endothermic reactions of char gasification. Introduction of a

small amount of oxygen (500 ppm) resulted in an increase in the CO_2 fraction and a decrease in the C_2 – C_4 hydrocarbons fraction due to combustion and tar reforming reactions. However, an increase in hydrogen fraction was also observed which was verified to be a result of increased temperature due to the release of combustion heat. Finally, a combination of increased temperature (930 °C) and 500 ppm of oxygen used in the steam gasification of RDF pellets resulted in the lowest tar generation (lowest tar proxies), the highest carbon recovery in the gas fraction (86.4%) and the highest thermal efficiency (81.9%).

6.2 Recommendation for future work

6.2.1 Langmuir-Hinshelwood kinetic models for RDF gasification in CO_2 and steam

Chapter 3 of the dissertation discussed the sharing of active sites between CO_2 and steam based on gas-switchover experiments. The reactivity of steam dominates over that of CO_2 in the co-gasification experiments with varying partial pressures of steam and CO_2 down to 30% steam – 70% CO_2 mixture. However, at low partial pressure of steam (0.01 MPa), replacing nitrogen with CO_2 increased the overall gasification reactivity. This implies that a fraction of the active sites are not occupied by steam in dilute conditions. Thus, at dilute conditions, active sites unoccupied by steam are occupied by CO_2. This leads to a deviation from the common active sites observation at concentrated steam conditions. This shift in kinetics is further complicated by the presence of hydrogen and CO released during the gasification process, which cause inhibition by adsorbing onto active sites [4,5]. The Langmuir-Hinshelwood mechanism is one of the most commonly used models to describe the gasification reaction kinetics [6,7]. Both common and separate

active site kinetics can be verified by using the L-H kinetic models in future studies. Various partial pressures of gasifying agents CO_2 and steam could be used along with externally introduced inhibiting agents, H_2 and CO. By determination of all the kinetic parameters associated with the gases, a comprehensive kinetic model can be established.

6.2.2 Optimization of the amount of oxygen required for steam gasification of RDF pellets in the BFBR

Use of small amounts of oxygen in the BFBR gasification serves two purposes: increased carbon recovery in the gas fraction by formation of more CO_2 and, supplementary energy provided by combustion heat. Additionally, results in Chapter 5 showed that the use of 500 ppm of oxygen in the steam gasification of RDF pellets increased the hydrogen fraction due to increased reactor temperature as a result of the heat generated through combustion. However, use of large amounts of oxygen would lead to predominantly a combustion reaction in the reactor, converting most of the carbon into CO_2 which is not a desirable product. Thus, a balance needs to be attained with the appropriate amount of oxygen needed to maximize the carbon and hydrogen recovery in the gas fraction while maintaining a reasonable quality (CO + H_2 content) of syngas produced. An economic analysis with respect to the cost involved with the use of oxygen and steam against the increased syngas quality is recommended to determine the optimized amount of oxygen required in the steam gasification of RDF pellets.

6.2.3 Co-gasification of RDF pellets with coal or biomass in the BFBR

The scale-up of gasification of RDF pellets to an industrial-scale BFBR may cause concerns regarding the cost associated with pre-processing large volumes of waste to make

it suitable for gasification [8]. Moreover, a higher amount of impurities associated with a waste feed stream may require additional syngas cleaning strategies. Instead, co-gasification of RDF feed with coal or biomass would result in decreased air pollutants from coal gasification [9], improved reliability of feed by compensating for the seasonal dependence associated with biomass [10] while decreasing the overall carbon losses [8,9]. The high energy content of coal would improve the overall thermal efficiency of the process, while requiring lower gasification temperatures, due to the synergy expected from the inorganics present in the RDF feed [11]. A reduction in the tar and particulate matter with increased carbon recovery in syngas with co-gasification of coal with biomass / waste has been reported [8,9]. Moreover, an easy incorporation of RDF feed into the well-established coal gasification infrastructure is also appealing. Hence, future studies could be carried out with a mixture of RDF pellets and coal or RDF pellets and biomass in the BFBR. Since feed flow rates need to be controlled at higher precision with feed mixing, an improved feeder for accurate feed dispersion is recommended.

6.3 References

[1] T. Yokoyama, Tanaka, Toyoshima, Miyahara, Yoshida, X-Ray photoelectron spectroscopic study of the surface of carbon doped with potassium carbonate, Chem. Lett. (1980) 599–602.

[2] C. Di Blasi, A. Galgano, C. Branca, Effects of Potassium Hydroxide Impregnation on Wood Pyrolysis, Energy & Fuels. 23 (2009) 1045–1054.

[3] D. Ross, R. Noda, M. Horio, A. Kosminski, P. Ashman, P. Mullinger, Axial gas profiles in a bubbling fluidised bed biomass gasifier, Fuel. 86 (2007) 1417–1429. doi:10.1016/j.fuel.2006.11.028.

[4] W. Klose, M. Wölki, On the intrinsic reaction rate of biomass char gasification with carbon dioxide and steam, Fuel. 84 (2005) 885–892. doi:10.1016/j.fuel.2004.11.016.

[5] M. Massoudi Farid, H.J. Jeong, J. Hwang, Kinetic study on coal–biomass mixed char co-gasification with H_2O in the presence of H_2, Fuel. 181 (2016) 1066–1073. doi:10.1016/j.fuel.2016.04.130.

[6] R. Zhang, Q.H. Wang, Z.Y. Luo, M.X. Fang, K.F. Cen, Coal Char Gasification in the Mixture of H_2O, CO_2 , H_2 , and CO under Pressured Conditions, Energy & Fuels. 28 (2014) 832–839. doi:10.1021/ef4018527.

[7] S. Umemoto, S. Kajitani, S. Hara, Modeling of coal char gasification in coexistence of CO_2 and H_2O considering sharing of active sites, Fuel. 103 (2013) 14–21. doi:10.1016/j.fuel.2011.11.030.

[8] M.L. Mastellone, L. Zaccariello, U. Arena, Co-gasification of coal, plastic waste and wood in a bubbling fluidized bed reactor, Fuel. 89 (2010) 2991–3000. doi:10.1016/j.fuel.2010.05.019.

[9] L. Emami-Taba, M.F. Irfan, W.M.A. Wan Daud, M.H. Chakrabarti, Fuel blending effects on the co-gasification of coal and biomass – A review, Biomass and Bioenergy. 57 (2013) 249–263. doi:10.1016/j.biombioe.2013.02.043.

[10] R.N. André, F. Pinto, C. Franco, M. Dias, I. Gulyurtlu, M.A.A. Matos, I. Cabrita, Fluidised bed co-gasification of coal and olive oil industry wastes, Fuel. 84 (2005) 1635–1644. doi:10.1016/j.fuel.2005.02.018.

[11] K. Sjöström, G. Chen, Q. Yu, C. Brage, C. Rosén, Promoted reactivity of char in co-gasification of biomass and coal: Synergies in the thermochemical process, Fuel. 78 (1999) 1189–1194

APPENDIX A. SUPPLEMENTARY INFORMATION FOR CHAPTER 2

Figure A.1. RDF composite in a. powder form (<106 um particles) b. 2 mm pellet c. 4 mm pellet.

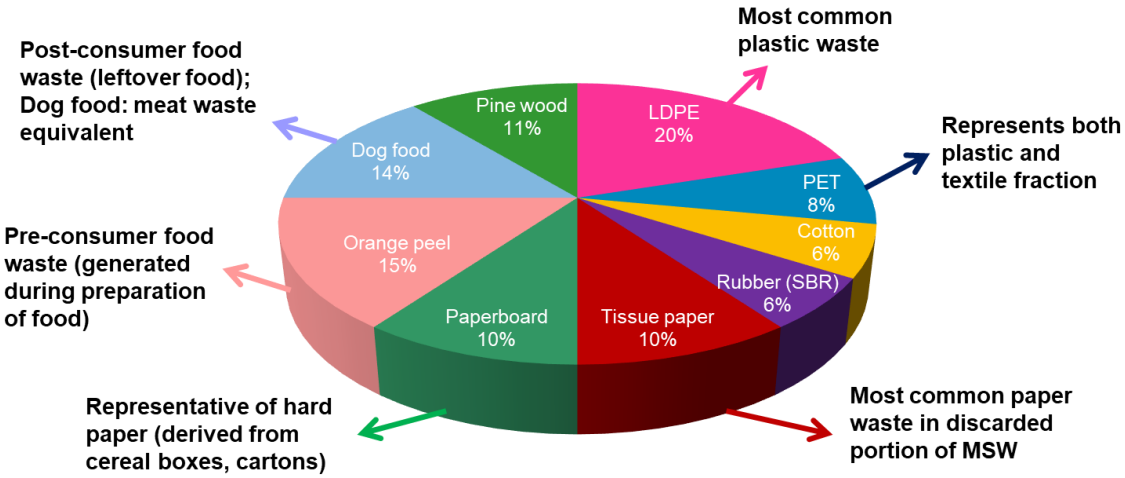

Figure A.2. Selection criteria for model RDF composition.

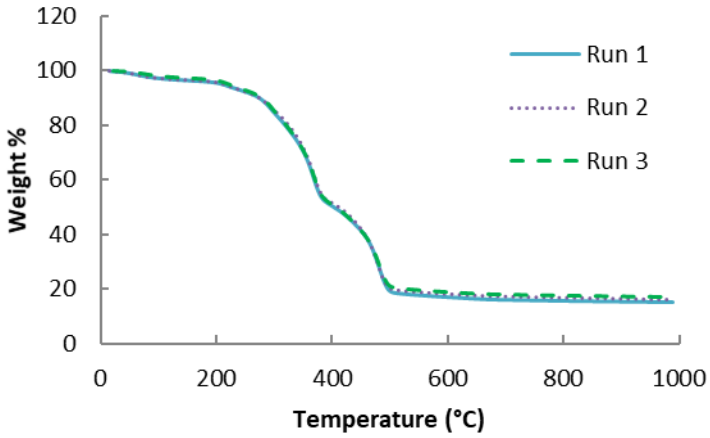

Figure A.3. Reproducibility of model RDF composite during pyrolysis (20 K/min).

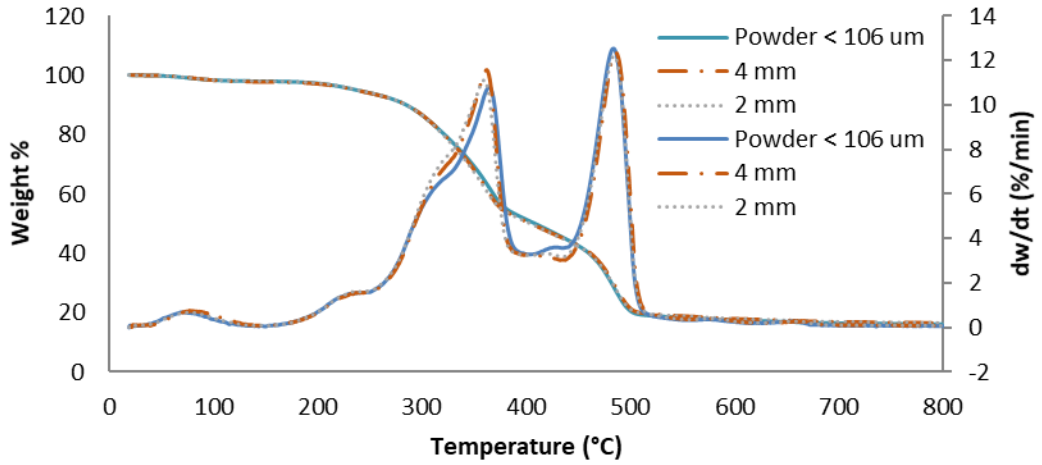

Figure A.4. TGA weight loss profiles of model RDF composite in powder form, 2 mm pellet form and 4 mm pellet form.

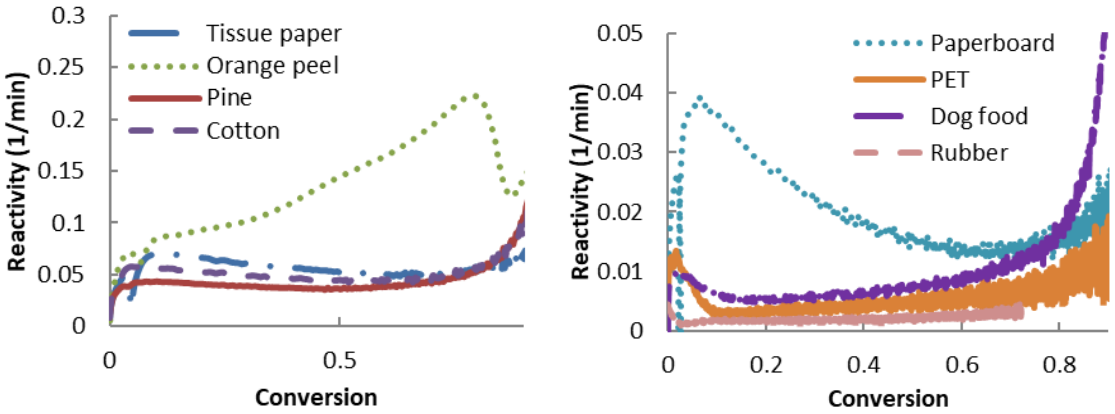

Figure A.5. Gasification reactivity profiles of individual component chars present in model RDF (divided into two plots due to different reactivity scales (y-axis); chars generated at 20 K/min up to 800 °C).

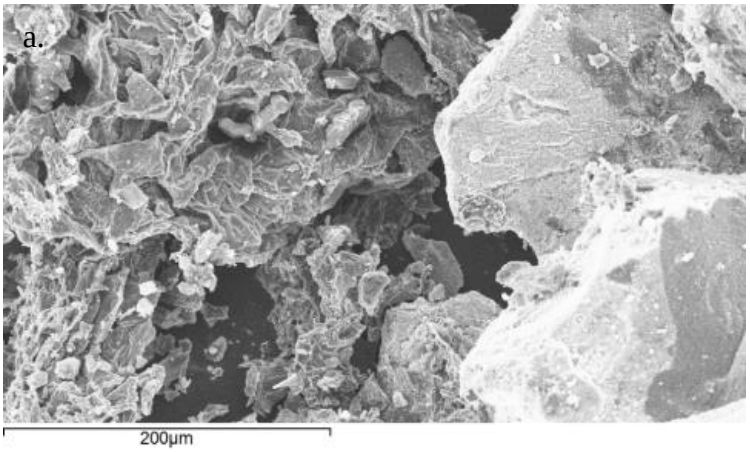

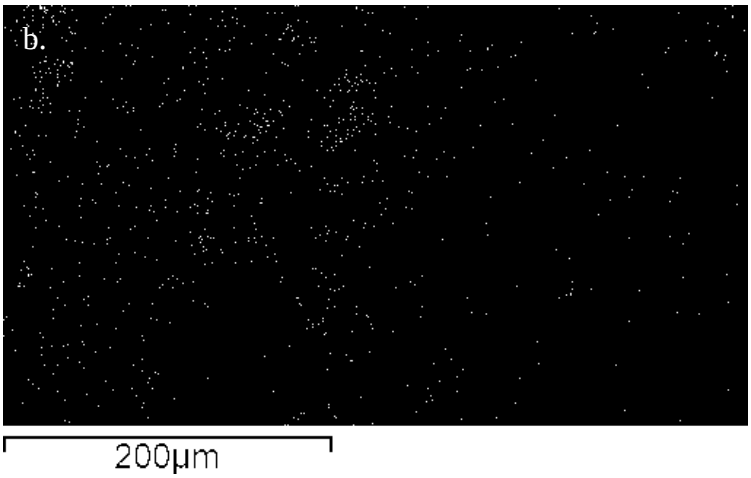

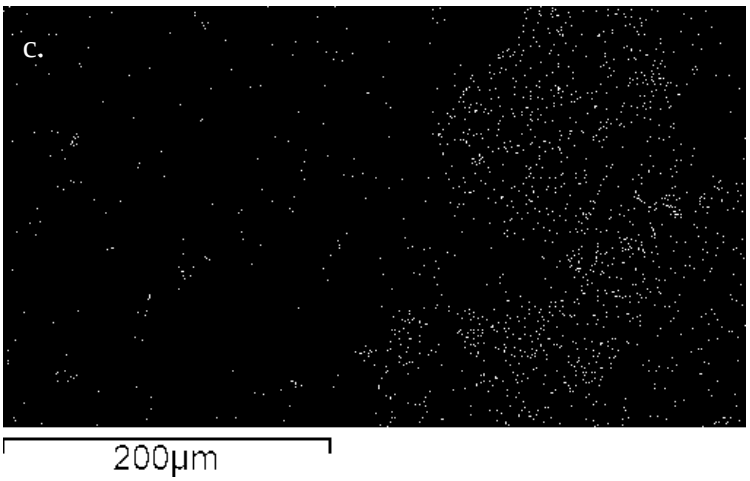

Figure A.6 a. SEM micrograph of a physical mixture of orange peel char and rubber char generated independently at 20 K/min up to 800 °C; EDX of the mixture showing b. potassium distribution over the mapped area and c. silicon distribution over the mapped area.

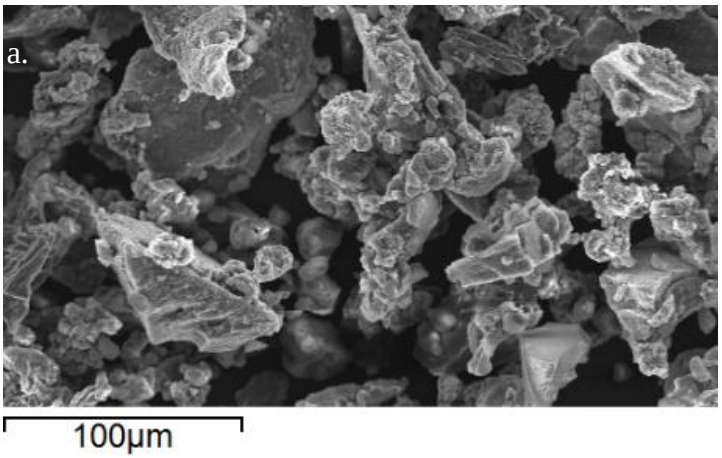

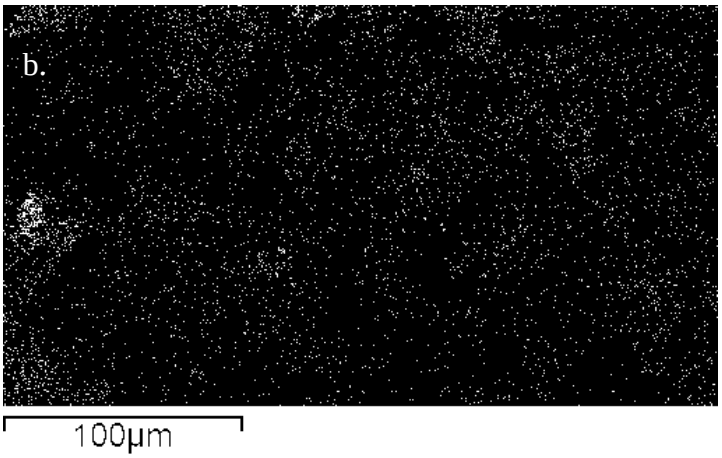

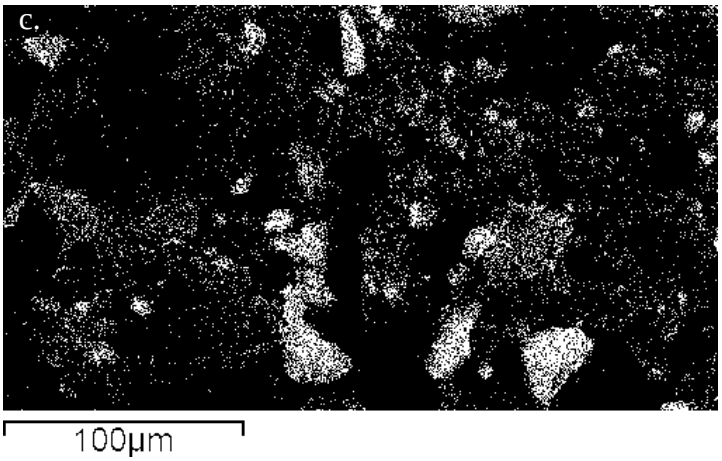

Figure A.7 a. SEM micrograph of orange peel char and rubber char mixture pyrolyzed together at 20 K/min up to 800 °C; EDX of the mixture showing b. potassium distribution over the mapped area c. silicon distribution over the mapped area.

APPENDIX B. SUPPLEMENTARY INFORMATION FOR CHAPTER 3

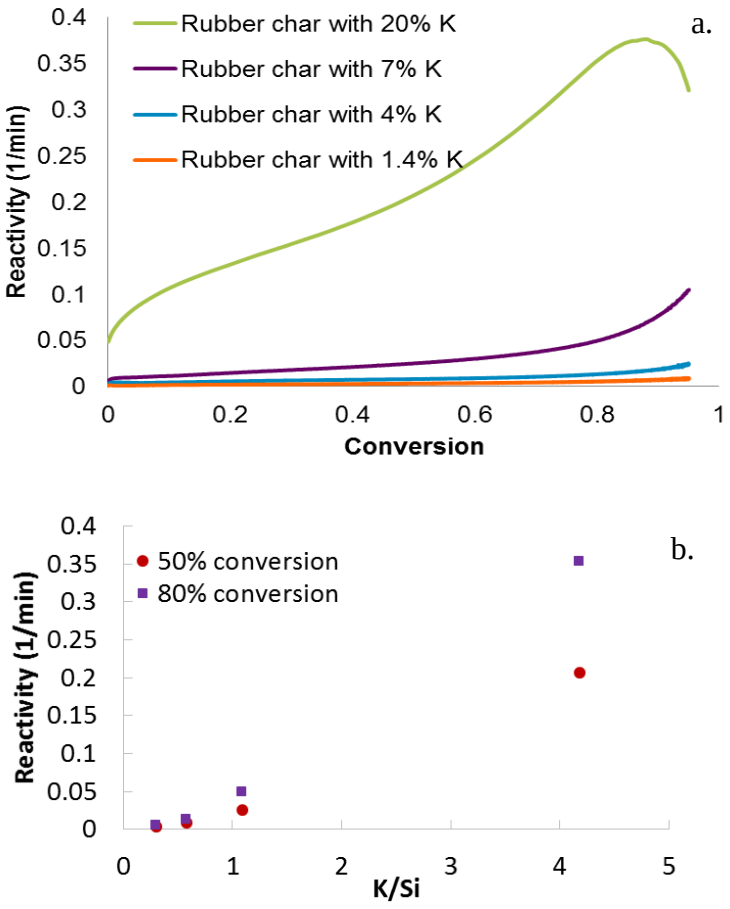

Figure B.1. CO_2 gasification reactivity of potassium-loaded rubber chars a. with varying potassium loadings b. at 50% and 80% conversions (chars generated by heating at 20 K/min up to 800 °C).

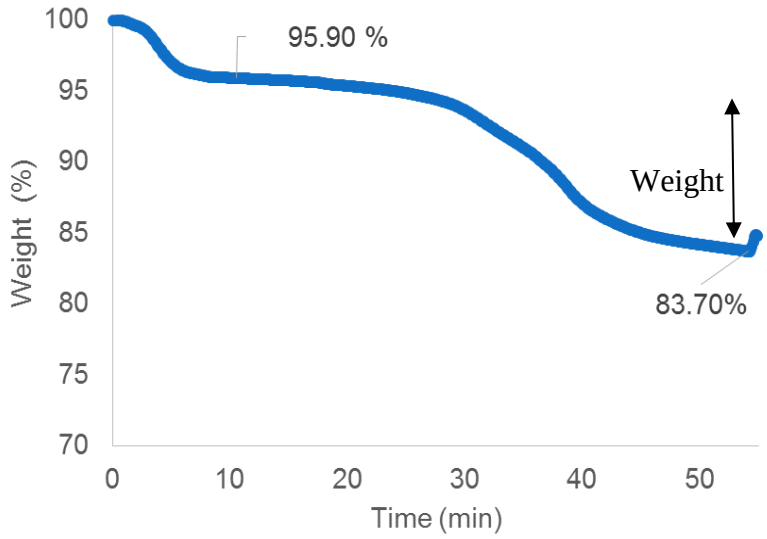

Figure B.2. Weight loss of Avicel char with 7.1% potassium during the heat-up stage (20 K/min and up to 800 °C) of the gasification in a TGA.

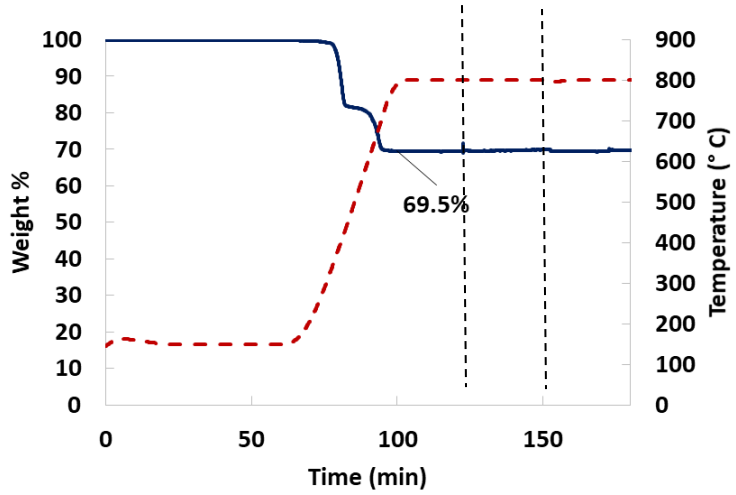

Figure B.3. Weight change analysis of calcium hydroxide in steam (20 K/min and up to 800 °C).

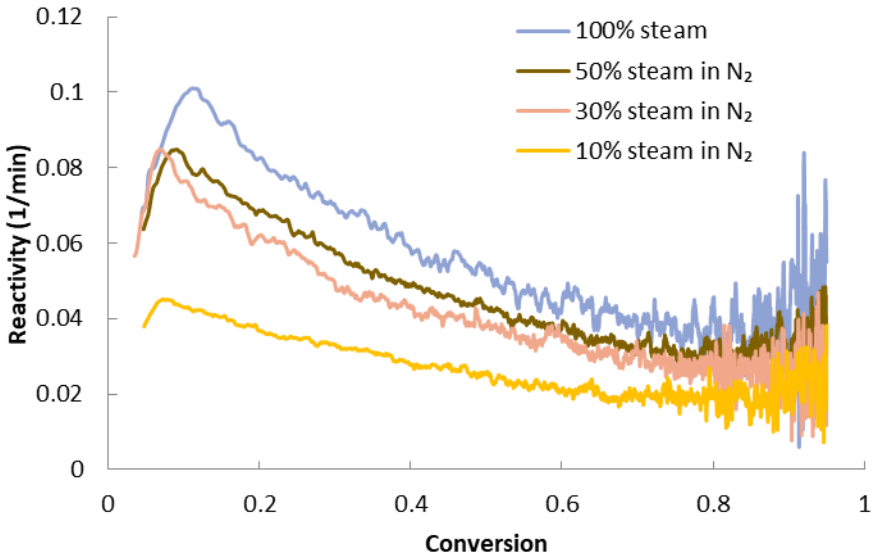

Figure B.4. Steam gasification reactivity of model RDF char at varying partial pressures of steam in a nitrogen environment.

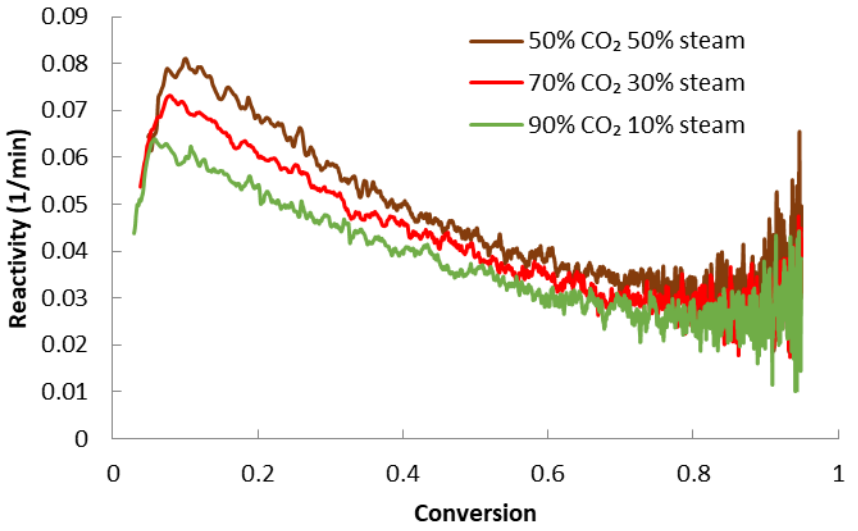

Figure B.5. Co-gasification reactivity of model RDF char at varying partial pressures of steam and CO_2 (20 K/min and up to 800 °C).

APPENDIX C. SUPPLEMENTARY INFORMATION FOR CHAPTER 4

Appendix C.1. Figures

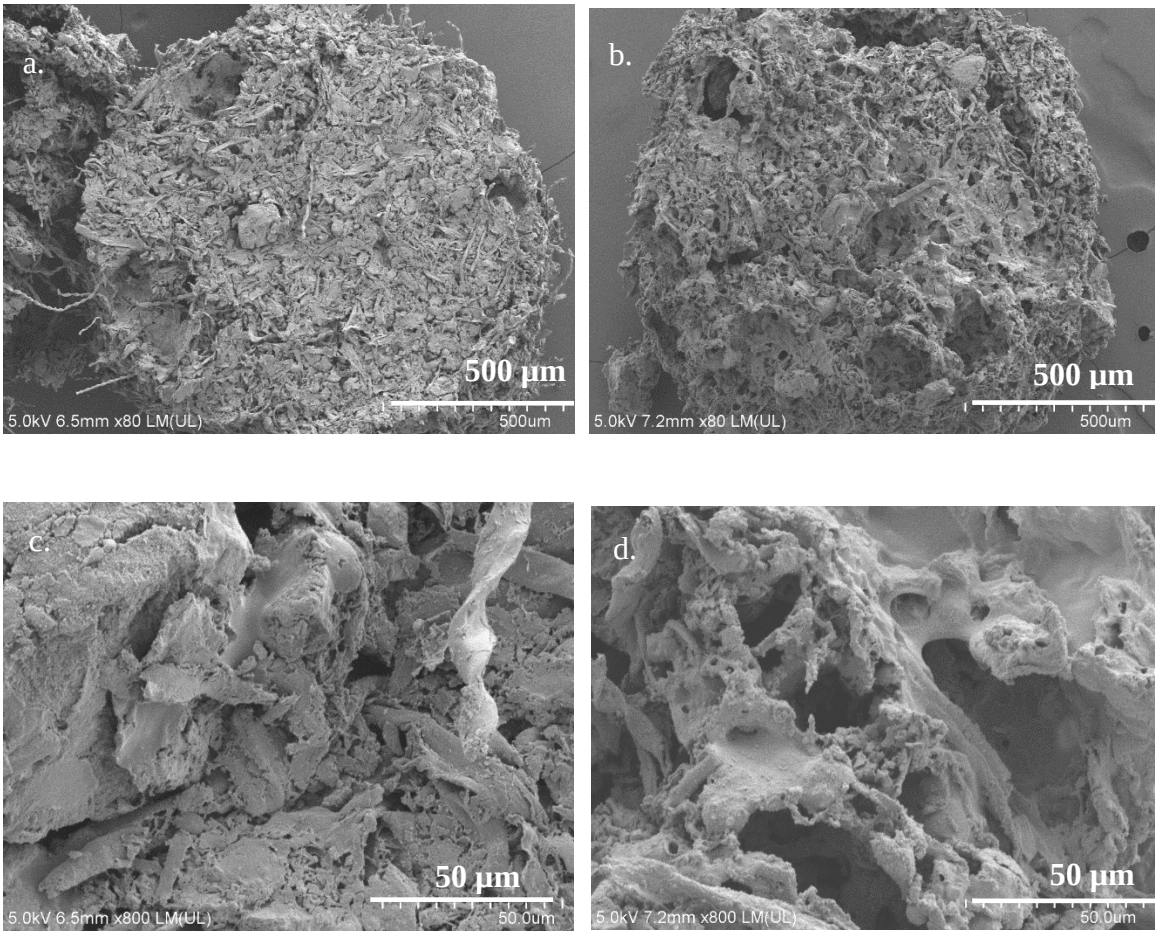

Figure C.1. Cross sectional view (top-view) of the RDF chars generated at 800 °C and a. LHR with X80 magnification b. HHR with X80 magnification c. LHR with X800 magnification d. HHR with X800 magnification.

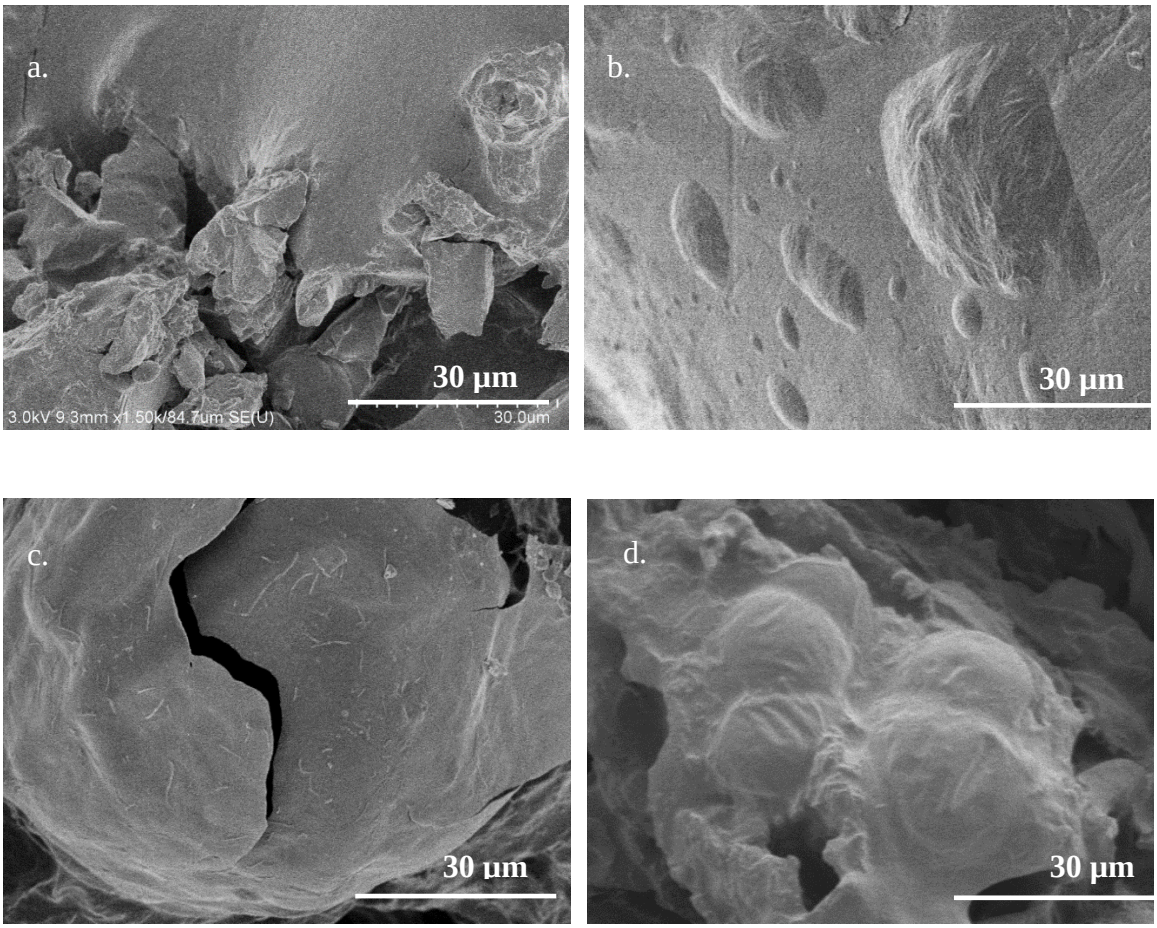

Figure C.2. SEM images of RDF HHR char produced at X1.5 K magnification generated at a and b. 250 °C, c and d. 400 °C.

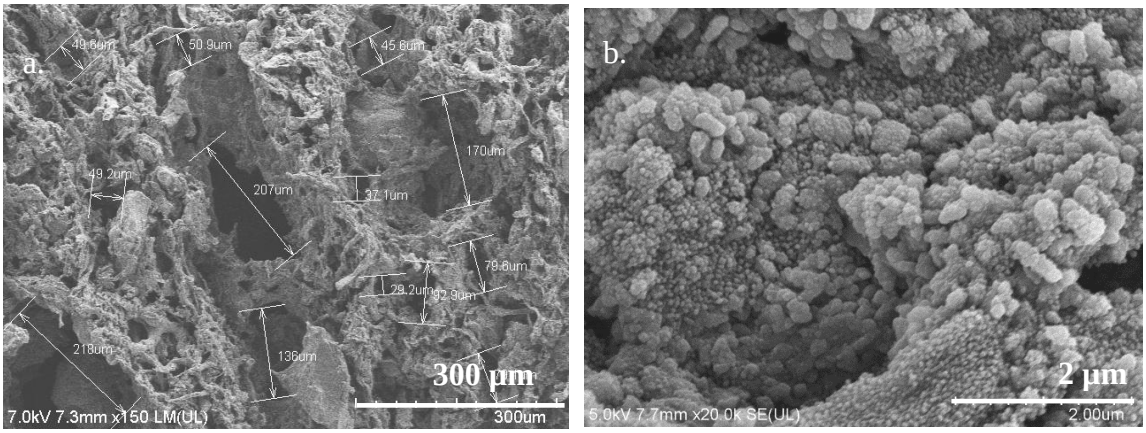

Figure C.3. SEM images of RDF HHR char with 10 seconds residence time at 800 °C with a. X150 magnification for pore measurement b. X20 K magnification.

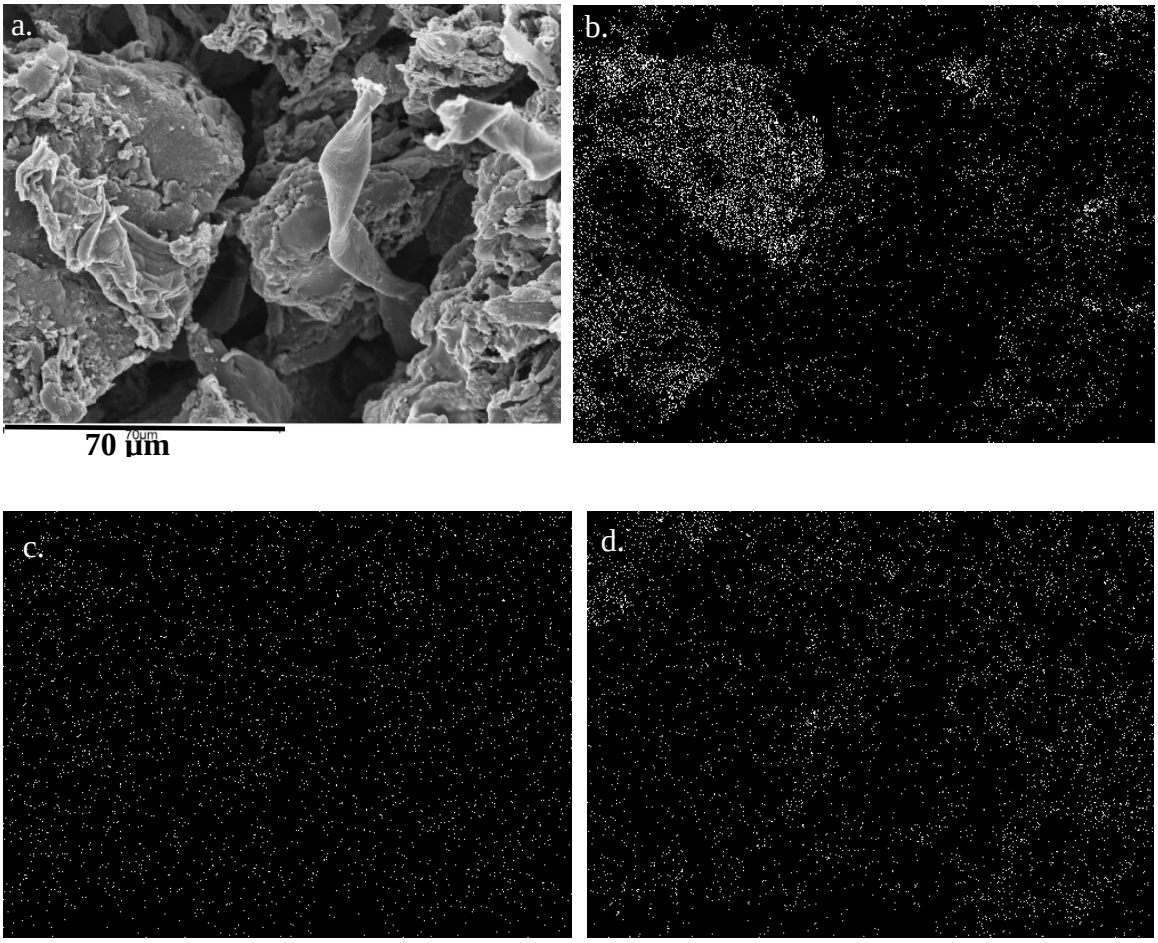

Figure C.4. EDX analysis of RDF LHR char (20 K/min and heated to 800 °C) with 1 minute residence time a. SEM image b. Silicon mapping c. Potassium mapping d. Calcium mapping.

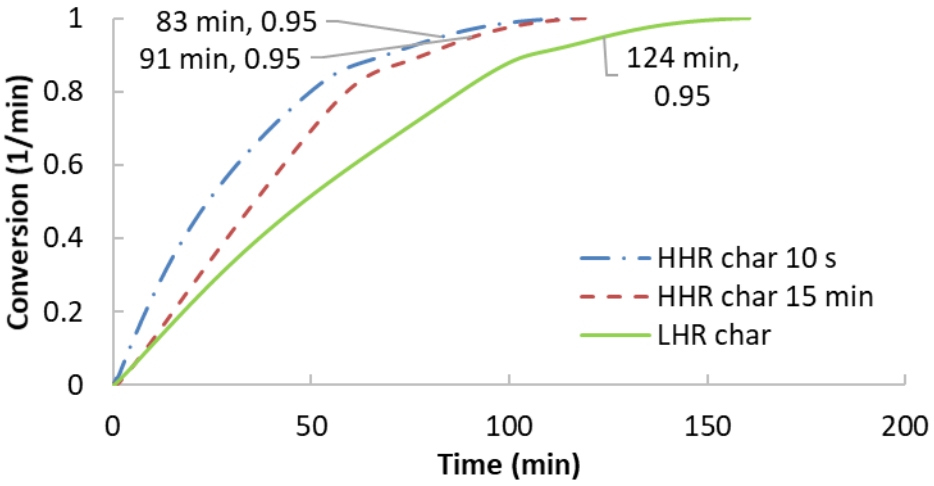

Figure C.5. Time taken to achieve complete conversion in the CO_2 gasification of RDF chars generated at different heating rates and residence times.

Appendix C.2. Tables

Table C.1. Composition of major inorganics present in the RDF chars produced at different heating rate and residence times

Pyrolysis Conditions	K (wt %)	Ca (wt %)	Si (wt %)
LHR	1.14	2.53	1.82
HHR 10s	1.50	2.44	1.89
HHR 15 min	1.15	2.23	1.83

Appendix C.3. MATLAB Program code for quantification of EDX maps

```
function output=Potassium(tif_string,grid_size)
a=imread(tif_string);        %reading the image
a=double(a(:,:,1));
[m,n]=size(a);             % reading the size of the image (dimensions)
for i=round(0.66*m):(m-1);    % getting rid of the white part with the
scale bar at the bottom
    x(i)=a(i+1,n)-a(i,n);
end
[~,i]=max(x);
b=double(im2bw(a(1:i,:),0.1));       % Making the grey scale to white
and black (increases contrast of the dots)
[m,n]=size(b);                          % reading the size of the new
cropped image
h=ceil(m/grid_size);                % height of each grid (small box)
w=ceil(n/grid_size);                % width of each grid (small box)
b(h*grid_size,w*grid_size)=0;       % Assigning a dummy matrix for the
storage of the values to be generated
number=zeros(grid_size);             % Giving each of them a value of
zero as a starting point
for j=1:grid_size                                % Actual calculation of
dots in each grid (box)
    for k=1:grid_size
        c=b(1+h*(j-1):h*j,1+w*(k-1):w*k);
        d=bwconncomp(c,1);                % In-built function to count
the dots
        number(j,k)=d.NumObjects;            % Number of dots in each
grid (box) and then the matrix of it
    end
end
output(:,:,1)=number;                        % Number of dots as output
output(:,:,2)=100*(number./(h*w));          % Percentage area as output
```

```
%% Heat Map Generator
e=max(max(number));
map=number/e;
map=uint8(map*255);
for j=1:grid_size
    for k=1:grid_size
        f(1+h*(j-1):h*j,1+w*(k-1):w*k)=map(j,k);
    end
end
f=uint8(f);
figure(1)
imshow(b)
figure(2)
imshow(f)
```

APPENDIX D. SUPPLEMENTARY INFORMATION FOR CHAPTER 5

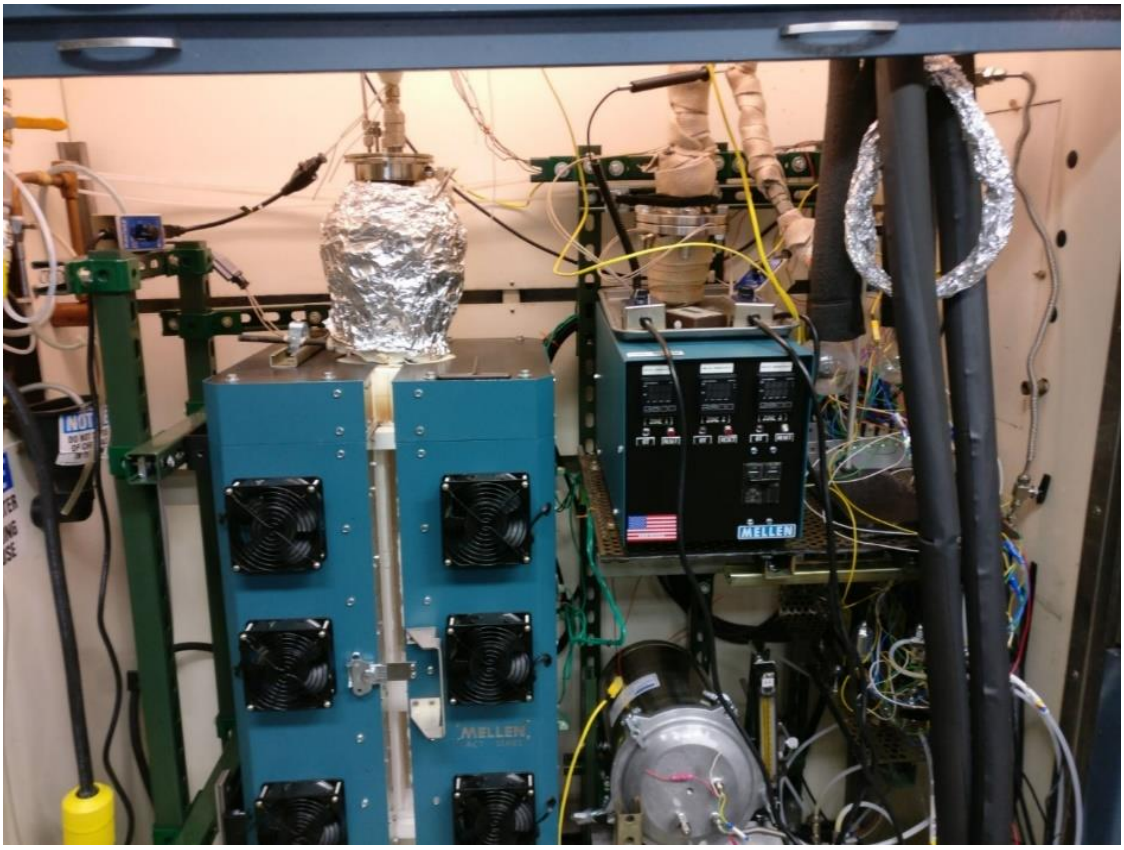

Figure D.1. Picture of the bubbling fluidized bed reactor setup.

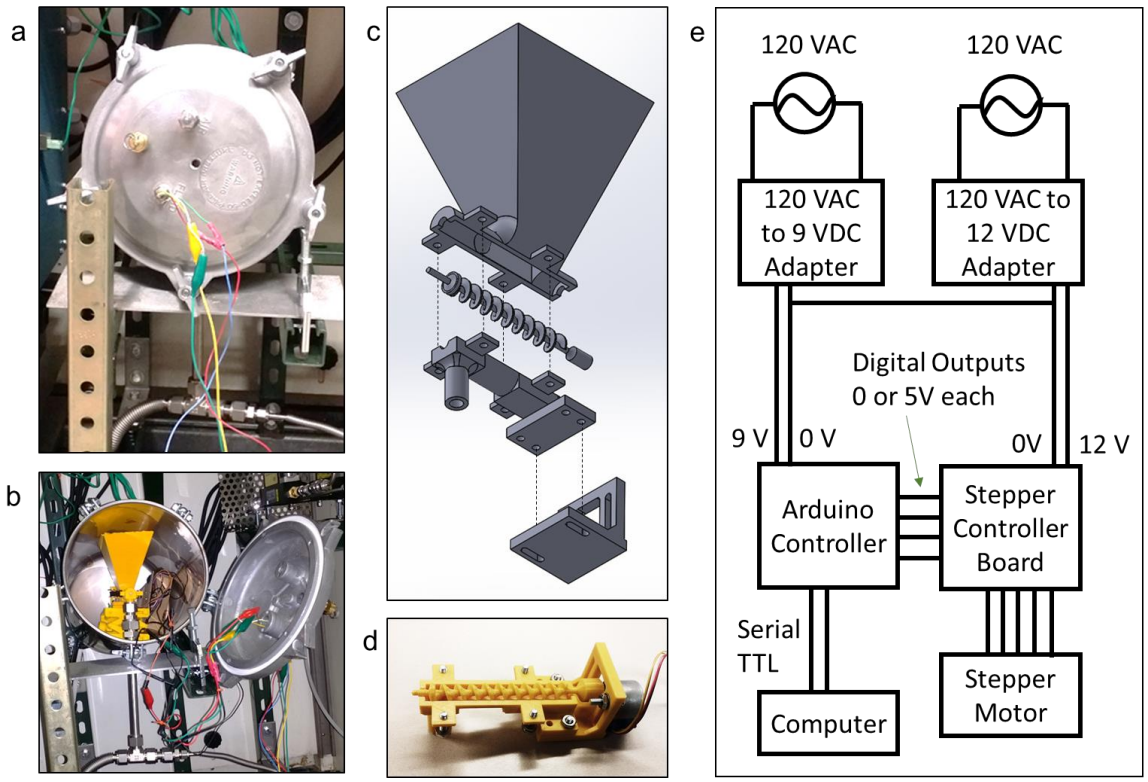

Figure D.2 a. Assembled pressure chamber for the screw feeder. b. Opened chamber showing the feeder inside c. Solidworks model for the feeder d. Feeder interior without the top e. Circuit diagram for the feeder motor.

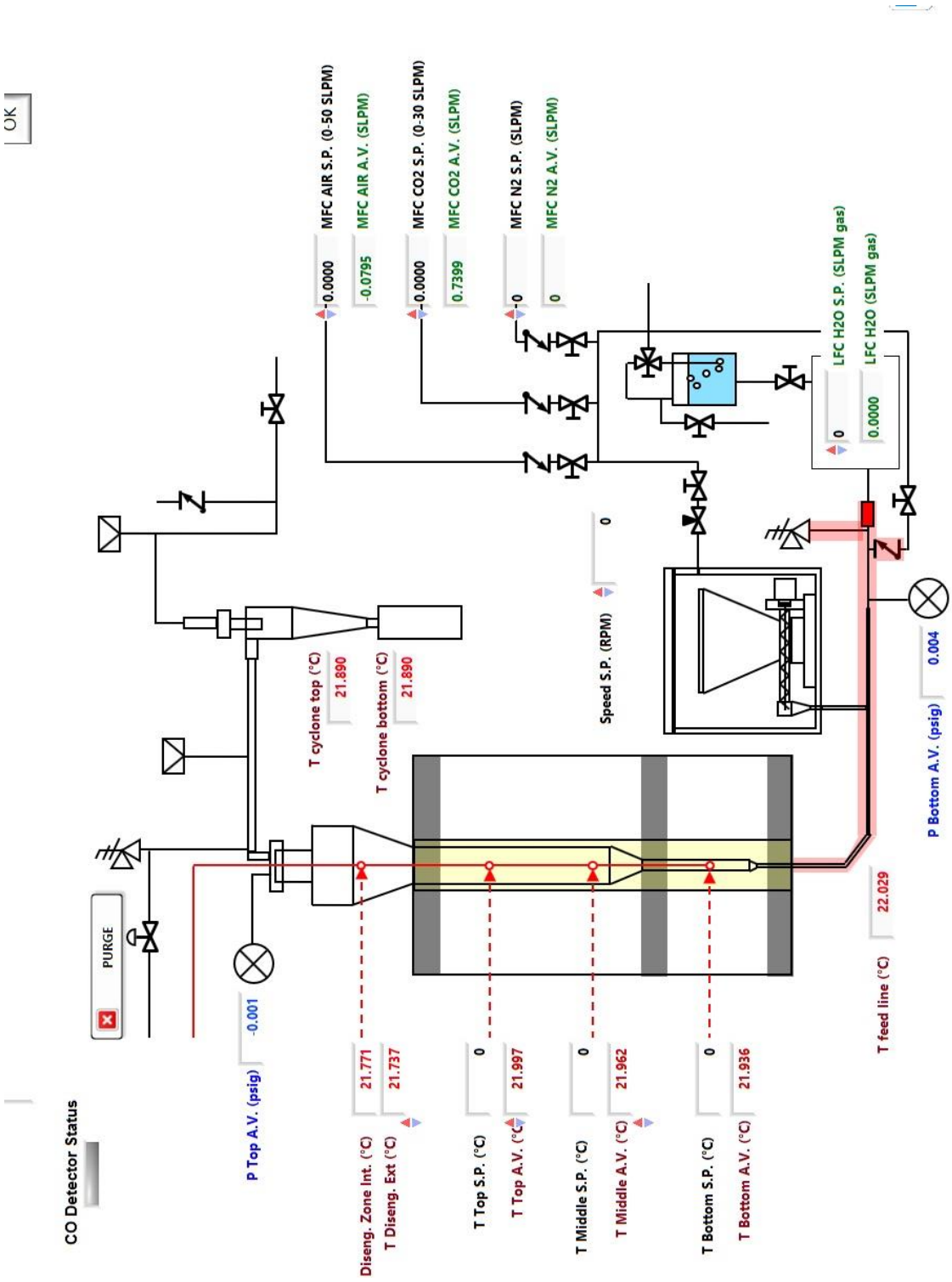

Figure D.3. LabView graphical user interface showing temperature, pressure and flow rate signals along with gas flow control capability.

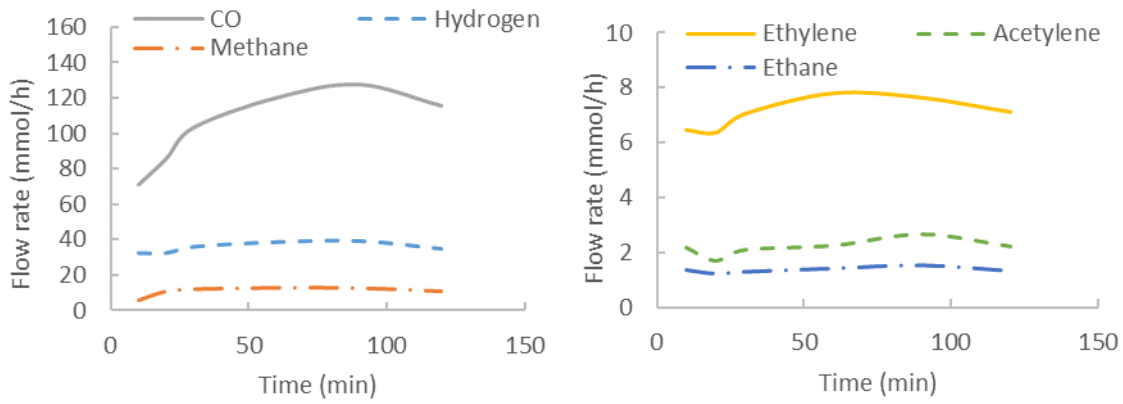

Figure D.4. Product gas flow rates from the CO_2 gasification of pine powder in the BFBR at 815 °C, 12 SLPM total gas and 7.26 g/h feed flow rate with a. major components b. minor components (nitrogen and CO_2 free basis).

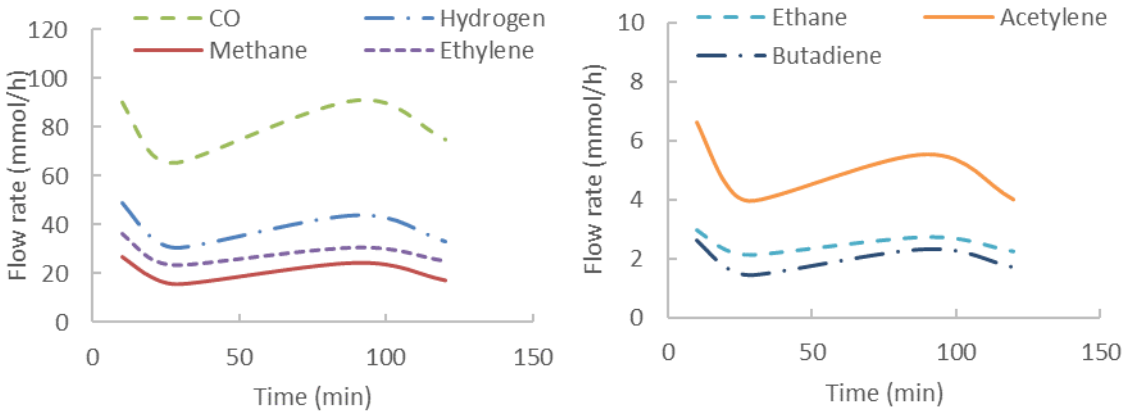

Figure D.5. Product gas flow rates from the CO_2 gasification of RDF pellets in the BFBR at at 815 °C, 18 SLPM total gas and 7 g/h feed flow rate with a. major components b. minor components (nitrogen and CO_2 free basis).

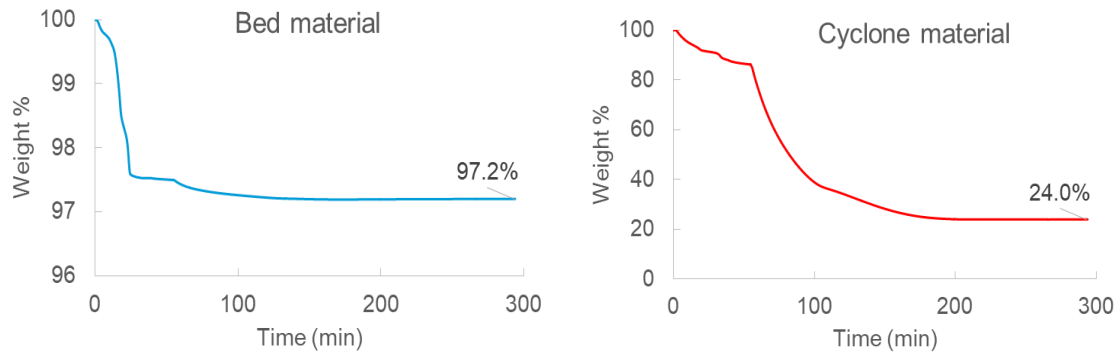

Figure D.6. TGA weight loss profile of the a. bed material and b. cyclone material obtained from the CO_2 gasification of RDF pellets in the BFBR at 815 °C, 18 SLPM total gas and 7 g/h feed flow rate.

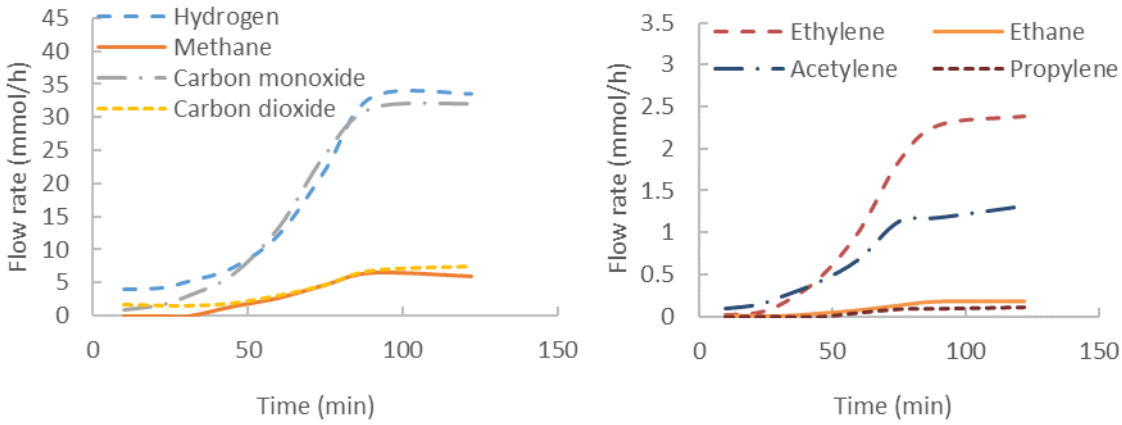

Figure D.7. Product gas flow rates from the steam gasification (20% steam, 80% N_2) of pine powder in the BFBR at 815 °C in the middle zone and 830 °C in the bottom zone, 15 SLPM total gas and 2.5 g/h feed flow rate with a. major components b. minor components (nitrogen free basis).